



Fifth Quarterly Report Phase II September 1, 2010

Prepared by
Prof. Nariman Farvardin, Provost
Principal Investigator and EERC Project Director

Prof. Avram Bar-Cohen, Chair
EERC Project Deputy Director

Dr. Azar Nazeri
EERC Research Manager



THE UNIVERSITY OF MARYLAND AND THE PETROLEUM INSTITUTE OF ABU DHABI, UAE

EERC Key Contributors

University of Maryland – College Park, MD, USA

Shapour Azarm
Balakumar Balachandran
David Bigio
Hugh A. Bruck
K.Y. Choi
Nikil Chopra
Avram Bar-Cohen
Serguei Dessiatoun
Bryan Eichhorn
Ashwani K. Gupta
Satyandra K. Gupta
Yunho Hwang
Greg Jackson
P.K. Kannan
Mohammad Modarres
Reinhard Radermacher
Amir Shooshtari

Petroleum Institute – Abu Dhabi, UAE

Youssef Abdel-Majid
Ahmed Al Shoaibi
Saleh Al Hashimi
Ebrahim Al-Hajri, Returning ADNOC Scholar
Ali Almansoori
Mohamed Alshehhi
Sai Cheong Fok
Afshin Goharzadeh
Didarul Islam
Hamad Karki
Isoroku Kubo
Ahmed Nafees
Michael Ohadi
Peter Rodgers
Abdenmour Seibi

Table of Contents

EERC Key Contributors	ii
Table of Contents	iii
Executive Summary	v
Introduction	1
Individual Project Reports	10
Thrust 1: Energy Recovery and Conversion	11
Sulfur Recovery from Gas Stream using Flameless and Flame Combustion Reactor A.K. Gupta, A. Al Shoaibi	12
Evaluating Solid Oxide Fuel Cell Systems for Operation on Petroleum Off-Gases with Contaminants G. Jackson, B. Eichhorn, A. Almansoori, A. Nafees	35
Separate Sensible and Latent Cooling with Solar Energy R. Radermacher, Y. Hwang, I. Kubo	43
Waste Heat Utilization in the Petroleum Industry R. Radermacher, Y. Hwang, S. Al Hashimi, P. Rodgers	48
Thrust 2: Energy-Efficient Transport Processes	55
Multidisciplinary Design and Characterization of Polymer Composite Seawater Heat Exchanger Module P. Rodgers, A. Bar-Cohen, S.K. Gupta, D. Bigio, H.A. Bruck	56
Study on Microchannel-Based Absorber/Stripper and Electrostatic Precipitators for CO ₂ Separation from Flue Gas S. Dessiatoun, A. Shooshtari, M. Ohadi, A. Goharzadeh	78
Microreactors for Oil and Gas Processes Using Microchannel Technologies S. Dessiatoun, A. Shooshtari, K.Y. Choi, M. Ohadi, A. Goharzadeh	98
Thrust 3: Energy System Management	115
Integration of Engineering and Business Decisions for Robust Optimization of Petrochemical Systems S. Azarm, P.K. Kannan, A. Almansoori, S. Al Hashimi	116

Dynamics and Control of Drill Strings B. Balachandran, H. Karki, Y. Abdelmagid, S.C. Fok	129
Studies on Mobile Sensor Platforms B. Balachandran, N. Chopra, H. Karki	140
Development of a Probabilistic Model for Degradation Effects of Corrosion-Fatigue Cracking in Oil and Gas Pipelines M. Modarres, M. Chookah, A. Seibi	154

Executive Summary

The following is a summary of the major project activities that have taken place over the completed quarter. For more detail, see the individual reports in the last section of this report.

Thrust 1: Energy Recovery and Conversion

Sulfur Recovery from Gas Stream using Flameless and Flame Combustion Reactor

A.K. Gupta, A. Al Shoaibi

- Fabricated experimental setup for hydrogen sulfide experiments with optical access for in-situ non-intrusive examination. Setup meets safety requirements for UMD environmental safety department.
- Investigated the effect of H_2S/O_2 equivalence ratio on combustion products. A methane/air mixture was used, under slightly lean conditions, as a heat source into which hydrogen sulfide was injected with different concentrations to obtain the aimed equivalence ratio. A gas chromatograph equipped with TDC and FPD was used for combustion products ultimate gas analysis.
- Identified excited sulfuric compounds emissions (SO_2 and S_2) and hydrocarbons radicals (OH , CH , and C_2) non-intrusively using an Acton 300i spectrometer coupled with ICCD-576-S/RB-G camera. Different spectrometer gratings were used according to the required spectral resolution.

Solid Oxide Fuel Cell Systems for Operation on Petroleum Off-Gases with Contaminants

G. Jackson, B. Eichhorn, A. Almansoori, A. Nafees

- Extended further the Aspen Plus fuel cell plant model (originally intended as a summer internship project).
- Completed rig modifications for H_2S testing and fabrication of many cells for durability studies with sulfur contamination.

Separate Sensible and Latent Cooling with Solar Energy

R. Radermacher, Y. Hwang, I. Kubo

- Created a Labview interface to record the experimental measurements.
- Finished the aluminum frame construction.
- Finished the supply, exhaust and conditioned space ducts.

Waste Heat Utilization in the Petroleum Industry

R. Radermacher, Y. Hwang, S. Al Hashimi, P. Rodgers

- Modeled the following in HYSYS:
 - CO_2 liquefaction and compression
 - APCI cycle optimization
 - Optimization of different gas-turbine triple-combined cycle configurations
- Prepared paper for ADIPEC 2010 conference
- Performed GASCO ASAB waste-heat energy audit

Thrust 2: Energy-Efficient Transport Process Projects

Multidisciplinary Design and Characterization of Polymer Composite Seawater Heat Exchanger Module

P. Rodgers, A. Bar-Cohen, S.K. Gupta, D. Bigio, H.A. Bruck

- Designed and machined injection molds for the selected spiral and L-channel geometries. Created injection-molded test samples at fixed system parameters and materials.
- Applied image processing methods to determine fiber orientation in experimental specimens and compared to Moldflow predictions.
- Installed upgraded experimental rig for testing polymer heat exchangers. It can accommodate a larger laboratory heat exchanger with an increased heat transfer rate, which will also increase the temperature differences across the heat exchanger, thereby reducing the relative uncertainty caused by the thermocouple measurements (~5%).
- Constructed a new test apparatus for hygrothermal aging conditions under load to complement the previous hygrothermal aging studies without load.
- Designed and constructed injection mold for producing specimens complying with ASTM international guidelines that are compatible with clevises of aging apparatus.
- Hygrothermally aged carbon-filled nylon testing specimens under tensile load at 60°C in an aqueous solution with a salinity of 45g/kg.
- Tensile tested carbon-filled nylon specimens that were stressed during aging to determine mechanical properties.
- Developed a finite element analysis (FEA) model using hygrothermally aged mechanical properties to assess feasibility of replacing metallic heat exchangers at the Das Island liquefied natural gas facility with polymer composite heat exchangers.
- Modified heat exchanger geometry to reduce stresses experienced by polymer composite heat exchanger. The additional water-side fin significantly reduced stresses and strains in the module.
- Assessed feasibility of modeling orthotropic heat exchanger module as an isotropic model with averaged properties. The substantial variation between the isotropic and orthotropic models may be an indication that a full anisotropic model should be developed to determine if the orthotropic model replicates the anisotropic model.

Study on Microchannel-Based Absorber/Stripper and Electrostatic Precipitators for CO₂ Separation from Flue Gas

S. Dessiatoun, A. Shooshtari, M. Ohadi, A. Goharzadeh

- Performed literature review.
- Identified target alkanolamine suitable for experimental study.
- Designed and fabricated laboratory-scale microchannel-based CO₂ separator.
- Performed experimental study on the absorption in microchannels.
- Developed a numerical/analytical model to enhance understanding of the process.

Microreactors for Oil and Gas Processes Using Microchannel Technologies

S. Dessiatoun, A. Shooshtari, M. Ohadi, A. Goharzadeh, E. Al-Hairi

- Identified the target reaction as polyethylene and polypropylene production
- Selected the target polymerization process of economical significance to the Abu Dhabi polymer industry.
- Selected the type and size of catalyst particles to be used in the process as 1-2 μm.
- Began the design and fabrication of a microreactor capable of selected polymerization processes.
- Began visualization study of mixing in microchannels.

Thrust 3: Energy System Management

Integration of Engineering and Business Decisions for Robust Optimization of Petrochemical Systems

S. Azarm, P.K. Kannan, A. Almansoori, S. Al Hashimi

- Remodeled the reactor-distillation process using process engineering simulation software: Aspen HYSYS:
- Established a computerized connection between Aspen HYSYS and Matlab programs:
- Reformulated the integrated business and engineering decision-making problem and obtained optimized decisions:
- Continued developing the Approximation Assisted Multi-objective collaborative Robust Optimization (AA-McRO) approach. Based on the AA-McRO approach, a paper is being prepared and will be submitted to 2010 AIAA/ISSMO MA&O conference. An extended abstract of this paper was recently accepted for this conference, and we are in the process of preparing the full paper.

Dynamics and Control of Drill Strings

B. Balachandran, H. Karki, Y. Abdelmagid

- Carried out experimental and numerical parametric investigations to gain greater understanding of drill-string dynamics. Experimental results were in good agreement with numerical model.
- Compared UMD's experimental data with data collected from field experiments. Both laboratory and field results captured similar bumping, rolling and sliding motions.

Studies on Mobile Sensor Platforms

B. Balachandran, N. Chopra, H. Karki, S.C. Fok

- Performed numerical simulations to gain fundamental insights. These simulations complement the source localization work reported previously.
- Acquired ground-based mobile agents to perform experimental measurements. The ground-based agent houses a microcontroller, two encoders, infrared sensors and a laser sensor.

Development of a Probabilistic Model for Degradation Effects of Corrosion-Fatigue Cracking in Oil and Gas Pipelines

M. Modarres, A. Seibi

- Performed literature review on specifying the stress dependencies of creep curve parameters.
- Reviewed mathematical and statistical methods for creep data evaluation.
- Applied mathematical models and statistical methods for creep data evaluation.
- Applied mathematical methods to pitting corrosion data obtained from Summer 2010 intern program.
- Separated corrosion fatigue WinBugs model program.
- Categorized creep model.
- Designed and made two three-point grips to apply definite stress on the samples.

Introduction

The fifth quarter of the EERC saw continued progress on the individual research projects and productive meetings between EERC members. Another successful summer internship program was completed at UMD, details of which are given below.

Summer 2010 Internship At University of Maryland

In the third year of the EERC Summer Internship program, eight PI students—seven from Mechanical Engineering and one from Electrical Engineering—were sponsored by five UMD professors. Each student worked with a UMD professor and graduate student supervisors on active EERC research projects. Our summer interns gained valuable hands-on experience in the labs while working with professors and students from culturally diverse backgrounds. Students also spent their free time exploring cultural, historical and scientific hallmarks, such as the Smithsonian National Air and Space Museum and monuments in Washington D.C., and traveling to such popular places as New York City and Niagara Falls.

Following is a summary of the research projects and tasks during the six-week internship of the eight students this summer.

- **Students: Omar Abdulla Ahmed Saif Hareb Al Suwaidi and Ghadayer Ali Hashel Hamad Al Kaabi**
- **Professor: B. Balachandran**
- **Project: Dynamics and Control of Drill Strings**

Omar Al Suwaid and Ghadayer Al Kaabi worked with Dr. Balachandran's group on Dynamics and Control of Drill Strings, studying drill string dynamics in both vertical and horizontal configurations. They became familiar with the concepts, processes, and structures of research by working with graduate students Nick Vlajic and Chien-Min Liao in the Vibrations Lab, where they learned about signal processing with Matlab and the data acquisition software Lab View. They also learned the fundamental usage of accelerometers through their study of the vibrations of vertical drill strings using an accelerometer stacked at the top of a drilling string; this allowed them to examine the deflection of the beam. They read materials about digital data acquisition and Fourier transforms, DFTs, and FFTs, which are useful tools for analyzing the vibration signals. They also spent a major portion of their time building the structural frame for a horizontal drill string experiment, as shown in Figure 1.

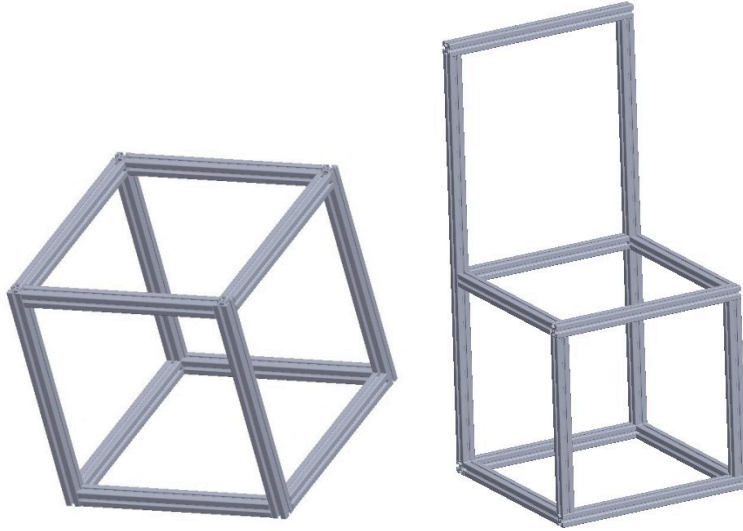


Figure 1. Stand drawings for the horizontal drilling string experiment.

During this internship they also attended events organized by Mechanical Engineering Graduate Student Association (MEGA), such as sessions on evaluating the impact of low-medium current densities on thermal fatigue, improving the reliability of solder interconnects, and mimicking how the fly hears.



Figure 2. Omar (left) and Ghadayer working on the vertical drill-string platform.



Figure 3. Omar and Ghadayer presenting their work on August 10th.

- **Students:** Yahya Fathi Ahmed Qaroot and Anouar Abdul Kader Zebidi
- **Pofessors:** Dr. S. Dessiatoun and Dr. A. Shoostari
- **Project:** Microreactors for Oil and Gas Processing Using Microchannel Technologies

Yahya Qaroot and Anouar Zebidi primarily focused on studying and using microreactor technology for the polymerization of olefin—that is, the production of polyethylene. Polyethylene is the world’s most used plastic, with a production rate reaching 80 million metric tons per year. Microreactors are two orders of magnitude smaller than conventional reactors, providing a significant increase in process controllability, a reduction of energy consumed, and better product quality and output. The main objectives in the project were to build and test a microchannel for ethylene polymerization. The microchannel was built using equipment found in the lab, such as syringes, T-junctions, and tubes. Then, the microchannel was mounted on a metal support, and a pump was used to mix water with the ethanol-catalyst mixture. The testing process was captured using a high-speed camera, where the mixture (water and ethanol-catalyst) was pumped through the channel with different flow rates in order to see the different type of flows. This process was repeated a number of times, each time with a different concentration of catalyst in ethanol. Finally, a matrix of concentrations and flow rates with a video segment corresponding to each concentration and flow rate was produced to help determine which concentration and speed of particle is most suitable for the dispersion of the catalyst particles in the water-ethanol solution.



Figure 4. Yahya working in the lab.



Figure 5. Anouar working in the lab.

- **Student: Tariq Ibrahim Abdul Rahim Al Jallad**
- **Professor: Dr. R. Radermacher**
- **Project: Separate Sensible and Latent Cooling with Solar Energy**

Tariq Al Jallad worked on the “Separate Sensible and Latent Cooling with Solar Energy” project. This project uses electric and thermal energy gained from photovoltaic cells (solar cells) to run a vapor compression cycle to cool an enclosed space such as a room. The project uses this system as efficiently as possible by running a desiccant wheel using the thermal energy acquired from the solar cells. The desiccant wheel dehumidifies the incoming air from outside before it enters a vapor compression cycle (VCC), which runs on the electrical energy acquired from the solar cells. As the air is less humid when it enters the VCC, the cycle should be able to operate at higher evaporator temperatures and pressures since it doesn’t have to accommodate the latent load. This should eventually lead to higher coefficients of performance (CoP).

At the time of this internship, the project was in the experiment-building phase. Tariq worked on building the experiment with Mr. Ali Al Alili, the ADNOC scholar and Ph.D. student in charge of the project. Tariq’s work involved building ducts and sealing them, and mounting different components of the system such as thermocouples, nozzles, meshes, air mixers, and pressure transducers. According to Tariq, this internship was very helpful in gaining hands-on experience, as well as learning about different standards and procedures through existing literature related to the work.



Figure 6. Tariq in the lab with the experimental setup.

- **Student: Taher Munther Taher Abu Seer**
- **Professor: Dr. M. Modarres**
- **Project: Development of Probabilistic Model for Degradation Effects of Corrosion-Fatigue Cracking in Oil and Gas Pipelines**

This project is a study of pitting corrosion rates in pipelines. This is the most dangerous type of corrosion due to the difficulties in detecting the pits and their growth, and thus a model is needed to capture the pit crack initiation and growth phase in the entire corrosion-fatigue process. The objective of the project is to improve the Kondo model, which represents pit-depth growth with time. This has been achieved by expanding the model and studying the dependencies of the constants on various physical parameters such as temperature and stress. Several experiments at different temperatures and stresses were performed on samples at three time-intervals at a constant concentration of H_2S as the corrosive medium. The pit depth and pit density of each sample was measured. Meanwhile, the distribution of the pit density and pit depth was observed using Weibull++ software, and the reliability of the material was studied in addition to the failure rate. Moreover, the parameters of the lognormal distribution were estimated using various methods such as paper plotting, linear regression, maximum likelihood estimator and Bayesian estimation using linear regression with matrices.



Figure 7. Taher in the lab.



Figure 8. Taher presenting his work.

- **Students: Ahmad Faissal El Ali and Osama Aneel Anwar Al Ameri**
- **Professor: Dr. B. Balachandran**
- **Project: Studies on Mobile Sensor Platforms**

Mobile sensor platforms can be employed in a variety of operations, including environmental and structural health monitoring operations in harsh and remote environments. The overall objective of this project is to carry out a combined analytical, numerical, and experimental effort to develop

mobile sensor platforms and appropriate simultaneous localization and mapping (SLAM) algorithms for cooperative sensor platforms to operate in a harsh environment. Due to the limited timeline of the project, the mentor decided to give the students smaller-scale tasks that would help meet the objectives of the main project. The students were given a robot and were asked to program it to make it able to avoid obstacles. The four wheels of the robot are connected in pairs by conveyor belts. A motor is connected to each pair to control the movement of the robot in all directions. In addition, the robot is provided with three ultrasonic sensors, located on the front and the right and left sides, in order to provide scans from multiple directions at the same time. Since one of the students was familiar with C++ language, the students chose to use it to program the robot.

Presentations: The internship program was wrapped up with a luncheon and student presentations of their projects in the presence of their supervisors.

Cultural Experience: When the students were not occupied in their labs, they took some time to visit several American cities and cultural landmarks, such as historical sites in Washington D.C. and New York City.



Figure 9. From left to right, Osama, Ahmad and Anouar outside the White House.



Figure 10. At the Smithsonian Air and Space Museum, Washington, D.C.



Figure 11. At the Air and Space Museum, Washington, D.C.



Figure 12. In front of the Statue of Liberty, New York.



Figure 13. On top of the Empire State Building.



Individual Project Reports



Thrust 1
Energy Recovery and Conversion

Sulfur Recovery from Gas Stream using Flameless and Flame Combustion Reactor

UMD Investigators: Ashwani K. Gupta
GRA: Hatem Selim
PI Investigator: Ahmed Al Shoaibi
Start Date: October 2006

1. Objectives / Abstract

The main objective is to obtain fundamental information on thermal process of sulfur recovery from sour gas by conventional flame combustion as well as flameless combustion, using numerical and experimental studies. Our ultimate goal is to determine optimal operating conditions for enhanced sulfur conversion. Therefore, an experimental study of the flameless combustion processes of the Claus furnace is proposed so that the results can be used in the normal flame process for determining improved performance. In this study we will explore different operating conditions and perform in flame and exhaust gas analyses of both flame and flameless modes of reactor operation in order to seek our quest for better understanding of the process with the goal to attain enhanced sulfur capture efficiency.

Specific objectives are to provide:

- A comprehensive literature review of the existing flame combustion process for sulfur removal with special reference to sulfur chemistry
- Near isothermal reactor conditions and how such conditions assist in the enhanced sulfur recovery process
- CFD simulation of the flame and flameless combustion in the furnace.
- Determination of the chemical kinetics and the major reaction pathways to seek for high performance
- Design of a reactor for experimental verification of the numerical results
- Measurements and characterization of the combustion furnace under various conditions, including the conditions that utilize high temperature air combustion principles for flameless combustion
- Experiments with different sulfur content gas streams using the flame and flameless combustion furnace modes of operation.
- Installation of the appropriate diagnostics for quantification of stable and intermediate sulfur compounds in the process and exit stream
- Flow, thermal and chemical speciation characteristics of the reactor
- Product gas stream characteristics and evaluation of sulfur recovery and performance in the process

2. Deliverables

- Experimental setup for hydrogen sulfide experiments was fabricated with optical access for in-situ non-intrusive examination. The experimental setup was placed inside a fume hood, which was tested for leaks and connected with an exhaust system that provides

the required induced air velocity for the experiments as assigned per the environmental safety department at UMD. The setup is also equipped with a hydrogen sulfide sensor for hydrogen sulfide leak detection.

- We have investigated the effect of H_2S/O_2 equivalence ratio on combustion products. A methane/air mixture was used, under slightly lean conditions, as a heat source into which hydrogen sulfide was injected with different concentrations to obtain the aimed equivalence ratio. A gas chromatograph equipped with TDC and FPD was used for combustion products ultimate gas analysis.
- We have identified excited sulfuric compounds emissions (SO_2 and S_2) and hydrocarbons radicals (OH, CH, and C_2) non-intrusively using an Acton 300i spectrometer coupled with ICCD-576-S/RB-G camera. Different spectrometer gratings were used according to the required spectral resolution.

3. Executive Summary

During the reported quarter, progress continued with major focus on the experimental part of the project. An experimental setup has been designed, fabricated and assembled for hydrogen sulfide experimentation. The setup contains a burner and a test section that is optically accessed for non-intrusive examination in the desired test region. A gas chromatograph with FPD detector was used for the detection of sulfur compounds. A spectrometer was used to detect excited emissions of certain species, including sulfur species. The experimental setup was placed inside a fume hood, which was tested and assembled according to the safety regulations of University of Maryland safety department. Two students were present to conduct the experiments due to safety issues associated with the use of H_2S and other sulfur gases. An exhaust duct was attached to the top of the fume hood and connected with an exhaust fan capable of generating the required induced air velocity into the fume hood. For the safety of the researchers, an H_2S purifying respirator was used by each experimenter and a hydrogen sulfide sensor as placed in close proximity of the experimental set-up for any H_2S leak detection.

The experiments started with an examination of the equivalence ratio of the H_2S/O_2 mixture in methane/air combustion. A methane/air mixture as burned under slightly fuel-lean conditions into which H_2S was injected at different concentrations in order to achieve the desired equivalence ratios of the flame. A gas chromatograph equipped with thermal conductivity detector and flame photometric detector was used for gas analysis from within the reactor. A sonic-throat quartz sampling probe was used to extract a representative sample from within the reactor. The sonic throat sampling probe was used to minimize the physical disturbance associated with the probe, alleviate the water cooling requirements, and simultaneously quench the gas sample from the temperature drop associated with the sonic expansion at the sample throat.

The emissions associated with excited sulfur compounds and hydrocarbon radicals that occur under different mixture conditions (fuel-rich, stoichiometric, and fuel-leans) and different flames were examined non-intrusively. An Acton 300i spectrometer coupled with an ICCD-576-S/RB-G camera was used for emissions spectra analysis.

4. Progress

4.1 Experimental Setup for Hydrogen Sulfide Experimentation

An experimental facility for safe hydrogen sulfide experimentation was designed, fabricated and assembled with special focus on optical access in the entire test section. The setup consists of a burner that has two concentric tubes and a bluff body flame stabilizer. A quartz tube reactor was used to provide non-intrusive optical access to the test section. A sonic-throat sampling probe was used for gas sampling. A computer-controlled traverse mechanism was used to position the sampling probe at the desired location in the reactor. The entire experimental setup was placed inside a fume hood, which was examined and approved by the University of Maryland safety department. The fume hood is attached to an exhaust duct, which was connected to a fan to

generate the required induced air velocity according to safety department regulations at the University of Maryland.

4.1.1 Burner Design

A double concentric tube burner was designed and used for all our experiments. The burner has a bluff body stabilizer at the exit to stabilize the flame immediately downstream from the burner exit. The gases inlets varied according to the type of flame desired for the experiments. Figure 1 shows a schematic diagram (left) and photograph (right) of the burner used in the experiments. During all the experiments an oxidizer (air or oxygen) was injected from the annulus, and hydrogen sulfide was injected from the central tube. When methane was used as the fuel, it was premixed with the oxidizer and injected into the outer annulus. However, when hydrogen was used as the fuel, it was premixed with H_2S and the oxidizer was injected only into the annulus.

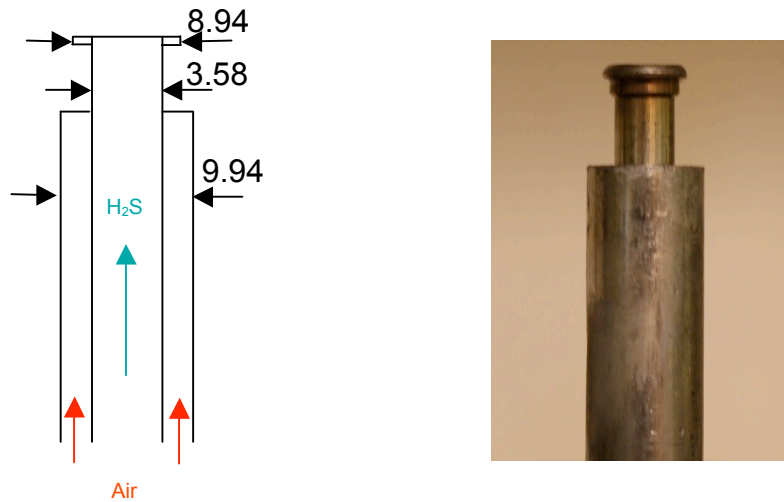


Figure 1. Schematic diagram (left) and photograph (right) of the burner used in the H_2S experiments.

4.1.2 Quartz Tube Reactor

A transparent quartz tube reactor was used for full optical access to the test region for non-intrusive examinations. The reactor is 9 inches in length and 1.6 inch in diameter. Two steel bases were fabricated with proper dimensions for housing the quartz reactor from both ends of the quartz tube. Figure 2 shows a photograph of the burner and quartz reactor assembled in the steel bases.

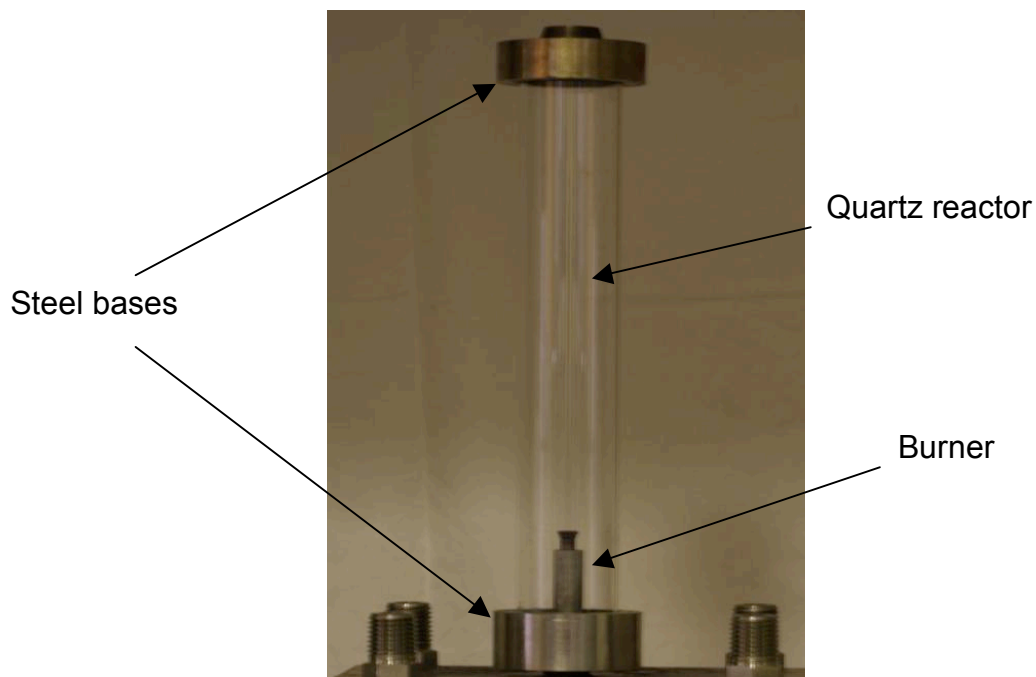


Figure 2. Quartz reactor and flame burner assembled inside steel housing.

4.1.3 Sampling Probe and Traverse Mechanism

A sonic-throat quartz sampling probe was used for extracting gas samples. A computer-controlled traversing mechanism was used to move the sampling probe along the centerline of the reactor. The resolution of its axial distance position is 0.0025 inches (25 microns). The sampling probe throat diameter is on the order of microns so that the flow was choked at its throat. The inner and outer diameters of the probe are 3 and 4 millimeters, respectively. For personnel safety, a purifying respirator was used by the experimenter and a hydrogen sulfide detector was placed in the experimental setup vicinity for leak detection. Figure 3 depicts the traverse mechanism, the purifying respirator for conducting experiments with H₂S gas flames, the H₂S detector and alarm unit (left photo), and the sonic throat sampling probe in a flame (right photo).

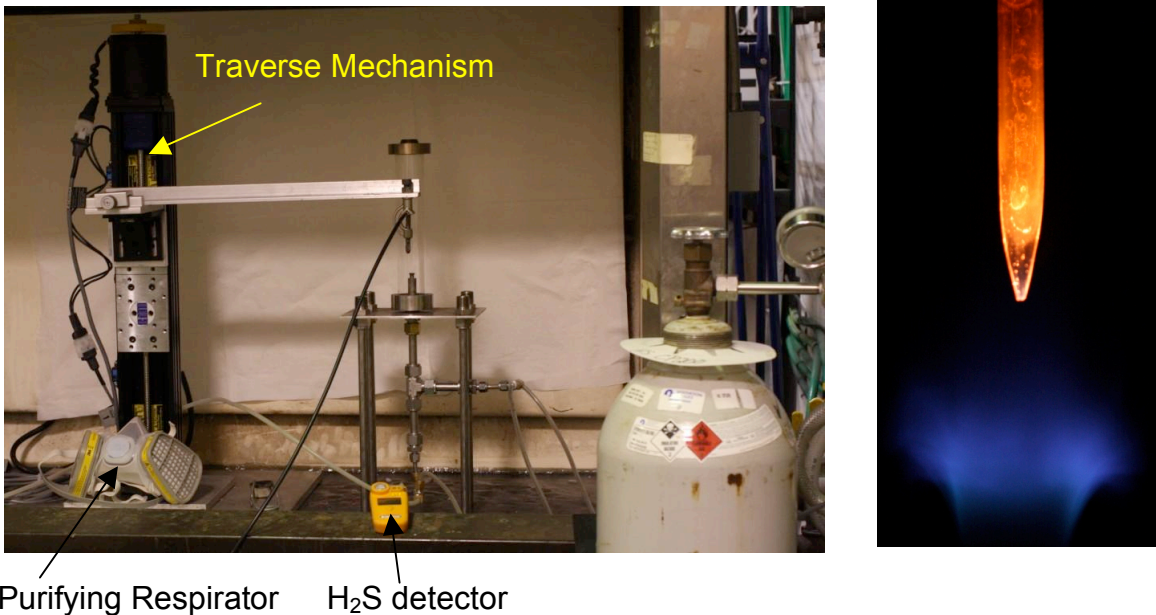


Figure 3. Traverse mechanism, purifying respirator, and H₂S detector (left), and the sampling probe tip (right).

4.1.4 Fume hood and exhaust duct

The entire experimental setup was placed inside the fume hood for safety purposes. The fume hood was connected to an exhaust duct where a fan is used to induce air into the fume hood. According to the University of Maryland safety department regulations, induced air velocity into the hood must be higher than 100 ft/min. The velocity of air induced into the fume hood was measured as 134 ft/min. This assured that levels of hydrogen sulfide were safe for the operator and lab personnel. Figure 4 shows the fume hood with the experimental setup placed inside and the exhaust duct.

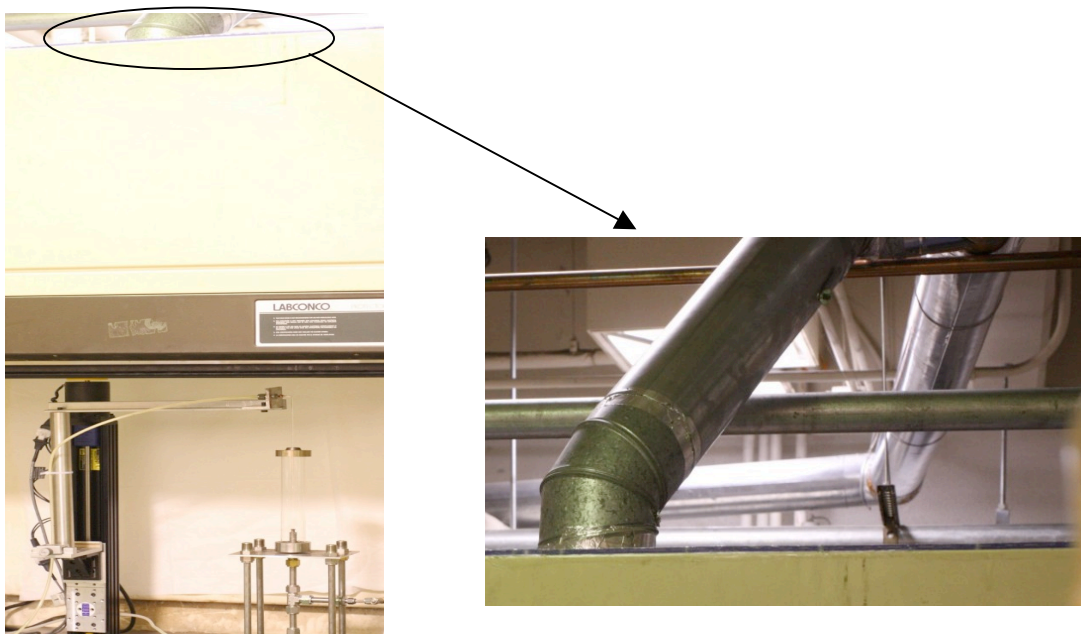


Figure 4. Fume hood and exhaust duct arrangement in the lab scale H₂S facility.

4.2 Effect of H₂S/O₂ Equivalence Ratio on Combustion Products in CH₄/air Flame

The experiments began with an examination of the effect of equivalence ratio of H₂S/O₂ mixture in methane/air combustion. A methane/air mixture was burned under slightly fuel-lean conditions in which H₂S was injected with different flow rates to vary the H₂S/O₂ equivalence ratio. Three H₂S/O₂ equivalence ratios have been studied during this quarter. Note that per the change of focus on primarily experiments at the May 2-4, 2010 meeting (as agreed upon by Dr. Ahmed Al Shoaibi, Ashwani Gupta and Azar Nazeri), we agreed to have a working experimental facility by August 2010. However, with significant help from other students on this project, we were able to obtain experimental results also. These are provided in the following.

The examined equivalence ratios ranged between Claus conditions, $\phi=3$ (very fuel-rich conditions), stoichiometric conditions ($\phi=1$), and very fuel-lean conditions ($\phi=0.5$). The sonic-throat sampling probe was used for gas sampling along the centerline of the reactor by using a computer-controlled traverse mechanism to position the sampling probe tip relative to the reactor position. The gas chromatograph equipped with a thermal conductivity detector and flame photometric detector was used for sample analysis.

Experimental procedure:

Adjust methane/air equivalence ratio to slightly fuel-lean conditions. Methane flow rate of 0.97 lit/min, and air flow rate of 9.7 were used to provide an equivalence ratio of 0.952 so that the excess oxygen flow rate is 0.068 lit/min.

Take gas samples at different axial locations, normally at (0, 0.25, 0.5, 0.75, 1.0, 1.5, 2.0, 2.5, 3.0, 4.0, 5.0, 6.0, 7.0, and 7.5) inches along the centerline of the reactor.

Introduce H₂S with the required flow rate to achieve a certain H₂S/O₂ equivalence ratio. For Claus conditions H₂S flow rate is 0.137 lit/min, for stoichiometric conditions H₂S flow rate is 0.046 lit/min, and for fuel-lean conditions H₂S flow rate is 0.023 lit/min.

Repeat step 2.

Change H₂S flow rate to a different equivalence ratio and repeat step 2.

The whole experiment from step 1 to step 5 was repeated three times for data repeatability and reliability.

The mole fraction of hydrogen at different equivalence ratios, both without and with addition of H₂S into the flame, is shown in Figures 5, 6, 7, and 8. The results were repeated three times. In the case of methane/air combustion, the hydrogen mole fraction decreased along the reactor centerline to reach zero mole fraction at the exit of the reactor. This is attributed to the fuel-lean conditions of the combustion, which help in the complete combustion of all the reactants. On the other hand, with H₂S addition, the hydrogen mole fraction peaks at a certain value and does not decay to zero value where its asymptotic value increases with the increase in hydrogen sulfide added to the reacting mixture. The hydrogen sulfide results showed good repeatability in terms of both qualitative and quantitative points of view. The small discrepancy in the mole fraction of hydrogen observed at low axial distance (close to burner exit) is attributed to molecular diffusion effects where the chemical reactions are dominant.

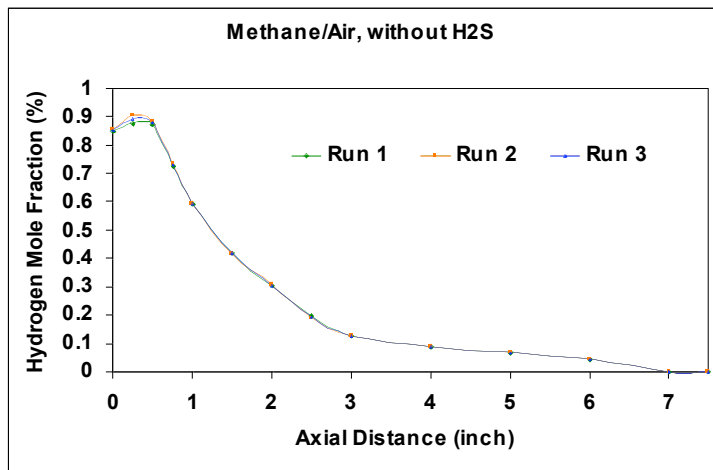


Figure 5. Hydrogen mole fraction, methane/air without H₂S.

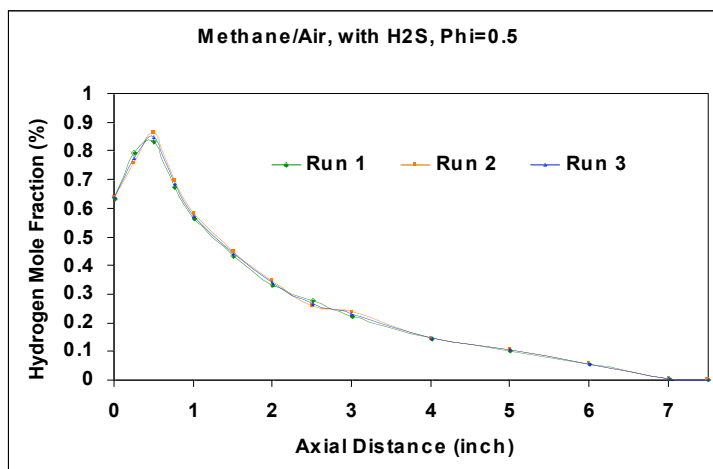


Figure 6. Hydrogen mole fraction, methane/air with H₂S, Phi=0.5.

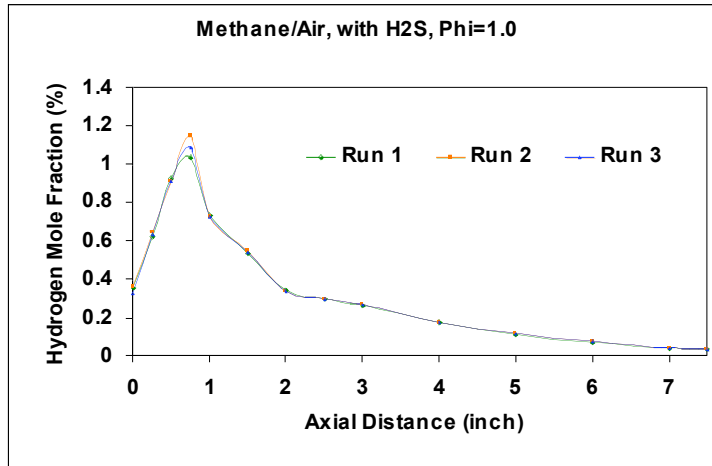


Figure 7. Hydrogen mole fraction, methane/air with H₂S, Phi=1.0.

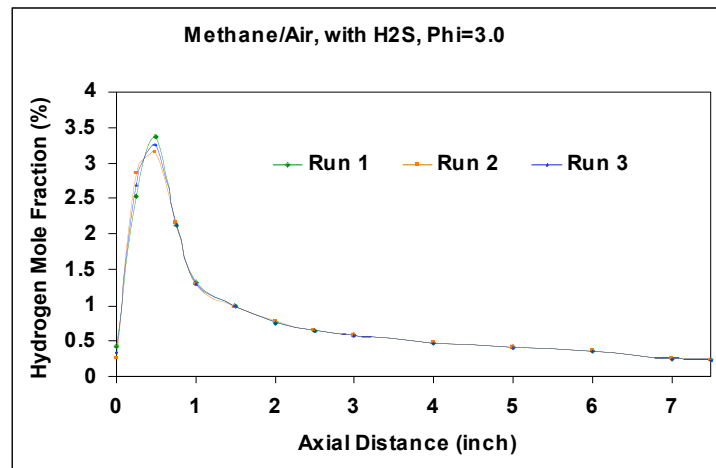


Figure 8. Hydrogen mole fraction, methane/air with H₂S, Phi=3.0.

The mole fractions of carbon monoxide, without and with the addition of H₂S at different equivalence ratios, are shown in Figures 9, 10, 11, and 12. The results are repeated three times to assure some data repeatability. For methane/air combustion, the carbon monoxide fraction decreases along the reactor centerline to reach zero mole fraction at the exit. Similarly, this is attributed to the fuel-lean conditions. However, with H₂S addition, the CO mole fraction increases to a peak, then it decays to an asymptotic value, but never reaches zero value. This is attributed to the direct effect of hydrogen sulfide addition, which causes depletion in the oxidizing medium. Similar to the H₂ mole fraction, the data showed good repeatability in terms of both qualitative and quantitative values.

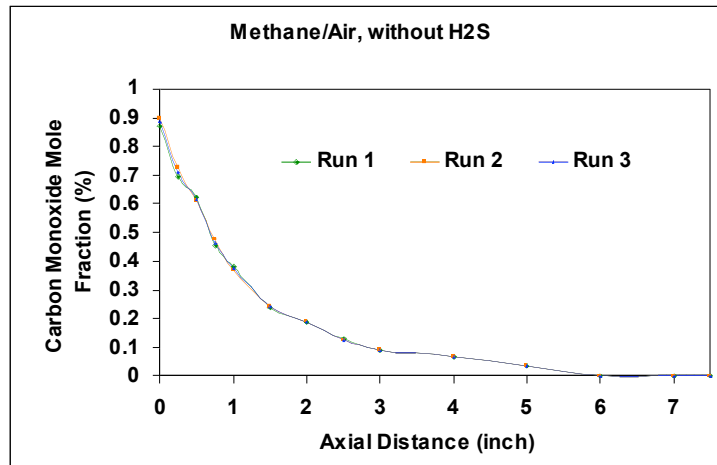


Figure 9. Carbon monoxide mole fraction, methane/air without H₂S.

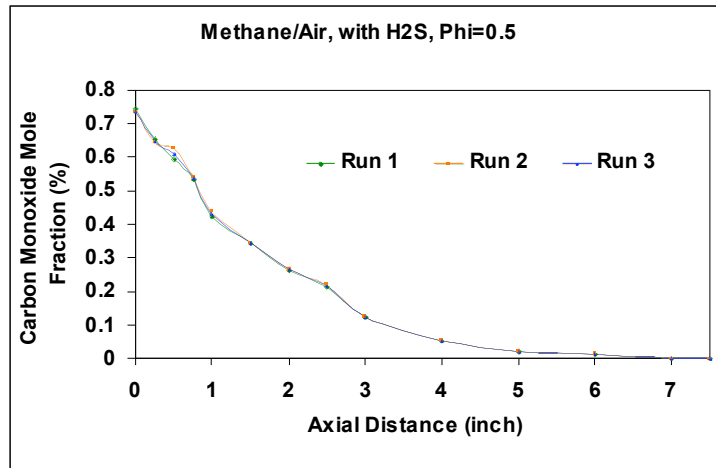


Figure 10. Carbon monoxide mole fraction, methane/air with H₂S, Phi=0.5.

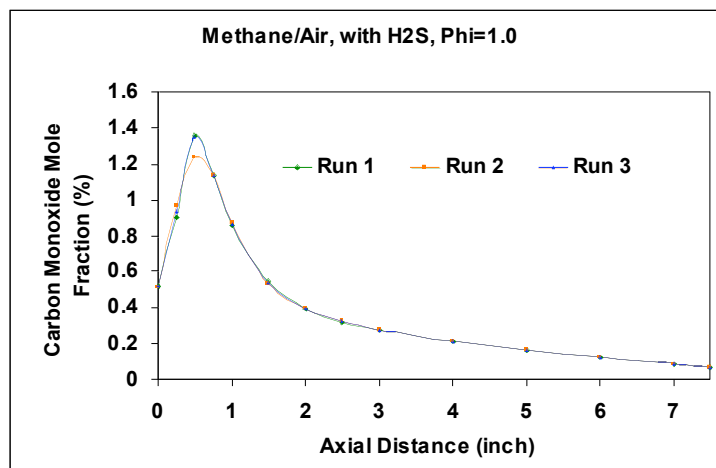


Figure 11. Carbon monoxide mole fraction, methane/air with H₂S, Phi=1.0.

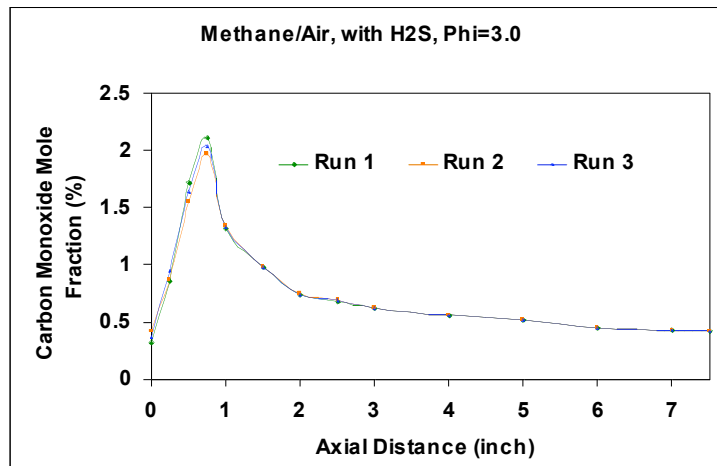


Figure 12. Carbon monoxide mole fraction, methane/air with H₂S, Phi=3.0.

The mole fractions of carbon dioxide and nitrogen without and with addition of H₂S at different equivalence ratios are shown in Figures 13, 14, 15, and 16. The results obtained during three different times showed good repeatability of data. For both, without and with hydrogen sulfide addition, the mole fraction of nitrogen and carbon dioxide did not show any significant change as compared to their average mole fraction value. Good data repeatability was obtained.

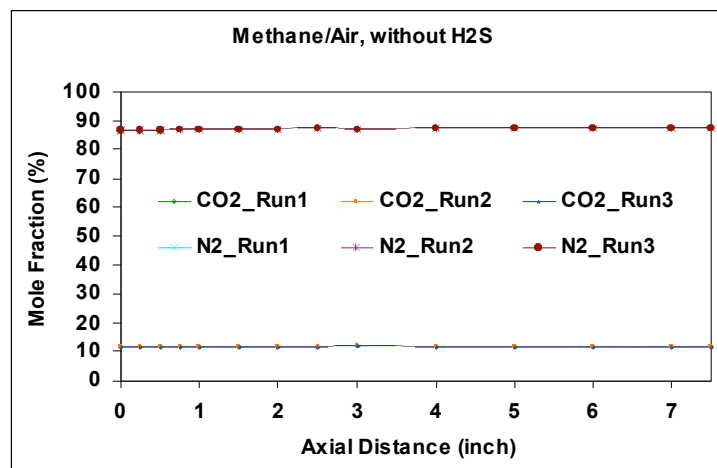


Figure 13. Carbon dioxide and nitrogen mole fractions, methane/air without H₂S.

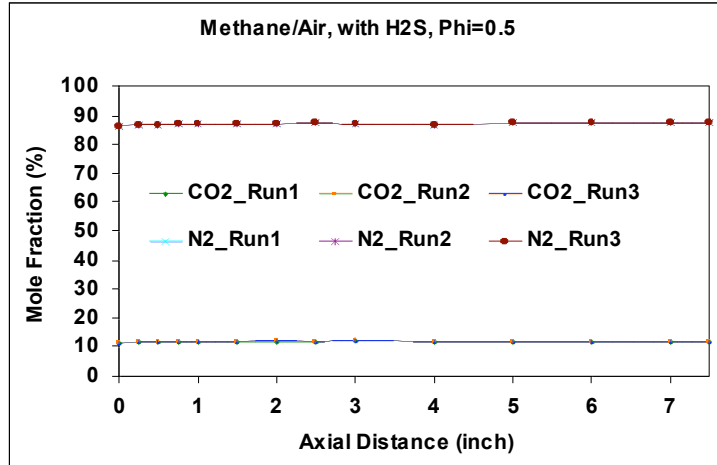


Figure 14. Carbon dioxide and nitrogen mole fractions, methane/air with H₂S, Phi=0.5.

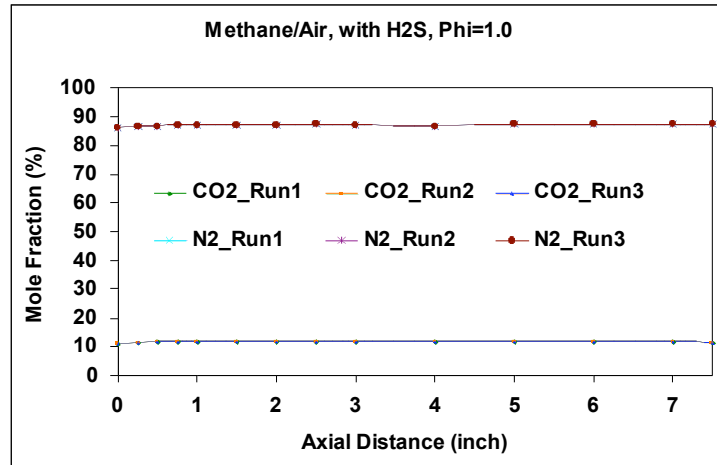


Figure 15. Carbon dioxide and nitrogen mole fractions, methane/air with H₂S, Phi=1.0.

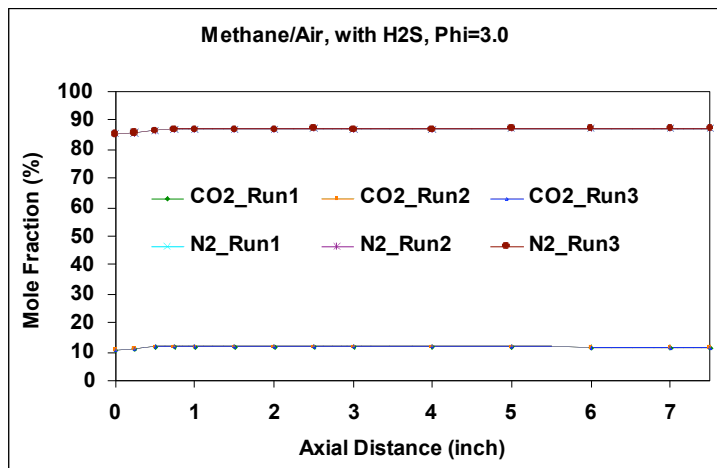


Figure 16. Carbon dioxide and nitrogen mole fractions, methane/air with H₂S, Phi=3.0.

The mole fractions of hydrogen sulfide for different H_2S/O_2 equivalence ratios are shown in Figures 17, 18, and 19. The results were obtained three times to assure data repeatability. One can see that H_2S mole fraction decays along reactor centerline for all cases. Hydrogen sulfide mole fraction does not decay to zero at $\phi=3.0$ where conditions are fuel-rich. (Note the different scale used in the different cases.) Since sampling occurs at reactor centerline, hydrogen sulfide mole fraction starts at a large value because of larger concentrations of H_2S near the burner exit.

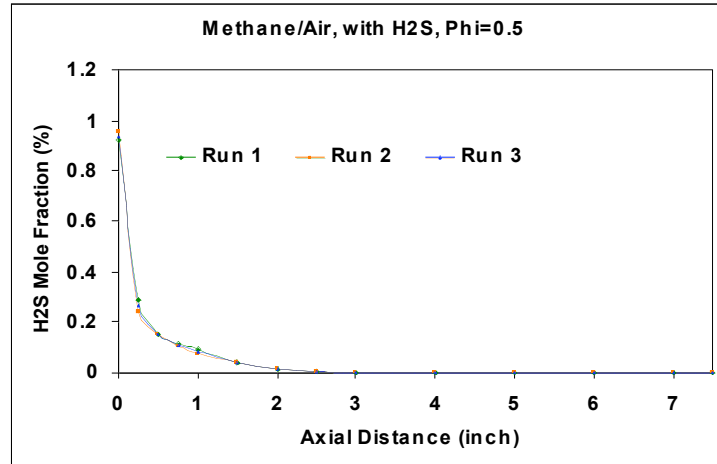


Figure 17. Hydrogen sulfide mole fractions, methane/air with H_2S , $\Phi=0.5$.

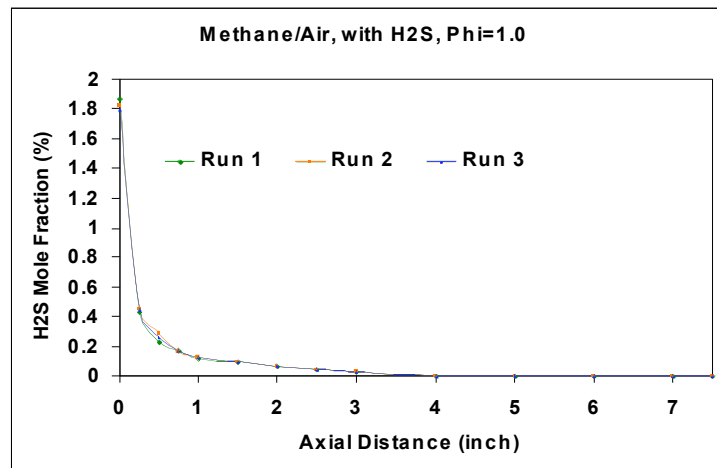


Figure 18. Hydrogen sulfide mole fractions, methane/air with H_2S , $\Phi=1.0$.

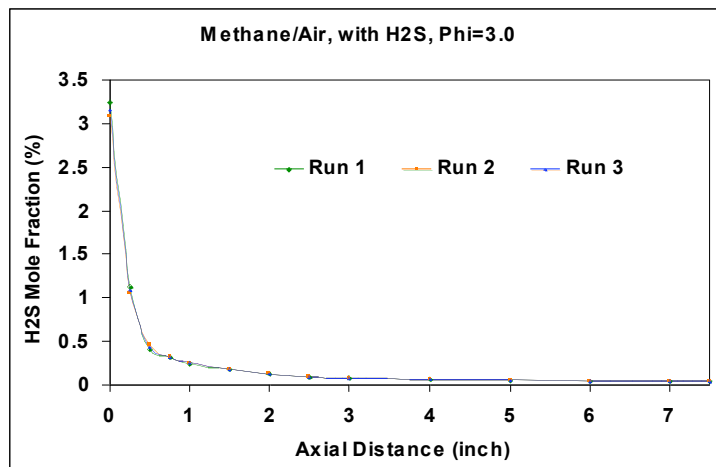


Figure 19. Hydrogen sulfide mole fractions, methane/air with H₂S, Phi=3.0.

The mole fractions of sulfur dioxide at different H₂S/O₂ equivalence ratios are shown in Figures 20, 21, and 22. The experiments were repeated three times for assuring data repeatability. At fuel-lean and stoichiometric conditions SO₂ mole fraction increases monotonically to reach steady state, which is attributed to the H₂S/O₂ reaction. However, at Claus conditions, sulfur dioxide mole fraction peaks at a maximum and starts decreasing to reach the asymptotic value. The peak in the beginning is attributed to the reaction of H₂S/O₂ to form SO₂. However, further downstream, SO₂ reacts with H₂S to form sulfur. Sulfur deposits can be clearly seen on cold regions of the reactor and inside the quartz sampling probe. Figures 23 and 24 show the extent of sulfur deposits after each experiment performed under Claus conditions.

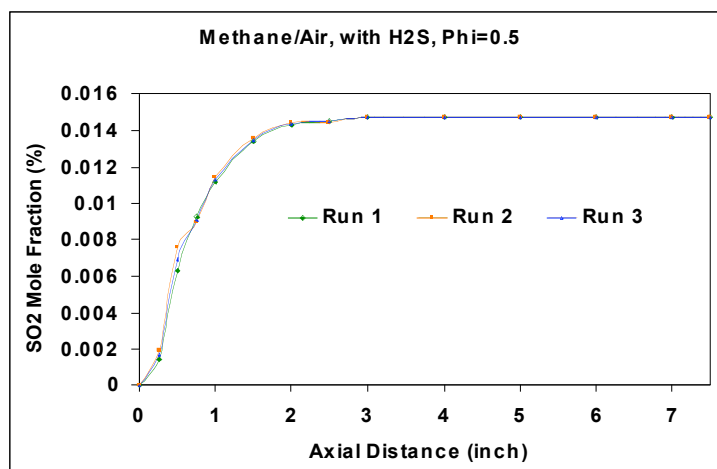


Figure 20. Sulfur dioxide mole fractions, methane/air with H₂S, Phi=0.5.

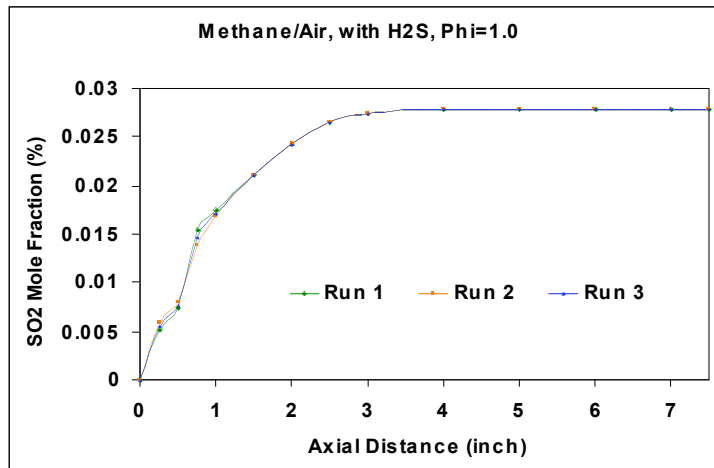


Figure 21. Sulfur dioxide mole fractions, methane/air with H₂S, Phi=1.0.

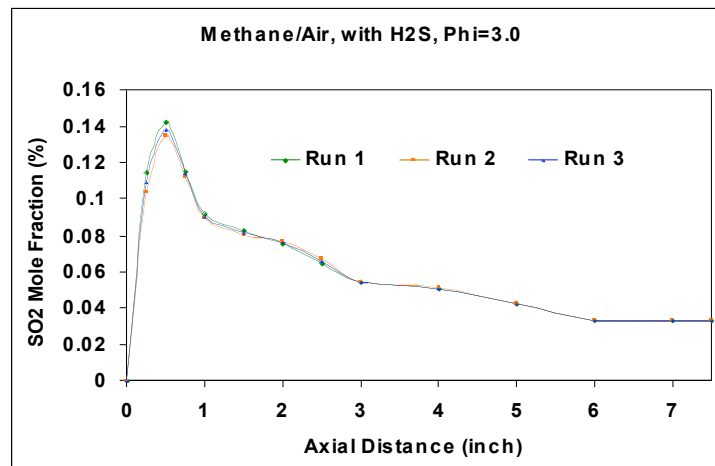


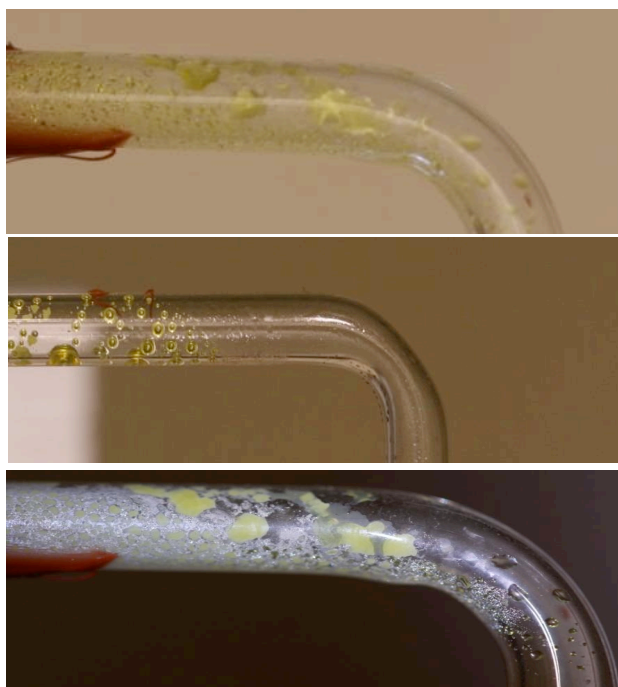
Figure 22. Sulfur dioxide mole fractions, methane/air with H₂S, Phi=3.0.



Run 1 Run 2 Run 3

Figure 23. Sulfur deposits on cold regions of the reactor.

Figure 25 shows higher hydrocarbons formed during the methane/air reaction with the injection of H_2S under Claus conditions. The findings by Sofranko et al. [1] support the possibility of having higher hydrocarbons in methane/air flame in case of having a coupling catalyst, which are metals and nonmetals oxides, in the reaction. Sulfur dioxide plays this role in this case, where it enhances the dimerization of CH_3 radical formed during the CH_4 reaction to form ethane. Dehydrogenation of ethane could form ethylene, which reacts with CH_3 to form propylene. These compounds have been detected here with the addition of H_2S in the reactor. This is significant, as this offers means to provide other value added products from the Claus reactor.



Run 1

Run 2

Run 3

Figure 24. Sulfur deposits on the sampling probe.

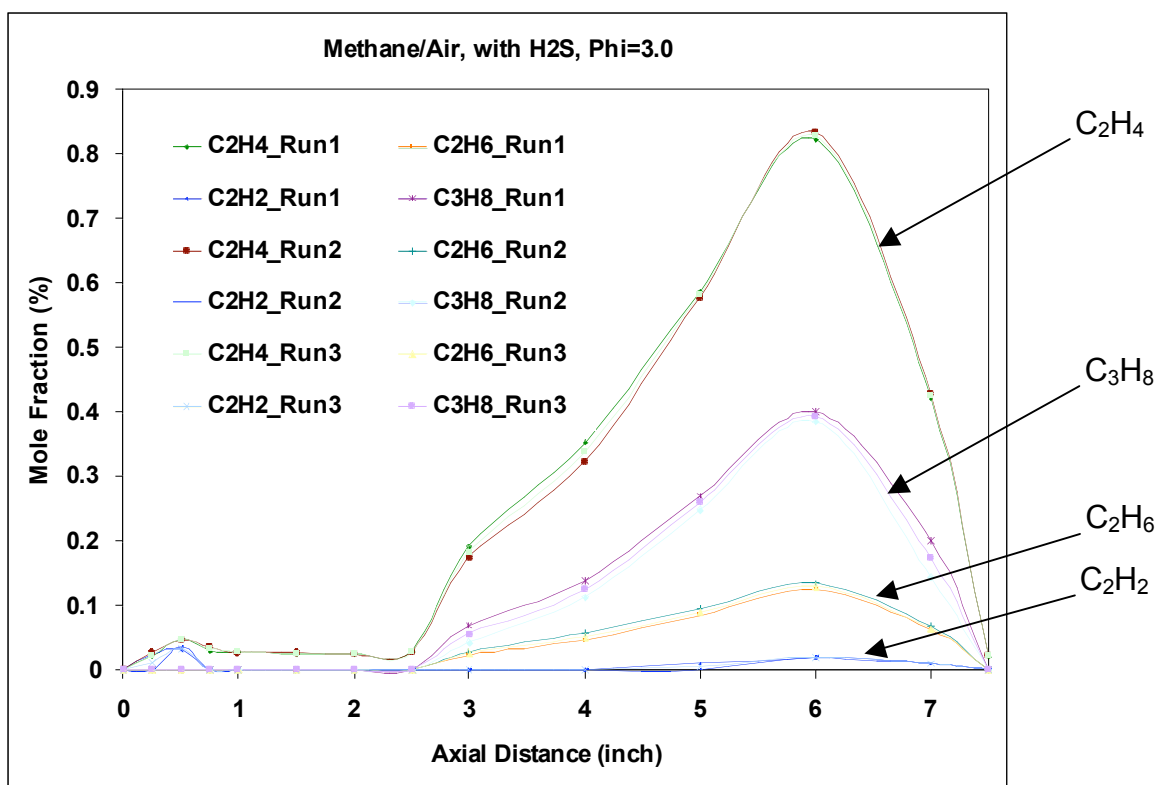


Figure 25. Hydrocarbons formed in methane/air combustion with H₂S. Phi=3.0.

4.3 Optical Emissions Spectroscopy for Sulfuric Compounds and Hydrocarbon Radicals

Excited emissions of sulfuric compounds (S₂ and SO₂) and hydrocarbon radicals (OH, CH, and C₂) were identified using the Acton 300i spectrometer coupled with an ICCD-576-S/RB-G camera. The spectrometer slit was set to 10 microns. The signal from the flame region was passed to the spectrometer using a fiber optic cable with a view angle of 30°. Figure 26 shows hydrocarbon radicals emissions for methane air flame under stoichiometric conditions. The “300BLZ=500 nm” grating was used for the tests to obtain coarse resolution of the spectra.

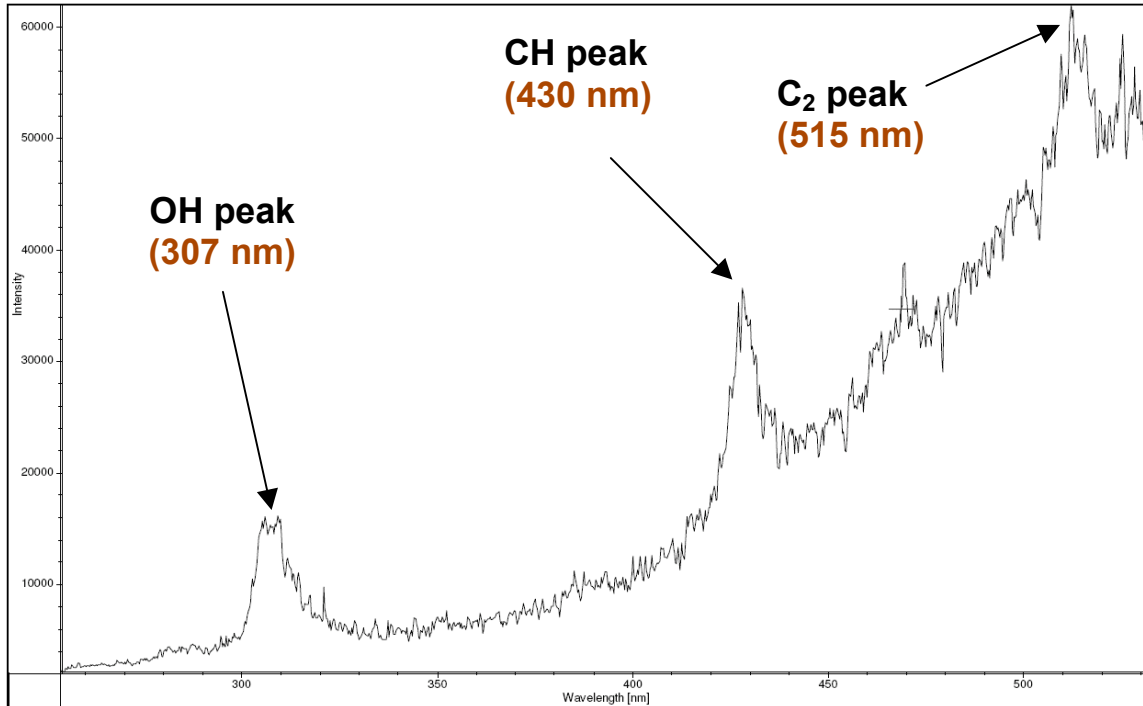


Figure 26. Emissions spectra for methane/air flame under stoichiometric conditions.

In the case of adding hydrogen sulfide into methane/air flame, the spectra did not show distinct difference as compared to the spectra in Figure 26. This is attributed to the high radical concentration of OH, CH, and C₂ as compared to low concentrations of sulfur compounds.

Figure 27 represents emissions spectra for hydrogen/air flame under slightly fuel-lean conditions without the addition of hydrogen sulfide.

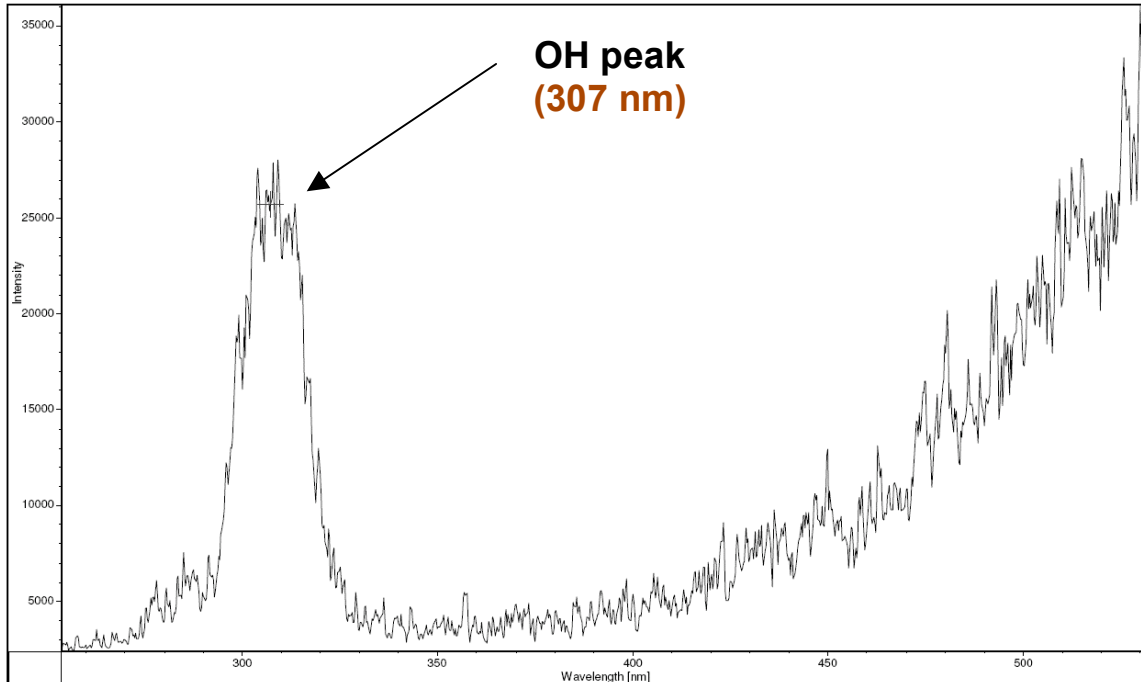


Figure 27. Emissions spectra for hydrogen/air flame.

Figure 28 shows the spectra of hydrogen/air under slightly fuel-lean conditions with the addition of H₂S at Claus condition. One can notice the suppressions of the OH peak. This is attributed to the addition of H₂S, which quickens the radicals decay since the addition of H₂S at Claus conditions makes the mixture slightly fuel-rich. However, there is no distinct signature (peak) associated with the sulfur compounds.

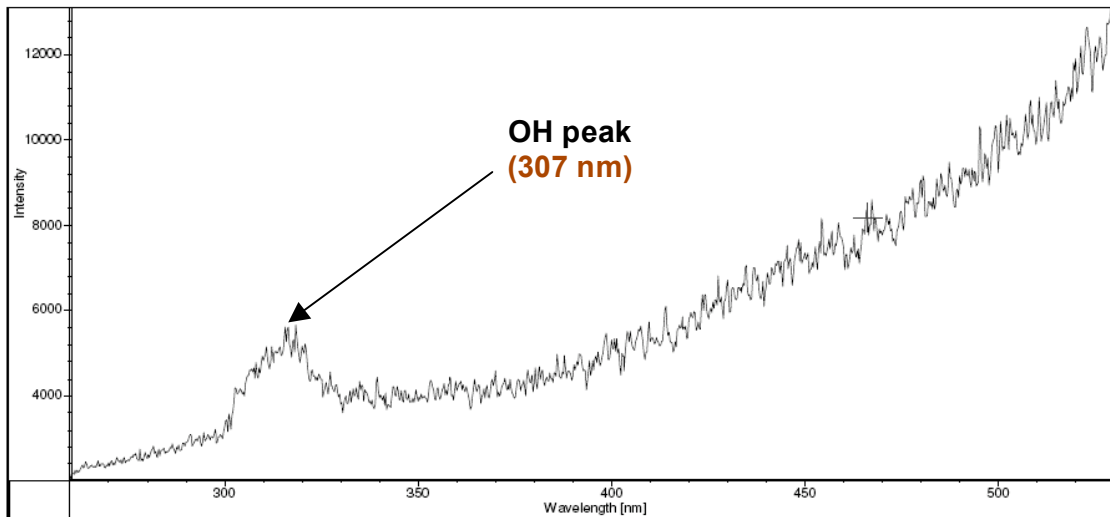


Figure 28. Emissions spectra for hydrogen/air flame with H₂S, Phi=3.0.

With the addition of a very slight amount of H₂S into H₂/air flame a small blue cone was formed inside the flame where emissions of excited sulfur compounds were distinctly observed. Figure 29

shows the formation of the bluish cone due to H₂S addition. Figure 30 shows the emissions spectra obtained from this cone.

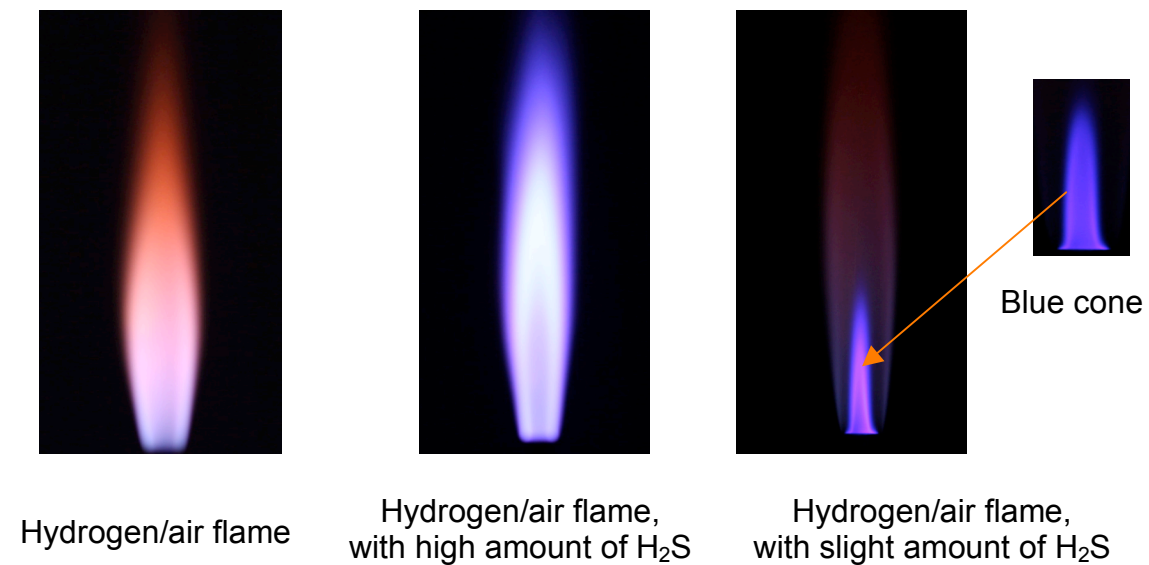


Figure 29. Hydrogen/air flame pictures without and with additions of hydrogen sulfide.

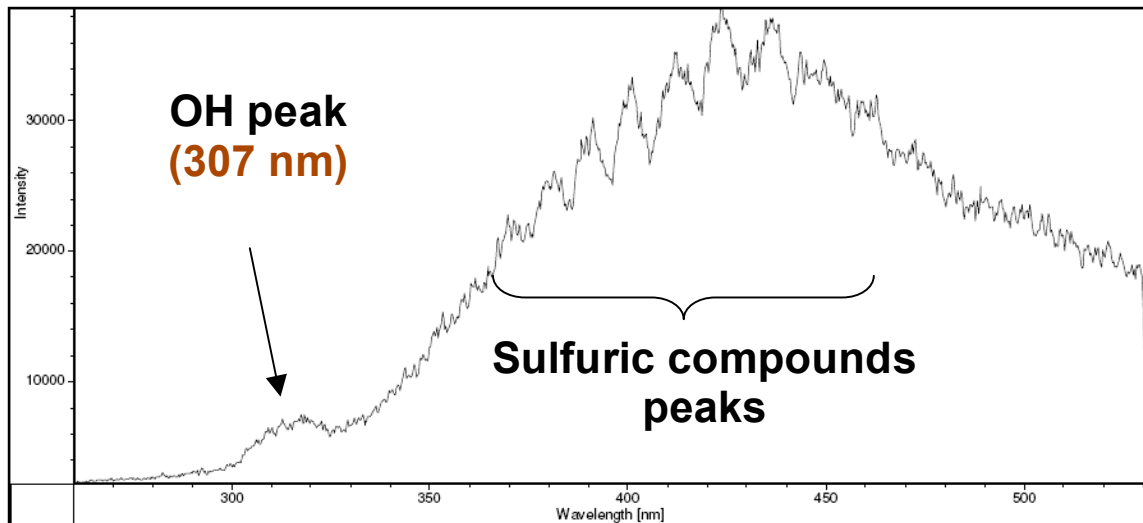


Figure 30. Emissions spectra for hydrogen/air flame with slight amount of H₂S.

Further investigations were undertaken in order to separate out the peaks of sulfur compounds and help identify as many of them as possible. For this purpose the “600BLZ=500 nm” grating was used for spectrometer calibration to obtain finer spectral resolution. Figure 31 shows the spectra of the blue cone between 340 and 400 nm. The results show very distinct presence of SO₂ and S₂ peaks at almost 350 nm and 394 nm, respectively. The other peaks formed are attributed to SO₂ and S₂, or peaks of some their polymer compounds. Further investigations are needed to identify these compounds.

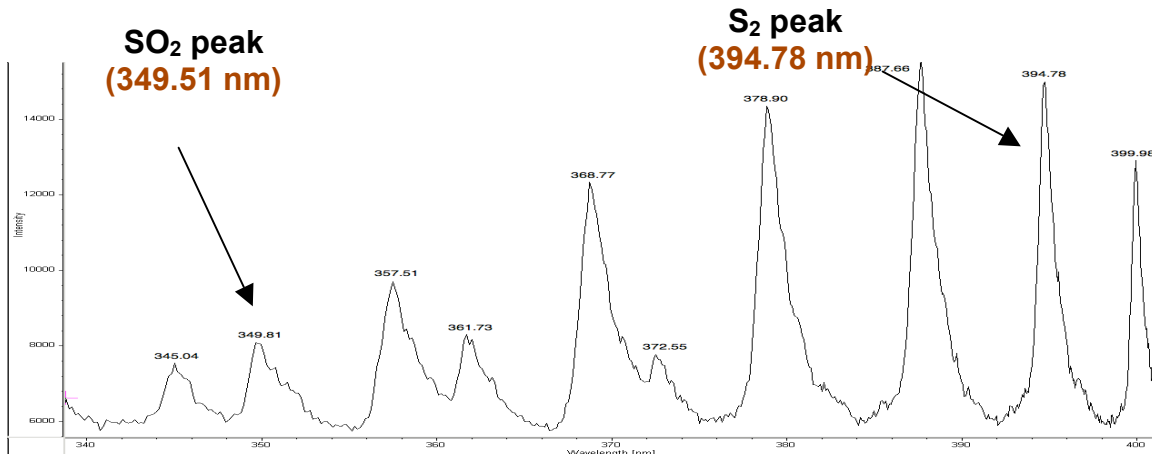


Figure 31. Emissions spectra of the blue cone between 340 and 400 nm.

5. Summary

An experimental setup was assembled for hydrogen sulfide experimentation. The setup consists of a transparent quartz reactor for non-intrusive examination. A spectrometer was used for the excited emissions detection. The reactor was placed in a steel housing where the burner was attached from the bottom steel base. A quartz sampling probe was used along with a computer-controlled traverse mechanism for gas sampling along reactor centerline. The experimental setup was placed inside a fume hood, which was tested and assembled according to the safety regulations of University of Maryland safety department. An exhaust duct was attached to the top of the fume hood and connected with an exhaust fan capable of generating the required induced air velocity into the fume hood. The experiments started with examination of the equivalence ratio of H₂S/O₂ mixture in methane/air combustion. A methane/air mixture was set under slightly fuel-lean conditions where H₂S was injected accordingly with different concentrations to achieve aimed equivalence ratios. A gas chromatograph equipped with a thermal conductivity detector and flame photometric detector was used for gas sampling analysis.

The results revealed that increase in H₂S addition corresponds to increase in asymptotic mole fraction of both carbon monoxide and oxygen. However, changes in both carbon dioxide and nitrogen mole fractions are negligible as compared to their average values. The hydrogen sulfide mole fraction decays monotonically along reactor centerline, but the H₂S mole fraction does not reach zero value at Claus conditions. The sulfur dioxide mole fraction showed a complicated trend. For stoichiometric and fuel-lean conditions the SO₂ mole fraction decreased along reactor centerline due to reaction of H₂S with oxygen. However, for Claus conditions, the SO₂ mole fractions peaked at a maximum value, and then decreased because of their reaction with H₂S to form sulfur. Sulfur deposits were clearly observed at cold regions of the reactor and sampling probe. All the experiments were repeated three times for data repeatability verification. Furthermore, a non-intrusive examination was performed for emissions of excited sulfuric compounds and hydrocarbon radicals under different mixture conditions (rich, stoichiometric, and leans) and different flames. An Acton 300i spectrometer coupled with an ICCD-576-S/RB-G camera was used for emissions spectra analysis. Hydrocarbons radicals emissions were distinctly identified using coarse spectra resolution. Sulfuric compounds emissions were identified by injecting slight amount of H₂S into hydrogen/air flame, where a blue cone formed. Sulfuring compounds emissions were clearly distinguishable using fine spectra resolution.

6. References

Sofranko, J. A., Leonard, J. J., Jones, C. A., "The oxidative conversion of methane to higher hydrocarbons," *Journal of Catalysis*, Vol. 103, February, 1987, pp. 301-310.

7. Difficulties Encountered/Overcome

None

8. Deliverables for the Next Quarter

- Use gas chromatograph for chemical speciation of sulfur in the blue cone (with small amounts of H₂S). Substantiate with optical spectrometry data.
- Repeat optical spectrometry experiments to investigate sulfur related compounds at other wavelengths (200-350 nm) and (400-500 nm).
- Determine chemical species in H₂S/air and H₂S/O₂ flames using gas chromatograph.
- Calculate sulfur mole fraction and conversion efficiency using different flames in a plug flow reactor with perfectly premixed reactants (air/oxygen, hydrogen/methane, and hydrogen sulfide)

9. Publications

1. Gupta, A. K. and Sassi, M. "Sulfur Recovery from Acid Gas Using the Claus Process and High Temperature Air Combustion Technology," American J. of Environmental Sciences, Vol. 4, No. 5, 2008, pp. 502-511.
2. Selim, H., Gupta, A. K. and Sassi, M. "Variation of Optimum Claus Reactor temperature with Acid Gas Composition," IECEC Conference, Cleveland, OH, July 28-30, 2008, Paper No. AIAA-2008-5797.
3. Selim, H., Gupta, A. K. and Sassi, M. "Reduced Mechanism for Hydrogen Sulfide Oxidation," 47th AIAA Aerospace Sciences Conference, Orlando, FL, January 5-8, 2009, Paper No. AIAA-2009-1392.
4. Selim, H. and Gupta, A. K. "Nonreactive Study for the Reactants Mixing in Claus Reactions," 7th Intl. Energy Conversion Engineering Conference (7th IECEC), Denver, CO, August 2-5, 2009, Paper No. AIAA-2009-4506.
5. Selim, H and Gupta, A. K. and Sassi, M. "Reduction and Validation of Detailed Kinetic Reactions in Thermal Stage of Claus Process," 48th AIAA Aerospace Sciences Conference, Orlando, FL, (accepted for presentation and Publication), January 3-7, 2010, Paper AIAA-2010-1356.
6. Al Amoodi, N., Selim, H., Gupta, A. K., Sassi, M. and Al Shoaibi, A. "Numerical Simulations of the Thermal Stage in Claus Process: Equilibrium and Kinetic Investigation," 48th AIAA Aerospace Sciences Conference, Orlando, FL, (accepted for presentation and publication), January 3-7, 2010, AIAA-2010-1355.
7. Selim, H. Vijayan, V., Al Shoaibi, A., and Gupta, A. K., "Numerical and Experimental Studies on Mixing and Product Species Distribution in a Claus Reactor," 8th Intl. Energy Conversion Engineering Conference (8th IECEC), Nashville, TN, August 2-5, 2009, Paper No. AIAA-2010-7183.

Appendix

Justification and Background

Hydrogen sulfide is present in numerous gaseous waste streams from natural gas plants, oil refineries, and wastewater treatment plants, among other processes. These streams usually also contain carbon dioxide, water vapor, trace quantities of hydrocarbons, sulfur, and ammonia. Waste gases with ammonia are called sour gases, while those without ammonia are called acid gases. Sulfur must be recovered from these waste streams before flaring them. Sulfur recovery from sour or acid gas typically involves application of the well-known Claus process, using the reaction between hydrogen sulfide and sulfur dioxide (produced at the Claus process furnace from the combustion of H₂S with air and/or oxygen), yielding elemental sulfur and water vapor: $2\text{H}_2\text{S}(\text{g}) + \text{SO}_2(\text{g}) = (3/n) \text{S}_n(\text{g}) + 2\text{H}_2\text{O}(\text{g})$ with $\Delta H_r = -108 \text{ kJ/mol}$. Therefore, higher conversions for this exothermic, equilibrium-limited reaction call for low temperatures, which lead to low reaction rates that dictate the use of a catalyst. The catalytic conversion is usually carried out in a multistage, fixed-bed, adsorptive reactor process, which counteracts the severe equilibrium limitations at high conversions. This technology process can convert about 96% to 97% of the influent sulfur in H₂S to S. However, higher removal requires critical examination of the process and use of a near isothermal reactor, since the conversion is critically dependent upon the exothermic and endothermic conditions of the reactions.

Flameless combustion has been shown to provide uniform thermal field in the reactor so that the reactor temperature is near uniform. Reactor size can also be reduced and combustion-generated pollutants emissions can be reduced by up to 50%. Energy efficiency can be increased by up to 30%. The application of this technology appears to offer great advantages for the processes under consideration. The UAE, which pumps about 2.4 million bpd of crude oil, is also home to the world's fifth biggest gas reserves at about 200 trillion cubic feet. Abu Dhabi Gas Industries (GASCO), an operating company of the Abu Dhabi National Oil Company (ADNOC), is leading a drive to boost gas production in the UAE from five to seven billion cubic feet per day. This calls for sulfur recovery capacity of over 3,000 metric tons per day with the associated SO_x and NO_x emissions. Therefore, the adoption and further development of flameless combustion technology for sulfur recovery among other commercial and industrial heating processes is expected to be crucial and beneficial, both economically and environmentally.

The conventional sulfur recovery process is based upon the withdrawal of sulfur by in situ condensation within the reactor. The selective removal of water should, however, be a far more effective technique, as its effect on the equilibrium composition in the mass action equation is much greater. The in situ combination of the heterogeneously catalyzed Claus reaction and an adsorptive water separation seems especially promising, as both reaction and adsorption exhibit similar kinetics, and pressure can be adapted to the needs of the adsorptive separation. Such an adsorptive reactor will lead to almost complete conversion as long as the adsorption capacity is not exhausted. There are numerous possibilities for implementing these two functions, ranging from fixed-beds with homogeneous catalyst/adsorbent mixtures to spatially structured distributions or even fluidized beds. Most of the previous studies have concentrated on the Claus catalytic conversion reactors and the TGTU. However, some previous studies have identified the Claus furnace as one of the most important yet least understood parts of the modified Claus process. The furnace is where the combustion reaction and the initial sulfur conversion (through an endothermic gaseous reaction) take place. It is also where the SO₂ required by the downstream catalytic stages is produced and the contaminants (such as ammonia and BTX (benzene, toluene, xylene) are supposedly destroyed. The main two reactions in the Claus furnace are: $\text{H}_2\text{S} + 3/2 \text{O}_2 = \text{SO}_2 + \text{H}_2\text{O}$, with $\Delta H_r = -518 \text{ kJ/mol}$, and $2\text{H}_2\text{S} + \text{SO}_2 = 3/2 \text{S}_2 + 2\text{H}_2\text{O}$, with $\Delta H_r = +47 \text{ kJ/mol}$. This last endothermic reaction is responsible for up to 67% conversion of the sulfur at about 1200 °C. Moreover, many side reactions take place in the furnace; these side reactions reduce sulfur recovery and/or produce unwanted components that end up as ambient

pollutant emissions. Therefore, it would be useful to combine the endothermic and exothermic process using an isothermal reactor offered by flameless oxidation combustion.

Approach

Critical review

We propose to conduct a critical review of the various approaches used for sulfur removal from the sour gas. The emphasis here will be on sulfur chemistry with due consideration to the fate of ammonia. Following the review, an experimental and a CFD numerical study of the flameless oxidation of the fuel will be conducted as follows:

CFD simulation

A numerical simulation study of the flame under normal and flameless oxidation of fuels in the furnace will be conducted using the available codes. Global features of the flow and thermal behavior will be obtained using the Fluent CFD and Chemkin computer codes. These codes provide detailed simulation of the flow, thermal and chemical behaviors (i.e., detailed chemistry) in the reactor flow using gas-phase reactants. The sulfur in the fuel is in gas phase, so we will be able to simulate and monitor the fate of sulfur during various stages of endothermic and exothermic reactions and over a range of temperature regimes, including those covered in the Claus furnace process. The simulation results will also guide the final design of the flameless furnace. The simulations will also help assist in the experimental program for data validation with the eventual goal of implementing the process for sulfur removal.

Experimental study

An experimental study of the flameless vs. normal flame combustion process for the conditions examined in the theoretical study, including that of Claus furnace, will be conducted. We will explore the operating conditions and the exhaust gas analysis under conditions of both flame and flameless modes to determine the extent of sulfur conversion under the two conditions over the temperatures that can simulate endothermic and exothermic conditions in the Claus furnace. The goal is to seek conditions that yield the highest sulfur recovery from a process. To some extent, these conditions will be based on the composition of the acid/sour gas, from sulfur-rich (> 50% H₂S) to lean (< 20% H₂S). It is expected that our fundamental information will contribute to the eventual design guidelines of an advanced sulfur recovery process furnace operating under flameless combustion mode.

Evaluating Solid Oxide Fuel Cell Systems for Operation on Petroleum Off-Gases with Contaminants

UMD Investigators: Greg Jackson, Bryan Eichhorn
UMD GRAs: Siddarth Patel, Lei Wang
PI Investigators: Ali Almansoori, Ahmed Nafees
Start Date: October 2006

1. Objective/Abstract

In this program, UMD and PI will build on the established collaboration from earlier work – both experimental and modeling – to explore the impact of petroleum off-gas composition including effects of contaminants (H_2S and HCl) on SOFC performance/design. Single-cell SOFC experiments will be used to enhance and validate existing single-cell SOFC models to incorporate the effects of hydrocarbon composition and H_2S on SOFC performance. These single cell models will then be translated to full stack evaluations in higher dimensions and these models will then be incorporated into process-level plant models to evaluate the effectiveness of SOFCs for capturing energy from petroleum gases and for providing a means for possible CO_2 capture within a plant context. This Phase II testing and development effort will also seek to bring an industrial collaborator to work with the team to explore design and implementation challenges for a future SOFC demonstration operating on relevant petroleum gas streams.

2. Deliverables for the Completed Quarter

Task 1: Establishing experimental facilities for MEA testing with trace contaminants

- No experimental modifications were done during this quarter.

Task 2: Long-term testing MEAs for selected fuels and syngas with trace H_2S and HCl

- Due to limited rig availability no experiments with the trace contaminants were performed this quarter. It was agreed in the development of a new project termination plan that tests would focus on the more significant H_2S durability for $Ni/CeO_2/YSZ$ anodes. The rig has been modified and durability tests are beginning in mid August 2010. These will be reported in the following quarterly report.

Task 3: Enhancing MEA models to evaluate contaminant-tolerant designs

- No further enhancement of the detailed models were pursued during this quarter. The addition of the H_2S contamination model will occur during the upcoming quarter after the testing provides some kinetic data for rates and some better understanding of how the CeO_2 influences NiS formation with post cell characterization.

Task 4: Performing system level analysis of integrated SOFC / off-gas processing plant

- UMD furthered the development of the Aspen Plus model with an SOFC linked to a reformer and an anode recycle loop. These results briefly presented in this report were performed at UMD by Mr. Lei Wang.

Task 5: Establishing SOFC-industry partner for future demonstration

- No activities were pursued for this task, and with the accelerated termination of this project this task has been dropped from the project.

3. Summary of UMD Project Activities for the Completed Quarter

The fifth quarter of this Phase II effort included the following:

- further extending the Aspen Plus fuel cell plant model (originally intended as a summer

- internship project).
- completion of rig modifications for H₂S testing and fabrication of many cells for durability studies with sulfur-contamination.

This quarter's progress was expected to be hastened by the working with two PI interns. Unfortunately, the one intern who came to the U.S. did not enjoy the chemical aspects of fuel cells and the intern chose to switch projects after the first week of training. As such, the UMD team refocused efforts to include some work on the Aspen Plus model.

Decisions have been made to terminate this project early, and the following is a plan by the UMD team to wrap up the program by the end of early fall 2010 and to deliver a final report with the next EERC quarterly report in the fall of 2010. Originally it was hoped to complete the shortened project by August 2010, but at no extra cost to the project, the UMD team will need to push the project into September. The long-term durability tests for the H₂S contamination were delayed by issues with the experimental rig and acquiring the gas mixes needed for the study.

On the experimental side, UMD is wrapping up testing with existing rigs on the stability of Ni/CeO₂/YSZ solid oxide fuel cell anodes with testing on the impact of trace H₂S on the reformat feeds. In addition to the electrochemical characterization from previous tests, the tests will also measure emissions in order to assess the nature of the conversion of the feeds. The stability of the novel SOFC anodes developed under this program and their potential impact on SOFC development will be assessed from these experiments, and implications for SOFC applications in petroleum processing will be presented in the final report. On the modeling side, UMD will build on its development of the ASPEN Plus model of a simple SOFC plant to explore the implications of SOFC implementation into petroleum off-gas processing. The model will look at the benefits of alternative reformer designs (external pre-reforming or internal reforming with direct hydrocarbon feeds) for SOFC implementation in a process plant. The results from this study will be preliminary.

Finally, for publications, UMD will complete the publication on the experimental testing (with Dr. Almansoori as a co-author) and will also publish work on the H₂S poisoning. The ASPEN Plus modeling may or may not lead to a joint publication, as it depends on the degree to which the work is completed by the end of this summer.

With this shortened project, the final deliverables will be provided by fall this project:

- 1) Report summarizing of unique Ni/CeO₂/YSZ SOFC anode performance and durability for operation with syngas and hydrocarbon feeds with and without H₂S contamination,
- 2) System-level modeling tool using ASPEN Plus with process evaluation for integration of SOFC into petroleum off-gas processing.

Progress on the individual tasks over the last quarter is given here.

Task 1: Establishing experimental facilities for MEA testing with trace contaminants

No additional changes to the experimental facility were pursued during the past quarter.

Task 2: Long-term testing MEAs for selected fuels and syngas with trace H₂S and HCl

Some modifications were needed to the experimental rig to allow for long-term testing with contaminants. These modifications included additional mass flow controllers and modification of the control software for long-term testing. In addition, numerous cells were fabricated and custom gases were purchased. All items and materials have been purchased for these tests, which are set up for completion in September. No additional costs related to materials will be required during this time of completion.

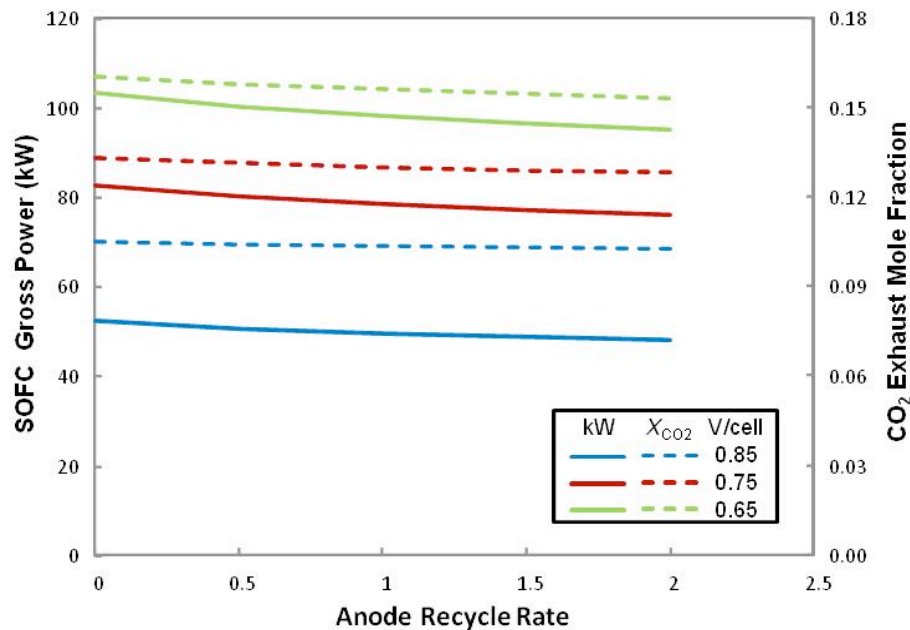


Figure 2. Aspen Plus simulation results of system in Figure 1 with 25 m² area SOFC with reformer feed of 0.1 kmol/s of C₄H₁₀ and an S/C = 2.5

Task 5: Establishing SOFC-industry partner for future demonstration

This task will no longer be pursued in this program.

4. Difficulties Encountered/Overcome

Difficulties in setting up the SOFC rig for H₂S and limited rig availability slowed down the H₂S testing, but all issues have been resolved and testing is ongoing for the next several weeks.

The loss of our intern students disrupted our plans for progress with the Aspen model.

5. Planned Project Activities for the Next Quarter

The following activities are planned at UMD for this upcoming quarter.

- Finish testing the Ni/CeO₂/YSZ anodes with syngas and trace H₂S for long-term sulfur-tolerance.
- Performing plant study with existing ASPEN Plus model for a range of operating conditions.
- Write final report for closing out project.

Appendix A

Justification and Background

There has been a movement for petroleum processing facilities to move to zero-flaring of off gases. These gases, derived from the petroleum extraction as well as downstream processing, can contain various hydrocarbons, some H₂S, and depending on the process, HCl (derived from processes for well stimulation). These gases can be returned to an oil well to maintain well pressure. However, it is also possible to extract useful power from these gases employing SOFCs, which can provide high energy conversion efficiencies (> 50% based on fuel heating value) while maintaining separation of fuel oxidation products from N₂ dilution that comes with conventional combustion processes. If SOFC architectures can be designed to operate effectively on such off-gases, then they can produce not only useful power but also concentrated CO₂ and H₂O streams which can be readily pumped to high pressure for oil-well re-injection. This provides a potential carbon footprint reduction of the petroleum processing both by producing power from waste streams and by providing an efficient means for re-injection of C-containing gases back into the well for sequestration. System level modeling in this program will show that such potential can be realized if stable SOFC systems are successfully developed.

Approach

This effort will extend earlier single membrane electrode assembly (MEA) testing and modeling at UMD and PI by looking at new gas compositions and the impact of trace H₂S and HCl contaminants on SOFC with potentially contaminant-tolerant materials and micro-architectures. UMD will employ additional MEA experiments with Raman spectroscopy to evaluate surface chemistry on selected SOFC materials (1). Functionally graded anode micro-architectures and material systems will be investigated for high power density and sulfur tolerance. These efforts will build on the earlier work exploring ceria/metal composite anodes and on recent work of others (2) showing the effectiveness of ceria nanoparticles for high-sulfur-tolerant SOFC anodes. The benefits of integrating an SOFC with an external steam or autothermal reformer will be explored by comparing SOFC performance with syngas vs. light hydrocarbon streams, where both are impacted by trace H₂S.

This work will rely on the progress made from integrating ceria (doped and/or un-doped with appropriate metal electrocatalysts for MEA designs tolerant of hydrocarbons). The testing will be done on selected fuels (CH₄, C₃H₈, C₄H₁₀) and on syngas contaminated with trace amounts of H₂S and separately trace amounts of HCl. Durability tests will be explored for preferred MEA designs. Modeling efforts will be expanded on both the micro-scale MEA level and on the large process scale to assess how contaminants handling will influence both SOFC design as well as overall process feasibility.

The simultaneous modeling effort in this program will also extend ongoing modeling efforts which will have explored both MEA models for micro-architecture design as well as higher level process models for assessing the potential for integrating SOFC systems into oil well operations. The micro-architecture MEA modeling will expand on Phase I efforts by developing the semi-empirical kinetic models for internal reforming of hydrocarbons and of H₂S decomposition. The engineering viability of an SOFC integrated into a petroleum facility for energy recovery and possible CO₂ capture (3) will be investigated via system modeling within the context of petroleum processes by combining the SOFC models with process simulation in ASPEN/Hisys available at PI and UMD. The process models will rely on full stack SOFC models derived from the MEA models to explore overall balance of plant, adequacy of fuel supplies, and power requirements for CO₂ capture. If possible, process simulation will be done in consultation with ADNOC experts to explore how SOFCs might be integrated into petroleum processing facilities.

Specific tasks for the program are summarized in the proposed schedule below. The testing and model development effort will also seek to bring an industrial collaborator to work with the team to

explore the possibility of a future demonstration SOFC system operating on petroleum processing offgases.

Task list: The overall approach can be summarized into 5 overarching tasks.

- 1) Establishing experimental facilities for MEA testing with trace contaminants
- 2) Long-term testing MEAs for selected fuels and syngas with trace H₂S and HCl
- 3) Enhancing MEA models to evaluate contaminant-tolerant designs
- 4) System level analysis of integrated SOFC / off-gas processing plant
- 5) Establishing industrial partner

Anticipated Deliverables: The following deliverables will be provided on this project:

- 1) Summary of MEA test results for preferred SOFC material and micro-architectures for high power density operation with syngas and hydrocarbons laden with selected contaminants,
- 2) MEA modeling results illustrating preferred micro-architectures with metal/ceria systems for contaminant-tolerant operation
- 3) System-level modeling tool with process evaluation for integration of SOFC into petroleum off-gas processing

Two-Year Schedule

Year 1:

- Upgrade SOFC MEA-testing facilities at UMD for handling trace contaminants
- Further development of SOFC experimental facilities at PI
- Perform post-testing material characterization for evaluation of long-term exposure to carbonaceous fuels
- Testing MEAs for selected fuels and syngas with trace H₂S and HCl
- Adopt SOFC models at UMD for hydrocarbon studies.
- Develop system level analysis of integrated SOFC / off-gas processing plant with analysis of contaminant flow

Year 2:

- Perform experiments with preferred material systems for typical off-gas compositions (with varying team loadings) for long-term durability with trace contaminants
- Enhance MEA models to evaluate micro-architectures for contaminant-tolerant operation
- Establish industrial partner in SOFC industry and ADNOC companies for development of demonstration project

References

- M.B. Pomfret, J. Marda, G.S. Jackson, B.W. Eichhorn, A.M. Dean, and R.A. Walker, *Journal Of Physical Chemistry C*, **112**(13), 5232 (2008).
- H. Kurokawa, T.Z. Shoklapper, C.P. Jacobson, L.C. De Jonghe, and S.J. Visco, *Electrochemical And Solid State Letters*, **10**(9), B135 (2007).
- B.F. Moller, J. Arriagada, M. Assadi, and I. Potts, *Journal of Power Sources*, **131**(1-2), 320 (2004).

Appendix

Justification and Background

There has been a movement for petroleum processing facilities to move to zero-flaring of off gases. These gases, derived from the petroleum extraction as well as downstream processing, can contain various hydrocarbons, some H₂S, and depending on the process, HCl (derived from processes for well stimulation). These gases can be returned to an oil well to maintain well pressure. However, it is also possible to extract useful power from these gases employing SOFCs, which can provide high energy conversion efficiencies (> 50% based on fuel heating value) while maintaining separation of fuel oxidation products from N₂ dilution that comes with conventional combustion processes. If SOFC architectures can be designed to operate effectively on such off-gases, then they can produce not only useful power but also concentrated CO₂ and H₂O streams which can be readily pumped to high pressure for oil-well re-injection. This provides a potential carbon footprint reduction of the petroleum processing both by producing power from waste streams and by providing an efficient means for re-injection of C-containing gases back into the well for sequestration. System level modeling in this program will show that such potential can be realized if stable SOFC systems are successfully developed.

Approach

This effort will extend earlier single membrane electrode assembly (MEA) testing and modeling at UMD and PI by looking at new gas compositions and the impact of trace H₂S and HCl contaminants on SOFC with potentially contaminant-tolerant materials and micro-architectures. UMD will employ additional MEA experiments with Raman spectroscopy to evaluate surface chemistry on selected SOFC materials (1). Functionally graded anode micro-architectures and material systems will be investigated for high power density and sulfur tolerance. These efforts will build on the earlier work exploring ceria/metal composite anodes and on recent work of others (5) showing the effectiveness of ceria nanoparticles for high-sulfur-tolerant SOFC anodes. The benefits of integrating an SOFC with an external steam or autothermal reformer will be explored by comparing SOFC performance with syngas vs. light hydrocarbon streams, where both are impacted by trace H₂S.

This work will rely on the progress made from integrating ceria (doped and/or un-doped with appropriate metal electrocatalysts for MEA designs tolerant of hydrocarbons). The testing will be done on selected fuels (CH₄, C₃H₈, C₄H₁₀) and on syngas contaminated with trace amounts of H₂S and separately trace amounts of HCl. Durability tests will be explored for preferred MEA designs. Modeling efforts will be expanded on both the micro-scale MEA level and on the large process scale to assess how contaminants handling will influence both SOFC design as well as overall process feasibility.

The simultaneous modeling effort in this program will also extend ongoing modeling efforts which will have explored both MEA models for micro-architecture design as well as higher level process models for assessing the potential for integrating SOFC systems into oil well operations. The micro-architecture MEA modeling will expand on Phase I efforts by developing the semi-empirical kinetic models for internal reforming of hydrocarbons and of H₂S decomposition. The engineering viability of an SOFC integrated into a petroleum facility for energy recovery and possible CO₂ capture (6) will be investigated via system modeling within the context of petroleum processes by combining the SOFC models with process simulation in ASPEN/Hisys available at PI and UMD. The process models will rely on full stack SOFC models derived from the MEA models to explore overall balance of plant, adequacy of fuel supplies, and power requirements for CO₂ capture. If possible, process simulation will be done in consultation with ADNOC experts to explore how SOFCs might be integrated into petroleum processing facilities.

Specific tasks for the program are summarized in the proposed schedule below. The testing and model development effort will also seek to bring an industrial collaborator to work with the team to

explore the possibility of a future demonstration SOFC system operating on petroleum processing offgases.

Task list: The overall approach can be summarized into 5 overarching tasks.

- 6) Establishing experimental facilities for MEA testing with trace contaminants
- 7) Long-term testing MEAs for selected fuels and syngas with trace H₂S and HCl
- 8) Enhancing MEA models to evaluate contaminant-tolerant designs
- 9) System level analysis of integrated SOFC / off-gas processing plant
- 10) Establishing industrial partner

Anticipated Deliverables: The following deliverables will be provided on this project:

- 1) Summary of MEA test results for preferred SOFC material and micro-architectures for high power density operation with syngas and hydrocarbons laden with selected contaminants,
- 2) MEA modeling results illustrating preferred micro-architectures with metal/ceria systems for contaminant-tolerant operation
- 3) System-level modeling tool with process evaluation for integration of SOFC into petroleum off-gas processing

Two-Year Schedule

Year 1:

- Upgrade SOFC MEA-testing facilities at UMD for handling trace contaminants
- Further development of SOFC experimental facilities at PI
- Perform post-testing material characterization for evaluation of long-term exposure to carbonaceous fuels
- Testing MEAs for selected fuels and syngas with trace H₂S and HCl
- Adopt SOFC models at UMD for hydrocarbon studies.
- Develop system level analysis of integrated SOFC / off-gas processing plant with analysis of contaminant flow

Year 2:

- Perform experiments with preferred material systems for typical off-gas compositions (with varying team loadings) for long-term durability with trace contaminants
- Enhance MEA models to evaluate micro-architectures for contaminant-tolerant operation
- Establish industrial partner in SOFC industry and ADNOC companies for development of demonstration project

References

1. M.B. Pomfret, J. Marda, G.S. Jackson, B.W. Eichhorn, A.M. Dean, and R.A. Walker, *Journal Of Physical Chemistry C*, **112**(13), 5232 (2008).
2. S. Patel, P.F. Jawlik, and G.S. Jackson. *Effects of Ceria Addition on Ni/YSZ Anodes for SOFCs Operating with Syngas and Hydrocarbons*. in *FUEL CELL 2009*. 2009. Newport Beach, CA: ASME.
3. S.C. DeCaluwe, *Quantifying the Role of Cerium Oxide as a Catalyst in Solid Oxide Fuel Cell Anodes*, in *Mechanical Engineering*. 2009, University of Maryland: College Park, MD.
4. S.C. DeCaluwe, H. Zhu, R.J. Kee, and G.S. Jackson, *Journal Of The Electrochemical Society*, **155**(6), B538 (2008).
5. H. Kurokawa, T.Z. Sholklapper, C.P. Jacobson, L.C. De Jonghe, and S.J. Visco, *Electrochemical And Solid State Letters*, **10**(9), B135 (2007).
6. B.F. Moller, J. Arriagada, M. Assadi, and I. Potts, *Journal of Power Sources*, **131**(1-2), 320 (2004).

Separate Sensible and Latent Cooling with Solar Energy

UMD Investigators: Reinhard Radermacher, Yunho Hwang

GRA: Ali Al-Alili

PI Investigator: Isoroku Kubo

Start Date: August 2007

1. Objective/Abstract

The main objective of this project is to design, fabricate and test a solar cooling system with the highest possible cooling COP measured to date. The approach involves combining a very efficient concentrating PV-T collector with a separate sensible and latent cooling approach developed at CEEE. This solar cooling system is expected to operate under the UAE's harsh climate conditions.

2. Deliverables for the Completed Quarter

These are the accomplished tasks:

- Created a Labview interface to record the experimental measurements
- Finished the aluminum frame construction
- Finished the supply, exhaust and conditioned space ducts

3. Summary of Project Activities for the Completed Quarter

The focus of this quarter was to construct the experiment setup. This process was started by creating a labview interface to display and record all the measured quantities. A few simple temperature measurements were carried out to check the functionality of the data acquisition system and debug the Labview code. Then, the aluminum frame was constructed to support the weight of the ducts and equipment. After that, the supply, exhaust and conditioned space ducts were constructed. The supply and exhaust ducts were moved into the chamber to start mounting the instrumentation, while the conditioned space duct was kept outside to provide more room for work inside the chamber.

3.1 Labview Interface

Labview was used to read the outputs of the instrumentation and record the data. Figure 1 shows the Labview installed and connected to the data acquisition system. The operation of the data acquisition system was checked by performing temperature measurements using thermocouples. This preliminary code will be improved once all the instruments are mounted inside the ducts.

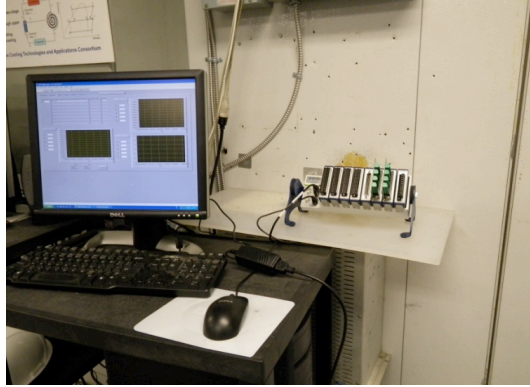


Figure 1. Labview interface.

3.2 Aluminum Frame Construction

The frame was constructed using 1515 aluminum. The assembled frame can be seen in Figure 2.



Figure 2. Aluminum frame.

3.3 Duct Construction

The exhaust and supply duct was constructed as shown in Figure 3. The conditioned space ducts were constructed in a similar manner except that the size was 26"x26".

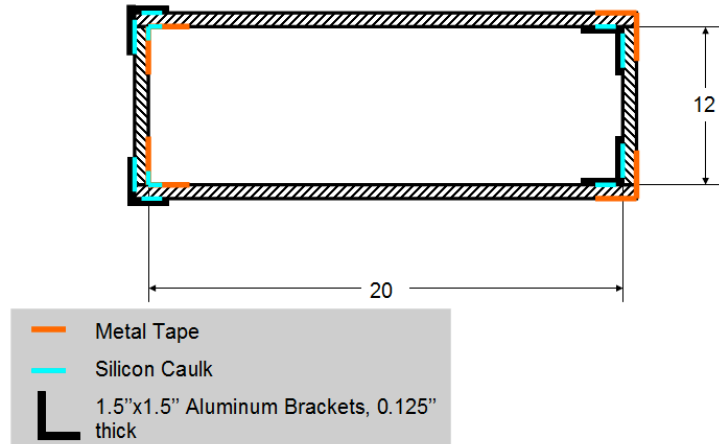


Figure 3. Exhaust and supply duct layout.

Once the supply and exhaust ducts were constructed, they were moved into the chamber and put on the frame, Figure 4.



Figure 4. Supply and exhaust ducts.

In addition, the conditioned space ducts were constructed as shown in Figure 5. Due to the size and weight of the ducts, they were not connected together until they were moved into the chamber. They will not be moved into the chamber until all the instrumentations are mounted into the supply and exhaust duct.



Figure 5. The two ducts used to construct the conditioned space.

4. Difficulties Encountered/Overcome

- Moving the ducts around the aluminum frame
- Available space inside the chamber

5. Planned Project Activities for the Next Quarter

The following activities are to be conducted in the next quarter:

- Continue the construction of the experiment
- Mounting and calibrating the instruments

Appendix

Key References

- [1] Stine, W.B., Geyer, W.B., 2001, Power from the sun, www.powerfromthesun.net.
- [2] Threlkeld, J., Kuehn, T., Ramsy, J., 1998, Thermal Environmental Engineering, Prentice-Hall, Inc, USA
- [3] http://www.nrel.gov/rredc/solar_data.html
- [4] http://rredc.nrel.gov/solar/old_data/nsrdb/tmy2/State.html
- [5] Notton, G., Poggi, P., Cristofari, C., 2006, Predicting hourly solar irradiations on inclined surfaces based on the horizontal measurements: Performances of the association of well-known mathematical models, *Energy Conversion and Management*, 47 1816–1829
- [6] http://rredc.nrel.gov/solar/old_data/nsrdb/1991-2005/siteonthefly.cgi?id=724060
- [7] ASHRAE, 1999, Applications Handbook, CH.32
- [8] Kreith, F. and Kreider, J.F., 1978, Principles of solar engineering, *Hemisphere publishing corporation* Washington USA
- [9] Kalogirou, S., 2004, Solar thermal collectors and applications, *Progress in Energy and Combustion Science* 30 pp. 231–295
- [10] Goswami, Y., Kreith, F. and Kreider, J.F., 2000, Principles of solar engineering, *Taylor and Francis*, PA, USA,
- [11] Duffie, J.A., Beckman, W.A., 1991, *Solar engineering of thermal processes*, Second edition, John Wiley & Sons, Inc., New York, ISBN: 0-471-51056-4.
- [12] Pasupathy, A., Velraj, R., Seeniraj, R.V., 2008, Phase change material-based building architecture for thermal management in residential and commercial establishments, *Renewable and Sustainable Energy Reviews*, pp.39–64
- [13] Dieng, A., Wang, R., 2001 Literature Review on Solar Adsorption Technologies of Ice-making and Air Conditioning Purposes and Recent Developments in Solar Technology, *Renewable and Sustainable Energy Reviews* 5 pp.313–342
- [14] Sumathy, K., Yeung, K., Yong, L., 2003, Technology Development in the Solar Adsorption Refrigeration Systems, *Progress in Energy and Combustion Science* 29 pp 301–327
- [15] Roger, A. Messenger, J. V., 2005, Photovoltaic Systems Engineering, 2nd ed. Taylor & Francis
- [16] <http://www.nfpa.org/>
- [17] <http://ieeexplore.ieee.org/iel5/7946/21930/01019771.pdf?arnumber=1019771>
- [18] TRANE, "Product Data: 4DCZ6036A through 4DCZ6060A" (2008), 22-1815-03
- [19] METEONORM, "Global Meteorological Database for Engineers, Planners and Education,"(2007)

Waste Heat Utilization in the Petroleum Industry

UMD Investigators: Reinhard Radermacher, Yunho Hwang

GRAs: Amir Mortazavi, Abdullah Alabdulkarem

PI Investigators: Saleh Al Hashimi, Peter Rodgers

GRAs: Sahil Popli, Alyas Ali Alshehhi

Start Date: October 2006

1. Objective/Abstract

The main objective of this project is to minimize overall energy consumption of gas or oil processing plants by utilizing waste heat and/or improving cycle design. Consideration will include the use of absorption chillers and steam cycles, among other options.

2. Deliverables for the Completed Quarter

2.1. HYSYS Modeling

The following were modeled using HYSYS:

- CO₂ liquefaction and compression
- Writing APCI cycle optimization paper
- Optimization of different gas-turbine triple-combined cycle configurations.

2.2. Conference Publication

A full-length paper will be published at the ADIPEC 2010 conference, titled:

Popli, S., Rodgers, P., Eveloy, V., Al Hashimi, S., Hwang, Y., Radermacher, R. "Opportunities for Energy Efficiency Enhancements in the Oil and Gas industry Using Waste Heat Powered Absorption Chillers," SPE 2010, Abu Dhabi International Petroleum Exhibition and Conference, ADIPEC Conference, November 1-4, 2010, Abu Dhabi, UAE.

The work presented explores the use of waste heat-powered absorption cooling to boost the efficiency of natural gas (NG) processing, enhance hydrocarbon recovery and reduce utility cost in a NG plant. This analysis will be developed further in the next quarter using waste heat field data collected from GASCO ASAB, which is presented in Section 3.3 of the present report, to model proposed waste heat recovery schemes.

2.3. Performed GASCO ASAB waste-heat energy audit

3. Summary of Project Activities for the Completed Quarter

HYSYS was used to model different configurations of CO₂ liquefaction cycles that are captured from flue gas of gas-turbine based power plant. Further, the compression plant was also modeled using HYSYS software.

3.1 CO₂ Liquefaction and Compression Plant

In order to inject the captured CO₂ into an oil well for enhancing the oil well recovery (EOR), it needs to be pressurized to a high pressure (e.g. 150 bar). This can be achieved in two ways: through multistage compression or through liquefaction and then pumping.

In our model for the combined cycle power plant and amine-based CO₂ capturing columns, 72.4 tons of CO₂/hr were captured, at 97.86% removal efficiency, for the proposed system and 69.3 tons of CO₂/hr, 93.6% removal efficiency, for the baseline system. The captured gas consists of 90% CO₂ by mass and 9% water and traces of nitrogen and oxygen.

The compression plant, shown in Figure 1, consists of eight compressor stages with intercooling to 40 °C. Each compressor has isentropic efficiency of 82%. The total compression power for compressing the captured gases from 1.8 bar to 150 bar is 6.1 MW.

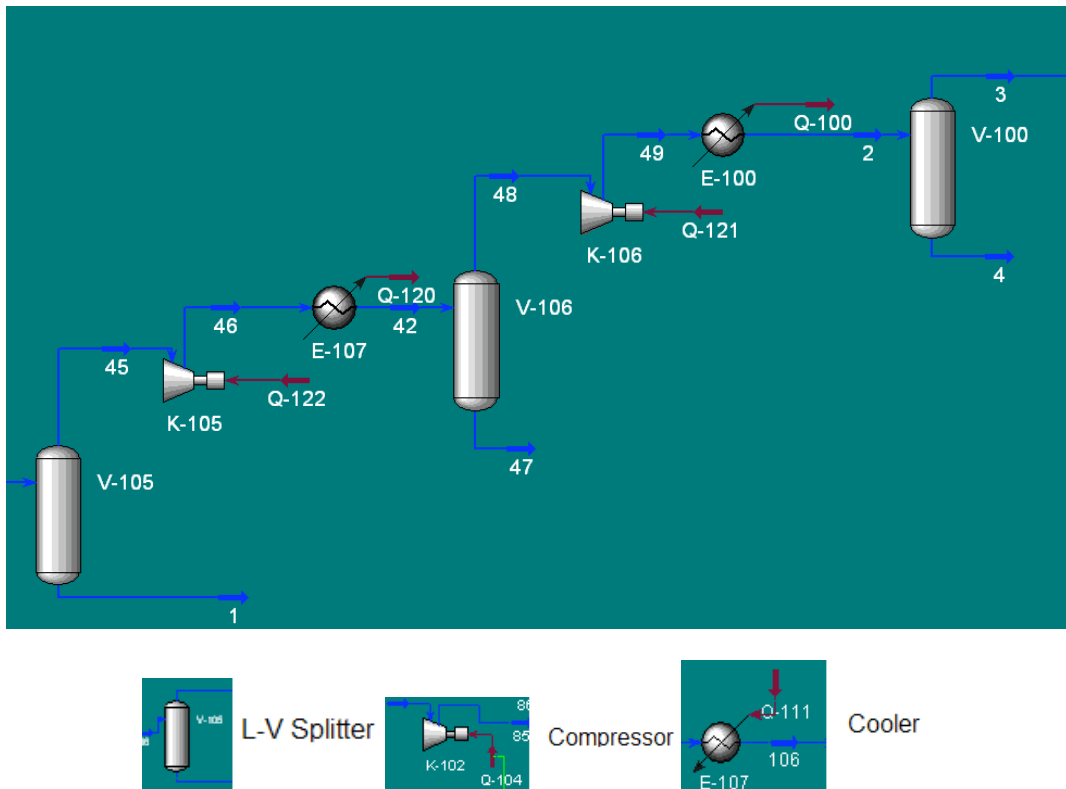


Figure 1. HYSYS model for the CO₂ compression plant (2 stages only shown here out of 8 stages).

In liquefying the CO₂ option, the captured flue gas after the stripper column is at 1.8 bar. Thus, it needs to be compressed to a pressure higher than the CO₂ triple point pressure (5.17 bar) so that no solid CO₂ will be formed in the evaporator of the liquefaction cycle. This stage is called the pre-liquefaction compression stage. It consists of three multistage compressions similar to Figure 1.

The liquefaction cycle, shown in Figure 2, uses ammonia as a refrigerant. It has two evaporators, one for CO₂ sensible cooling and one for latent cooling. The performance of this cycle is summarized in Table 1.

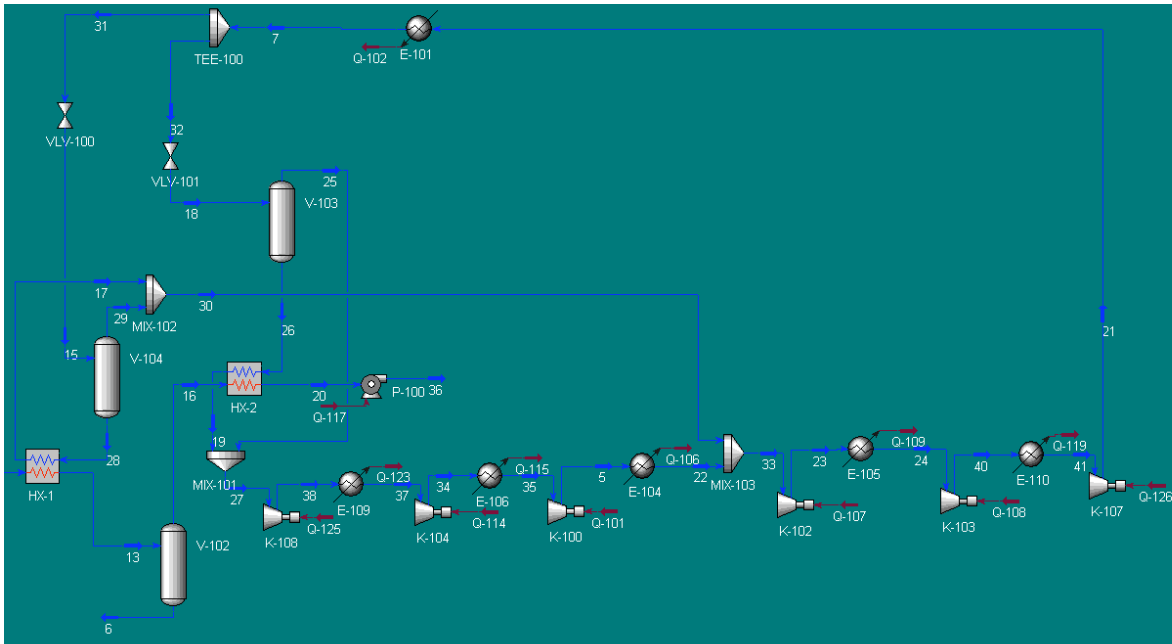


Figure 2. HYSYS model for the CO₂ liquefaction plant.

Table 1. CO₂ liquefaction plant performance using ammonia as a refrigerant

Liquefaction load (MW) to -53 C	9
Pumping power (MW) to 152 atm (-47 C)	0.33
Recoverable Heat (MW) to -47 to 37 C	3.69
Vapor compression cycle (VCC) compressor power (MW)	6.29
Minimum reversible liquefaction power from exergy difference (MW)	4.97
VCC COP	1.48
2nd Law eff	0.82
Compressors Power (MW) (from 1.8 bar to 6 bar)	1.98
Total power (MW)	8.38

Using the same configuration as in Figure 2, different refrigerants were used to determine which one would result in the least compression power. Ammonia resulted in the least power, as shown in Table 2.

Table 2. Vapor compression cycle compressor power using different refrigerant for liquefying CO₂ at 6 bar

Refrigerant	Compressor Power (MW)
Propane	7.86
NH ₃	6.29
R134a	7.73

The liquefied CO₂ at 6 bar and -53 °C is pumped to 152 bar with a temperature of -47 °C. This cold CO₂ is recovered by using it in either liquefying the CO₂ (i.e., reducing the VCC power) or liquefying the natural gas in the APCI cycle. The latter option resulted in reducing the power of the propane cycle in the APCI LNG plant from 43.7 MW to 42.38 MW, or 3% savings. In the first option, the CO₂ is replaced the first evaporator in Figure 2 so that it precools the CO₂ and subcools the ammonia refrigerant as shown in Figure 3. The VCC power is reduced from 6.29 to 4.39 MW, or 30.2% savings.

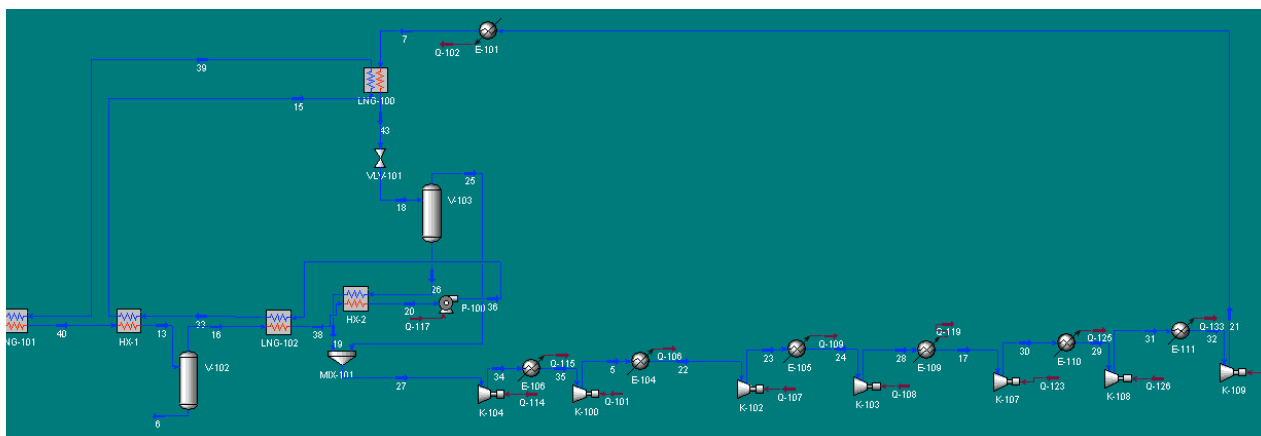


Figure 3. HYSYS model for the CO₂ liquefaction plant with CO₂ cold energy recovery.

3.2 Optimization of different gas-turbine triple-combined cycle configurations

In order to investigate the potential of the gas turbine, steam and absorption chiller combined cycle as an APCI LNG plant driver, the performance of the driver system should be optimized. Moreover, to fully appreciate the benefits of this system it should be compared to the optimized conventional technologies. Matlab software was used as an optimization tool. It was connected to HYSYS, which was used to model the driver cycles. The comparison of different driver technologies is shown in Table 3. As is shown in Table 3, the most efficient driver configuration is the gas-turbine single-pressure steam and single-effect water-Li/Br absorption chiller triple-combined cycle. It has the least fuel consumption. Moreover, it maintains its advantages by varying the steam turbine efficiency and minimum exhaust temperature. Its efficiency is 36% and 4% higher than conventional gas turbines and gas-turbine and steam combined-cycle drivers, respectively.

Table 3. Comparison of different driver cycle technologies

Cycle	Fuel Consumption (kg/s)			Efficiency Enhancement (%)			Translated Efficiency (%)		
Steam Turbine Efficiency (%)	86	90	90	86	90	90	86	90	90
Exhaust Temperature (°C)	180	180	110	180	180	110	180	180	110
Base Cycle With Gas Turbine as a Driver	6.575	6.575	6.575	---	---	---	33.45	33.45	33.45
Combined Gas turbine and Double effect Absorption Chiller	5.174	5.174	5.174	21.31	21.31	21.31	42.51	42.51	42.51
Combined Gas-Turbine and Single-Pressure Steam Cycle	4.571	4.541	4.407	30.48	30.93	32.98	48.16	48.43	49.91
Triple Cycle with Double-Effect Absorption Chiller	4.742	4.706	4.694	27.88	28.42	28.61	46.38	46.73	46.85
Triple Cycle with Single-Effect Absorption Chiller	4.251	4.235	4.219	35.35	35.59	35.84	51.74	51.93	52.13

3.3 GASCO ASAB Waste-Heat Energy Audit

An energy audit was conducted at the GASCO ASAB plant in collaboration with Mr. Alyas Al Shehhi, Mechanical Engineering student. This audit identified potential waste heat sources at two ASAB facilities, ASAB0 and ASAB1, and revealed an abundant source of potential waste heat in the form of gas-turbine exhaust gases, both at ASAB0 and ASAB1. It is proposed that the gas-turbine exhaust gases could be used to provide enhanced process cooling capacity to the natural gas liquid (NGL) plant through absorption cooling. The data obtained from the audit permitted a preliminary waste heat recovery analysis to be undertaken.

Based on this analysis it was found that a total of 500 MW of waste heat is available from gas turbine exhaust gases at GASCO, out of which 280 MW waste heat is available at ASAB1, and

220 MW at ASAB0. While ASAB1 utilizes waste heat recovery steam generators to generate process plant steam, ASAB0 has no such energy recovery schemes. Thus, approximately 220 MW of waste heat is available at ASAB0 in the form of gas turbine exhaust gases, and 150 MW of waste heat is available at ASAB1 in the form of excess steam. It is proposed that this waste heat could be used to power double-effect LiBr absorption chillers, which both provide refrigeration to the NGL plant and meet a part of furnace heating-load.

The following proposals are to be modeled for the GASCO ASAB NGL plant using HYSYS, for the next phase of this analysis:

(i) Reduce Furnace Heating Load:

A natural gas-fired furnace is currently being used for lean gas regeneration at the GASCO NGL plant. It is proposed that the waste heat from turbine exhaust gases at ASAB0, and excess low-pressure process steam at ASAB1 could be utilized for lean gas regeneration at ASAB0. This could potentially reduce the furnace heating load, save hydrocarbon fuel, and reduce emission of harmful gases such as CO, NO_x and SO_x.

(ii) Absorption Chillers for Enhanced Cooling:

NGL extraction at GASCO ASAB involves cooling the associated gas received from ADCO. Propane vapor compression refrigeration is utilized to provide required refrigeration. It is proposed that gas turbine exhaust gases from ASAB0 and excess low-pressure steam from ASAB1 could power absorption chillers, which could provide enhanced propane cooling capacity to the NGL plant, reduce electrical energy consumption, and improve overall plant efficiency.

(iii) Process Stream Air-Cooling:

Process gases at GASCO ASAB are motor-driven process air-coolers that run continuously and consume electrical energy. It is proposed that gas turbine exhaust gases from ASAB0 and excess low pressure steam from ASAB1 could power absorption chillers, which could provide enhanced process gas cooling capacity to the NGL plant, reduce electrical energy consumption, and improve overall plant efficiency.

The proposed waste heat recovery schemes, such as absorption refrigeration systems (ARS), are being modeled using EES to assess feasibility and performance.

4. Difficulties Encountered/Overcome

None.

5. Planned Project Activities for the Next Quarter

The following activities are to be conducted in the next quarter:

- Model and optimize cascade cycle
- Evaluate the overall system performance
- Optimize the split design of gas-turbine, steam and absorption chiller triple-combined cycle as a driver of the APCI LNG plant.
- Modeling of the proposed ASAB waste heat recovery schemes will be completed to assess feasibility and performance.

Appendix

Justification and Background

Waste heat utilization opportunities are abundant in the oil and gas industry. Proper use of waste heat could result in improved cycle efficiency, reduced energy usage, reduction in CO₂ emissions, and increased production capacity.

CEEE at the University of Maryland has extensive experience in the design and implementation of integrated combined cooling, heating, and power (CCHP) projects. The faculty at PI has experience in the design and operation of petroleum processing plants. Jointly the team is well equipped to address the challenge posed by this project.

References

- [1] Alefeld, G., Radermacher, R., 1994, "Heat conversion systems", CRC Press, Boca Raton.
- [2] Al-Hamdan, Q.Z., Ebaid, M.S.Y., 2006, "Modeling and simulation of a gas turbine engine for power generation", ASME Journal of Engineering for Gas Turbines and Power, Vol. 128, pp. 302-311.
- [3] LNG technology selection, http://www.fwc.com/publications/tech_papers/files/TariqLNG.pdf, last access, June, 2008.
- [4] Haring, H., 2008, "Industrial Gas Processing", Wiley-VCH, Weinheim
- [5] ASHRAE, 2002, "ASHRAE Refrigeration Handbook", American Society of Heating, Refrigeration and Air-Conditioning Engineers, Atlanta, GA, USA.
- [6] ASHRAE, 2005, "ASHRAE Fundamentals Handbook", American Society of Heating, Refrigeration and Air-Conditioning Engineers, Atlanta, GA, USA.
- [7] Brant, B., Brueske, S., Erickson, D.C., Papar, R., 1998, "New waste-heat refrigeration unit cuts flaring, reduces pollution", Oil & Gas Journal, May 18, pp.61-64.
- [8] Brooks, F.,J., 2000 "GE gas turbine performance characteristics", GE Power Systems Schenectady, NY, GER-3567H.
- [9] Cohen, H., Rogers, G.F.C., Saravanamuttoo, H.I.H., 1996, "Gas turbine theory", 4th edition, Longman Scientific & Technical, Singapore.
- [10] Erickson, D.C., 2000 "LPG recovery from reformer treat gas", US Patent 6,158,241.
- [11] Erickson, D.C., Anand, G., Papar, R.A., Tang, J., 1998, "Refinery waste heat powered absorption refrigeration – cycle specification and design", Proceeding of the ASME Advanced Energy System Division, AES-Vol. 38, pp.391-402.
- [12] Erickson, D.C., Kelly, F., 1998, "LPG recovery from refinery by waste heat powered absorption refrigeration", IECEC-98-079, 33rd Intersociety Engineering Conference on Energy Conversion, Colorado Springs, CO.
- [13] Giampaolo, T., 2003, "The gas turbine handbook: principles and practices", 2nd edition, The Fairmont Press, Lilburn, GA.
- [14] Herold, K.E.; Radermacher, R., Klein, S, 1996, "Absorption chillers and heat pumps", CRC Press, Boca Raton.
- [15] Kim, T.S., Hwang, S.H., 2006, "Part load performance analysis of recuperated gas turbine considering engine configuration and operation strategy", Energy, Vol. 31, pp., 260-277.
- [16] Klein, S.A., 2005, "Engineering Equation Solver" F-Chart Software.
- [17] Kurz, R., 2005, "Gas turbine performance", 44th Turbomachinery Symposium, pp.131-146.
- [18] Kurzke, J., 2003, "Model based gas turbine parameter corrections", GT2003-38234, Proceedings of 2003 ASME TURBO EXPO: Power for Land, Sea, & Air, Atlanta, GA, USA.
- [19] Li, Y.G., Pilidis, P., Newby, M.A., 2006, "An adaptation approach for gas turbine design-point performance simulation", Journal of Engineering for Gas Turbines and Power, Vol. 128, pp. 789-795.
- [20] Orlando, J. A., 1996, "Cogeneration design guide", American Society of Heating, Refrigeration and Air-Conditioning Engineers, Atlanta, GA.
- [21] Pande, M., 1996, "Tools for fractionator design in ammonia-water absorption machines", Master Thesis, University of Maryland, College Park.
- [22] Walsh, P.P., Fletcher, P., 1998, "Gas turbine performance", Blackwell Science, Oxford.



Thrust 2
Energy-Efficient Transport Processes

Multidisciplinary Design and Characterization of Polymer Composite Seawater Heat Exchanger Module

PI Investigator: Peter Rodgers

UMD Investigators: Avram Bar-Cohen, Satyandra K. Gupta, David Bigio, H.A. Bruck

GRAs: Juan Cevallos, F. Robinson, T. Hall, W. Pappas

Start Date: Oct 2006

1. Introduction

Heat exchangers are extensively used in all oil and gas processing operations with seawater as the preferred coolant in near-shore operations. The performance and cost effectiveness of conventional metallic heat exchangers in such environments are severely constrained by corrosion and scale deposits. Polymer heat exchangers, currently under investigation by the EERC team, offer a promising alternative to metallic heat exchangers for the fossil fuel industry. Recent advances in carbon-fiber polymer composites, yielding polymer materials with thermal conductivities equal to or higher than titanium, can be applied to the development of low-cost and low-weight compact heat exchangers for corrosive fluids. These attributes, combined with the low energy investment in the formation and fabrication of these polymer heat exchangers and their ease of manufacturing, appear to make near-term applications of seawater polymer heat exchangers viable. Numerical simulations and laboratory experiments, performed by the UMD/PI EERC team in the first phase of this research, strongly support these conclusions.

2. Milestones/Deliverables Scheduled for the Completed Quarter (related project task shown in parenthesis, see Appendix 6.2)

- I. Develop specimens for experimental validation of fiber orientation predictions (Task B2)
- II. Apply image processing methods to determine fiber orientation in experimental specimens and compare to Moldflow[®] predictions (Task B2)
- III. Upgrade experimental rig for testing polymer heat exchangers (Task A2)
- IV. Construct apparatus for application of tensile stress to carbon-filled nylon samples undergoing hygrothermal aging in aqueous saline environment at an elevated temperature (Task A5)
- V. Design and construct injection mold for producing carbon-filled nylon testing specimens in accordance with ASTM International guidelines and that are compatible with clevises of aging apparatus (Task A5)
- VI. Hygrothermally age carbon-filled nylon testing specimens under tensile load at 60°C in an aqueous solution with a salinity of 45g/kg (Task A5)
- VII. Tensile test carbon-filled nylon specimens which were stressed during aging to determine mechanical properties (Task A5)
- VIII. Develop finite element analysis (FEA) model using hygrothermally aged mechanical properties to assess feasibility of replacing metallic heat exchangers at the Das Island liquefied natural gas facility with polymer composite heat exchangers (Task A5)
- IX. Modify heat exchanger geometry to reduce stresses experienced by polymer composite heat exchanger (Task A5)

- X. Assess feasibility of modeling orthotropic heat exchanger module as an isotropic model with averaged properties (Task A5)
- XI. A paper entitled “Incorporating Moldability Considerations during the Design of Thermally Enhanced Polymer Heat Exchangers” is undergoing revisions following comments from the editors of ASME Journal of Mechanical Design **Error! Reference source not found.**
- XII. A paper entitled “Thermal Anisotropy in Injection Molded Polymer Composite Fins” was presented, via poster presentation, at the 14th International Heat Transfer Conference (IHTC14) **Error! Reference source not found.**

3. Summary of Project Activities for the Completed Quarter

I. Develop specimens for experimental validation of fiber orientation predictions

- a. **Motivation:** Fiber orientation is critical to thermal and mechanical performance, and the use of highly-filled, thermally-enhanced polymers and complex geometry necessitates validation of Moldflow[®] predictions of fiber orientation.
- b. **Action Plan:** Develop test geometries representing critical flow behavior in polymer heat exchangers, design and machine injection molds for the chosen geometries, injection mold test specimens, develop and implement a sectioning and polishing routine in preparation for microscopy, and collect microscope samples of points of interest.
- c. **Findings:**
 - Created spiral and L-channel geometries (shown in Figure 1) representing slow and fast changes in velocity gradient, respectively.

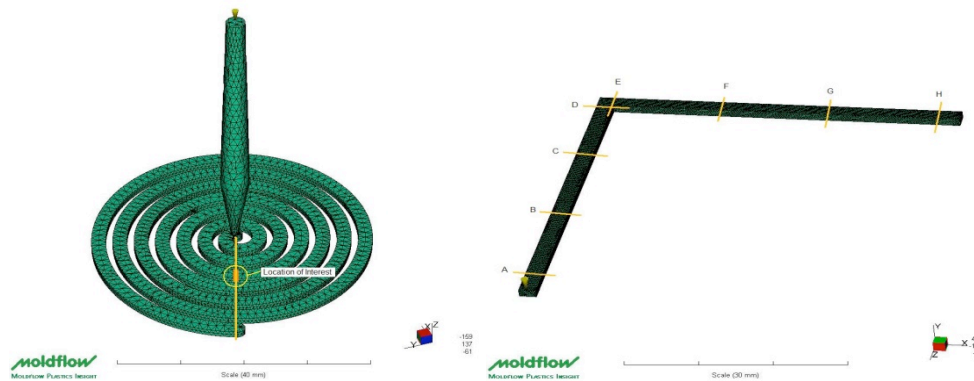


Figure 1. Spiral and L-channel geometries.

- Designed and machined injection molds for the selected spiral and L-channel geometries. Created injection molded test samples at fixed system parameters and material
 - Material: PolyOne NJ-6000 TC Black (51.8%wt)
 - Injection temperature: 285°C
 - Pressure: 164 MPa
 - Flow rate: 12 cm³/s
 - Mold temperature: 30°C

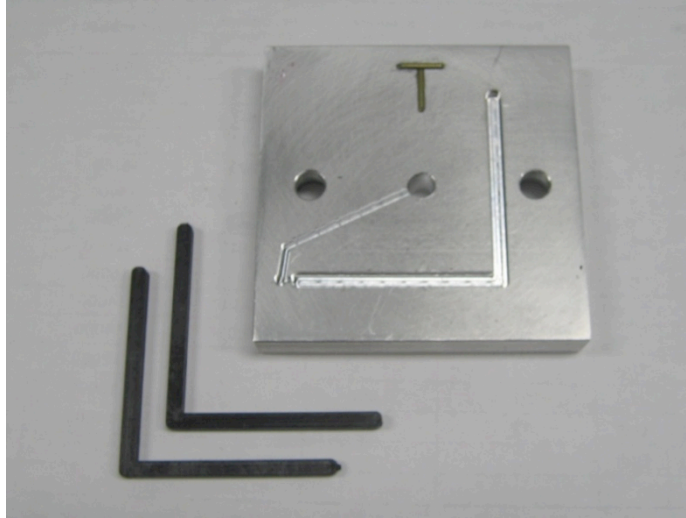


Figure 2. L-channel mold and injection molded specimens.

- Sectioned L-Channel specimens to the mid-plane. Implemented polishing routine based on the recommendations given in the following books for preparing the specimens for light microscopy:
 - Hemsley, D. A. *Applied Polymer Light Microscopy*. London: Elsevier Applied Science, 1989.
 - Sawyer, Linda C., and David T. Grubb. *Polymer Microscopy*. London: Chapman and Hall, 1987.
- Microscope images were collected at relatively low magnification (3x and 5x) for the target location at the direction change of the L-Channel. The microscope was adjusted to the following primary settings so that the fibers would reflect light and therefore appear white. The matrix absorbed light and therefore appears black in the collected images (Figure 3).
 - Light source: Reflected
 - Polarization: 0° and 60°

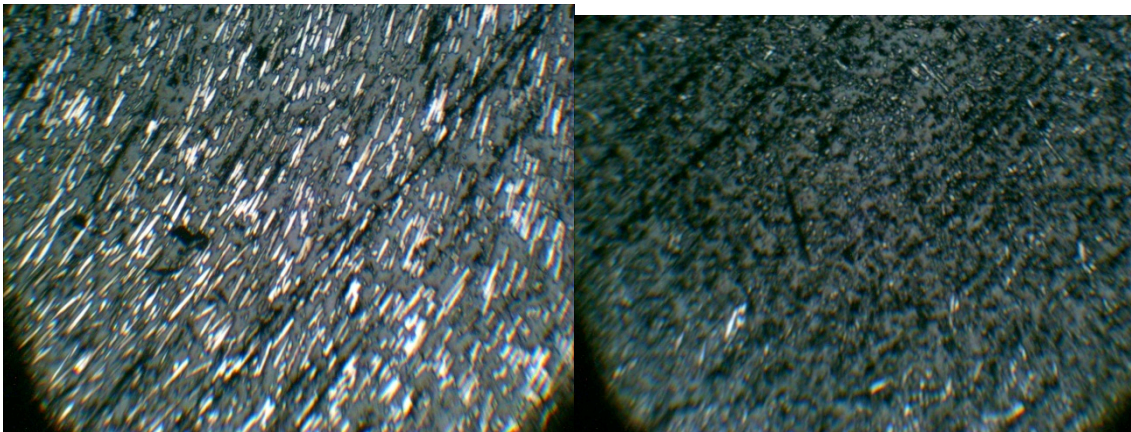


Figure 3. Example microscope images. Left represents fiber in-plane, right, out-of-plane.

II. Apply image processing methods to determine fiber orientation in experimental specimens and compare to Moldflow® predictions

- a. Motivation:** Manual identification of fiber orientation in microscope images is time-intensive and potentially error prone.
- b. Approach:** Apply image processing techniques to identify fiber orientation in microscope images and convert Moldflow® tensor results for direct comparison to experimental results formatting
- c. Findings:**

- From the original image, perform the following analysis:
 - Convert to grayscale
 - Perform thresholding based on intensity value for fibers (determined experimentally)
 - Convert to binary image using edge detection
 - Apply Hough transform to the binary image
 - Apply threshold to accumulator results from Hough transform to ensure significance
 - Create histogram of Hough transform results by orientation angle, weighted by number of occurrences in the accumulator array

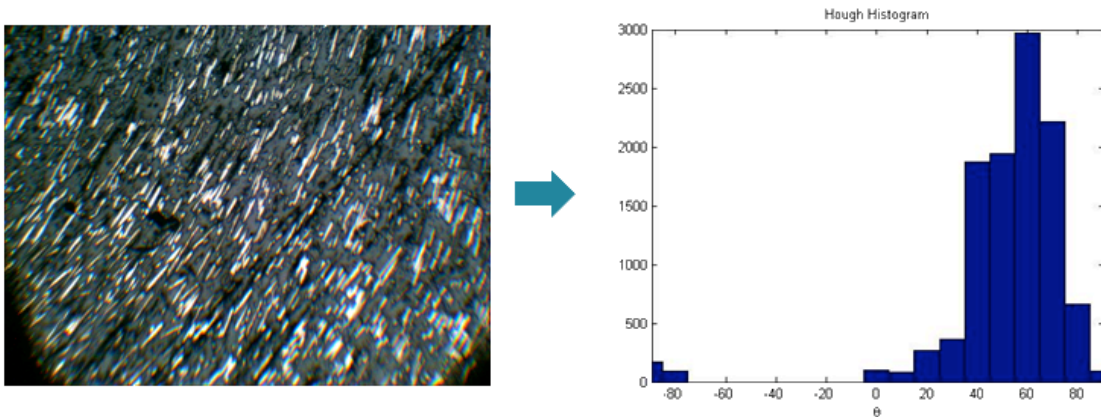


Figure 4. Original image and the weighted histogram results of the image processing.

- Moldflow® represents fiber orientation predictions as tensor values, which are not directly comparable to the experimental results. Tensor values were collected from Moldflow® for the desired location and the distribution was recovered using the technique outlined by the following paper:
 - Advani, Suresh G., and Charles L. Tucker. "The Use of Tensors to Describe and Predict Fiber Orientation in Short Fiber Composites." *Journal of Rheology* 31.8 (1987): 751-84

Alternatively, the principle orientation values and directions can be determined and utilized for comparison to experimental results.

III. Upgrade experimental rig for testing polymer heat exchangers

- The previous experimental setup involved a small-scale heat exchanger and provided limited heat transfer rates and temperature change. The latter causes the relative uncertainty of the calculated heat transfer rate to be high (~16%).
- A new test rig was installed at UMD. It can accommodate a larger laboratory heat exchanger with an increased heat transfer rate, which will also increase the temperature differences across the heat exchanger, thereby reducing the relative uncertainty caused by the thermocouple measurements (~5%).
- New features of the upgraded rig include:
 - A 2800RPM DC fan that provides flow rates of up to 12,800 cm³/s (4x the previous maximum flow rate)
 - A 2450W finned tubular air heater that serves to elevate the bulk temperature of the air to upwards of 120 °C
 - A PID temperature controller coupled with a silicon-controlled rectifier, or SCR, that control the power delivered to the tubular heater
 - A vortex-shedding flow meter that measures the air flow rate to an accuracy of ±1%
 - A shell and tube brass heat exchanger with a surface area of 1.5 m² that will cool the air down to room temperature following the PHX
- Figure 5 shows a schematic of the upgraded test rig. Figure 6 shows a picture of the test rig assembled at a UMD laboratory

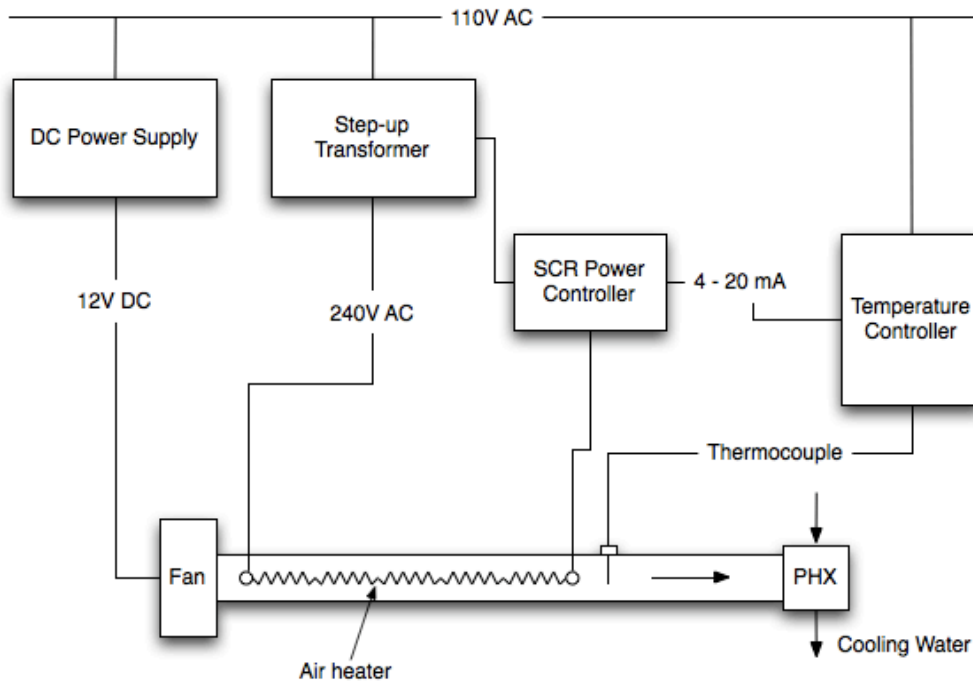


Figure 5. Schematic of upgraded PHX test rig.

(Following the PHX air will flow into flow meter and secondary HX)

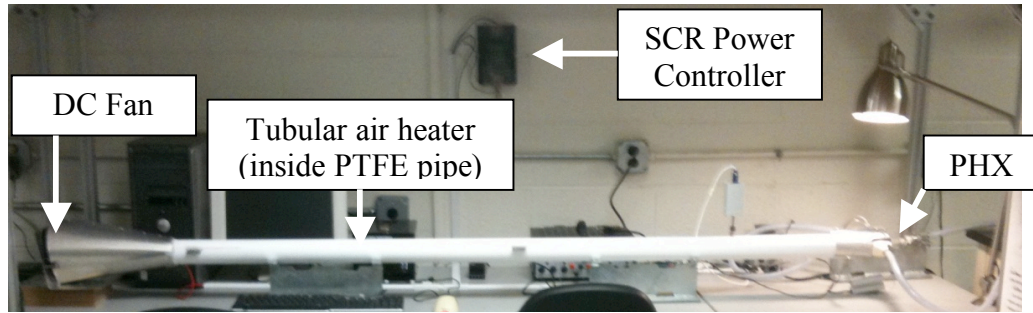


Figure 6. Upgraded PHX test rig.

- Following this upgrade, a larger polymer heat exchanger will be fabricated. Table 1 below shows a side-by-side comparison of the new and old HX designs. The plate length was tripled, and the number of air-side fins was increased to eighteen. Also, the number of plates was doubled for each fluid. Note that the surface area has been increased almost an order of magnitude.

Table 1. Side-by-side comparison of experimental designs

	Previous HX	New HX
Plate Length (cm)	5	15
Wall and fin thickness (mm)	2.5	2.5
No. of fins air side	5	18
No. of fins water side	2	10
No. of plates (per fluid side)	3	6
Air-side surface area (m²)	0.0044	0.043
Water-side surface area (m²)	0.0033	0.034

- With a larger heat exchanger, the heat transfer rate is expected to increase to more than 500W, and the temperature drop across the heat exchanger on the air-side is increased to 42K, while the temperature rise on the water-side is increased to at least 4K.
- Figure 7 below shows two plots of HX heat transfer rate and thermal conductance that compare the predicted performance of the previous prototypical PHX to the new laboratory-scale PHX. Note that maximum air flow rate previously achieved (~3000 cm³/s) is now shown as the low bound of the flow rate in the new design. Looking at the heat transfer rate for a flow rate of 3000 cm³/s, the previous design only transferred about 20 W, while the new design transfers close to 200 W. If the flow rate is increased to 12800 cm³/s, the new design is expected to transfer 500 W of heat. Comparing the thermal conductance reveals that an order of magnitude increase is expected, with the previous PHX having a thermal conductance of ~0.6 W/K at 3000 cm³/s, while the new PHX will transfer 7 W/K at 12800 cm³/s.

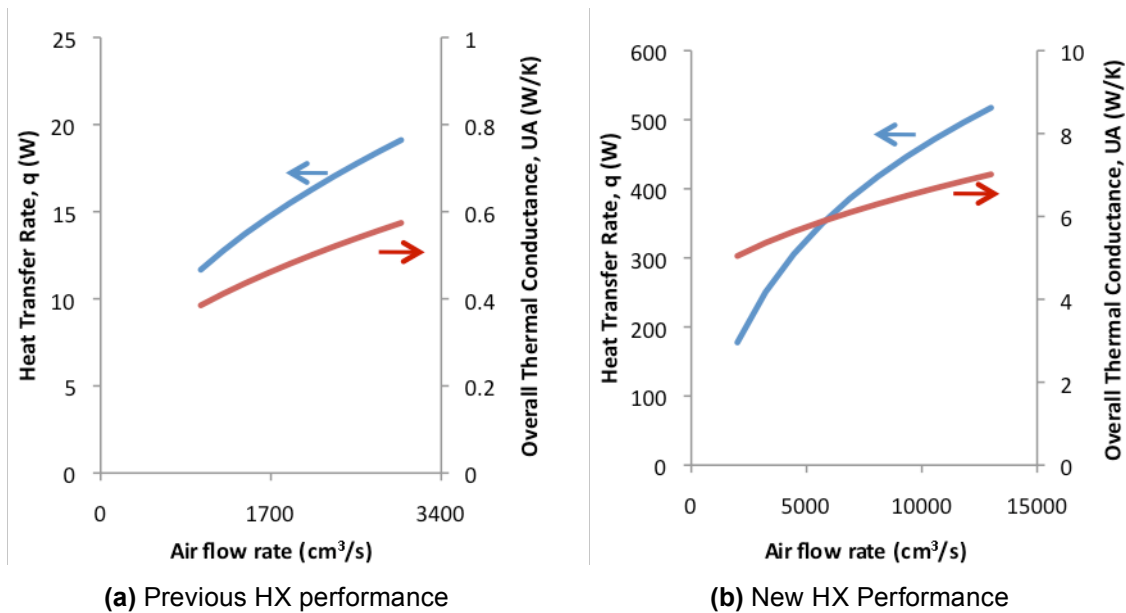


Figure 7. Performance comparison of previous HX to new HX design.

IV. Design and construction of new test apparatus for hygrothermal aging under load

- Because the properties of pure and filled polymer specimens may change at different rates under load during hygrothermal aging, a new test apparatus was constructed for hygrothermal aging under load to complement the previous hygrothermal aging studies without load. The apparatus was designed to handle up to 6 specimens with hygrothermal aging conditions identical to the specimens that were prepared without load. A dead weight loading system was chosen to maintain constant stress during aging.
- The apparatus consists of an existing workbench, aluminum framing, pulleys, six-liter buckets (or alternative adjustable weight containers such as canvas bags), a 30-liter glass aquarium, stainless steel eyebolts, stainless steel clevises, a magnetic impeller pump, nylon test cord, and a Teflon covered heating element was constructed (shown in Figure 8, Figure 9, and Figure 10).
- Test specimens of carbon-filled nylon are pinned on one end by a clevis attached to an eyebolt at the base of the tank and on the other end by a clevis attached to the nylon test line. The test line is run through a pulley and tied to a six-liter bucket. The bucket is then filled with the correct weight to create the necessary stress in the carbon-filled nylon test specimen. The geometry of these specimens is identical to those previously tested using the Imada load frame.
- The aquarium is filled with 30 liters of water at the desired salinity (either freshwater or 45 g/kg).
- The heater maintains the water temperature at the set temperature (currently up to 60 °C).
- The pump circulates the water in the tank to prevent temperature and salinity stratification.

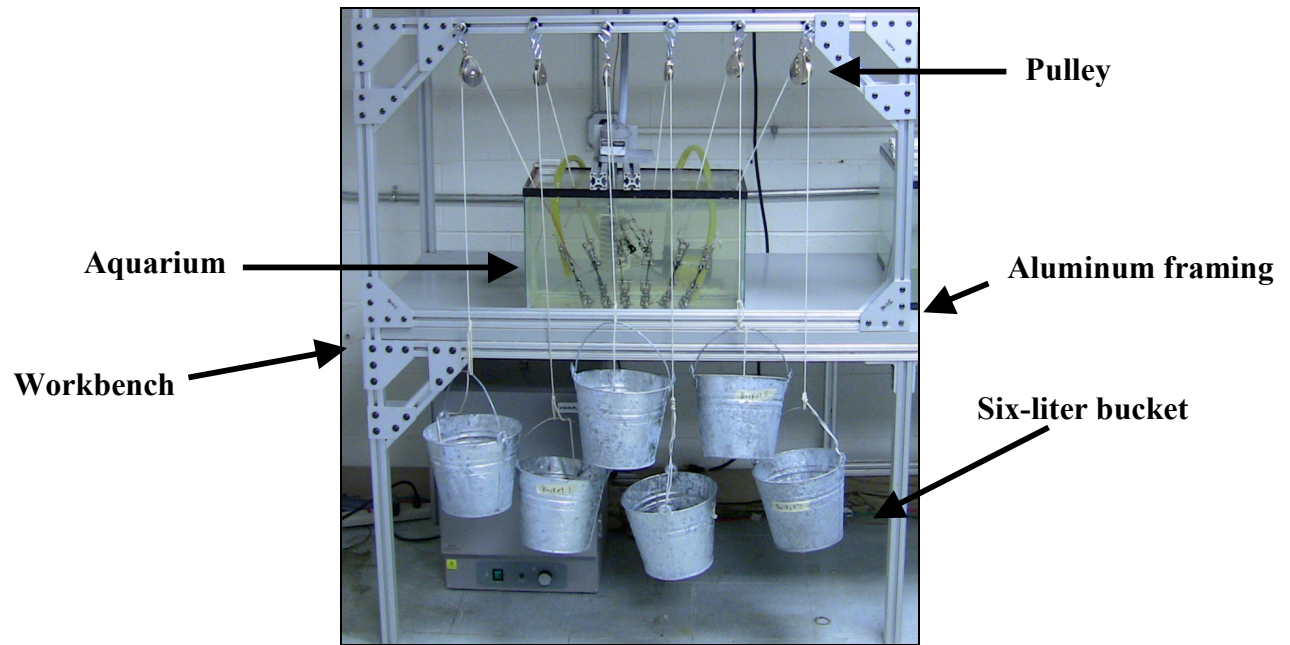


Figure 8. Side view of apparatus for aging specimens under stress.

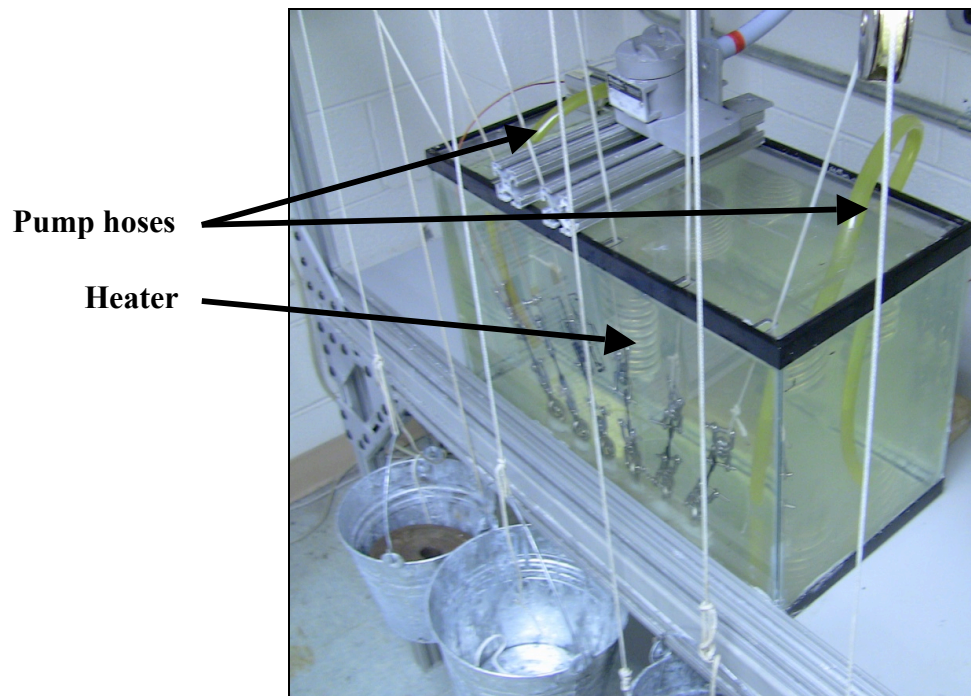


Figure 9. Top-angled view of apparatus for aging specimens under stress.

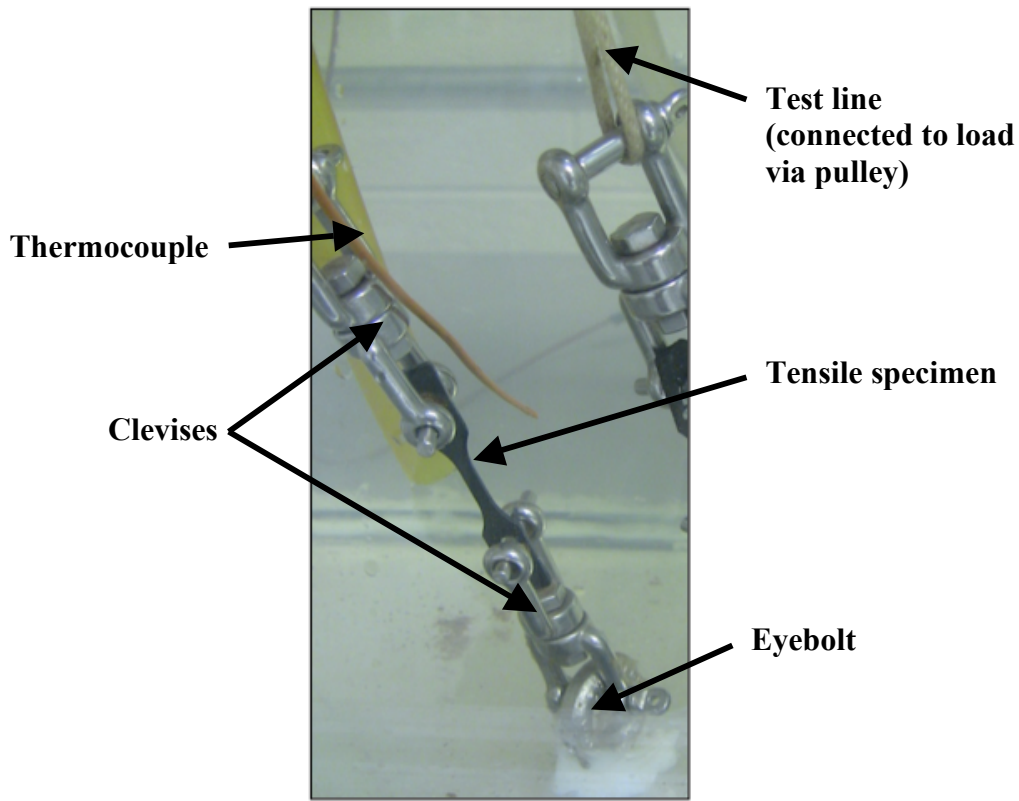


Figure 10. Close-up view of tensile specimen aging under stress.

V. Design and construct injection mold for producing specimens complying with ASTM international guidelines that are compatible with clevises of aging apparatus

- A computer model of an injection mold for the desired testing specimen was created using computer-aided design software ProEngineer.
- A computed numerically controlled (CNC) machining file of the mold was created, also using Pro-Engineer.
- A CNC mill in the University of Maryland's Advanced Manufacturing Laboratory was used to create the designed injection mold.
- Carbon-filled nylon testing specimens were molded at an injection-molding machine in the Advanced Manufacturing Laboratory.
- A single specimen is shown in Figure 11.



Figure 11. Carbon reinforced nylon tensile specimen.

VI. *Hygrothermally age carbon-filled nylon testing specimens under tensile load at 60°C in an aqueous solution with a salinity of 45g/kg*

- Six specimens were aged at 60% of their yield stress (determined by the research group's previous experiments) in the aforementioned conditions until the specimens were fully saturated with saltwater (122 hours).
- The time required for the samples to achieve saltwater saturation was calculated using Fickian diffusion equations.
- The load required to create 60% of the samples' yield stress was determined based upon the samples' cross-sectional area.
- The load was created by placing lead weights and sand in the six-liter buckets of the testing apparatus.

VII. *Tensile test carbon-filled nylon specimens which were stressed during aging to determine mechanical properties*

- Three aged specimens were tensile tested in the Multiscale Measurements Laboratory.
- The testing results of the aged specimens are shown in Table 2.
- The results from this experiment are highlighted in grey and shown alongside the mechanical properties of the carbon-filled nylon aged for similar times under similar hydrothermal conditions at no stress, obtained during previous experiments conducted by the research group.

Table 2. Comparison of reinforced nylon testing results

	Yield Strength (MPa)		Elongation at Yield (%)		Failure Strength (MPa)		Elongation at Failure (%)		Elastic Modulus (GPa)	
	Avg.	Std. Dev.	Avg.	Std. Dev.	Avg.	Std. Dev.	Avg.	Std. Dev.	Avg.	Std. Dev.
Aged in 60°C Saltwater (zero stress)	62.38	8.58	0.96	0.21	87.03	6.20	2.89	0.54	8.66	2.34
Aged in 60°C Saltwater (60% of yield stress)	65.33	3.06	0.77	0.12	79.69	4.96	0.85	0.05	8.52	0.96
Difference	2.95	-5.53	-0.19	-.09	-7.34	-1.24	-2.04	-0.49	-0.14	-1.38
t-statistic	0.752		-1.733		-1.923		-9.119		-0.126	
p-value	0.477		0.127		0.113		0.000		0.903	

- A two-sample t-test was conducted to compare the measured mechanical properties of the carbon-filled nylon specimens aged under 60% of their yield stress and those aged under zero-stress conditions.

- The p-values associated with the t-statistics indicate that there is not enough evidence to conclude there is a difference between the yield strengths, elongations at yield, failure strengths and elastic moduli of the two types of aged nylon.
- The p-value from the comparison of the nylons' elongation at failure was less than 0.05, indicating that this property of the nylon aged under 60% of its yield stress (yield strength) was different from that aged under zero-stress conditions
- As only three samples aged under 60% of their yield stress were tested, this data shown in Table 2 only provides an initial comparison.

VIII. Develop finite element analysis (FEA) model using hygrothermally aged mechanical properties to assess feasibility of replacing metallic heat exchangers at the Das Island liquefied natural gas facility with polymer composite heat exchangers

a. Purpose

- Carbon fiber reinforced composites have lower elastic moduli, lower yield strengths and greater ductility than their metallic counterparts. Moreover, their mechanical properties present significant anisotropy. These differences affect material behavior under loading. Before implementing polymer composite materials in heat exchangers, the behavior of these materials as they are exposed to the pressure loads exerted by the gases cooled during the liquefaction of natural gas must be understood.
- Modeling fiber reinforced polymers is more challenging than modeling metals due to the inherent anisotropy that results from fiber orientation in the matrix. Elastic modulus and yield strength are greater in the direction of the fiber orientation. Thus, structural models must account for anisotropy to provide accurate results.

b. Orthotropic Model Properties

- An orthotropic three-dimensional FEA model was developed for a laboratory-scale polymer composite heat exchanger that can serve as a vehicle for exploring the effects of gas pressure on a notional polymer composite heat exchanger.
- The measured 60°C properties for hygrothermally-aged reinforced PA12 were used in this model for the mechanical properties in the fiber-aligned direction. Available analytical formulations were used to determine the off-axis properties of the reinforced PA12, based on the fiber concentration and fiber geometry.
- The elastic modulus of the fibers after aging was found according to Cox's [5] shear-lag model, which is used for analysis of stress transfer between the fiber and matrix in composites. The Cox model estimates the longitudinal elastic modulus as

$$E_L = E_f \left[1 - \frac{\tanh\left(\frac{\beta l}{2}\right)}{\frac{\beta l}{2}} \right] V_f + E_m(1 - V_f) \quad (1)$$

where β is the shear lag parameter, E_f is the elastic modulus of the fibers, l is the average fiber length, V_f is the volume fraction of the fibers and E_m is the elastic modulus of the matrix.

- The shear lag parameter is given by

$$\beta = \left[\frac{2\pi G_m}{E_f (\pi r_f^2) \ln\left(\frac{R}{r_f}\right)} \right]^{\frac{1}{2}} \quad (2)$$

where G_m is the shear modulus of the matrix, r_f is the radius of the fibers and R is the mean separation of the fibers normal to their length. For a square packing arrangement,

$$\ln \frac{R}{r_f} = \frac{1}{2} \ln \left(\frac{\pi}{V_f} \right) \quad (3)$$

- The shear modulus of the matrix was calculated using a matrix Poisson's ratio of 0.408 provided by Amado-Becker et al [6]. The matrix shear modulus is given by

$$G_m = \frac{E_m}{2(1 + \nu_m)} \quad (4)$$

where ν_m is the Poisson's ratio of the matrix.

- Several theories exist regarding the calculation of the mechanical properties of fiber-reinforced composites. The Halpin-Tsai equations [7] are commonly used to calculate these properties. Properties were also calculated using the Tsai-Hahn [8] equations to provide a comparison. A similar methodology was shown by Pegoretti et al [9].
- The Halpin-Tsai equation for the transverse elastic modulus is

$$E_T = E_m \frac{1 + \xi \eta V_f}{1 - \eta V_f} \quad (5)$$

where

$$\eta = \frac{E_f - E_m}{E_f + \xi E_m} \quad (6)$$

and $\xi = 2$ for fibers with a round cross-section.

- The Tsai-Hahn equation for the transverse elastic modulus is

$$\frac{1}{E_T} = \frac{1}{V_f + \eta V_m} \left(\frac{V_f}{E_f} + \eta \frac{V_m}{E_m} \right) \quad (7)$$

where $\eta = \frac{1}{2}$ and V_m is the volume fraction of the matrix material.

- Neither form of the transverse elastic modulus equation has a factor for the aspect ratio of the fibers because the transverse elastic modulus is nearly independent of the fiber aspect ratio [10].
- The Halpin-Tsai equation for the in-plane shear modulus is

$$G_{LT} = G_m \frac{1 + \xi \eta V_f}{1 - \eta V_f} \quad (8)$$

where

$$\eta = \frac{G_f - G_m}{G_f + \xi G_m} \quad (9)$$

and $\xi = 1$ for fibers with a round cross-section.

- The Tsai-Hahn equation for the in-plane shear modulus is

$$\frac{1}{G_{LT}} = \frac{1}{V_f + \eta V_m} \left(\frac{V_f}{G_f} + \eta \frac{V_m}{G_m} \right) \quad (10)$$

where

$$\eta = \frac{1}{2} \left(1 + \frac{G_m}{G_f} \right) \quad (11)$$

- The Poisson's ratio ν_{LT} was evaluated by the rule of mixtures:

$$\nu_{LT} = \nu_f V_f + \nu_m V_m \quad (12)$$

- The Poisson's ratio ν'_{TT} was evaluated using the following equation proposed by Foye [11]:

$$\nu'_{TT} = \nu_f V_f + \nu_m V_m \Phi \quad (13)$$

- where

$$\Phi = \frac{1 + \nu_m - \nu_{LT} \left(\frac{E_m}{E_L} \right)}{1 - \nu_m^2 + \nu_m \nu_{LT} \left(\frac{E_m}{E_L} \right)} \quad (14)$$

- The shear modulus G_{TT} can be calculated as follows:

$$G'_{TT} = \frac{E_T}{2(1 + \nu'_{TT})} \quad (15)$$

- The parameters that served as inputs to Equations 1-3 are from experimental results and material properties from other researchers. A summary of these properties is provided in Table 3.

Table 3. Equation parameters and their values

Parameter	Value
E_L (GPa)	9.26
E_m (GPa)	0.62
G_m (GPa)	0.21
V_f (-)	0.33
l (μm) [8]	200
r_f (μm) [8]	5

- The calculated elastic modulus of the fibers (E_f) was 65.5 GPa, which is much lower than the 690 GPa estimate provided by the fiber manufacturer [12]. The calculated values provide an estimate of the effective elastic modulus of the fibers because the fibers are discontinuous. In the same way that the rule of mixtures does not apply to the short fiber reinforced polymer's thermal conductivity, the result of mixtures does not apply to the calculation of the elastic modulus of the composite. The large disparity between the estimated fiber properties and manufacturer specified properties could also indicate that aging causes debonding between the fibers and the matrix. A literature review on shear lag models that account for debonding is being performed for the next quarterly report.
- The results of the comparison of the Halpin-Tsai and Tsai-Hahn models are shown in Table 4.

Table 4. Mechanical properties comparison from Halpin-Tsai and Tsai-Hahn models

Property	E_t (GPa)	G_{tt} (GPa)	G_{tt} (GPa)
Halpin-Tsai	1.50	0.432	0.496
Tsai-Hahn	1.22	0.432	0.403

Average	1.36	0.432	0.449
----------------	-------------	--------------	--------------

- The collective set of mechanical properties entered for the orthotropic model is shown in Table 5. These properties are the collection of experimentally determined properties, manufacturer specified properties and calculated properties based on the equations described previously. The l subscript represents the longitudinal (i.e., reinforced) direction and the t subscript represents transverse (i.e., unreinforced) direction.

Table 5. Mechanical properties of aged polymer composite

Property	Value
E_l (GPa)	9.26
E_t (GPa)	1.36
G_{lt} (GPa)	0.432
G_{tt} (GPa)	0.449
ν_{lt}	0.336
ν_{tt}	0.512

c. Orthotropic Model Methodology

- The orthotropic properties were assigned based on the expected orientation that results from injection molding of composite finned plates. The expected flow direction was assigned the longitudinal properties and the assigned transverse properties were assigned to the two directions perpendicular to the longitudinal direction.
- An injection flow pattern of a finned plate is shown in Figure 12. In the bottom plate area, the x-direction was assigned the longitudinal, reinforced properties. In the vertical fins, the y-direction was assigned the longitudinal, reinforced properties. All other directions were assigned transverse properties.

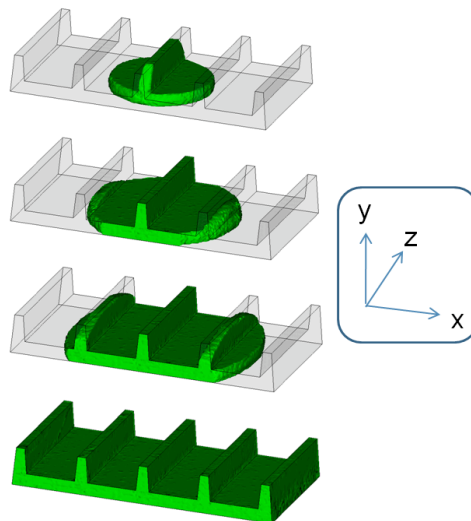


Figure 12. Flow front movement during filling of finned plate [1].

- Initial models utilized the heat exchanger geometry shown in Figure 13. All shown dimensions are in millimeters. The depth of the heat exchanger module was 50 mm. The corner radius of 2 mm was selected after varying the radius from 0.5 mm to 2.5 mm. The 2 mm radius provided significant stress reductions relative to the 0.5 mm radius without significantly increasing mass or hampering moldability.

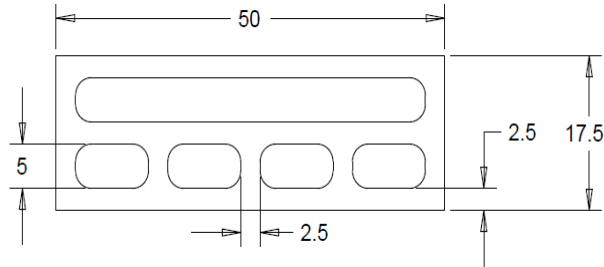


Figure 13. Initial heat exchanger geometry.

- Quarter-symmetry modeling allowed for greater mesh refinement and shorter computation time.
- The boundary conditions for the model are shown in Figure 14. The two pressures, one for the methane-side and one for the water-side, are representative of the highest pressures seen by the Das Island heat exchangers for which pressure information was available. The gas-side pressure was 5.87 MPa and the water-side pressure was 0.40 MPa. The “S” characters represent symmetric boundary conditions. The bottom center of the heat exchanger is fixed, which is representative of the heat exchanger resting on a flat surface.

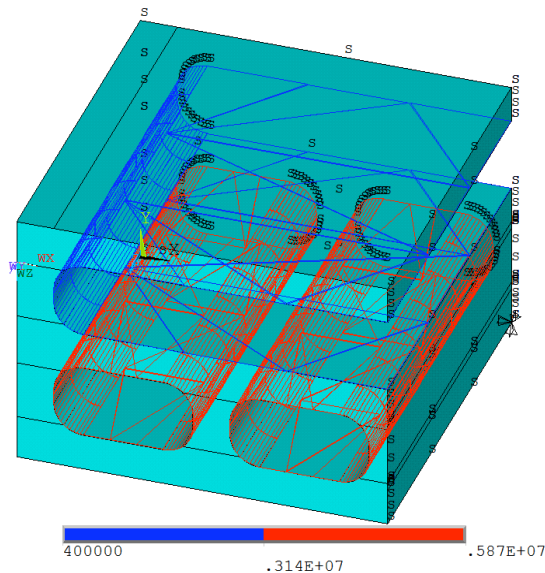


Figure 14. Boundary conditions of orthotropic heat exchanger module (units: Pa).

d. Orthotropic Model Results

- A mesh convergence study was performed to ensure correct results while minimizing element count and computation time.
- The model with the minimum element count with results consistent with those of models that are more refined had about 800,000 elements.
- Figure 15 shows the oblique view of the Y-stress contours of the orthotropic heat exchanger. The maximum stress occurs along the gas side left fin, where the stress is equal to 90.5 MPa.

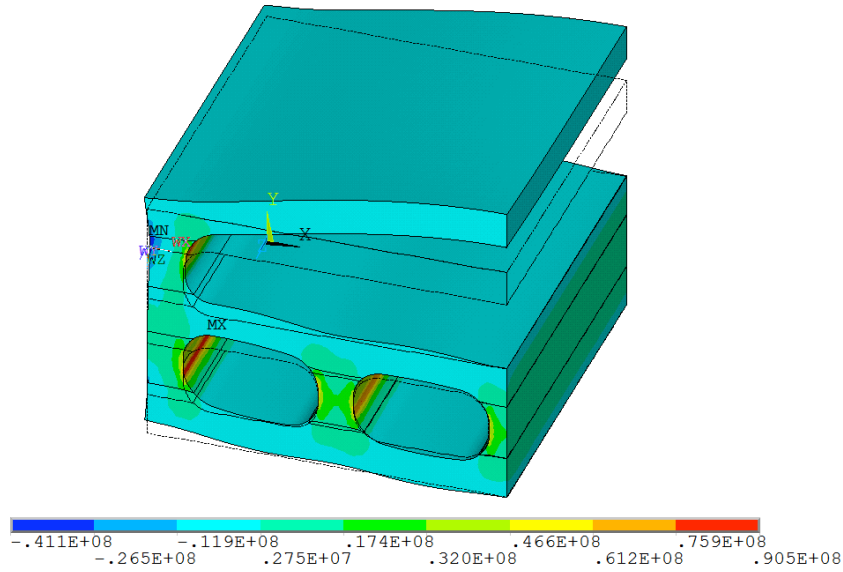


Figure 15. Oblique view of Y-stress contours of orthotropic heat exchanger with deformation scaled four times (units: Pa).

- Table 6 shows the collection of stress and strain results for the orthotropic model. The highest stresses occur in the X and Y directions. Of the shear stresses, the XY shear stress is the largest. For a comparison of these results with the material properties of the composite, see Table 7.

Table 6. Maximum stresses and strain of orthotropic model

	Direction					
	X	Y	Z	XY	YZ	XZ
Maximum stress (MPa)	86.0	90.5	12.7	17.4	3.94	3.51
Maximum strain (%)	0.955	1.21	0.981	4.02	0.912	0.812

Table 7. Material properties of aged unreinforced and reinforced PA12

Material	Elastic Modulus (GPa)	Yield Stress (MPa)	Elongation at Yield (%)	Failure Strength (MPa)	Elongation at Failure (%)
Unreinforced PA12 Aged at 60°C	0.62	19.05	3.25	37.31	Not tested
Reinforced PA12 Aged at 60°C	9.26	60.15	0.88	85.99	3.06

IX. Modify heat exchanger geometry to reduce stresses experienced by polymer composite heat exchanger

a. Orthotropic Results after Addition of Water-Side Fin

- Heat exchanger module geometry must be modified to minimize stress and strain levels to ensure longevity of the module.
- From the results shown previously in Figure 15, deformation along the top plate on the water side is excessive. To reduce the magnitude of this deformation, a fin was added at the center of the water side.
- Figure 16 shows the oblique view of the of the Y-stress contours of the orthotropic heat exchanger after the addition of a fin on the water side.

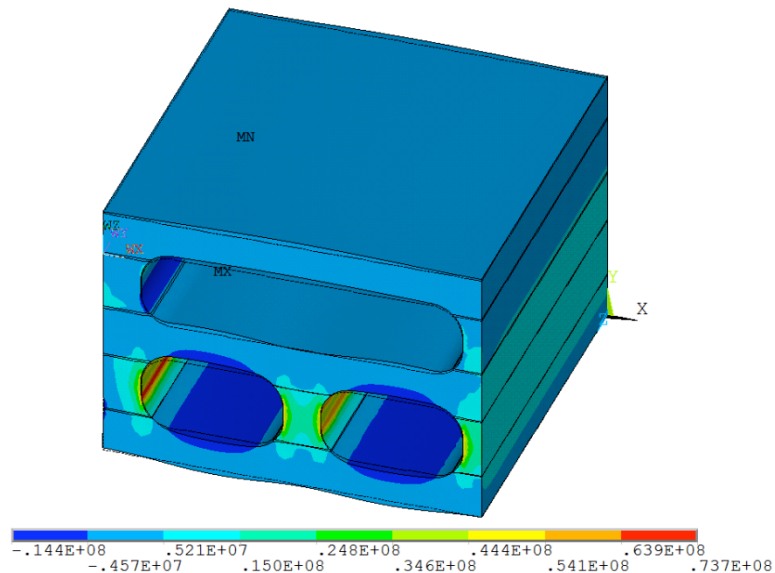


Figure 16. Oblique view of Y-stress contours of orthotropic heat exchanger with additional water-side fin with deformation scaled four times (units: Pa)

- A comparison of all of the stresses and strains before and after the addition of another water-side fin is provided in Table 8.

Table 8. Stress and strain values after addition of water-side fin to orthotropic heat exchanger model

		Direction					
		X	Y	Z	XY	YZ	XZ
Maximum Stress (MPa)	Before addition of fin	86.0	90.5	12.7	17.4	3.94	3.51
	After addition of fin	53.7	73.7	10.0	14.7	3.01	3.05
	Change (%)	-37.6	-18.6	-21.3	-15.5	-23.6	-13.1
Maximum Strain (%)	Before addition of fin	0.955	1.21	0.981	4.02	0.912	0.812
	After addition of fin	0.654	0.985	0.329	3.41	0.696	0.707
	Change (%)	-31.5	-18.6	-66.5	-15.2	-23.7	-12.9

- The addition of the fin significantly reduced stresses and strains in the heat exchanger module. As the research team develops a better understanding of the stress and thermal constraints of the heat exchanger, additional geometric changes will be evaluated.

X. Assess feasibility of modeling orthotropic heat exchanger module as an isotropic model with averaged properties

- Isotropic models are much simpler than orthotropic and anisotropic heat exchanger models. Thus, if the mechanical behavior of an anisotropic model could be replicated using an isotropic model, the result would be consistent results that require less computation time.
- An isotropic model was developed using properties between the maximum and minimum elastic moduli and Poisson's ratio of the orthotropic model.
- The isotropic model was found to have identical stress distributions over the range of moduli tested (at constant Poisson's ratio). This is a reasonable result because the stress distribution in an isotropic study is largely a function of the geometry of the heat exchanger module (particularly when the Poisson's ratio is held constant). The isotropic results and the orthotropic results are shown in Table 1.

Table 1 Comparison of isotropic and orthotropic stresses

	Maximum Stress (MPa)					
	X	Y	Z	XY	YZ	XZ
Isotropic	33.7	43.0	11.9	23.4	2.37	4.87
Orthotropic	53.7	73.7	10.0	14.7	3.01	3.05

- Additional simulations were completed while holding the isotropic elastic modulus constant at 5 GPa and varying the Poisson's ratio from 0.29 to 0.44. The stress results showed some variation but remained very different from those of the orthotropic study.
- The substantial variation between the isotropic and orthotropic models may be an indication that a full anisotropic model should be developed to determine if the orthotropic model replicates the anisotropic model. Additional refinement of these comparisons and the development of an anisotropic model will be included in the next quarterly report.

4. Difficulties Encountered/Overcome

Aging apparatus aquarium failure

- The glass aquarium of the aging apparatus shown in Figure 8 and Figure 9 was modified to accommodate stainless steel eyebolts used to secure the aquarium to the workbench.
- The glass panel that served as the aquarium's base was removed and replaced by a panel of acrylic plastic of the same dimensions.
- As the saltwater in the aquarium was heated to 60°C during the experiments, the aquarium's left panel developed a crack, which caused the aquarium to leak.
- It was determined that the elevated temperature of the water in the aquarium caused the acrylic base panel to expand, generating enough stress to crack the glass side-panel of the aquarium.
- A second glass aquarium was modified to use the acrylic base plate: two millimeters were removed from the length of the acrylic base panel, and the gap was sealed with caulk, solving the problem.

5. Planned Project Activities for the Next Quarter

- Generalize volume scaling mold filling metamodel in order to expand range of possible applications and verify using geometry with randomly generated features including ribs, bosses, and curved features.
- Complete image processing workflow and apply to additional test specimens and geometries.
- Design a cross-flow heat exchanger to be molded with thermally enhanced polymer, for use in new HX test rig.
- Continue evaluation of thermal performance of candidate polymer heat exchanger designs.
- Perform literature review of shear-lag models that account for debonding and use models to estimate mechanical properties to carbon fiber reinforced PA12 after hygrothermal aging.
- Develop anisotropic model using fiber orientation predictions from commercially available, injection molding simulation software Moldflow.
- Compare anisotropic results to orthotropic and isotropic results to determine if anisotropic model can be simplified to reduce computation time.

6. Appendix

6.1 Goals

The goal of the proposed 3-year EERC II polymer composite heat exchanger (PCHX) project is to develop the science and technology needed to underpin the systematic design of polymer-fiber composite heat exchanger modules that address the needs of the fossil fuel industry. The project team, lead by A. Bar-Cohen, brings together expertise in thermal science and technology (Bar-Cohen, Rodgers) with polymer composite molding and manufacturing (Gupta, Bigio). Design studies and molding simulations, as well as fabrication and testing of laboratory-scale polymer composite heat exchangers, during the first phase of this project, have provided the foundation for aggressive pursuit of such polymer composite heat exchangers.

Successful development of cost-effective, high-performance PCHX's will require a detailed understanding of the limitations imposed on the thermal performance, mechanical integrity, and cost of such heat exchange devices by the candidate polymer material; carbon fiber geometry, orientation, and concentration; thermal and mechanical anisotropy of the polymer-fiber composite; molding processes; thermal and structural failure mechanisms in the molded heat exchanger; and the energy investment in the fabrication and formation of the heat exchangers. The development and experimental as well as numerical validation of a multi-disciplinary computerized design methodology, along with the fabrication and testing of scaled polymer heat exchanger modules, would provide a unique knowledge-base from which low-life-cycle-cost heat exchange systems for the petroleum and gas industries could be developed.

6.2 Project Tasks

A. Thermal Design and Characterization of Polymer Composite Heat Exchanger Module (Prof. Avram Bar-Cohen - UMD, Prof. Peter Rodgers - PI)

1. ***Design and thermofluid evaluation of PHX concepts for LNG applications***, including sensitivity of thermal performance to key parameters, quantification of primary thermal and exergy figures-of-merit (metrics), comparison to conventional heat exchangers, and identification of least-mass/least-energy designs;
2. ***Detailed design, fabrication, and thermal characterization of least-energy PCHX module***, including mold fabrication for most promising design, assembly and instrumentation of laboratory prototype, analysis of thermal and structural performance under simulated LNG processing conditions;
3. ***Development of predictive models for anisotropic heat exchanger modules***, including use of molding CFD software for prediction of fiber orientation and effective thermal/ structural properties, numerical and analytical models for molded anisotropic fins, derivation of least-material anisotropic fin equations, determination of heat flow sensitivity to fiber geometry/concentration/orientation;
4. ***Evaluation of convective enhancement features in molded channels***, including identification of "best practices" in conventional heat exchangers, manufacturability analysis of candidate features with attention to mold complexity, part ejection, and warpage, polymer composite molding of 3-5 candidate enhanced channels; thermofluid characterization of candidate enhanced channels under simulated LNG processing conditions; and
5. ***Determination of seawater effects on polymer composite finned plates***, including design and molding of test samples, immersion in saltwater tanks at different temperatures and concentrations for pre-determined periods, surface/bulk imaging and mechanical characterization before and after immersion, analysis and correlation of effects.

B. Manufacturability Analysis and Mold Design for Polymer Composite Heat Exchanger Module (Prof. SK Gupta – UMD):

1. Development of an improved meta-model for mold filling predictions: We plan to develop an improved meta-model for predicting mold filling for typical heat exchanger geometries. This meta-model will account for multiple gates with adjustable spacing. The data for developing this meta-model will be generated using mold flow simulations. We plan to utilize radial basis function based meta-models to provide the right balance of accuracy and computational speed.

2 Creation of a computational framework for gate placement to optimize fiber orientation: We plan to develop a computational framework for placing gates to optimize the fiber orientation, utilizing simulated fiber orientations to select the gates. The sensitivity of the gate locations on fiber orientation will be developed. Gradient-based optimization techniques will be used to optimize the fiber orientation. The optimization problem will incorporate the constraint satisfaction formulation of the weld-line locations to ensure that the fiber orientation formulation produces acceptable weld-lines.

3. Generation of insert molding process models to incorporate connectors at the weld-lines: In order to ensure that the weld lines do not compromise the structural integrity, we plan to embed metal connectors at the expected weld-lines locations. In order to accurately place these metal connectors in the structures, we plan to develop process models of the insert molding process and mold design templates for performing insert molding.

C. Polymer-Fiber Interactions in Polymer Composite Heat Exchanger Modules (Prof. David Bigio):

1. Develop key relationships for the dependence of fiber orientation on the flow geometry of the finned-plate PCHX module, in commercially available polymer composites, including the effect of carbon fiber length and diameter, for high and low fiber concentrations, for both base plate and fin passages in the mold, and the effect of fiber orientation/distribution on thermo-mechanical properties, verify relationships with suitable small scale experiments;

2. Determine achievable thermo-mechanical property enhancement through control of carbon fiber orientation, in the commercially available polymer composites, with attention to flow regimes, mixing processes in the flow of the melt, and heat exchanger module design, and verify experimentally;

3. Explore optimization of PCHX polymer composite properties through the creation of novel polymer composite compositions, including multi-scale filler geometries, develop the molding methods for the desired geometries, create the novel composites and experimentally verify improved thermo-mechanical polymer composite properties.

6.3 Key References

- [1] Bar-Cohen, A., Luckow, P., Cevallos, J.G., Gupta, S.K., 2010, Thermal Anisotropy in Injection Molded Polymer Composite Fins, International Heat Transfer Conference 14 at Washington DC
- [2] Cevallos, J.G., Gupta, S.K., Bar-Cohen, A., Incorporating Moldability Considerations during the Design of Thermally Enhanced Polymer Heat Exchangers (under revisions)
- [3] Cevallos, J.G., Bar-Cohen, A., Bergles, A.E., Gupta, S.K., Rodgers, P., Polymer Heat Exchangers – History, Opportunities, and Challenges (in progress)
- [4] Luckow, P., A. Bar-Cohen, P. Rodgers, 2009, “Minimum Mass Polymer Seawater Heat Exchanger for LNG Applications,” accepted for publication, ASME TSEA, January 2010
- [5] Cox, H.L., 1951, “The elasticity and strength of paper and other fibrous materials,” Brit. J. Appl. Phys., 3(3), pp. 72-79.

- [6] Amado-Becker, A., Ramos-Grez, J., Yanez, M.J., Vargas, Y., and Gaete, L., 2008, "Elastic tensor stiffness coefficients for SLS Nylon 12 under different degrees of desensification as measured by ultrasonic technique," *Rapid Proto. J.*, 14(5), pp. 260-270.
- [7] Halpin, J.C., and Kardos, J.L., 1976, "The Halpin-Tsai Equations: A Review," *J. Poly. Eng. and Sci.*, 16(5), pp. 344-352.
- [8] Hahn, H.T., and Tsai, S.W., 1980, *Introduction to Composite Materials*, Technomic Publishing Co., Lancaster, PA.
- [9] Pegoretti, A., Fambri, L., Zappini, G., and Bianchetti, M., 2001, "Finite element analysis of a glass fibre reinforced composite endodontic post," *Biomaterials*, 23, pp. 2667-2682.
- [10] Fu, S., and Lauke, B., 1997, "The elastic modulus of misaligned short-fiber-reinforced polymers," *Comp. Sci. and Tech.*, 58, pp. 389-400.
- [11] Foye, R.L., 1972, "The Transverse Poisson's Ratio of Composites," *J. Comp. Mater.*, 6(2), pp. 293-295.
- [12] "Thermal Graph DKD," Cytec Industries, Accessed 26 May 2010, <http://www.cytec.com/engineered-materials/products/cfThermalGraphDKDX.htm>.

Study on Microchannel-Based Absorber/Stripper and Electrostatic Precipitators for CO₂ Separation from Flue Gas

UMD Investigators: Serguei Dessiatoun, Amir Shoostari

GRAs: Paul Breuninger, Toni Pfennig

PI Investigators: Michael Ohadi, Afshin Goharzadeh, Mohamed Alshehhi

Start Date: Oct 2006

1. Objective/Abstract

This project is focused on the development of a high-efficiency CO₂ separation process from flue gas flows, with application to CO₂ capture for enhanced oil recovery applications. The project addresses three stages of the separation process: cooling down the flue gas, separating the solid particles and condensed water droplets, and separating the CO₂ using the absorption process. A microchannel-based CO₂ separator, utilizing an advanced force-fed system will be developed in this project, will significantly increase controllability of the thermal state of the reaction and the efficiency of the separation process while decreasing the reaction time and energy consumption. Moreover, using such technology will lead to a reduction of equipment size and therefore minimize the footprint and cost of the equipment.

Flue gas also usually contains many contaminants in solid and liquid forms. The bulk of them are separated in gravity and inertia-driven feed gas separators. However, fine particles are carried on with the flow and can damage compressors, contaminate the gas absorption process, and reduce the quality of gas products. Currently, electrostatic separation is the most effective technique for separation of those particles and will be used in this project. The current stage of this study intends to address separation of droplets and particles using an EHD gas-liquid separation technique to remove conductive and nonconductive liquid particles suspended in a moving gaseous medium. Later, the special microchannel will separate the CO₂ from the fluid once the fine particles in the flow have been removed.

The project is being conducted jointly by the teams at UMD and PI. The team at PI is focusing on EHD separation, while the team at UMD has focused on the experimental work utilizing the microchannel and absorption solution.

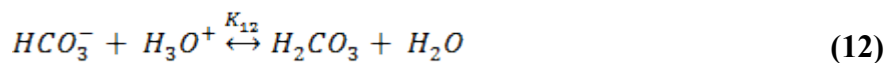
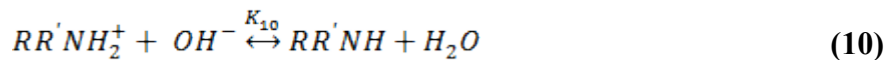
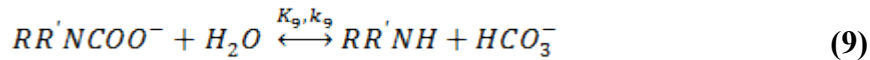
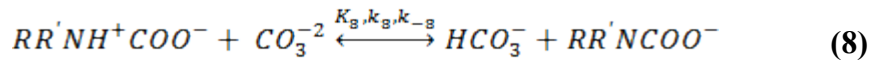
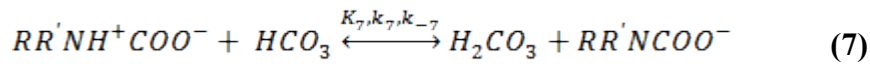
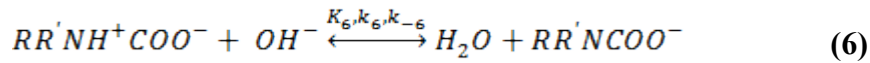
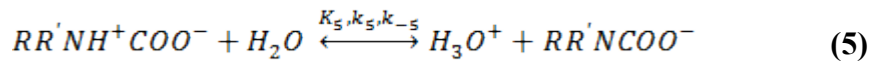
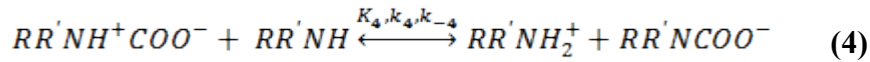
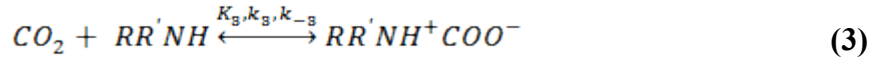
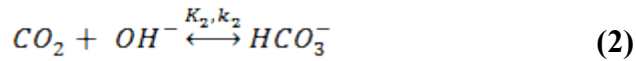
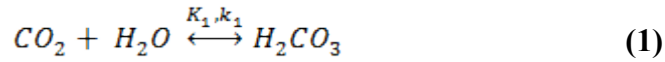
2. Milestones/Deliverables Scheduled for the Completed Quarter

- Literature review
- Identification of the target alkanolamine suitable for experimental study
- Design and fabrication of laboratory scale microchannel-based CO₂ separator
- Experimental study on the absorption in microchannels
- Development of a numerical/analytical model to enhance understanding of the process

3. Summary of Project Activities for the Completed Quarter

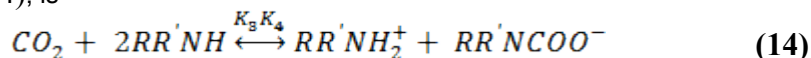
Literature Review

During this reporting period, further study was conducted on the chemical reaction mechanism of CO₂ with dethanolamine. According to Rinker et al. (Rinker, Ashour and Sandall 1996), when CO₂ is absorbed into an aqueous solution of a primary or a secondary alkanolamine, RR'NH, the following reactions may occur:



where reaction (3) is the formation of the zwitterion and reactions (4)-(8) are the zwitterion deprotonation reactions. For diethanolamine (DEA), we have R= R'= CH₂-CH₂OH. K_i, k_i, and k_{-i} are the equilibrium constant, the forward rate coefficient, and the reverse rate coefficient for

reaction (i), respectively. Reactions (1)-(9) are considered to be reversible with finite reaction rates, whereas reactions (10)-(13) are considered reversible and instantaneous with respect to mass transfer and at equilibrium, since they involve only proton transfers. Rinker et al. (Rinker, Ashour and Sandall 1996) concluded that for their laminar-liquid jet absorber, the gas-liquid contact times were very short, and as a result the contribution of many of above reactions was negligible. Under this situation the main agent acting as a deprotonating base was the amine (i.e. Eq. (4)). Therefore, the overall reaction between CO₂ and DEA, which is the sum of reactions (3) and (4), is



From this equation it can be concluded that under a fast reaction between DEA and CO₂ when the contact time is short, each mole of CO₂ reacts with two moles of DEA. However, this conclusion may not hold for the reaction of CO₂ and DEA in microchannels where reaction area and time are higher than the reactor used in Rinker's study.

Identification of the Target Alkanolamine

As described in the previous quarterly report, aqueous DEA has been selected as the adsorbent for current study. DEA has a lower corrosivity of absorption products compared to monoethanolamine (MEA), lower heat of reaction, lower heat of regeneration, lower vapor pressure, and better desorption than MEA, and also it exhibits high stability in presence of carbonyl sulfide. Moreover, its reaction products with species such as COS and CS₂ can be conveniently regenerated, and it also is less toxic than methylethanolamine. DEA does not create irremovable heat stable salts.

Design and Fabrication of the Test section

In the previous quarterly report, we reported fabrication of an absorber test section consisting of multi microchannels. Our preliminary absorption tests with ammonia-water indicated that there was some instability in the gas pressure. The source of this instability was not clearly understood. However, we decided that a single microchannel reactor would be fabricated in order to improve controllability of the reaction and to eliminate any interaction between the flow in the parallel channels. This design, while simple, provides better resilience to corrosion, avoids flow maldistribution, and accommodates better visualization access. The microchannel consists of an inlet header, a transparent tube, and an outlet port. The inlet header shown in Figure 1 consists of a slim tube placed in the center of the outer transparent tube to eject the gas to the stream of the amine solution. The amine solution is directed through the upright port, flows around the centric tube and comes in contact with the flowing gas at the exit of the slim centric tube.

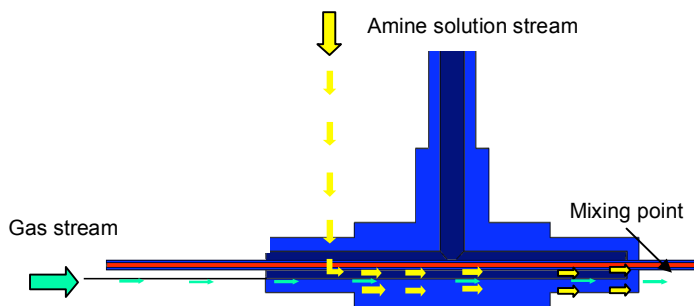


Figure 1. Microchannel reactor inlet header.

Figure 2 shows a schematic sketch of the microchannel test section. The diameter of the tube is 0.75 mm. A thermocouple sensor is mounted in the outlet port to measure the temperature of the stream at the microchannel exit.

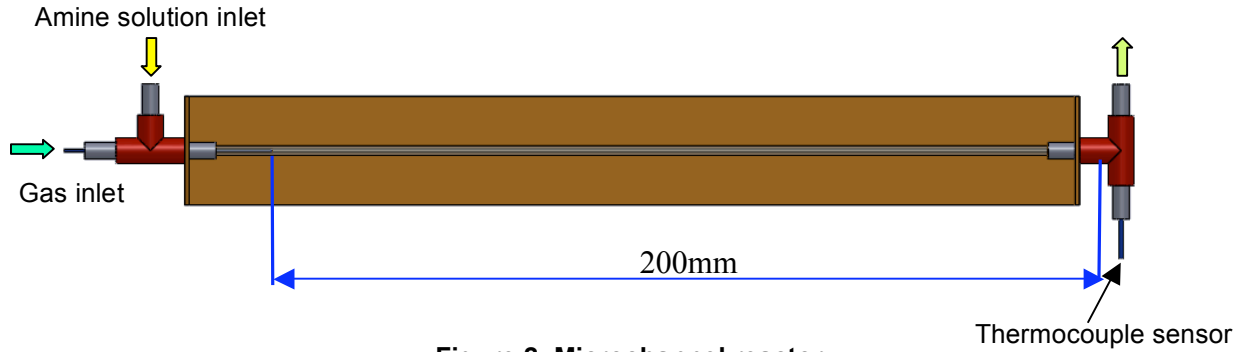


Figure 2. Microchannel reactor.

In order to assess the performance of experimental setup, a series of preliminary tests was conducted on the absorption of ammonia in water. This process is a physical absorption process based on the dissolution of ammonia gas into liquid water. A schematic layout of the experimental setup used for these tests is shown in Figure 3. The flowmeter unit used in this setup (no. 5) is a coriolis mass flowmeter placed 80 cm downstream of the test section to measure mass flow rate, density of the water-ammonia mixture, and the temperature.

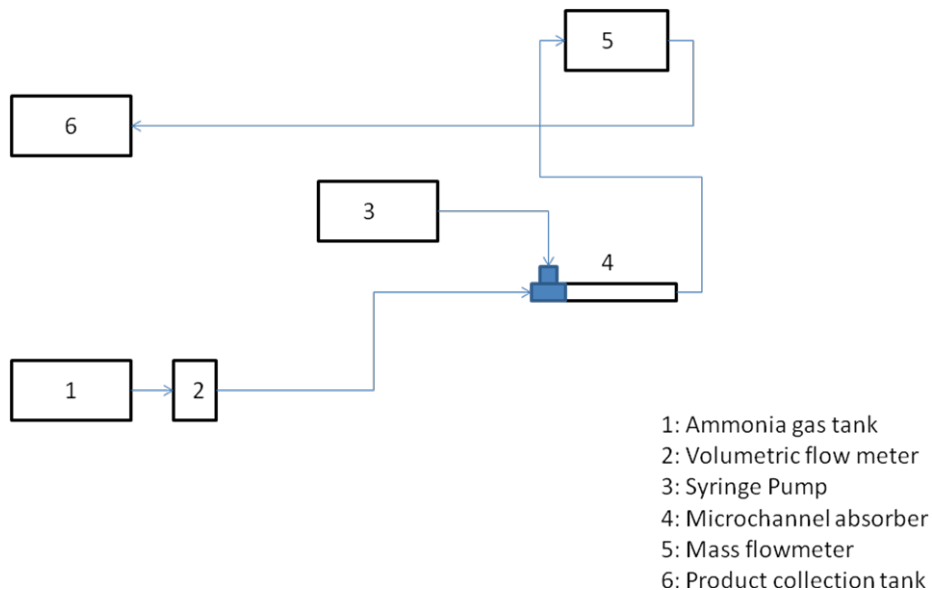


Figure 3. Water-ammonia experimental setup.

After preliminary tests on absorption of ammonia-water the experimental setup was modified for absorption of CO₂ in Diethanolamine as presented in Figure 4. In the

modified setup the liquid electrical conductivity (or resistivity) measurement was used to evaluate the efficiency of the absorption process.

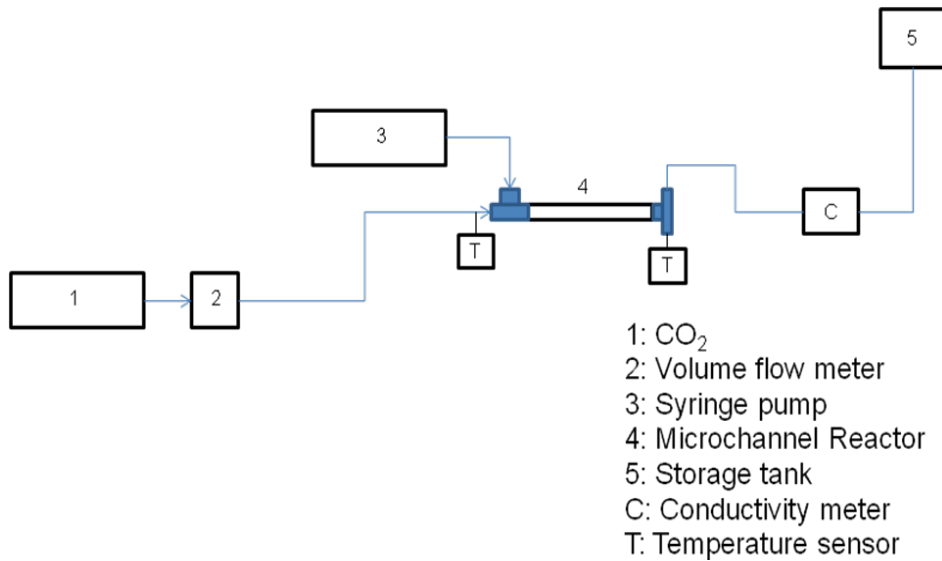


Figure 4. CO₂-amine absorption setup.

This measurement concept is based on the fact that the electrical conductivity of an ionic solution varies significantly as the gas is absorbed by the liquid. The concentration of ions depends on the amount of CO₂ reacting with the amine. Therefore, there is a direct relationship between the concentration of the absorbed gas and the measured electrical conductivity. The conductivity measurement was performed using an in-house fabricated conductivity cell. The conductivity cell shown in Figure 5 consists of two metal tubes acting as electrodes connected through a plastic tube. A known electrical potential is supplied to these electrodes, and the electrical current between two electrodes is measured. Once the liquid fills the space between the two electrodes an electrical current is established. By measuring the voltage and current of the cell the electrical conductivity of the liquid can be calculated.

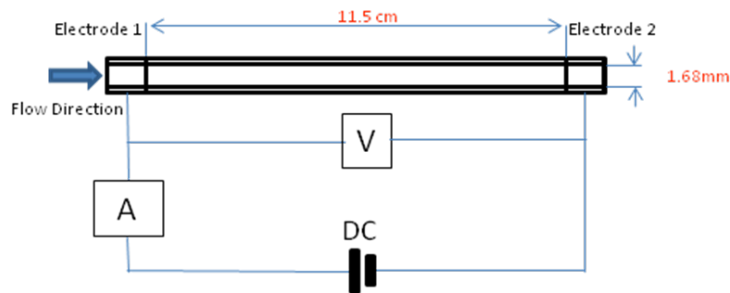


Figure 5. Conductivity measurement cell.

Experimental Results

Ammonia-Water Absorption

The experimental test matrix for ammonia-water absorption is given in Table 1. The tests were carried out for a range of ammonia and water mass flow rates. In this table C

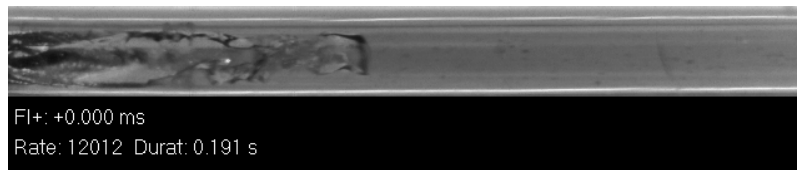
represents the mass basis ammonia concentration. The mixture temperature, density and mass flow rates are measured by the coriolis mass flowmeter. Some information in the test matrix is missing because the experiments for these cases have not been completed.

Table 1. Ammonia-water absorption test matrix

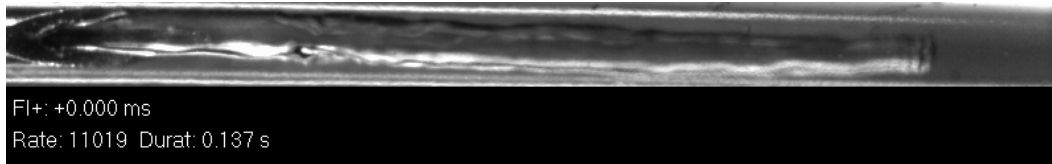
Ammonia mass flow rate [mg/s]		Water mass flow rate [mg/s]				
		83.0	166.67	333.33	500	1000
1.157	Test #	6	5	8	18	22
	C %[]	1.37	0.69	0.35	0.23	
	T _{mix} [°C]	30.111	29.389	28.722	28.222	
	ρ _{mix} [kg/m ³]	981.5	989.2	992.2	993.3	
	\dot{m}_{mix} [mg/s]		167	331.5	497	
2.3	Test #	2	1	4	17	21
	C %[]		1.36	0.69	0.46	
	T _{mix} [°C]		30.83	29.56	29.83	
	ρ _{mix} [kg/m ³]		981.8	987.6	990.37	
	\dot{m}_{mix} [mg/s]		169	334	480	
4.6	Test #	10	9	12	19	23
	C %[]		2.69	1.36	0.91	
	T _{mix} [°C]		41.056	36.194	33.000	
	ρ _{mix} [kg/m ³]		959.1	976	981.64	
	\dot{m}_{mix} [mg/s]		175	340	501	
6.94	Test #	14	13	16	20	24
	C %[]				1.36	0.69
	T _{mix} [°C]				38.333	33.500
	ρ _{mix} [kg/m ³]				974.2	984.4
	\dot{m}_{mix} [mg/s]				512	1005

The flow visualization for all the cases given in Table 1 indicates that, for the range of the flow rates tested, if pure ammonia is supplied the full absorption was always achieved within less than 15 mm channel length. The results clearly demonstrate the effectiveness of the microchannel technology for the ammonia absorption process. Moreover, two different flow regimes were observed. In a number of experiments a stable interface between water and ammonia was established which remained stationary during the experiment. In some other experiments a dynamic and instable interface was observed where the effective absorption length fluctuated. For these cases precise

measurement of the absorption length was not straightforward. A further study revealed that this behavior depends on the mass flow rate ratios. For a given mass flow rate of ammonia, if the mass flow rate of water increases, the interface becomes more stable. In other words, for each row in Table 1 the flow becomes more stable when one moves from left to right. Also for a given water mass flow rate, the interface becomes more stable if the ammonia flow rate decreases. That is, for each column in Table 1, the stability of flow increases if one moves from bottom to top. Figure 6 shows the stable and instable interfaces between ammonia and water phases.



(a)



(b)

Figure 6. (a)-Instable phase interface regime, ammonia flow rate 600mL/min, water flow rate 30mL/min volume flow rate ratio: 20, mass flow rate ratio: 0.138 (b)-Stable phase interface regime, ammonia flow rate 200mL/min, water flow rate 19.7 mL/min volume flow rate ratio: 10, mass flow rate ratio: 0.007.

Variation of the temperature rise with the water flow rate for different ammonia mass flow rates is shown in Figure 7. As expected, the temperature increases when the ratio of ammonia to water flow rate increases. However, one should note that since the temperature measurement is achieved about 80 cm downstream of the channel, it does not represent the mixture temperature in the microchannel caused by the absorption process. This problem has been resolved for the CO₂ experimental setup with the addition of a temperature sensor at the channel exit as shown in Figure 4.

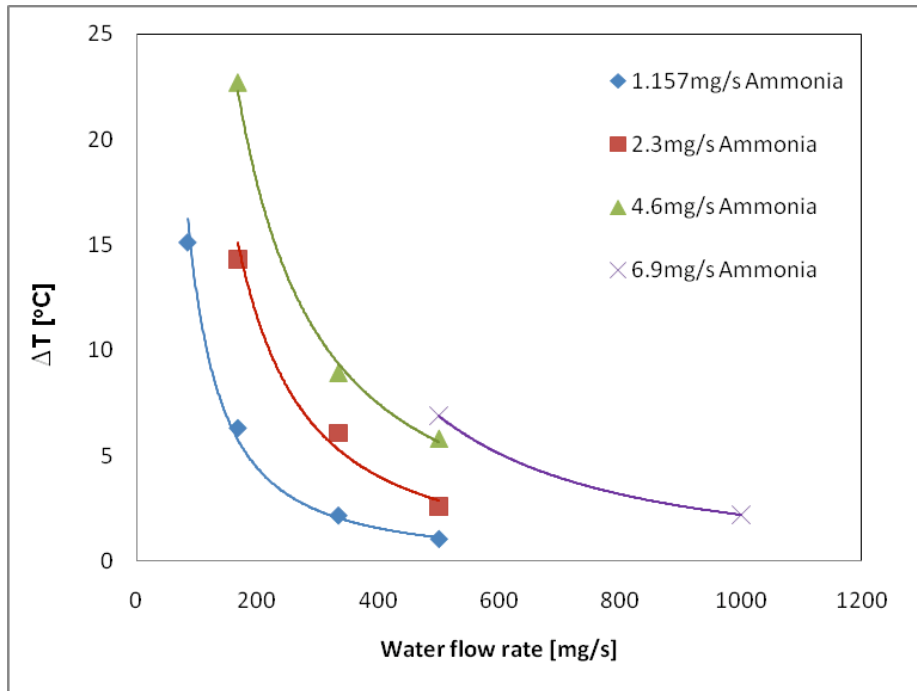


Figure 7. Temperature increase for absorption of ammonia in water.

Figure 8 shows variation of the density of the water/ammonia mixture with the water and ammonia flow rates. As can be seen, as the concentration of ammonia in water increases, the density of the mixture decreases. Therefore, a lower mixture density indicates a higher absorption of ammonia in water. Although the measurement is carried out about 80 cm downstream of the microchannel, it is expected that the density does not vary significantly. This is because the full absorption in microchannel is attained and the process does not continue after the mixture leaves the microchannel.

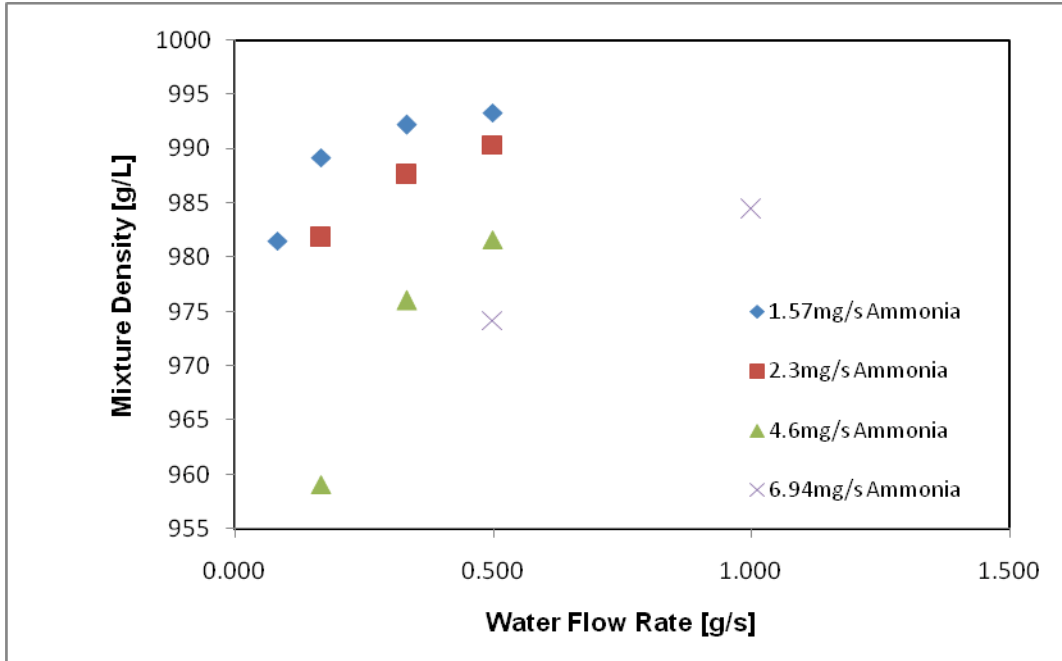


Figure 8. Mixture density variation for the absorption of ammonia in water in the microchannel.

The measured density of the mixture can be used to determine whether the absorption process is fully achieved. Assuming an ideal mixture, the mass concentration can be calculated as follows:

$$C = \frac{\rho_{mix} - \rho_{H_2O}}{\rho_{NH_3} - \rho_{H_2O}} \quad (15)$$

The actual mass concentration can be determined from the mass flow rates of ammonia and water as given in Table 1. Now, one can graph the calculated concentration versus the actual concentration. This is shown in Figure 9. As we can see, the concentration from Eq. (15) was estimated higher from what was found based on the supplied mass flow rates. This could be because of the ideal mixture assumption, in which the effect of excess density of mixture is disregarded. Also, we believe the gas flow measurement technique needs to be improved to improve the accuracy of the results.

CO₂-Amine Absorption

Preliminary experiments on CO₂-amine absorption were successfully carried out. The amine was diluted with water to adjust the mass basis concentration to 20% (C = 2.37 mole/L). As previously discussed, the conductivity measurement was used to estimate the efficiency of the absorption process. This method is based on the assumption that the conductivity (or resistivity) of the mixture is linearly proportional to the concentration of the absorbed CO₂. Therefore, to calibrate the conductivity measurement cell, one needs to measure both the conductivity of the fresh aqueous solution where the concentration of CO₂ is almost zero and also the conductivity of the saturated aqueous solution where the maximum amount of CO₂ is absorbed.

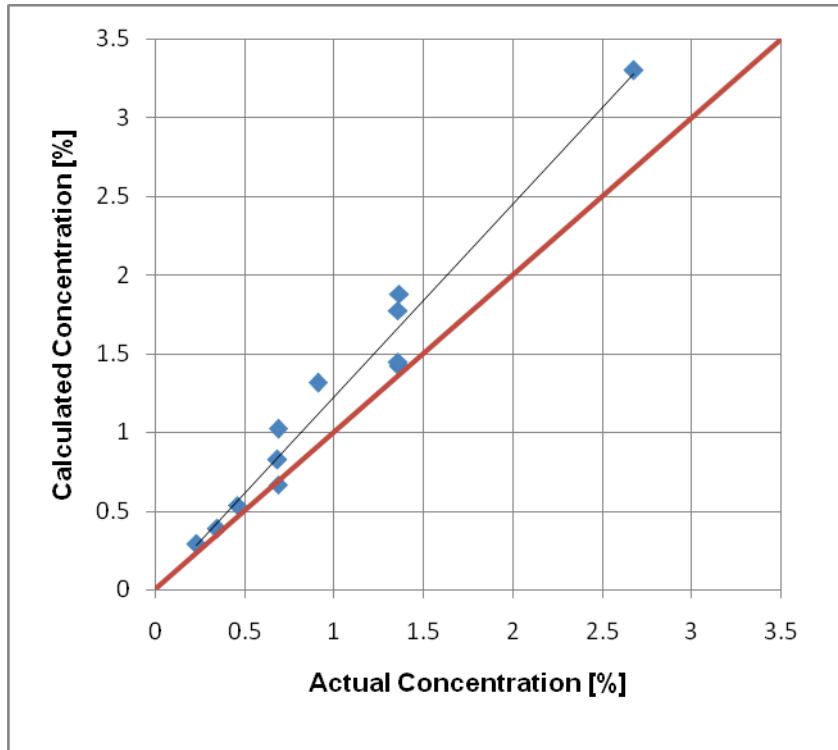


Figure 9. Calculated concentration versus actual concentration.

The results of the electrical conductivity measurement of fresh aqueous solution of amine are presented in Figure 10.

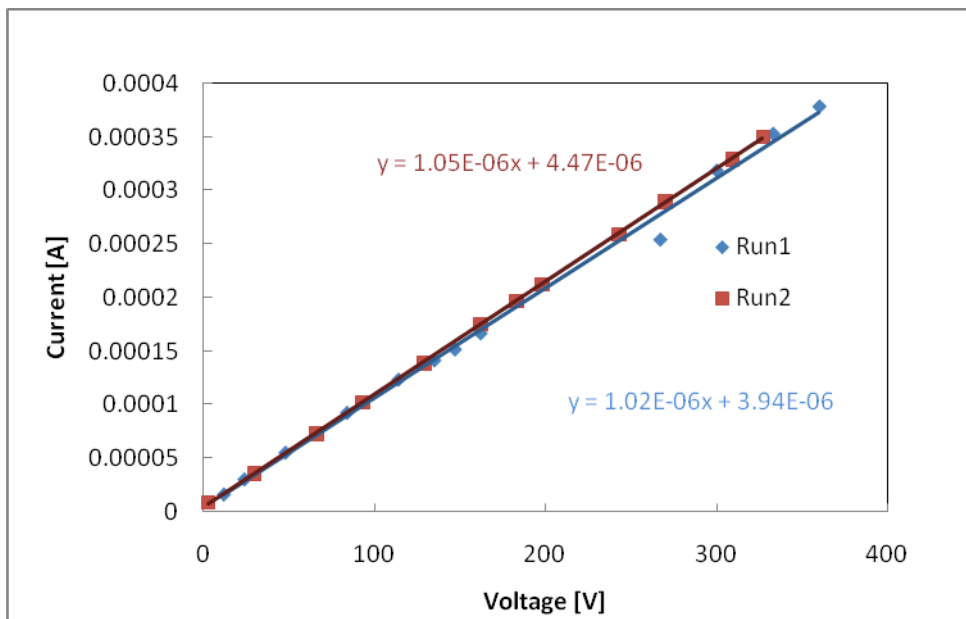


Figure 10. Electrical conductivity measurement for fresh 20% aqueous solution.

To conduct the experiment, the volume flow rate was set to 10 ml/min and the applied voltage was varied from zero to 350V. The experiment was repeated twice. As seen, a linear trend is obvious and the difference between the runs is insignificant. The slope of the trend line represents the conductivity of the solution. The average electrical conductivity and resistance are as follows:

$$\Sigma = 1.035 \times 10^{-6} [S]$$

$$R = 966183 [\Omega]$$

Using the area of the tube connecting the two electrodes and the distance between the electrodes, the specific conductivity and resistivity are as follows:

$$\sigma_e = 0.054 [Sm^{-1}]$$

$$\rho_e = 18.62 [\Omega m]$$

To measure the conductivity of the saturated solution, first the amine solution was cooled to 10°C. This was done to maximize the absorption of CO₂ in the Diethanolamine solution. Then the CO₂ gas was bubbled through 60mL of the solution for at least 10 min. Then the solution was left to reach equilibrium with room temperature. The results of conductivity measurement are presented in Figure 11. The experimented was repeated 5 times.

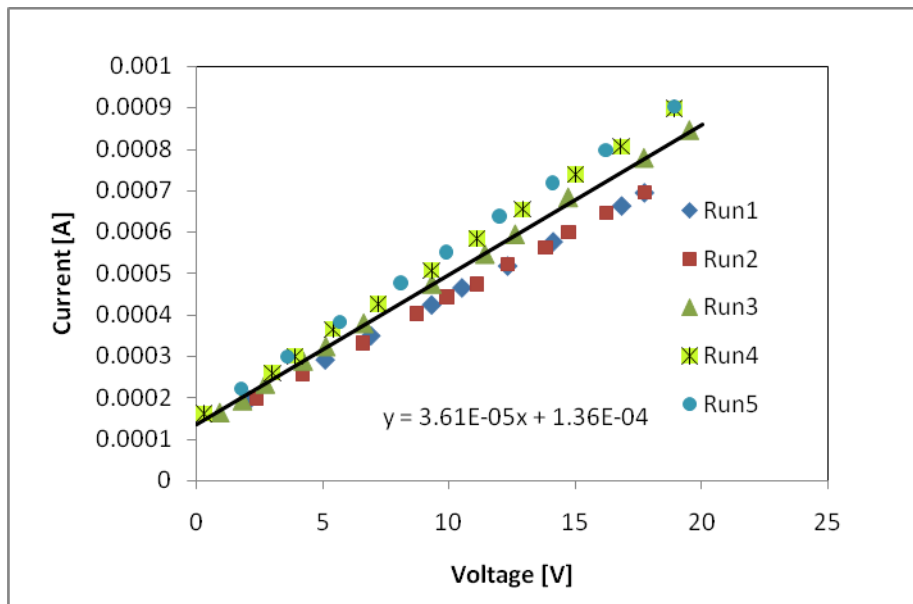


Figure 11. Electrical conductivity measurement for CO₂ saturated aqueous solution.

The average electrical conductivity and resistance are as follows:

$$\Sigma = 3.61 \times 10^{-5} \text{ [S]}$$

$$R = 27700 \text{ [\Omega]}$$

The specific conductivity and resistivity are as follows:

$$\sigma_e = 1.88 \text{ [Sm}^{-1}\text{]}$$

$$\rho_e = 0.53 \text{ [\Omega m]}$$

In Figure 12 these two points are plotted on a diagram showing the percentage of CO₂ loading of the liquid vs. the specific resistivity. As can be seen, the resistivity of the solution significantly (~40 times) decreases once it becomes saturated with the absorbed CO₂ gas. This radical change in resistivity provides an efficient way for measurement of the loading capacity. However, it should be noted that this method is susceptible to the presence of gas bubbles in the space between two electrodes. Such bubbles can significantly increase the measured resistivity. Therefore, if there is the possibility of presence of bubbles, it is advisable to collect several current and voltage data points and select those points which result in lower values of the resistivity.

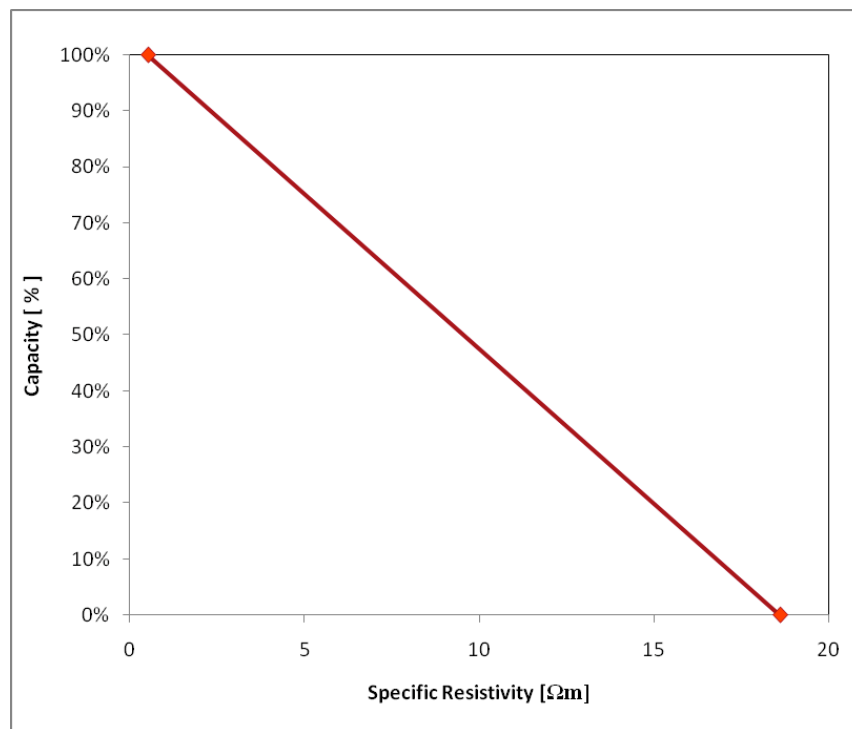


Figure 12. CO₂ absorption capacity versus electrical specific resistivity for Diethanolamine aqueous solution with 20% mass concentration.

After establishing the relationship between the measured resistivity and CO₂ absorption capacity, a number of experiments were conducted using the experimental setup shown in Figure 4. In these tests the volume flow rate of the aqueous Diethanolamine was kept constant at 20 ml/min while the volume flow rate of CO₂ was changed from 75 ml/min to 200 ml/min. Visualization of the flow indicated that for all the cases tested the full absorption inside the tube was not realized and some gas in bubble form escaped from the microchannel reactor. Despite the presence of the gas bubbles, the electrical conductivity measurement was successfully carried out and the absorption effectiveness was evaluated. The experimental results of this study are presented in Figure 13. For each CO₂ flow rate, the experiment was repeated several times. The results show that absorption efficiency in the range of 60-92% is achievable. The maximum efficiency was attained for a gas flow rate of 100 ml/min. At lower or higher gas flow rates lower absorption rates were observed.

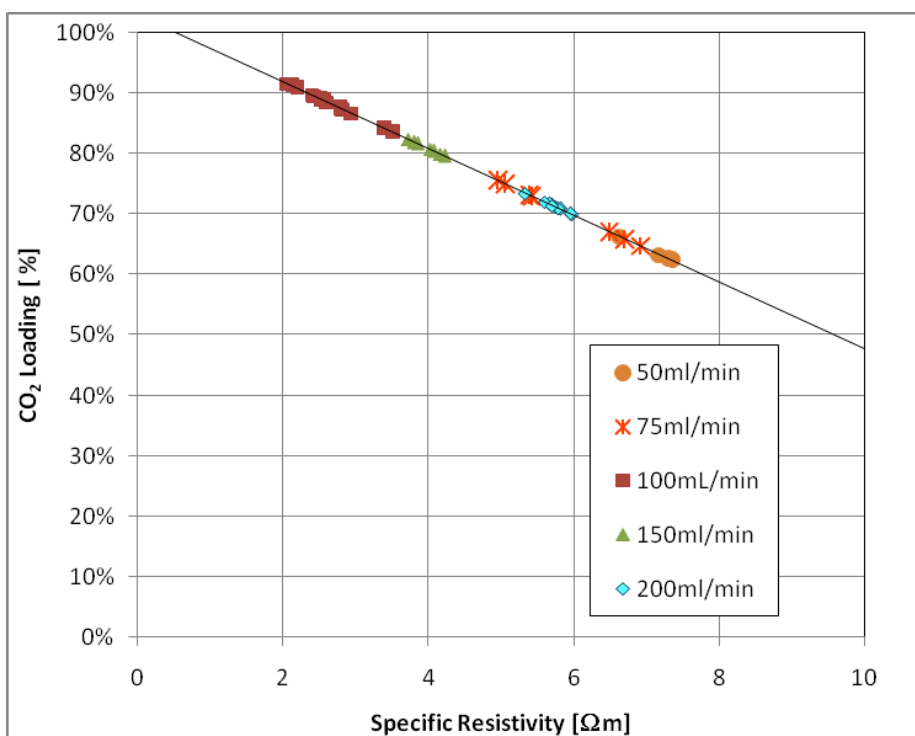


Figure 13. Percentage of CO₂ absorption for various gas flow rates; the volume flow rate of the aqueous Diethanolamine was kept constant at 20 ml/min.

For a given gas flow rate the measured resistivity is averaged and the results are presented in Figure 13. The error bars correspond to the standard deviation of the measured resistivity. The measurement data points are more scattered for the gas flow rates lower than 100 ml/min. This could be due to the inadequate measurement precision of the gas flow rate at lower ranges. Therefore, the gas measurement needs to be improved. For higher flow rates, the measurement error could be due to the presence of the gas bubbles in the conductivity measurement cell. The accuracy of the measurement could be improved if the unabsorbed CO₂ is separated from the flow in a separator placed after the microchannel and before the conductivity measurement cell. Figure 15 shows the gas absorption efficiency versus molar ratio. As seen, the maximum efficiency is attained at the molar ratio of 0.11. From Eq. (14) it is expected that for the

stoichiometric reaction the theoretical molar ratio of CO₂ to Diethanolamine should be 0.5. However, we should remember that Eq. (14) is valid for the laminar-liquid jet absorber where the gas-liquid contact time is very short. Further experimental study is needed to verify the data collected and the trend obtained in Figure 15.

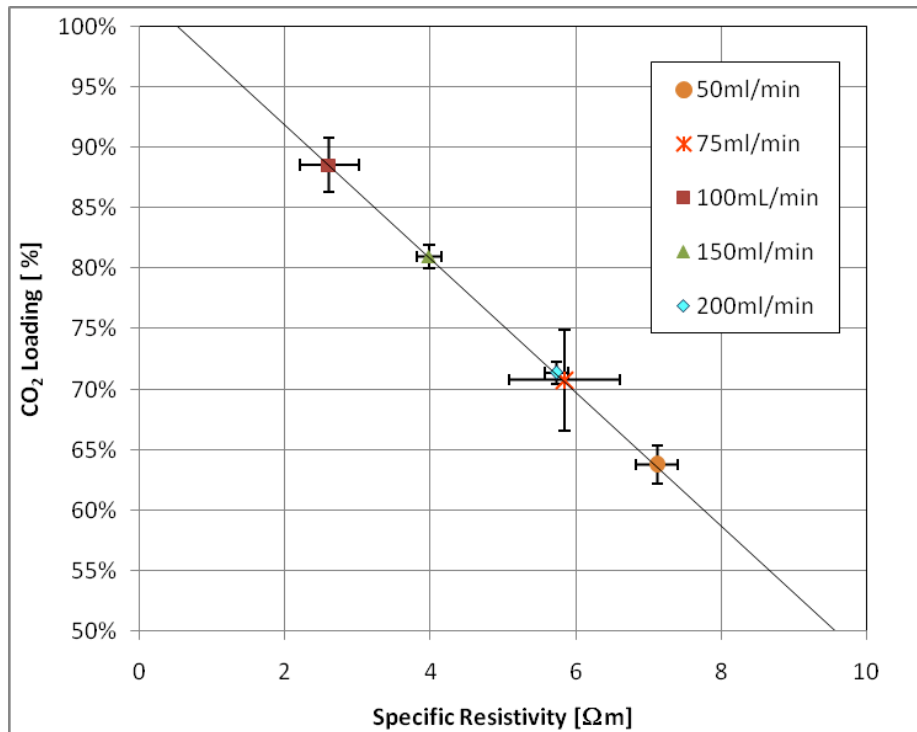


Figure 14. Gas absorption percentage versus averaged specific resistivity.

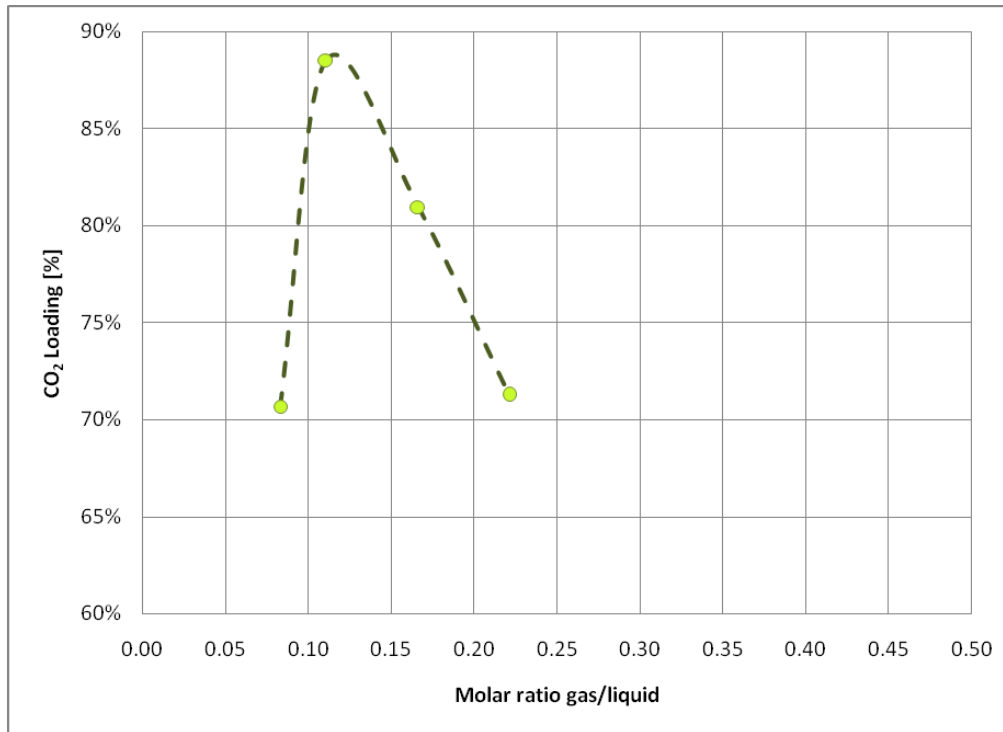


Figure 15. Gas absorption efficiency vs. molar ratio.

Development of a Numerical/Analytical Model

During this reporting period some preliminary work on the development of a numerical model was achieved. Comsol Multiphysics® was selected as the computational software, and its latest version was purchased. Some of the relevant tutorial examples were reviewed to familiarize ourselves with the modeling procedure for the new version of the software. The goal is to create a model of the process in three stages. In the first stage only the two-phase flow of the gas and liquid will be modeled where no reaction is present. The goal is to track the interface between the two phases. In the second stage, the physical absorption and diffusion of the gas into the liquid will be added to the interface tracking model. In the last stage the chemical reaction will be incorporated to the model.

Flow visualization of the EHD induced flow

During this period a conference paper was prepared and submitted to IMECE2010 which is currently under review (Kong, et al. 2010). In this article, results of electrohydrodynamic (EHD) flow field in a wire-plate air-oil droplet electrostatic separator under positive polarity were presented. Using Particle Image Velocimetry (PIV), the structure of EHD flow under fully developed primary laminar gas flow was investigated and corresponding flow patterns were studied. Velocity distribution results showed that the drift velocity induced by EHD flow depends significantly on applied voltage and the cross-section plane position of the separator.

An extended version of this article will soon be submitted to the ASME Journal of Fluid Engineering.

4. Difficulties Encountered/Overcome

None to report.

5. Planned Project Activities for the Next Quarter

- Continue on literature survey
- Improve the experimental setup and testing methodology
- Continue the investigation on the possibility of development of a numerical model for absorption process
- Continue on collaboration work with the PI partners to compare PIV measurements with numerical modeling results for the electrostatic separation process

Appendix

Justification and Background

The development of environmentally friendly process in industry is one of the major goals that have to be achieved. One way to approach cleaner environment is capturing or minimizing harmful gas components before emission to the atmosphere. One of the main gases which contribute significantly in global warming is CO₂. Due to a necessity to develop more efficient techniques for CO₂ capturing, scientific research in this area has been expanded rapidly. Since in the past very little R&D was devoted to CO₂ capture and separation technologies, opportunities for revolutionary improvements in CO₂ separation technologies is very high. To maintain its competitiveness and bring environmental friendly industry to the region, ADNOC has adopted various policies and approached it via many plans including “zero-flare” policy, acquiring more energy efficient process and the agreement signed with MASDAR to develop CO₂ capture technology. CO₂ separated from flue gases will be re-injected in oil wells, increasing oil production.

One of the promising concepts which can lead to major technology advancement is microchannel-based absorption units with enhanced kinetics. The objective of this study is to develop a full process of CO₂ separation from flue gas with incorporating micro-channel absorption technology at laboratory scale. The project addresses various stages of separation process: separation of solid particles and condensed water droplets and CO₂ separation using absorption process. Microchannel absorption CO₂ separator developed in this project will, significantly, increase the efficiency of separation process while decreasing energy consumption involved in such operation. Moreover, development of such technology will lead to reduction of equipment’s size and, therefore, minimizing the footprint and cost of equipment. An electrostatic separator will be used prior to CO₂ separation to remove solid and liquid contaminants from flue gas. The ultimate objective is to design all separation stages such that the overall performance will be optimized.

Approach

Detailed analysis and identification of the phenomena and the design challenges involved in effective implementation of the mechanism. Parametric study of existing and improved separators. Design iterations, including numerical flow and field simulations, fabrication, and testing. Creation of database and engineering design correlations.

Three-Year Schedule

The schedule below reflects the revised scope approved by both sides

Year 1:

- Conduct literature review to understand the basic of mass transfer in micreactor and separation of flue gas;
- Evaluate existing technologies and assess their applicability to CO₂ separation of flue gas;
- Repeat and implement some previous classical examples of microchannel separation to get familiarized with fundamentals and basic challenge;
- Analyze mixing in microchannels and possibility to use it in CO₂ separation;
- Continue improving efficiency of EHD separator for the fine liquid and solid particles;
- Conduct visualization study of liquid and solid particles migration in the electrical field.

Year 2:

- Continue on literature survey;
- Selection of the target alkanolamine;
- Simulate mixing and separation phenomena in microreactor via modeling and analytical means;
- Develop laboratory scale microchannel absorber and desorber for CO₂ separation;
- Conduct Experimental study and design optimization study;
- Continue on visualization study of liquid and solid particles migration in the electrical field.
-

Year 3:

- Conduct visualization study on absorption and desorption in microchannels;
- Design iterations and implementation;
- Parametric study of CO₂ separation process and experiment on different designs;
- Continue on simulation of mixing and separation phenomena in microreactor via modeling and analytical means;
- Present the best design to ADNOC group of companies;
- Develop design correlation;
- Prepare report.

References

- [1] Aaron, Douglas, and Costas Tsouris. "Separation of CO₂ from Flue Gas: A Review." *Separation Science and Technology* 40 (2005): 321-348.
- [2] Aresta, Michael, ed. *Carbon Dioxide Recovery and Utilization*. Kluwer Academic Publishers, 2003.
- [3] Blauwhoff, P. M. M., G. F. Versteeg, and W. P. M. van Swaaij. "A study on the reaction between CO₂ and alkanolamines in aqueous solutions." *Chem. Eng. Sci.* 39 (1984): 207-225.
- [4] Caplow, Michael. "Kinetics of Carbamate Formation and Breakdown." *J. Am. Chem. Soc.* 90, no. 24 (1968): 6795-6803.
- [5] Danckwerts, P. V. "The Reaction of CO₂ with Ethanolamines." *Chemical Engineering Science* 34, no. 4 (1979): 443-446 .
- [6] Glasscock, D. A., J. E. Critchfield, and G. T. Rochelle. "CO₂ absorption/desorption in mixtures of methyldiethanolamine with monoethanolamine or diethanolamine." *Chem. Eng. Sci.* 46 (1991): 2829-2845.
- [7] Herzog, H., D. Golomb, and S. Zemba. "Feasibility, modeling and economics of sequestering power plant CO₂ emissions in the deep ocean." *Environmental Progress* 10 , no. 1 (1991): 64-74.
- [8] Herzog, Howard. "An Introduction to CO₂ Separation and Capture Technologies." MIT Energy Laboratory, 1999.
- [9] Kockmann, N. *Transport Phenomena in Micro Process Engineering*. Berlin: Springer-Verlag, 2008.
- [10] Kohl, Arthur L., and Richard B. Nielsen. *Gas purification*. Houston, Texas: Gulf Publishing Company, 1985.
- [11] Kong, X., M. Alshehhi, A. Goharzadeh, A. Shooshtari, S. Dessiatoun, and M. Ohadi. "Experiemntal Characterization of EHD Flow in an Electrostatic Air-Oil Droplet Separator Using Particle Image Velocimetry." *IMECE2010*. Montreal, Canada, 2010.
- [12] Littel, R. J., G. F. Versteeg, and W. P. M. van Swaaij. "Kinetics of CO₂ with primary and secondary amines in aqueous solutions-II. Influence of temperature on zwitterion formation and deprotonation rates." *Chem. Eng. Sci.* 47 (1992): 2037-2045.

- [13] Rinker, Edward B., Sami S. Ashour, and Orville C. Sandall. "Kinetics and Modeling of Carbon Dioxide Absorption into Aqueous Solutions of Diethanolamine." *Ind. Eng. Chem. Res.* 35, no. 4 (1996): 1107–1114.
- [14] Sada, E., H. Kumazawa, Q. Han, and H. Matsuyama. "Chemical kinetics of the reaction of carbon dioxide with ethanolamines in nonaqueous solvents." *AIChE J.* 31 (1985): 1297-1303.
- [15] Seader, J. d., and Ernest J. Henley. *Separation Process Principles*. Edited by Ernest J. Henley. Wiley, 2006.
- [16] Versteeg, G. F., and M. H. Oyevaar. "The reaction between CO₂ and diethanolamine at 298 K." *Chem. Eng. Sci.* 44 (1989): 1264-1268.
- [17] Versteeg, G. F., and W. P. M. van Swaaij. "On the kinetics between CO₂ and alkanolamines both in aqueous and nonaqueous solutions-I. Primary and secondary amines." *Chem. Eng. Sci.* 43 (1988): 573-585.
- [18] Versteeg, G. F., and W. P. M. van Swaaij. "On the kinetics between CO₂ and alkanolamines both in aqueous and nonaqueous solutions-II. Tertiary amines." *Chem. Eng. Sci.* 43 (1988): 587-591.
- [19] Yaghi, Basma, and Omar Houache. "Solubility of Nitrous Oxide in Amine Aqueous Solutions." *Journal of Engineering, Computing and Architecture* 2, no. 1 (2008).

Microreactors for Oil and Gas Processes Using Microchannel Technologies

UMD Investigators: Serguei Dessiatoun, Michael Ohadi, Amir Shooshtari, K.Y. Choi
GRA: Pradeep Kumar Singh
PI Investigators: Afshin Goharzadeh, Ebrahim Al-Hajri (Returning ADNOC Scholar)
Start Date: Oct 2006

1. Objective/Abstract

Micro and heat and mass exchangers are receiving interest in the energy and petrochemical industries because of the substantial improvement in the energy and mass transfer processes and the resulting reduction in the size and cost of these systems. In addition to the already demonstrated substantial improvement in chemical reaction rates, microfabricated chemical systems are expected to have a number of other advantages for chemical synthesis, chemical kinetics studies, and process development. Chemical processing advantages from better control over the size and structure of molecules in advanced micro systems can result in innovative polymers and polymer characteristics that would be otherwise impossible to obtain with conventional systems.

Quantitative assessment of a microreactor's potential to produce cost-effective innovative polymers and polymer derivatives of significance to the UAE's polymer industry is one of the main objectives of the current project. The application of microreactors in the polymerization of ethylene and propylene is of particular interest. Preliminary evaluations suggest potential feasibility and significant promise for production of cost effective innovative polymers, thus expanding Abu Dhabi's polymer industry markets.

2. Milestones/Deliverables Scheduled for the Completed Quarter

- Identification of the target reaction(s)
- Selection of the target polymerization process of economical significance to the Abu Dhabi polymer industry
- Selection of the type and size of catalyst particles to be used in the process
- Beginning of the design and fabrication of a microreactor capable of selected polymerization processes
- Visualization study of mixing in microchannels

3. Summary of Project Activities for the Completed Quarter

In the following a brief summary of the progress made during the current reporting period for each of the items above is given.

Identifying the target reaction--Polyethylene and Polypropylene production

UAE industrial development has effectively taken advantage of its huge petrochemical resources to develop innovative polymer products that are cost effective and competitive in international markets. This advantage, combined with the advanced technologies offered through its subsidiary company Borealis and the associated Borstar technology, makes polymer production in UAE potentially very profitable. Borouge, a polymer business venture branch of ADNOC and Borealis

together, have the potential to become a world largest producer of the products derived from common polymers such as polyethylene (PE) and polypropylene (PP).

Polyethylene and polypropylene are typically produced with Ziegler–Natta catalyst systems [1–3], but how the Ziegler–Natta system really works is not entirely understood. Better understanding of the behavior would offer significant support to catalyst design and development. Catalyst polymerization and fragmentation behavior greatly depends on the type of catalyst and the nature of the catalyst support [4]. It is widely believed that the catalyst needs to be highly porous so that the monomer can diffuse into the particle. The mechanical strength of the catalyst structure must be high enough to withstand handling of the catalyst, but at the same time low enough to break up in polymerization. Fragmentation of catalyst particles affords higher polymer yields and ensures the absence of big catalyst fragments in the final product. The active sites should also be well distributed over the catalyst particle so that the polymer is evenly formed within the catalyst [4–6].

The growth and the fragmentation of catalyst particles in olefin polymerization have been studied by several research groups, and at least three different models for particle morphology in polymer growth have been presented. In the core–shell model, also known as the layer-by-layer model, the catalyst particle does not break up at the beginning of the polymerization process. The polymerization reaction occurs on the surface of the particle, which acts as a core, and the polymer grows in the form of a shell around the core. The monomer diffuses through the accumulated polymer to the catalyst surface, where it reacts. According to some investigations [8,9], this kind of polymer growth proceeds in slurry phase polymerization of propylene when the porosity of the catalyst is low (monomer diffusion is limited). In the case of a highly porous catalyst the monomer diffusion is less limited; the monomer can penetrate into the pores of the catalyst more easily and the polymer grows throughout the particle. The result is an immediate fragmentation of the catalyst particle [8,9]. This particle morphology model, known as the multigrain model, is one of the most popular and simple models for the particle growth in olefin polymerization [10,11]. According to the multigrain model, immediately after the polymerization starts the catalyst particles break up into small fragments (microparticles), and the polymerization reaction occurs on the surface of these microparticles following the core–shell model. The microparticles together form porous macroparticles [10,11]. The third model is the polymeric flowmodel. In this model it is also assumed that the catalyst particles break up at the beginning of the polymerization [10]. Polymer and catalyst fragments are considered as one phase, and the polymerization reaction occurs at active sites that are embedded in the polymer and move radially outward with the forming polymer [10]. The multigrain and polymeric flow models are the models most commonly used to explain the replication phenomena [7].

This complex polymerization process affects polymer molecular weight, density and mechanical properties. Borstar® polymerization technology allows variation of polymerization conditions at a different stage of the process as a result of production of the polymers with the desirable properties. The Borstar® process includes at least two reactors working in series. It also may include a pre-polymerization reactor (Figure 1) that adds significant flexibility to manipulate the polymer morphology. The feed to the reactor consists of ethylene, comonomer, hydrogen, inerts, and catalyst. A stream of unreacted gases flows from the top of the reactor and is cooled by passing through a heat exchanger in counter-current flow with cooling water. Cooling rates in the heat exchanger are adjusted by instantaneously blending cold and warm water streams while maintaining a constant total cooling water flowrate through the heat exchanger. Change in the feed product temperature usually results in the fluctuation of the reactor temperature that can reach a few degrees (C°) and may take a few hours to stabilize, as shown in Figure 2, even using best control strategies [32].

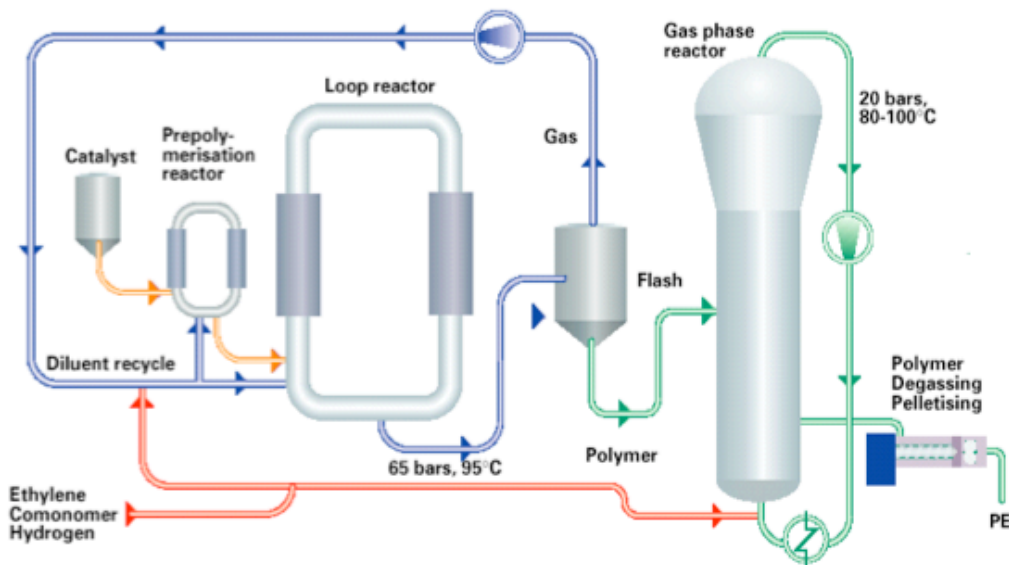


Figure 1. Borstar® polymerization process diagram.

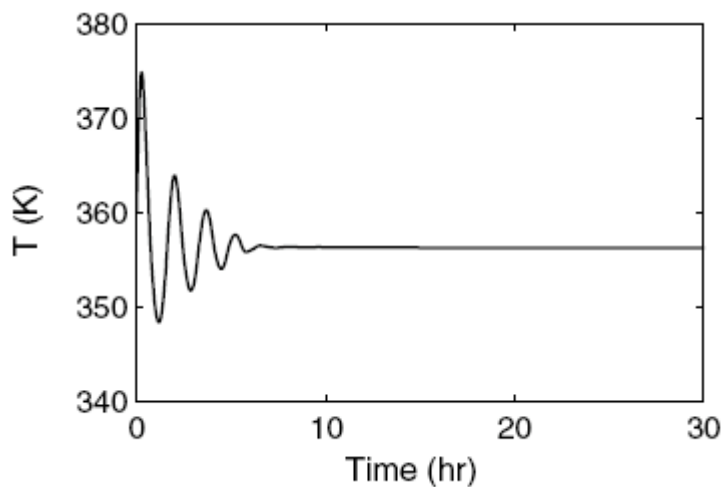


Figure 2. Reactor temperature variations.

The flexibility provided by the multi-reactor arrangement of the Borstar® process is significantly diminished with an increase in the reaction temperature variations, which is generally proportional to the reactor size. Figure 3 demonstrates temperature influence on the polypropylene particle morphology. The increase in the scale of polymer production of the Bourouge reactors inevitably increases the complexity of temperature control in the reactors and may result in the decrease in polymer quality. Application of microreactors, on the other hand, provides the most flexibility of the temperature and composition control and would be extremely beneficial to the polymer quality, particularly if it is used on the initial stage of polymerization or on the pre-polymerization stage. Its effect on polymer production in UAE and their quality could be significant. One of the main objectives of the current project is to evaluate the application of microreactor technology for development of next-generation innovative polymers, with superior properties to the conventional

products, while also being cost-effective and in-line with UAE heavy investment in the petrochemical industry.

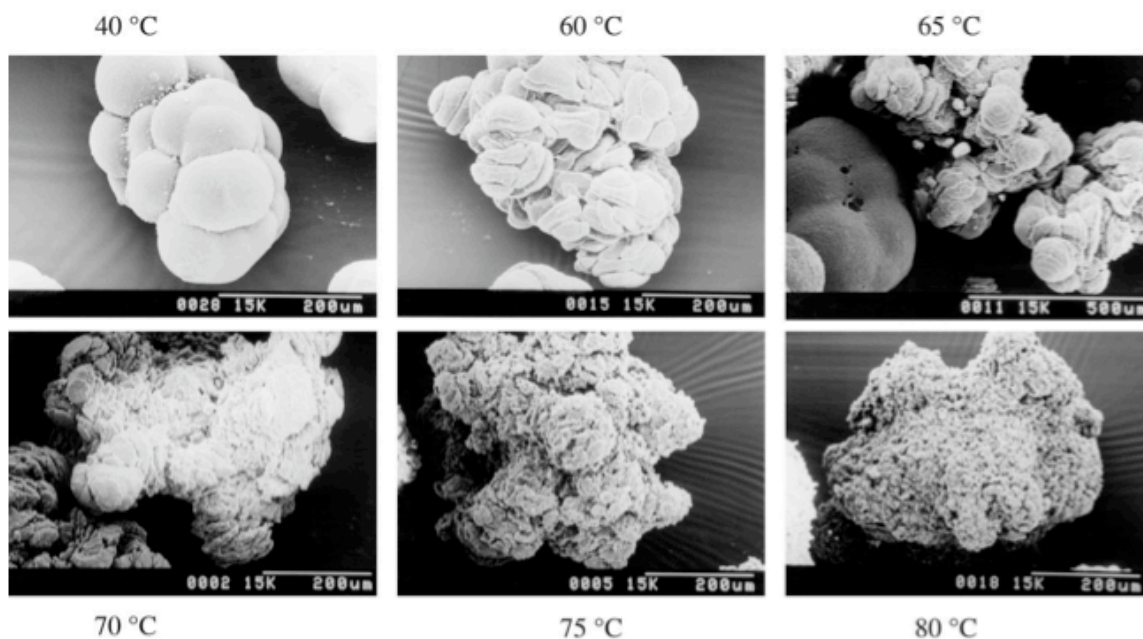


Figure 3. Temperature influence on morphology; Ziegler-Natta polymerization of propylene.

Selection of the target polymerization process

Although the polyolefins industry is maturing, there is a strong need to develop advanced olefin polymers that can replace environmentally less benign thermoplastics such as polyvinylchloride (PVC) and find new applications. The combination of olefins and other functional monomers can open up new business opportunities for polyolefin manufacturers to secure competitiveness in the next decades. The creative design of polymer architecture through innovative polymer reaction and process engineering will provide new breakthrough in developing polymers with exciting new properties. Microreactor technology in industrial applications is in its infancy, especially in polymerization industries. The unique characteristics of catalytic polymerization kinetics of olefin polymerization make it an ideal process system where both technologies can result in enormous synergistic effects.

Ethylene or propylene polymers can be modified by being copolymerized with higher alpha olefins to add flexibility to the copolymer. It may not be possible to reproduce all the properties of PVC, but there are already many on-going industrial efforts to refine polyolefins to match the properties of PVC. This microreactor research project can offer an excellent testbed for the design of low density and flexible olefin copolymers through innovative reactor design and operational strategies.

The polymer materials technology must be integrated with polymerization chemistry, reaction engineering, characterization (analytical) techniques, reactor technology, and process engineering. Bulk polyolefins have low margins for profit, and the global competition for market share is stiff. It has become necessary to design and produce the polymers of precisely controlled molecular architecture. The creation of new properties through the use of novel functional monomers, catalysts and microreactor technology will be the key in the future to maintain

sustainability. The reaction conditions can be designed and precisely controlled in a microreactor, thus producing refined polymers with properties and characteristics unmatched by conventional technologies. For example, the microreactor can be designed in such a way that low volume, high value-added polyolefins that cannot be produced by large-scale reactor processes can readily be produced. The reaction can be completed in short reaction times by taking advantage of very high initial catalyst activity in microreactor systems.

Selection of type and size of catalyst particles to be used in the process

Catalyst development is an essential part of olefin polymerization. The polyolefin industry has made substantial progress over the years (Figure 4). But the most important factor in the future scientific, technological and commercial development of this field is not just the increase in the catalyst activity itself, but rather the capability of the ideal catalyst to reduce in parallel the process constraints, maximizing the technology versatility so as to have a significant expansion of the product property envelope. Today, it is universally recognized that the real key to the outstanding commercial growth of the polyolefin materials has been the continuous and dynamic development of several generations of Ziegler-Natta catalysts (Table 1). At the current state of technology several tons of polymer can be produced using 1 gram of catalyst.

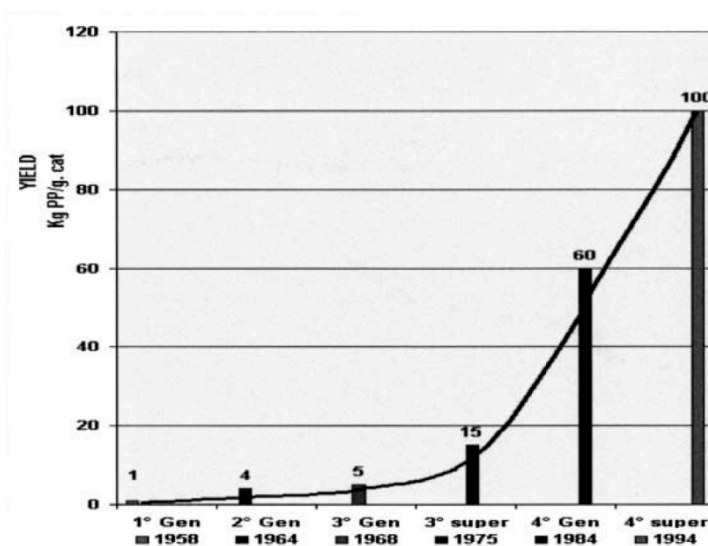


Figure 4. Relative yield improvement in polyolefin production.

Table 1. Performances of the different catalyst generations

Generation	Composition and structure	Productivity (kg PP/g Cat)	II (wt%)	Technology control	Process requirements
1st (1957–1970)	3TiCl ₃ AlCl ₃ /AlEt ₂ Cl	0.8–1.2	88–91	Irregular powder	Need of purification and atactic removal
2nd (1970–1978)	TiCl ₃ /AlEt ₂ Cl	3–5	95	Irregular powder	Need of purification and atactic removal
3rd (1978–1980)	TiCl ₄ /Ester/MgCl ₂ + AlEt ₃ /Ester	5–15	98	Regular/irregular powder	No purification, need of atactic removal
4th (1980) RGT	TiCl ₄ /Diester/MgCl ₂ + AlEt ₃ /silane three-dimensional catalyst granule architecture	20–60	99	Particles with regular shape and adjustable size and PSD. Designed distribution of the different products inside each particle.	No purification. No atactic removal. No pelletisation
	TiCl ₄ /Diether/MgCl ₂ + AlEt ₃ three-dimensional catalyst granule architecture	50–120	99	Particles with regular shape and adjustable size and PSD. Designed distribution of the different products inside each particle.	No purification. No atactic removal. No pelletisation
5th Metallocenes	Zirconocene + MAO	(5–9) × 10 ³ (on Zr)	90–99	To be improved	
6th Multicatalyst RGT	Mixed catalysis: ZN + radical initiators, ZN + single site (catalysts)			Particles with designed distribution of both olefinic and non-olefinic materials	

Single-site catalysts offer superior control over the molecular architecture. Polyethylenes polymerized with single-site catalysts usually have a very narrow MWD and a uniform composition distribution. Therefore, in addition to improved toughness, with the same comonomer content they have clearly lower extractables and melting and sealing temperatures than the corresponding Ziegler-Natta and chromium catalyzed materials. The main problem with single-site materials has been their poor processability—e.g. in film blowing. As a result, the Ziegler-Natta catalysts still dominate polyolefin production.

There is a strong relation between the morphology of polyolefins and the morphology of the catalyst used to produce them, since the polymer replicates the catalyst particle. Polymer particles with uniform and high standard morphology are desirable in the standard polymerization process because they readily fluidize in the reactor, and the pelletizing step can be eliminated from the industrial process. In addition, controlling the polymer particle size is important since finely or coarsely grained particles may be desired depending on the application.

During the formation of the polymer, the catalyst particle becomes dispersed throughout the polymer particle. The architecture of the catalyst particle is largely determined by the method used for its synthesis. Secondary catalyst particles can be large (20 to 40 μm), but they comprise many smaller particles in a range of 0.01 to 0.10 μm diameter [4].

A regular characteristic of the olefin polymerization process is the fracture of the initial catalyst particles into small fragments, with dimensions thousands of times smaller than the initial size. This process is particularly critical in the first stages of polymerization because too-fast growth of particles could cause the catalyst “explosion” and prevent regular replication. Process conditions have an especially important effect on particle morphology during the initial stages of polymerization, as the polymer bulk density decreases with increasing operating temperature. The combination of high temperature and low pressure results in lower polymer bulk density mostly by increasing the voids within the particles. It was observed that no change in the shape of particle size distribution takes place with temperature.

Many of traditional restraints on catalyst particle dimensions are not applicable to polymerization in microchannels. We expect that the polymerization process in the microreactor will be much more intense, with much shorter residential time. We also expect that much smaller catalyst particles will be optimal for the microreactor polymerization. Therefore, we are starting our particle distribution experiment with average particle size 1-2 μm .

Design and fabrication of the microreactor for the selected polymerization processes

Microreactors represent a relatively new area of chemical process technology. Inspired by progress in micro-fabrication technology of electronics, they have slowly progressed into microfluidics, lab-on-a-chip applications, and gas-to-gas or liquid-to-liquid reaction processes. In many cases the same silicon micro-fabrication technology is used to fabricate microreactors. A typical microreactor is shown on Figure 5 [15]. It comprises a stack of etched silicon wafers bonded or compressed together. The key advantage of microreactors lies in their ability to control precisely the temperature, relative concentration and reaction time. This can significantly improve both the quality and reproducibility of the chemistry. The chemistry may not be new, but it is certainly better. Numerous applications have been cited as "proof of principle." Microreactors have been used in commodity syntheses, for example, ethylene oxide [16] and the preparation of HCN [17], methane reforming. Figure 5 depicts a typical microreactor fabrication sequence. In all, more than 60 reactions from different reaction classes have been performed successfully in microreaction systems [18]. In most cases, a positive effect can be detected in terms of yield and/or selectivity. The suitability of the system was successfully put to the test with the full adaptation of the synthesis of a blockbuster pharmaceutical (Ciprofloxazin®) to the microreactor.

There have been very few attempts to realize olefin polymerization in microreactors. Dow Chemical conducted extensive research to set up an electro-thermal continuous flow polymerization microreactor [19], which resulted in several internal and external publications and a US patent. The main focus of this work was on the effect of operating conditions and flow composition, mainly the number of existing phases, on the molecular weight of the polymer. A series of polymerization experiments was performed in single-phase (liquid) and two-phase (vapor-liquid) flow regimes. In single-phase polymerization, the ethylene concentration falls continuously along the length of the reactor. This will have a significant effect on the kinetics of polymerization, particularly the molecular weight of the produced polymer. A key advantage of operating in the two-phase region is that an almost constant ethylene concentration is maintained along the length of the reactor. In effect, the vapor phase serves as a reservoir that replenishes the ethylene consumed in the liquid phase by polymerization. The molecular weight data show that this assumption is valid provided that the rate of mass transfer is significantly higher than the rate of the polymerization reaction.

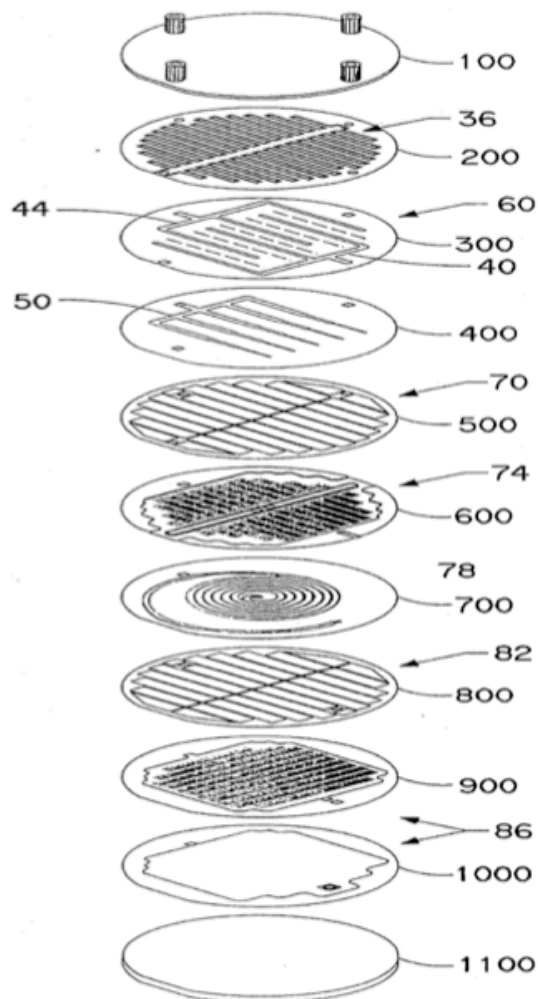


Figure 5. Typical microreactor fabricated by silicon microfabrication technology.

Figure 6 demonstrates the schematic of a tubular polymerization reactor. The reactor was comprised of a 1.27 mm ID, 1450 mm long, electrically heated stainless steel tube that was divided into preheat and reactor zones. The catalyst was introduced in the middle trough T-connection.

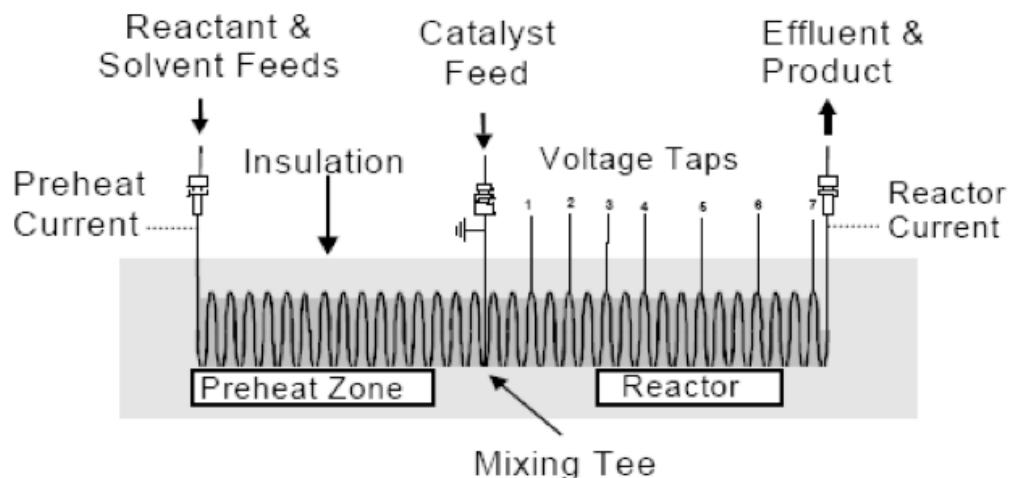


Figure 6. Continuous flow tubular polymerization microreactor.

Polymer samples were dissolved in 1, 2, and 4-trichlorobenzene (TCB) as solvent. All GPC experiments were carried out at 160 °C and at a flow rate of 1 mL/min. Reactor components and flow diagram are shown in Figure 7.

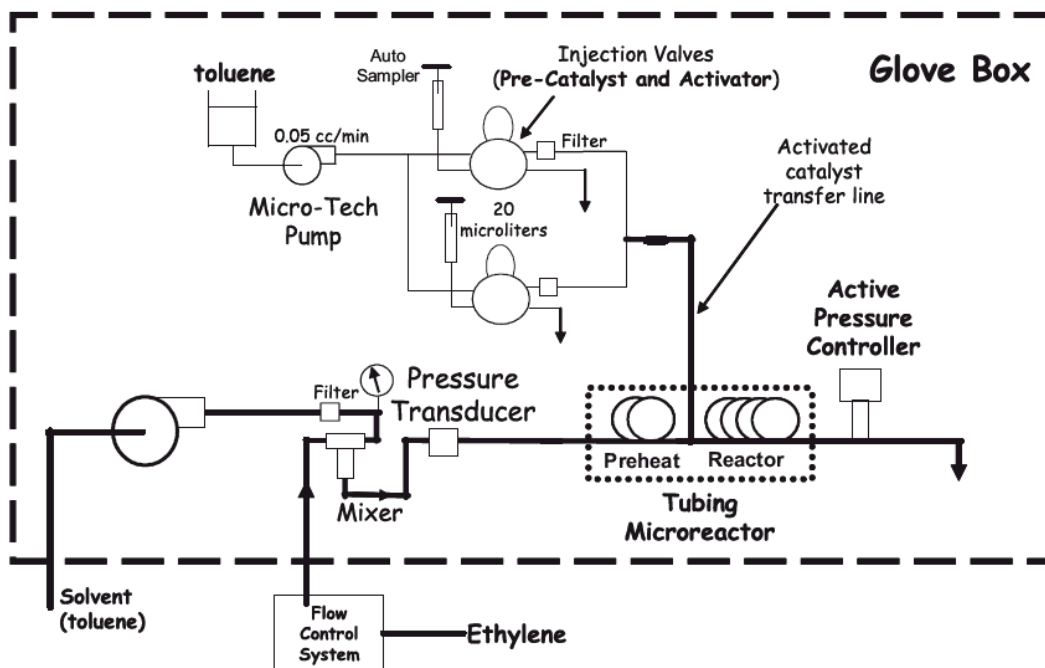


Figure 7. Reactor components and flow schematic diagram for tubular microreactor.

The most common olefin polymerization process involves a multi-phase process in which the solid state of the catalyst and/or polymer is present. The slurry or gas-phase polymerization process, on the other hand, is difficult to realize in a microreactor. At the initial stage of polymerization microreactor development we are considering constructing a microreactor similar to Dow Chemical's polymerization reactor. One important feature we are adding to our reactor is visualization. This will allow us to analyze catalyst and polymer particle propagation in the microreactor and will help to optimize the reactor geometry.

Visualization study of mixing in microchannels

Figure 8 depicts the experimental apparatus that was used in the current project. The apparatus in some respects represents the slurry loop reactor which serves as the basis for Borstar® polymerization process used by Borealis and Borouge. The efficiency of this process very much depends on the even distribution of a small amount of catalyst through a large volume of reactant and diluent mixture. Even distribution of the catalyst is a challenge for the microchannel reactor of the type used in the current project. Therefore, a critical step in microreactor design is the development of an efficient process of mixing of catalyst with the reactant. Accordingly, a visualization study of catalyst distribution is essential for the optimum design of the mixer.

As seen in the figure, the setup for the visualization study is comprised of a reactant pump, catalyst pump, mixing chamber, transparent microchannel, and collecting reservoir. The syringe pump Harvard Apparatus PHD 2000 Infusion was used in the current experiments.

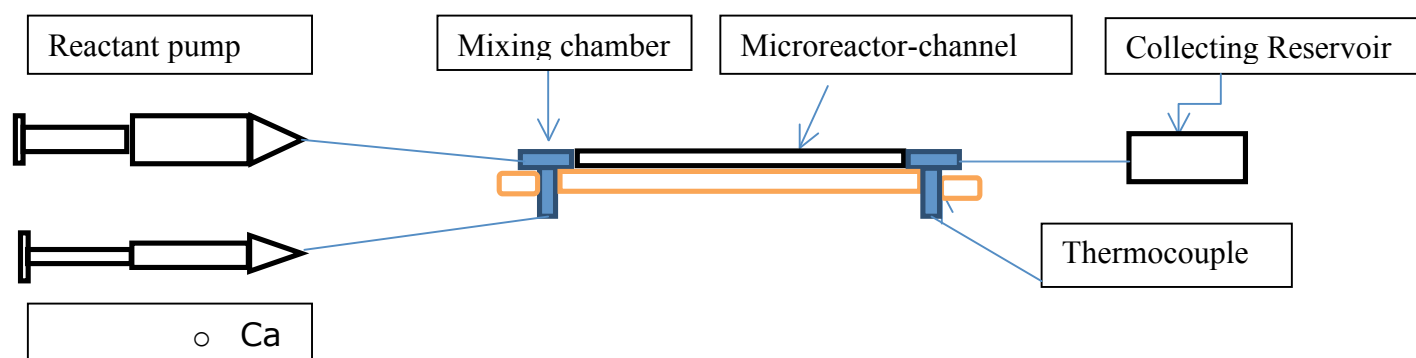


Figure 8. Experimental setup diagram.

In order to perform this experiment successfully some procedures had to be followed. The first step of this experiment was to build a suitable supporter for the microchannel reactor. Therefore, a small rectangular metal piece with certain dimensions was selected, and two holes were made on both ends of the metal piece using a drilling machine. Finally a hammer was used to tilt both ends so that the input and output T-junctions could be placed upon these two holes, providing support to the microchannel by holding it in place. The final shape of the support is shown in Figure 9.



Figure 9. Channel support in the microreactor.

The next phase was connecting the mixing T-junctions, Figure 10, with the designated microchannel. Therefore, small needles were inserted in the small tubes and were sealed within the T-junction using circular rubber seals.

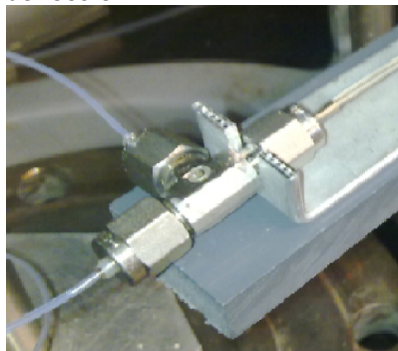


Figure 10. Mixing junction.

After that, two syringes with different diameters were selected, as shown Figure 11. At first, their diameters were measured and then their areas were calculated. Next, the bigger syringe was filled with distilled water and the smaller syringe was filled with ethanol-catalyst mixture. The catalyst particles were weighed using an electronic balance, and the volume of ethanol was determined by filling a small beaker to the desired volume. Then both the catalyst and ethanol were mixed together and the concentration of the ethanol-catalyst mixture was calculated. Since this part of the experiment deals with visualizing the catalyst particles in the flow, silica-based particles with mean diameter of $2\ \mu\text{m}$ were used as a catalyst simulating for the flow visualization. However, it was later found that silica particles were too dark to be visualized on a PC. Therefore, as a substitute, “Kallirscope Tracers” (white particles) were used instead. Moreover, an ultrasonic mixer was used to uniformly mix the catalyst particles within the ethanol solution, which produces sound waves that cause the ethanol and catalyst particles to vibrate and eventually produce a temporary stable mixture.



Figure 11. Syringe pump with different diameter of syringes.

A Phantom VR 806 8025 MIRO-4M camera was used in the experiments to conduct the flow visualization studies, shown in Figure 12.



Figure 12. Phantom MIRO - 4M high-speed camera.

Because the catalyst particles may have negative effects on the flow meter, an outer syringe was connected to the output T-junction to collect the output mixture and to prevent any leakage. Furthermore, a high-speed camera was connected to the PC to monitor and visualize the flow of the catalyst particles within the microchannel with the help of visualization software.

Finally, once all the connections were made the experiment was run several times and under variable parameters, including changing the velocity and flow rate of the catalysts particles, changing the ethanol-catalyst concentration, and changing the catalyst type. The final setup of the experiment is shown in Figure 13.



Figure 13. Setup assembly.

Figure 14 is an illustration of the particle distribution in microchannel. 14-a shows silica particles. Particle distribution is clear on the video and can be analyzed using Matlab image processing tool. The catalyst injection nozzle was positioned off-center, and it took at least 15 diameters for particles to distribute over the channel area. Changing the particle color to a more reflective type color (14-b) improved the visibility of the particle flow. Figure 14-c introduces the swirl into

reactant flow; however, particles stayed in the center of flow. A more successful approach was an axial introduction of particles with relatively high reactant flow that created some tabulating zones at the exit of catalyst channel and caught up the particle flow. Currently the experiment is still in progress. Its purpose is to perform a parametric study to quantify the effect of different geometric and flow characterization parameters on catalyst particle mixing with the reactant flow.

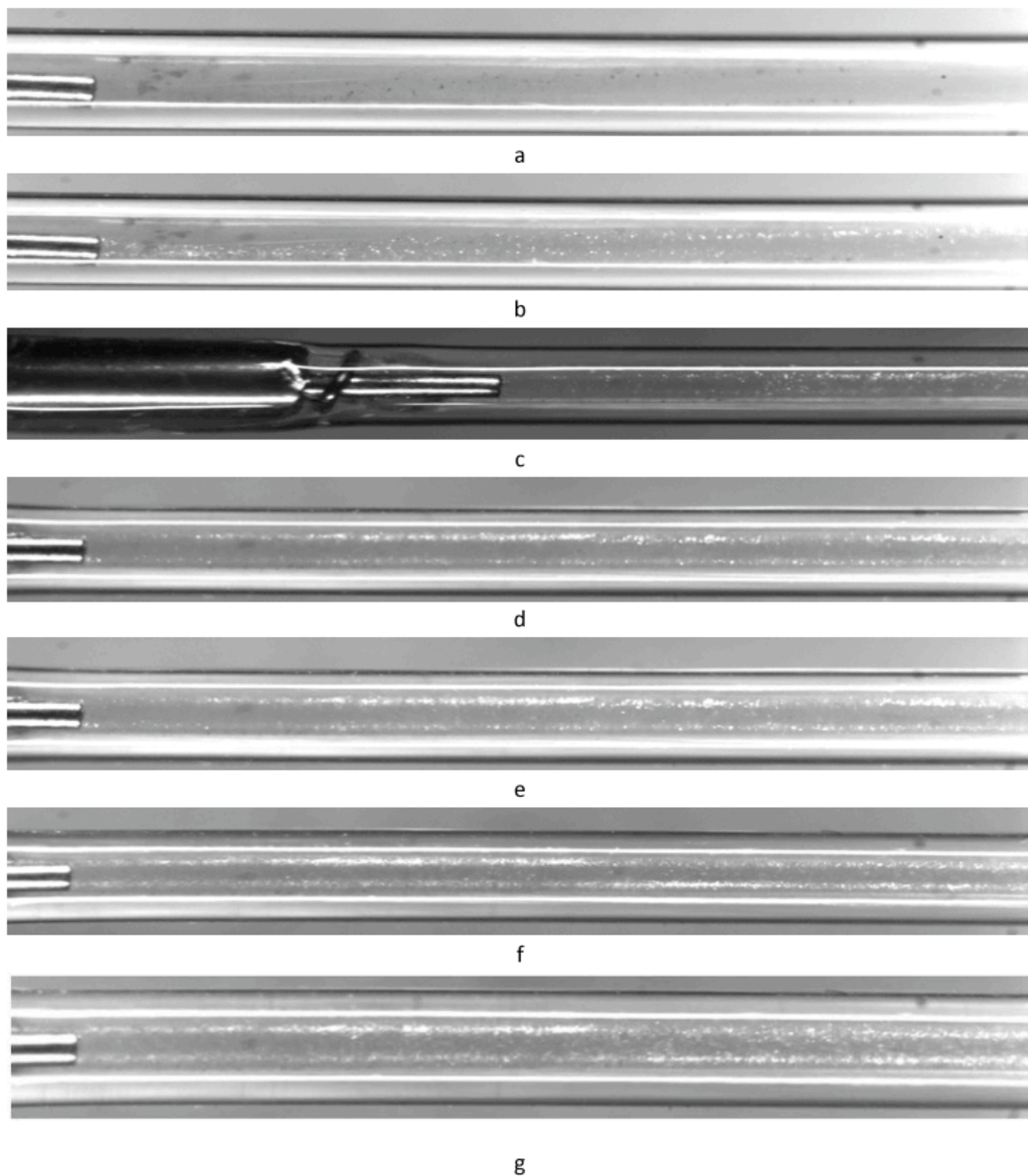


Figure 14. Particle distribution in the microchannel of the reactor.

4. Difficulties Encountered/Overcome

Visualization of actual polymerization process at high pressure and temperature in a microreactor is a challenging job. We are working closely with Professor Choi from the chemical engineering department to develop suitable improved solutions.

5. Planned Project Activities for the Next Quarter

- Design and fabrication of a microreactor capable of realization of selected polymerization process.
- Selection in cooperation with Borouge of the catalyst for the target polymerization process for realization in microreactors
- Preparation of a microreactor testing facility

6. Summary

We believe the achieved milestones and deliverables in the current reporting period demonstrate the good progress made in this project. Additionally, recently we were able to secure support from the PI for involvement of Professor Choi in this project. The graduate student has also been recruited, and essential equipment needs have been identified. The flow visualization studies conducted for the first time further verify the strong potential of this technology from both scientific and economic viewpoints.

Appendix

Justification and Background

Microreactors form a basis for the potential future downscaling of existing chemical processes, allowing tremendous reductions in capital and operating cost. They provide finer control of conditions, allow for faster process times, and improve safety in operation. Also, they should not encounter a significant problem in scaling from laboratory-sized systems to commercial-sized systems, since their operating principle will simply allow them to be stacked together modularly.

Of critical importance to the microreactors' capability to make the jump into industrial applications is the mixing efficiency, which controls the reaction rates and the yield expected from a reactor. Due to the scale of the systems, laminar flow is almost always encountered, which means that the vortices typically associated with turbulent flow are often missing. Instilling vortices into the flows to encourage mixing is accordingly a matter of construction of mixer channels.

Correct design parameters of microreactor influence the process yield. Designing microreactor for appropriate reaction conditions is very important for the reactions to be fast. Microreactors can be energy efficient too by appropriately designing and visualizing heat transfer. The channel dimensions have direct impact on diffusive mixing of reactants.

Approach

- Literature survey of the microreactor technologies as well as microchannel fabrication technologies.
- Selection of the target process for realization in microreactors with maximum benefit.
- Selection of microchannel fabrication technology suitable for microchannel mass production.
- Design and fabrication of a microreactor using microchannel fabricating technology suitable for mass production.
- Microreactor demonstration.
- Prepare experimental set-up and conduct the experiments.

Two-Year Schedule

The schedule below reflects the revised scope and schedule approved by both sides

Year 1:

- Conduct literature review to study current technologies for microreactors, micromixers, and incorporation of catalysts into microreaction technology.
- Evaluate existing microchannel formation techniques and their applications to microreactor construction.
- Selection of the target process for realization in microreactors with maximum benefit to ADNOC.
- Selection of microchannel manufacturing process most suitable for mass production.
- Preparation of a microreactor testing facility.
- Visualization study of mixing in microchannels.

Year 2:

- Literature survey of the olefin polymerization technologies focus on microchannels
- Selection of the target polymerization process for realization in microreactors with maximum

- benefit.
- Design and fabrication of a microreactor capable of realization of selected polymerization process
- Select type and size of catalyst particles to be used in the process
- Investigate propagation of selected catalyst particles in microchannels
- Investigate polymerization and polymer particle behavior in microchannels
- Parametric study of polymerization process at different temperatures, catalyst and reactant concentration.
- Microreactor demonstration.
- PI-side participation:
 1. Selection in cooperation with Borouge of the catalyst for the target polymerization process for realization in microreactors.
 2. Prepare a microreactor testing facility.
 3. Visualization study of mixing in microchannels
 4. Combine PI/UMD testing of the microreactor
 5. Microreactor demonstration to ADNOC representatives
 6. Prepare final project report and recommendations.

References

- [1] "The discovery and progress of MgCl₂-supported TiCl₄ catalysts". N. Kashiwa, J. Polym. Sci. A: Polym. Chem. 42 (1–8) (2004) 1.
- [2] J.J.A. Dusseault, C.C. Hsu, J. Macromol. Sci. Rev. Macromol. Chem. Phys. C 33 (2) (1993) 103.
- [3] S. Kojoh, T. Fujita, N. Kashiwa, Recent Res. Dev. Polym. Sci. 5 (2001) 43.
- [4] J.T.M. Pater, G. Weickert, J. Loos, W.P.M. van Swaaij, Chem. Eng. Sci. 56 (2001) 4107.
- [5] J.T.M. Pater, G. Weickert, W.P.M. van Swaaij, J. Appl. Polym. Sci. 87 (2003) 1421.
- [6] G. Weickert, G.B. Meier, J.T.M. Pater, K.R. Westerterp, Chem. Eng. Sci. 54 (1999) 3291.
- [7] L. Noristi, E. Marchetti, G. Baruzzi, P. Sgarzi, J. Polym. Sci. A: Polym. Chem. 32 (1994) 3047.
- [8] X. Zheng, J. Loos, [Morphology evolution in the early stages of olefin polymerization](#), Macromol. Symp., 236, 249-258, (2006).
- [9] X. Zheng, M.S. Pimplapure, G. Weickert, J. Loos, [Influence of porosity on the fragmentation of Ziegler-Natta catalysts in the early stages of propylene polymerization](#), e-Polym., 028, 1-10, (2006).
- [10] M. Bartke, in: J.R. Severn, J.C. Chadwick (Eds.), Tailor-Made Polymers. Via Immobilization of Alpha-Olefin Polymerization Catalyst, Wiley-VCH Verlag GmbH & Co. KGaA, Weinheim, 2008.
- [11] G. Cecchin, E. Marchetti, G. Baruzzi, Macromol. Chem. Phys. 202 (2001) 1987.
- [12] Adiwinata G., Prashant M., Panagiotis D. C., Fault-tolerant control of a polyethylene reactor, Journal of Process Control 17 (2007) 439–451
- [13] Hilikka Knuuttila, Arja Lehtinen, Auli Nummila-Pakarinen, Advanced Polyethylene Technologies - Controlled Material Properties, Adv Polym Sci (2004) 169:13–27
DOI: 10.1007/b13519

[14] Marcos A. S. Costa, Fernanda M. B. Coutinho, and Luiz C. Santa Maria, The influence of some synthesis parameter on Ziegler-Natta catalyst performance, Polymer Bulletin 31, 249-254, 1993.

[15] Integrated chemical processing apparatus and a process for preparation thereof, US Pat # 5534328.

[16] Kerstenbaum H, Lange de Oliveira A, Schmidt W, et al. (1999). Proceedings of the 3rd International Conference on Microreaction Technology, Frankfurt am Main.

[17] Hessel V, Ehrfeld W, Golbig K, Wörz O (1999). GIT, 10, 1100.

[18] CPC Cellular Process Chemistry GmbH. Website: www.cpc-net.com.

[19] Daryoosh Beigzadeh, Charles A. Nielsen, Study of Ethylene Polymerization Under Single Liquid Phase and Vapor-Liquid Phase Conditions in a Continuous-Flow Tubular Reactor, Chem. Eng. Technol. 2007, 30, No. 8, 1088–1093.



Thrust 3
Energy System Management

Integration of Engineering and Business Decisions for Robust Optimization of Petrochemical Systems

UMD Investigators: Shapour Azarm, P.K. Kannan
PI Investigators: Ali Almansoori, Saleh Al Hashimi
UMD GRA: Weiwei Hu
PI GRA: Naveen Al Qasas
Start Date: Oct 2006

1. Objective/Abstract

The overall objective of this project is to develop a framework for integrating engineering and business decisions. Towards that objective, a robust decision support system is being developed that can be used for multi-objective and multi-disciplinary optimization and sensitivity analysis, under uncertainty, of oil, gas and petrochemical systems. In this research quarter, we remodeled the reactor-distillation process in the refinery engineering domain using Aspen HYSYS. The HYSYS model was then connected with the business model through the optimization program in Matlab. One motivation in developing an engineering model in HYSYS is that the energy consumption can be calculated automatically. This allows us to perform a rigorous economic analysis in terms of energy cost in the engineering process. Moreover, as our methodology of integrating business and engineering decisions in the refinery continues to improve, the engineering model based on Aspen HYSYS can be further extended to consider and include other refinery processes, based on Aspen HYSYS's state-of-the-art modeling capability. However, one challenge in obtaining the optimal decisions for the integrated business and engineering models is associated with the computational cost in evaluating robustness (sensitivity) of the decisions. The situation becomes worse when the new HYSYS model is developed and used for engineering analysis because each HYSYS run or calculation call requires considerably more time than the previous engineering model considered. Since our last quarterly report, we have proposed to use approximation-assisted optimization approaches to address the computational difficulties in handling decision-making problems under uncertainty. The proposed approach is again used to solve the problem with the new engineering model in this research quarter. The optimal decisions using approximation-assisted optimization approaches are obtained and compared with the deterministic decisions as detailed in this quarterly report.

2. Deliverables for the Completed Quarter

- Remodeled the reactor-distillation process using process engineering simulation software: Aspen HYSYS:
 - Developed a preliminary model for the reactor-distillation process in Aspen HYSYS for the integration of business and engineering decisions.
 - Obtained convergence on the material and energy streams in HYSYS simulation case.
 - Identified a set of engineering decision variables and their ranges for the engineering model.
- Established a computerized connection between Aspen HYSYS and Matlab programs:
 - The reactor-distillation engineering model developed in HYSYS can be run programmatically from the Matlab command.
 - The optimization program in Matlab connects to both engineering and business

models and allows data to be exchanged between the models.

- Reformulated the integrated business and engineering decision-making problem and obtained optimized decisions:
Uncertainty in business and engineering parameters was considered, and the reformulated problem was solved using an AA-MORO approach.
- Continued developing the Approximation Assisted Multi-objective collaborative Robust Optimization (AA-McRO) approach. Based on the AA-McRO approach, a paper is being prepared and will be submitted to 2010 AIAA/ISSMO MA&O conference. An extended abstract of this paper was recently accepted for this conference, and we are in the process of preparing the full paper.
- Progress on recent joint publications:
 - Hu, W., M. Li, S. Azarm, and A. Almansoori, 2010 “On Improving Multi-Objective Robust Optimization Under Interval Uncertainty Using Worst Possible Point Constraint Cuts,” *Journal of Mechanical Design* (first round review was completed recently, the paper is under revision and will be resubmitted for further review).
 - W. Hu, A. Almansoori, P.K. Kannan and S. Azarm, 2010, “Corporate Dashboards for Multi-Unit Firms: An Agent-Based Approach for Supply Chain Optimization” (about to finalize for submission to “Decision Support Systems”).
 - Hu, W., S. Azarm, and A. Almansoori, 2010 “Approximation Assisted Multi-objective collaborative Robust Optimization (AA-McRO) under Interval Uncertainty” Extended abstract accepted, full paper is due to the 2010 AIAA/ISSMO Ma&O Conference in late August.

3. Summary of Project Activities for the Completed Quarter

Weiwei Hu successfully completed his Ph.D. proposal defense on April 30. Prof. Almansoori from PI served on the proposal defense committee through a video conference with other faculty committee members from the UMD.

During the video conference of May 12, a presentation was given by Weiwei to PI and UMD faculty and researchers. The presentation highlighted recent and upcoming research activities and plans, including integration of business and engineering decisions for the petrochemical company, and efficient approximation-assisted approaches for optimizing business and engineering decisions in the integration framework.

Teleconference meetings (via MSN’s Windows Live Messenger) were held between UMD and PI project collaborators. During the meeting, Prof. Azarm and Prof. Kannan updated progress on the joint publication. The summer research and collaboration schedule was discussed. Weiwei presented his research plans for the summer 2010.

Development of Aspen HYSYS Simulation Model

The engineering model is focused on a reactor-distillation process for producing phthalic anhydride, as shown in Figure 1. The raw materials of this process include some intermediate product during crude oil refining such as o-xylene. In the previous quarters, the reactor-distillation process was simulated in Matlab. Since our proposed integration and optimization framework is also developed on the Matlab platform, the Matlab based engineering model could be easily connected with the optimizer. However, one limitation in the previous Matlab-based engineering simulation model was that a rigorous calculation of the energy consumptions in the reactor-distillation process was not in place. This made it impossible to perform an accurate economical analysis, for example, to calculate energy cost. To address this limitation, we rebuilt the reactor-

distillation model using Aspen HYSYS in this research quarter. Aspen HYSYS is an accepted simulation software for chemical and process engineering. With the energy stream integrated in the operations, Aspen HYSYS can generate data on energy consumption automatically. This can help us to obtain energy cost from the engineering model. More importantly, the HYSYS-based simulation model can be further expanded to include other processes in the refinery. Next, we briefly explain the procedure in the HYSYS model development and the connection established between HYSYS and Matlab.

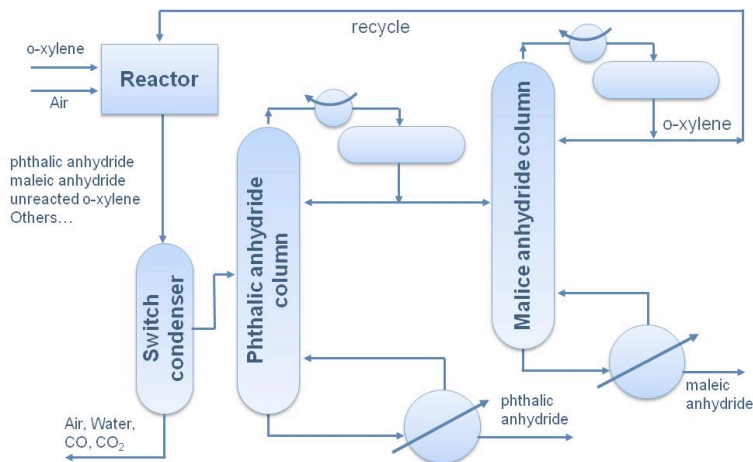


Figure 1. Flow diagram of the reactor-distillation process.

The engineering model in the integrated decision support framework is focused on a reactor-distillation process as shown in the flow diagram in Figure 1. In this process, the raw materials are air and o-xylene, and the expected product is phthalic anhydride. The process starts with the vaporized o-xylene and hot air, which are mixed and then sent to the reactor. Inside the reactor, o-xylene is oxidized to form phthalic anhydride, but some maleic anhydride can also be formed. The reactor effluent enters the switch condenser where light gases and water are removed. The remaining anhydride and unreacted o-xylene are forwarded to a series of distillation columns: (phthalic anhydride column and maleic anhydride column, as shown in Figure 1. The first distillation columns separate phthalic anhydride from the rest of the components; and the second distillation column removes impurities in the unreacted o-xylene, which is recycled with the raw material.

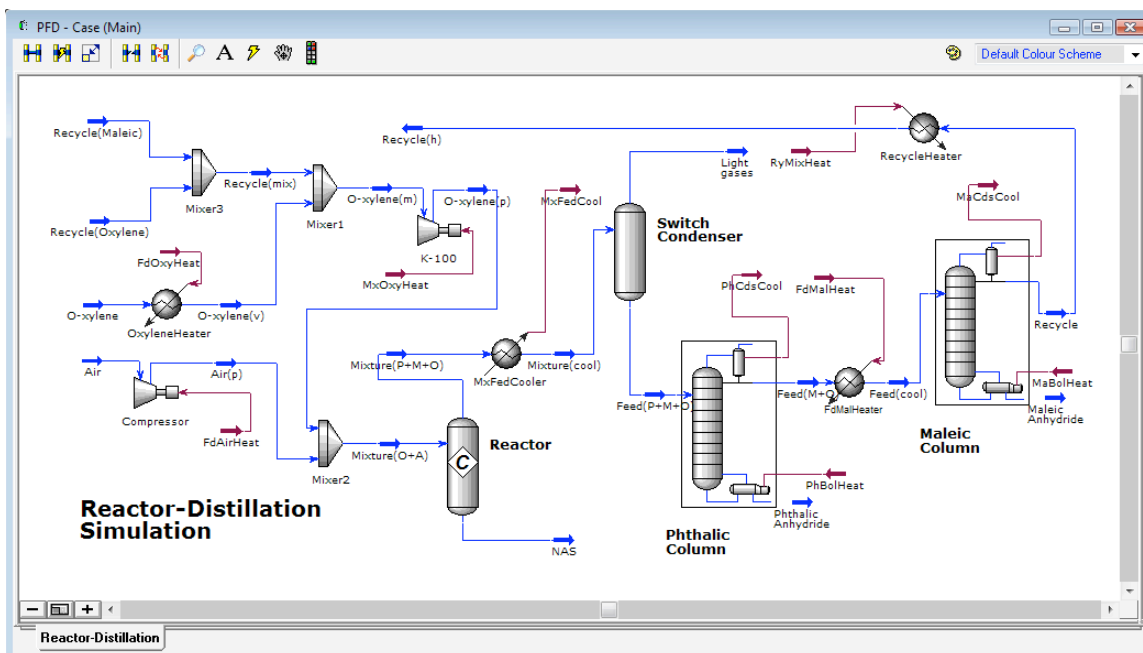
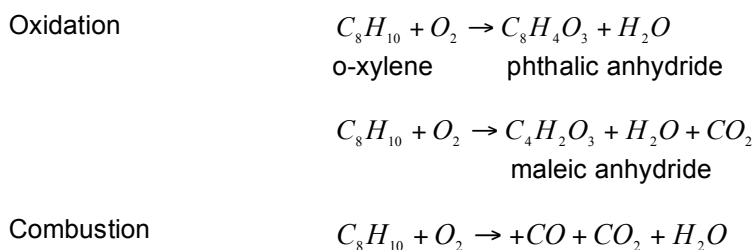


Figure 2. Aspen HYSYS Process Flow Diagram (PFD) of reactor-distillation simulation.

Figure 2 is the main PFD window of the reactor-distillation simulation as produced by Aspen HYSYS. The blue-arrowed lines in the PFD indicate the material streams, which have been converged in this case. The red line denotes the energy streams that are used by some of the equipment operations. For example, the compressor and heater both need input energy streams. The compressor increases the pressure of air feed from 1 atm to 3 atm, while the o-xylene heater vaporizes o-xylene. The preheated material streams are mixed with recycled o-xylene and compressed and then fed to the reactor for oxidation of o-xylene. The reaction of o-xylene and oxygen are modeled in a general “conversion reactor” in HYSYS. The majority of the reaction is in the form of producing phthalic anhydride. However, It is assumed that incomplete combustion occurs such that maleic anhydride, carbon dioxide, and carbon monoxide are also formed during the reaction. A series of equations, as shown next, are used to describe these reactions:



The effluent from the reactor is fed to the switch condenser, which is modeled as a “separator” in HYSYS. The heavy stream of switch condenser is forwarded to the distillation columns. The distillation columns are both modeled with total condenser. The reflux ratio and distillate rate are specified as the decision variables in the engineering model. It is required that the bottom product from the phthalic column should contain phthalic anhydride with relatively high purity. Also, the top stream from the maleic column can only contain a small amount of impurities (such as the anhydrides) in the unreacted o-xylene. The properties of the material stream and their composition for the base case in the reactor-distillation simulation are shown in Figure 3 (a) and (b). The values of energy streams in the HYSYS model are shown in Figure 3 (c). Note that the energy streams are automatically calculated in HYSYS after a user specifies such properties as

the pressure and temperature in the equipment's input and output materials streams.

Workbook - Case (Main)

Name	O-xylene	Air(p)	O-xylene(v)	Mixture(O+A)	Mixture(P+M+O)	Light gases	Feed(P+M+O)
Vapour Fraction	0.0000	1.0000	1.0000	1.0000	1.0000	1.0000	0.0000
Temperature [C]	26.85	349.9	349.9	356.1	1031	75.27	75.27
Pressure [kg/cm2]	1.033	3.100	1.033	3.100	3.100	1.033	1.033
Molar Flow [kgmole/s]	2.933e-002	0.9338	2.933e-002	0.9639	0.9714	0.9585	1.290e-002
Mass Flow [kg/s]	3.114	26.94	3.114	30.13	30.13	28.39	1.741
Liquid Volume Flow [m3/h]	12.69	112.1	12.69	125.1	124.7	119.7	4.934
Heat Flow [kJ/s]	-738.2	9144	2367	1.180e+004	1.180e+004	-2.013e+004	-4977
Name	Feed(M+O)	Phthalic Anhydr	Recycle	Air	Maleic Anhydric	Feed(cool)	Recycle(h)
Vapour Fraction	0.0016	0.0000	0.0021	1.0000	0.0000	0.0027	1.0000
Temperature [C]	-154.4	273.0	-196.5	26.85	203.0	90.62	350.0
Pressure [kg/cm2]	1.033	1.033	1.033	1.033	1.033	1.033	1.033
Molar Flow [kgmole/s]	2.000e-003	1.052e-002	1.350e-003	0.9338	6.500e-004	2.000e-003	1.350e-003
Mass Flow [kg/s]	0.2042	1.530	0.1399	26.94	6.436e-002	0.2042	0.1399
Liquid Volume Flow [m3/h]	0.6970	4.212	0.5218	112.1	0.1752	0.6970	0.5218
Heat Flow [kJ/s]	-530.2	-4108	-230.1	42.79	-274.4	-456.8	-49.57
Name	Mixture(cool)	Recycle(Oxylen)	O-xylene(m)	O-xylene(p)	Recycle(Maleic)	Recycle(mx)	NAS
Vapour Fraction	0.9867	1.0000	1.0000	1.0000	1.0000	1.0000	0.0000
Temperature [C]	75.27	350.0	349.9	382.3	350.0	350.0	1031
Pressure [kg/cm2]	1.033	1.033	1.033	3.100	1.033	1.033	3.100
Molar Flow [kgmole/s]	0.9714	7.375e-004	3.007e-002	3.007e-002	5.792e-006	7.433e-004	0.0000
Mass Flow [kg/s]	30.13	7.830e-002	3.193	3.193	5.680e-004	7.887e-002	0.0000
Liquid Volume Flow [m3/h]	124.7	0.3192	13.01	13.01	1.546e-003	0.3207	0.0000
Heat Flow [kJ/s]	-2.511e+004	59.55	2425	2653	-2.035	57.51	0.0000

Material Streams Compositions Energy Streams Unit Ops

FeederBlock: O-xylene
OxyleneHeater

Fluid Pkg: All

Include Sub-Flowsheets
 Show Name Only
Number of Hidden Objects: 0

Horizontal Matrix

(a) Material stream

Workbook - Case (Main)

Name	O-xylene	Air(p)	O-xylene(v)	Mixture(O+A)	Mixture(P+M+O)	Light gases	Feed(P+M+O)
Comp Mole Frac (Oxygen)	0.0000	0.2100	0.0000	0.2034	0.1271	0.1288	0.0001
Comp Mole Frac (Nitrogen)	0.0000	0.7900	0.0000	0.7654	0.7594	0.7696	0.0003
Comp Mole Frac (CO2)	0.0000	0.0000	0.0000	0.0000	0.0190	0.0192	0.0001
Comp Mole Frac (H2O)	0.0000	0.0000	0.0000	0.0000	0.0538	0.0541	0.0298
Comp Mole Frac (o-xylene)	1.0000	0.0000	1.0000	0.0312	0.0151	0.0143	0.0759
Comp Mole Frac (PhthalicAnhydr)	0.0000	0.0000	0.0000	0.0000	0.0111	0.0008	0.7727
Comp Mole Frac (CO)	0.0000	0.0000	0.0000	0.0000	0.0114	0.0115	0.0000
Comp Mole Frac (MaleicAnhydr)	0.0000	0.0000	0.0000	0.0000	0.0032	0.0016	0.1210
Name	Feed(M+O)	Phthalic Anhydr	Recycle	Air	Maleic Anhydric	Feed(cool)	Recycle(h)
Comp Mole Frac (Oxygen)	0.0007	0.0000	0.0010	0.2100	0.0000	0.0007	0.0010
Comp Mole Frac (Nitrogen)	0.0018	0.0000	0.0026	0.7900	0.0000	0.0018	0.0026
Comp Mole Frac (CO2)	0.0009	0.0000	0.0013	0.0000	0.0000	0.0009	0.0013
Comp Mole Frac (H2O)	0.0000	0.0000	0.0000	0.0000	0.0000	0.0000	0.0000
Comp Mole Frac (o-xylene)	0.4895	0.0000	0.7252	0.0000	0.0000	0.4895	0.7252
Comp Mole Frac (PhthalicAnhydr)	0.0062	0.9467	0.0000	0.0000	0.0191	0.0062	0.0000
Comp Mole Frac (CO)	0.0000	0.0000	0.0000	0.0000	0.0000	0.0000	0.0000
Comp Mole Frac (MaleicAnhydr)	0.5009	0.0533	0.2698	0.0000	0.9809	0.5009	0.2698
Name	Mixture(cool)	Recycle(Oxylen)	O-xylene(m)	O-xylene(p)	Recycle(Maleic)	Recycle(mx)	NAS
Comp Mole Frac (Oxygen)	0.1271	0.0000	0.0000	0.0000	0.0000	0.0000	0.1271
Comp Mole Frac (Nitrogen)	0.7594	0.0000	0.0000	0.0000	0.0000	0.0000	0.7594
Comp Mole Frac (CO2)	0.0190	0.0000	0.0000	0.0000	0.0000	0.0000	0.0190
Comp Mole Frac (H2O)	0.0538	0.0000	0.0000	0.0000	0.0000	0.0000	0.0538
Comp Mole Frac (o-xylene)	0.0151	1.0000	0.9998	0.9998	0.0000	0.9922	0.0151
Comp Mole Frac (PhthalicAnhydr)	0.0111	0.0000	0.0000	0.0000	0.0000	0.0000	0.0111
Comp Mole Frac (CO)	0.0114	0.0000	0.0000	0.0000	0.0000	0.0000	0.0114
Comp Mole Frac (MaleicAnhydr)	0.0032	0.0000	0.0002	0.0002	1.0000	0.0078	0.0032

Material Streams Compositions Energy Streams Unit Ops

FeederBlock: O-xylene
OxyleneHeater

Fluid Pkg: All

Include Sub-Flowsheets
 Show Name Only
Number of Hidden Objects: 0

Horizontal Matrix

(b) Material stream composition

Name	PhCdsCool	PhBolHeat	MaCdsCool
Heat Flow [kJ/s]	303.8	526.1	177.4
Name	MaBolHeat	RyMixHeat	MxFedCool
Heat Flow [kJ/s]	129.6	180.6	3.691e+004
Name	FdMalHeat	FdAirHeat	FdOxyHeat
Heat Flow [kJ/s]	73.43	9101	3105
Name	MxOxyHeat	** New **	
Heat Flow [kJ/s]	228.4		

Material Streams | Compositions | **Energy Streams** | Unit Ops

Phthalic Column

Fluid Pkg: All

Include Sub-Flowsheets
 Show Name Only
 Horizontal Matrix
Number of Hidden Objects: 0

(c) Energy stream

Figure 3. HYSYS workbook of reactor-distillation simulation.

Connection (interface) between Aspen HYSYS and Matlab

The purpose of establishing a computerized connection between HYSYS and Matlab is to allow Matlab to programmatically execute HYSYS. This is called 'Automation' in Aspen HYSYS. Through automation, a particular objective in HYSYS as in a spreadsheet can be embedded in another object, and changes to values in the spreadsheet would automatically be updated in the embedded object. The HYSYS object is essentially like a container that holds a set of related functions and variables values. In HYSYS automation, the path to get to a specific property is referred to as the object hierarchy. For instance, the value of the fresh o-xylene feed stream flow rate can be located and modified by calling its object handle through the following code:

```
% open simulation case
HyApp = actxserver('Hysys.Application');
HyApp.visible = 1;
SimCase = hyApp.simulationCases;
RecSim = a.Open('C:\Program
Files\AspenTech\Models\RecDstSim.HSC');

% obtain stream object property
FeedStream = RecSim.Flowsheet.Streams.Item('O-
xylene').MassFlowValue
```

Figure 4. Object hierarchy in Aspen HYSYS automation.

Therefore, by changing the properties of HYSYS streams and operations following the object hierarchy, the optimization problem in Matlab can be connected and can interact with the engineering model in HYSYS. Using HYSYS automation, the engineering decision variables can be changed through the optimization problem in Matlab and connected with the business analysis model, as will be discussed next.

The Integrated Decision-Making Problem

Based on the HYSYS model for engineering and the Netlogo model for business, the engineering decision variables are considered as shown in Table 1. Note the target variables are also specified for the recycled streams in the engineering model.

Table 1. Engineering decision and target variables and descriptions in Aspen HYSYS

Variable	Description of decision variables
x_{B1}	Daily crude oil purchase (bbl/d)
x_{B2}	Percentage of crude oil sold to external market
x_{B3}	Percentage of finished product sent to inventory
x_{B4}	Percentage of finished product sent to external market
x_{B5}	Percentage of inventory storage released to external market
x_{E1}	Target mass flow rate of recycled o-xylend (kg/s)
x_{E2}	Target mass flow rate of recycled maleic anhydride (kg/s)
x_{E3}	Mass flow rate of feed air (kg/s)
x_{E4}	Temperature of cooled mixture (C)
x_{E5}	Pressure of colled mixture (kPa)
x_{E6}	Temperature of feed of anhydrides to phthalic column (C)
x_{E7}	Temperature of recycled steam of o-xylene (C)
x_{E8}	Distillation molar flow rate of phthalic column (kgmol/s)
x_{E9}	Phthalic column reflux ratio

Figure 5 shows the framework for optimizing business and engineering decisions. The integrated decision-making problem can be solved using an AA-MORO optimization approach, which was presented in the third quarterly report. Notice that the purpose of employing AA-MORO is to obtain multi-objective robust optimal decisions (i.e., optimum and relatively insensitive solutions) for both business and engineering domains under uncertainty, and to reduce computational cost by using approximation models for business and engineering simulations. In the integrated decision-making framework, the business objective is to maximize the profit over the planning horizon, and the engineering objective is to maximize purity of phthalic anhydride. The optimizer attempts to maximize the expected profit over a planning horizon of the oil refinery and at the same time maximize purity of phthalic anhydride.

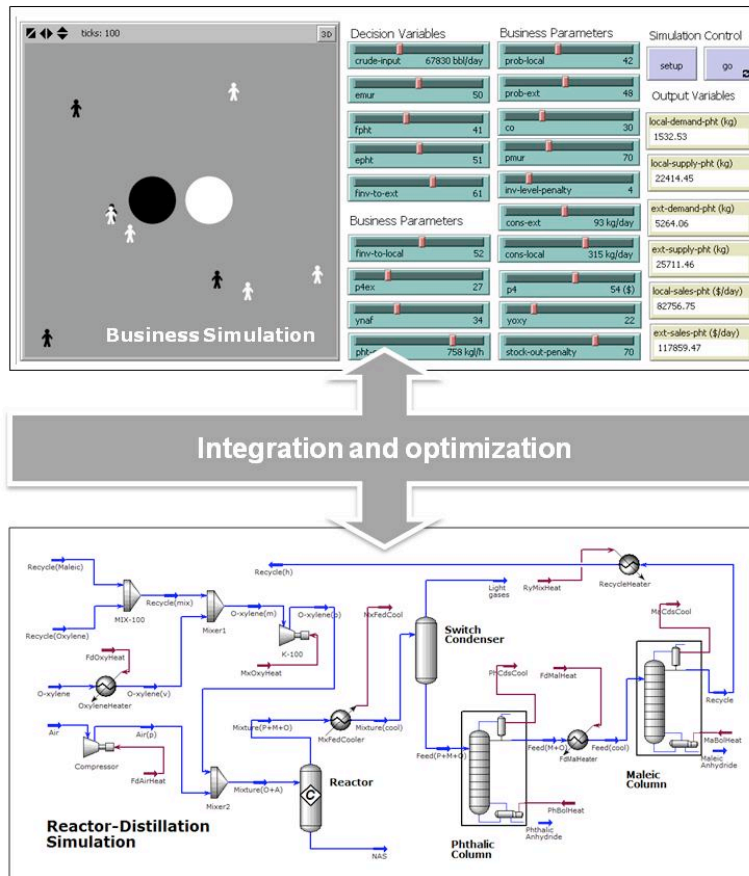


Figure 5. Integration and optimization of business and engineering decisions.

For the business objective, profit is calculated from the sales of phthalic anhydride minus material costs, inventory costs and engineering operating costs (including energy and labor costs). The purity of phthalic anhydride is obtained as a direct output from the engineering analysis model. All decision variables are defined in Table 1. The optimization should consider constraints on the equipment and inventory capability and the bounds on all decision variables. Market and engineering parameter uncertainties are also considered in the model. For instance, the price of phthalic anhydride is assumed to be within a $\pm 5\%$ interval and the pressure drop in the phthalic column is assumed to be within a $\pm 0.5\%$ interval. In order to obtain robust optimal decisions in the above problem, acceptable variation ranges for each objective need to be defined. We assume the acceptable range for each objective is between $\pm 5\%$ of the nominal objective value.

Optimization Result

The integrated business and engineering decision-making problem is solved using a deterministic optimization approach and AA-MORO. In the deterministic optimization approach, we assume all parameters are fixed (without any uncertainty). In AA-MORO, however, the parameters are allowed to vary in the corresponding intervals. The optimal solutions for both deterministic and robust optimization are shown in Figure 6. It can be seen that robust optimal solutions are slightly inferior to the deterministic ones from a multi-objective optimization perspective. This intuitively makes sense since the decision-maker is willing to sacrifice business and engineering performance in exchange for the robustness (i.e., cushion for uncertainty).

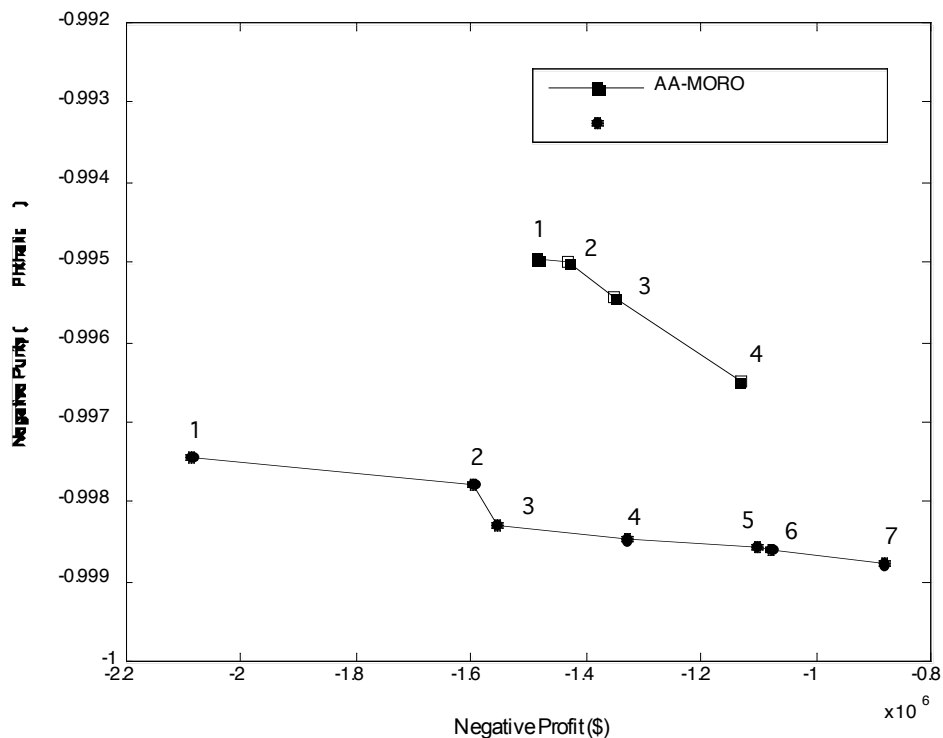


Figure 6. Optimal Pareto solution from the integrated optimization in the case study.

Table 2. Optimal decision variables for deterministic and robust optimization

		X _{E1}	X _{E2}	X _{E3}	X _{E4}	X _{E5}	X _{E6}	X _{E7}	X _{E8}	X _{E9}	X _{B1}	X _{B2}	X _{B3}	X _{B4}	X _{B5}
Deterministic	①	0.086	0.051	25.30	75.20	103.38	90.71	309.52	0.00257	1.36	97161	58.21	0.37	50.29	50.75
	②	0.086	0.052	25.20	75.20	103.21	90.49	309.99	0.00257	1.28	97127	58.38	0.49	50.18	50.75
	③	0.086	0.051	25.41	75.22	101.49	90.45	307.87	0.00258	1.43	93962	56.35	0.53	50.37	50.66
	④	0.086	0.052	25.20	75.20	102.45	90.73	309.26	0.00257	1.55	97099	58.35	0.27	50.29	50.61
	⑤	0.087	0.051	25.32	75.21	102.30	90.66	307.66	0.00256	1.52	96197	57.85	0.38	50.25	50.62
	⑥	0.086	0.051	25.63	75.20	102.09	90.42	313.04	0.00260	1.90	92677	55.48	0.55	50.39	51.34
	⑦	0.086	0.052	26.09	75.19	102.23	90.42	312.38	0.00259	1.79	92911	55.40	0.55	50.35	50.87
AA-MORO	①	0.086	0.053	24.57	75.19	102.31	90.42	302.43	0.00257	0.91	95699	57.91	0.78	0.43	76.45
	②	0.085	0.053	25.42	75.21	102.49	90.48	306.96	0.00256	0.69	94952	56.78	0.87	0.68	69.86
	③	0.084	0.053	25.44	75.21	102.40	90.55	307.29	0.00256	0.72	94650	56.72	1.04	0.61	65.48
	④	0.085	0.054	25.51	75.20	102.13	90.52	311.62	0.00256	0.74	95454	57.03	1.05	0.67	67.86

The optimal decision variables for each point shown in Figure 6 are given in Table 2. Among the engineering decisions (column 1 to column 9), the temperature of recycled stream (x_{E7}) and the reflux ratio in the phthalic column (x_{E9}) are more critical than the others in affecting the objective

functions. The critical business decision variables include the daily crude oil purchase (x_{B1}) and the percentage of finished product sent to inventory (x_{B3}). These observations match our intuition; however, additional test and experimental data are required to validate these preliminary observations. The other engineering and business decision variables, although having some impact on the objectives, seem insignificant in changing the optimal objective values. Among the two objectives, the purity of phthalic anhydride is less sensitive to the decision values than the other objective.

4. Difficulties Encountered/Overcome

In this quarter, we have been focusing on remodeling the engineering process in Aspen HYSYS, which is a process simulation software widely used in the chemical industry. Aspen HYSYS provides many well-developed modules suitable for simulating various chemical processes and situations. However, achieving convergence on the material and energy streams and equipment operations is a delicate task. Moreover, it is difficult to identify the ranges for the selected decision variables in HYSYS since a randomly selected input value could generate erroneous output, preventing the model from converging. Another challenge was in connecting Aspen HYSYS with the optimization program in Matlab with limited references from the existing literature. At the time this quarterly report was completed, a preliminary HYSYS model for the reactor-distillation process had been developed and connected with the Matlab program. However, additional tests and work are required to verify the simulation model, possibly with experimental data from the previous literature.

The integrated business and engineering decision-making problem has been formulated both as a single-disciplinary multi-objective optimization problem, and a multi-disciplinary multi-objective optimization problem. For the single-disciplinary case, the AA-MORO approach can be used to optimize the decision variables. The AA-MORO optimization has completed, and we have reported the robust optimal decisions in this report based on the AA-MORO approach. The multi-disciplinary formulation of the problem can be solved using the AA-McRO approach that was proposed in the last quarterly report. The work on the AA-McRO is still ongoing, and we are planning to report additional results in the next quarterly report.

5. Planned Project Activities for the Next Quarter

- Verify the preliminary engineering simulation model in Aspen HYSYS with additional test case studies.
- Solve the integrated business and engineering decision-making problem using the AA-McRO approach, and compare the AA-McRO solution with the AA-MORO solutions.
- Modify the business analysis model and develop an agent-based approach using Matlab.
- Expand the engineering model and include other processes in the refinery model.
- Continue refining the user interface in the proposed dashboard.

Appendix

Justification and Background

Many oil, gas and petrochemical systems involve numerous coupled subsystems. These systems and their subsystems usually have uncertain inputs and thus it can be difficult to make the “best” engineering and business decisions in terms of independent operations of these complex systems. It becomes even more difficult to make those decisions when the system consists of many units or plants producing different products. This difficulty presents an opportunity taken on in this project; a review of mainstream literature has revealed that previous models in management of petrochemical systems have been in majority based on either engineering or business decisions but not both. There is a significant gap in the literature as to how these two types of decisions should be devised and integrated. To address this important gap, the focus of this investigation is to develop an integrated robust decision support framework considering both engineering and business models under uncertain conditions. Our overall objective has several underlying research issues or objectives, including: (i) how to develop business models that include management decisions in a multi-unit organization and at the same time account for engineering aspects; (ii) how to determine the relative importance and effects of uncertain system and/or subsystem input parameters on subsystem and/or system outputs (e.g., system performance); (iii) defining a set of metrics, a dashboard, that will serve as a visualization tool to keep track of the company’s financial status and provide for easy communication between various levels in the company, and (iii) how to extend our current single-level robust optimization method to multi-subsystem problems and maintain reasonable computational complexity for the method. These underlying objectives will be organized into tasks throughout the time frame allocated to the project. The details of the tasks are explained in the next section.

Approach

There are two main tasks in this investigation as detailed in the following.

Task 1 (PI):

Develop and implement engineering analysis models, in a Matlab (or Matlab compatible) environment, for a crude distillation unit case study model.

Task 1.1: Develop a multi-input multi-output analysis model for a representative petrochemical system with corresponding subsystem analysis models.

Task 1.2: Extend the analysis model in Task 1.1 to include: (i) additional complexity, (ii) subsystem details and uncertainty to include reasonable representation of engineering side of a plant. The ultimate goal is to develop an integrated multi-subsystem petrochemical analysis model for a plant or a group of units in a plant.

Task 2 (UMD):

Develop and implement a Robust Decision Support System (RDSS).

Engineering Tasks

Task 2.1: Develop a single level (all-at-once) approximation-assisted robust optimization technique that is able to significantly reduce the computational efforts of making robust decisions.

Task 2.2: Demonstrate an application of the approach from Task 2.1 with a case study in petrochemical systems which will be developed by PI as a part of Task 1.

Task 2.3: Develop an approximation assisted multi-objective multi-disciplinary robust optimization approach, which is an extension to Task 2.1.

Task 2.4: Demonstrate an application of the approach from Task 2.3 with a case study in petrochemical systems which will be developed by PI as part of Task 1.

Business Tasks

- Task 2.5: Develop business models in Netlogo and solve a simplified refinery supply chain optimization problem with Matlab.
- Task 2.6: Develop a Dashboard and test the robustness and sensitivity of the Dashboard's elements for the model in Task 2.5.

Integration Tasks

- Task 2.7: Inspect engineering and business problems to determine coupling variables between two problems.
- Task 2.8: Integrate Tasks 2.1 to 2.4 with Tasks 2.5 to 2.6 to formulate a refinery optimization problem that considers both engineering and business objectives and constraints.
- Task 2.9: make the supply chain management problem more realistic by considering more decision levels, more finished products and a wider market, and by increasing the size of the refinery's internal network and then repeat Task 2.8.
- Task 2.10: Verify and validate the integrated model.

References

- [1] Aspen HYSYS, <http://www.aspentech.com>, Aspen Technology (2009).
- [2] Douglas, J.M., 1988, "Conceptual Design of Chemical Processes", McGraw-Hill, New York, USA.
- [3] Forbes, R.J., 1948, "Short History of the Art of Distillation", Brill, Leiden, Holland.
- [4] Gargeya, V., 2005, "Plant Level Performance Measurement: An Exploratory Case Study of a Pharmaceutical Encapsulation Company", *Technovation*, 25(12), 1457-1467.
- [5] Gattu, G., Palavajhala, S., and Robertson, D. 2003, "Are Oil Refineries Ready for Non-Linear Control and Optimization?" International Symposium on Process Systems Engineering and Control, Mumbai, India.
- [6] Grossmann, I. E., 2005, "Enterprise-Wide Optimization: A New Frontier in Process Systems Engineering," *AIChE Journal*, 51(7), p. 1846-1857.
- [7] Halemane K. P., Grossmann I. E., 1983, "Optimal Process Design under Uncertainty," *AIChE Journal*, 29(3), 425-433.
- [8] Jackson, J., Hofmann, J., Wassick, J. and Grossmann, I., 2003, "A nonlinear multi-period process optimization model for production planning in multi-plant facilities", *Proceedings FOCAPO2003*, 281-284..
- [9] Janak, L., Lin, X. and Floudas, C. A., 2007, "A New Robust Optimization Approach for Scheduling Under Uncertainty: II. Uncertainty with Known Probability Distribution," *Computers and Chemical Engineering*, 31(3), 171-195.
- [10] Kaplan, R. and Norton, D., 1996, "Using the Balanced Scorecard As a Strategic Management System", *Harvard Business Review*, 74(1), 75-85.
- [11] Kleijnen, J. and Smits, M., 2003, "Performance metrics in supply chain management". *Journal of the Operational Research Society*, 54(5), 507-514.
- [12] Kroo, I., and Manning, V., 2000, "Collaborative Optimization: Status and Directions," *Proceedings of the 8th AIAA/NASA/ISSMO Symposium on Multidisciplinary Analysis and Optimization*, Long Beach, CA, pp. AIAA 2000-4721.
- [13] Lin, X., Janak, S. L. and Floudas, C. A., 2004, "A New Robust Optimization Approach for Scheduling Under Uncertainty: I. Bounded Uncertainty," *Computers and Chemical Engineering*, 28(6-7), 1069-1085.
- [14] Li, M., Azarm, S., and Boyars, A., 2006, "A New Deterministic Approach Using Sensitivity Region Measures for Multi-Objective Robust and Feasibility Robust Design Optimization,"

- Journal of Mechanical Design, 128(4), pp. 874-883.
- [15] Li, M., and Azarm, S., 2008, "Multiobjective Collaborative Robust Optimization with Interval Uncertainty and Interdisciplinary Uncertainty Propagation," *Journal of Mechanical Design*, 130(8), pp. 081402-11.
 - [16] Micheletto, S. R., Carvalho, M. C. A. and Pinto, J. M., 2008, "Operational Optimization of the Utility System of an Oil Refinery," *Computers and Chemical Engineering*, 32(1-2), 170-185.
 - [17] Netlogo, <http://ccl.northwestern.edu/netlogo/>
 - [18] Pinto, J., Joly, M. and Moro, L., 2000, "Planning and scheduling models for refinery operations", *Computers and Chemical Engineering*, 24(9), 2259–2276.
 - [19] Sahdev, M., Jain, K., Srivastava, P., "Petroleum Refinery Planning and optimization Using Linear Programming", *The Chemical Engineers' Resource Page*, http://www.cheresources.com/refinery_planning_optimization.shtml
 - [20] Simpson, T. W., and Mistree, F., 2001, "Kriging Models for Global Approximation in Simulation-Based Multidisciplinary Design Optimization," *AIAA Journal*, 39(12), pp. 2233-2241.
 - [21] Suresh, S. Pitty, Li, W., Adhitya, A., Srinivasan, R., Karimi, A., 2008, "Decision support for integrated refinery supply chains", *Computer and Chemical Engineering*, 32, 2767–2786.
 - [22] Hu, W., M. Li, S. Azarm, S. Al Hashimi, A. Almansoori, and N. Al Qasas, "On Improving Multi-Objective Robust Optimization Under Interval Uncertainty Using Worst Possible Point Constraint Cuts," *CD-ROM Proceedings of the ASME 2009 International Design Engineering Technical Conferences*, Aug. 30 – Sep. 2, 2009, San Diego, CA, USA.

Dynamics and Control of Drill Strings

UMD Investigator: Balakumar Balachandran
PI Investigators: Hamad Karki and Youssef Abdelmagid
GRA: Chien-Min Liao (started in Spring 2007)
Start Date: Oct 2006

1. Objective/Abstract

Drill-string dynamics need to be better understood to understand drill-string failures and to control drill-string motions and steer them to their appropriate locations in oil wells. Although a considerable amount of work has been carried out on understanding drill-string vibrations (for example, Leine and van Campen, 2002; Melakhessou *et al.*, 2003; Spanos *et al.*, 2003; Liao *et al.*, 2009), the nonlinear dynamics of this system are only partially understood given that the drill string can undergo axial, torsional, and lateral vibrations, and that operational difficulties include sticking, buckling, and fatiguing of strings. In addition, the prior models focus on either bending or torsional or axial motions. Hence, it is important to consider coupled axial-bending-torsional vibrations and contact instability in oil and gas well drilling. A better understanding of these vibrations can help keep the drill string close to the center of the borehole and help realize near-circular bores during drilling operations.

The overall goal of the proposed research is to understand the nonlinear dynamics of the drill string and to develop a control-theoretic framework for its stabilization, enabling energy-efficient drilling with longer equipment life spans. Specific research objectives of this project are the following: i) building on Phase I efforts, develop and study control-oriented models for the drill strings through analytical and numerical means, ii) investigate the control of an under-actuated nonlinear system (drill string) with complex interactions with the environment, and iii) use the drill-string test-beds constructed at the Petroleum Institute (PI) & the University of Maryland (UMD) to validate the analytical findings and suggest possible strategies to mitigate drill-string failures in fixed and floating platform environments.

2. Summary of Results for the Completed Quarter

In drilling operations, often, the drill-string trajectories are examined in the plane, to better understand the nature of the dynamics. With this in mind, parametric studies were conducted and rotor-motion trajectories were examined through experimental investigations and numerical investigations with a reduced-order model. Such studies can help generate systematic information for enhancement of drilling operations. For instance, by observing qualitative changes that occur in certain parameter windows, appropriate operation parameter windows can be established. The results of the present work suggest that there may be benefits in operating at low rotation speeds in cases with high friction and that in cases where the drill string has a curved configuration, the rotation speeds need to be carefully chosen to avoid bumping motions.

The rest of this section is organized as follows. In Section 2.1, experimental results are presented and discussed. Following that, in Section 2.2, the numerical results generated by integrating the reduced-order model are presented and compared with experimental results. In Section 2.3, a discussion is included.

2.1 Experimental Studies

In the experiments, the arrangement described in the previous reports was used and qualitative changes were studied with respect to the following three system parameters: i) rotation speed of

drive motor, ii) magnitude of unbalanced mass attached to the disc, and iii) friction coefficient between the outer shell and the disk at the bottom of the drill string.

2.1.1 Experimental Arrangement

For these studies, the arrangement shown in Figure 1 was used. A string with a bottom disc is driven by a motor with a constant rotating speed, which ranges from 40 rpm (revolutions per minute) to 190 rpm. The motor speed is controlled with a DC voltage input. The relationship between the voltage input and the rotation speed is shown in Figure 2. (In a field drilling operation, the rotation speed is generally lower than 300 rpm.) Five different levels of unbalanced masses were used, and the corresponding masses were 0.0 grams, 28.1 grams, 48.1 grams, 61.7 grams, and 87.1 grams. As the unbalanced mass increased, the curvature of the drill string was enhanced; that is, with no unbalanced mass attached to the bottom disc, the rotating string was close to a straight drilling configuration. During a drilling operation, as the drill goes through different layers of rock, there is a change in the contact friction coefficient. To better understand the influence of the friction coefficient on the system dynamics, three different levels of friction coefficient were considered.

Motion images, which were captured through a video camera, were used to monitor the system response in these experiments. Rotor trajectories were constructed by analyzing each video frame, through an image processing procedure. The capture rate from the high-speed camera used was 110 FPS (frame per second), which is sufficient for capturing the response excited by a range of rotation speeds ranging to a maximum rotating speed of 190 rpm. An example of a typical image of the rotor as seen from the camera is shown on the right-hand side of Figure 1. The rotor motions can be clearly seen as one goes from Figure 1 (a) to Figure 1 (b); the rotor is at a 3 o'clock position within the shell region in (a) and at a 12 o'clock position in (b).

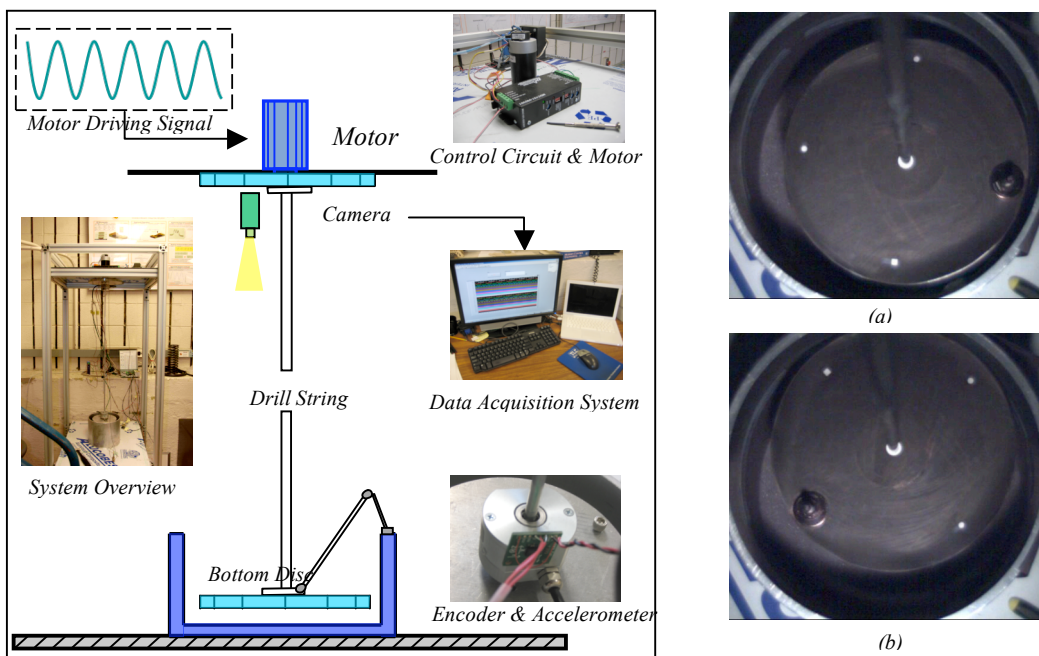


Figure 1. Experimental setup and procedure.

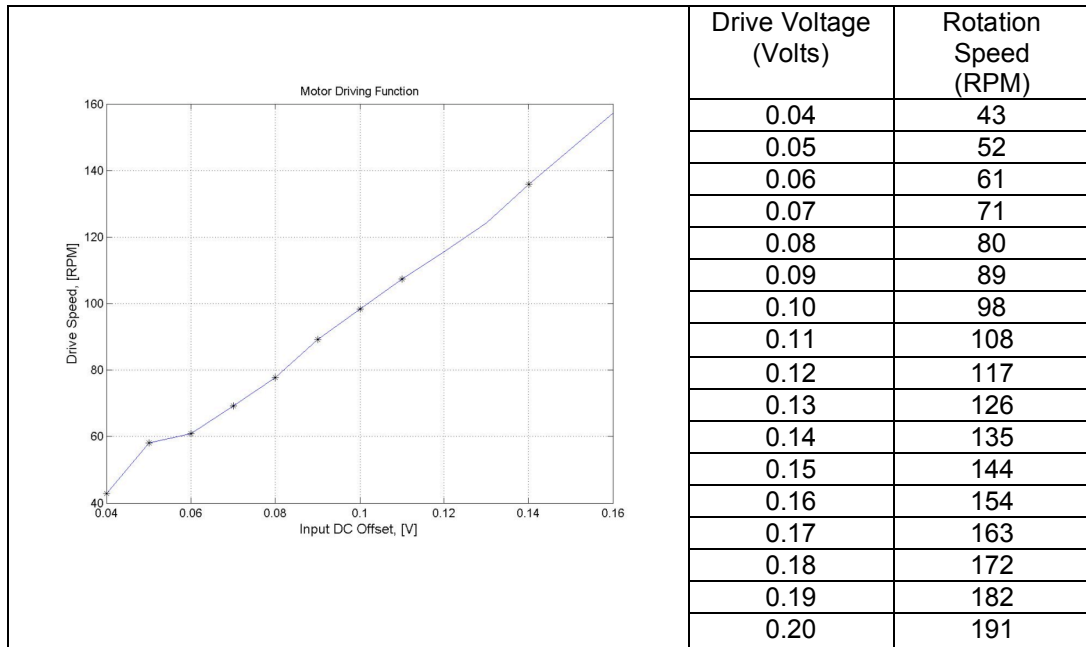
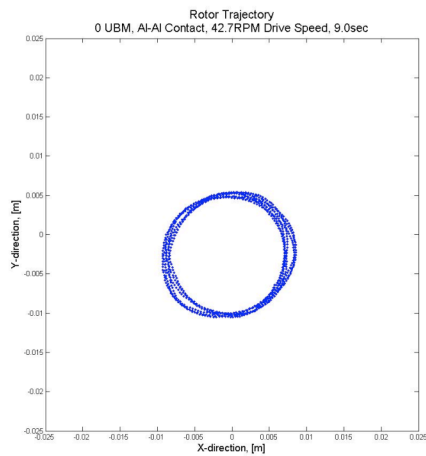


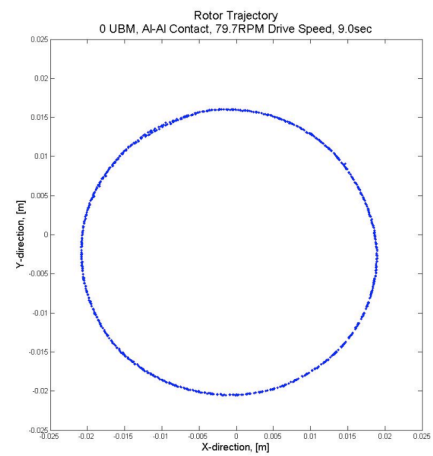
Figure 2. Drive speed versus motor input.

2.1.2 Experimental Results

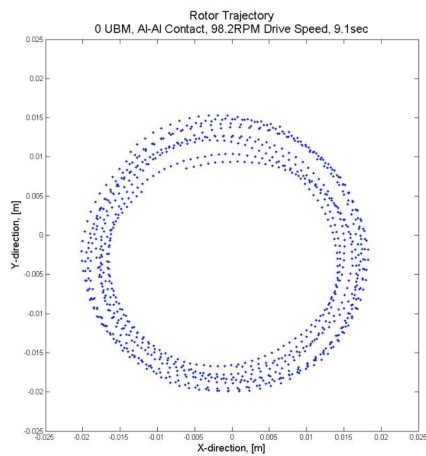
The rotor trajectory results generated for the case with no unbalanced mass and different levels of friction coefficient are shown in Figure 3 to Figure 5. In Figure 3, the results are shown for a case when an aluminum rotor can make contact with an aluminum shell. The Al-Al (aluminum-aluminum) contact case is the case with the lowest friction coefficient compared to the cases with aluminum-rubber and rubber-rubber contacts. For the lowest rotation speed of 42.7 rpm shown in Figure 3 (a), the rotor stays in the shell center without making any contact with the outer shell. The rotor trajectory is nearly circular. (Due to the screen resolution, the trajectory appears to be elliptical.) With increasing rotation speed, the rotor travels from the center to the edge of shell while rotating around it as shown in Figure 3 (b). When the rotation speed reaches 98.2 rpm, as shown in Figure 3 (c), the rotor loses contact with the shell edge and only makes light contact. This is because the shell surface cannot offer sufficient friction force to support rotor travel around it. At the fastest speed of 135 rpm, for which the results are shown in Figure 3 (d), the rotor moves from one contact point to another in a bumping motion.



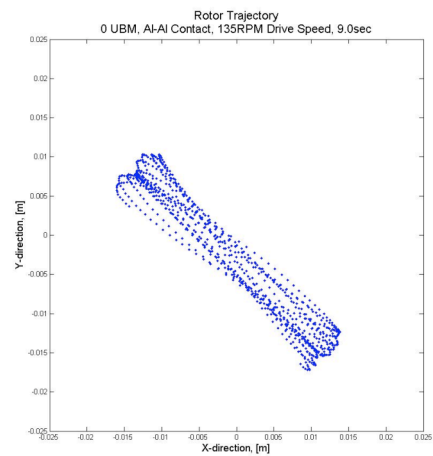
(a)



(b)



(c)



(d)

Figure 3. Rotor trajectories of aluminum rotor with aluminum shell: (a) rotation speed of 42.7 rpm, (b) rotation speed of 79.7 rpm, (c) rotation speed of 98.2 rpm, and (d) rotation speed of 135.0 rpm.

Rotor trajectories of a rubber-covered rotor that can make contact with an aluminum shell surface are shown in Figure 4. For the lowest rotation speed case, the results for which are shown in Figure 4 (a), the rotor stays in the center of shell region with no contact. When the rotation speed increases to 79.7 rpm, the results for which are shown in Figure 4 (b), the rotor rotates on the shell surface and there is also some sliding, which helps the rotor move away from the shell surface. This movement is close to what was observed in Figure 3 (c). As seen in Figure 4 (c), increasing the rotation speed to 98.2 rpm causes the rotor to move from point to point with almost no rotational motions; this behavior is close to that seen in Figure 3 (d). For the high-speed case shown in Figure 4 (d), the rotor shows sticking and sliding, which leads to an elliptical trajectory. Compared to the low friction force case, in this case, the high friction force can help keep the rotor on the surface of shell when contact occurs.

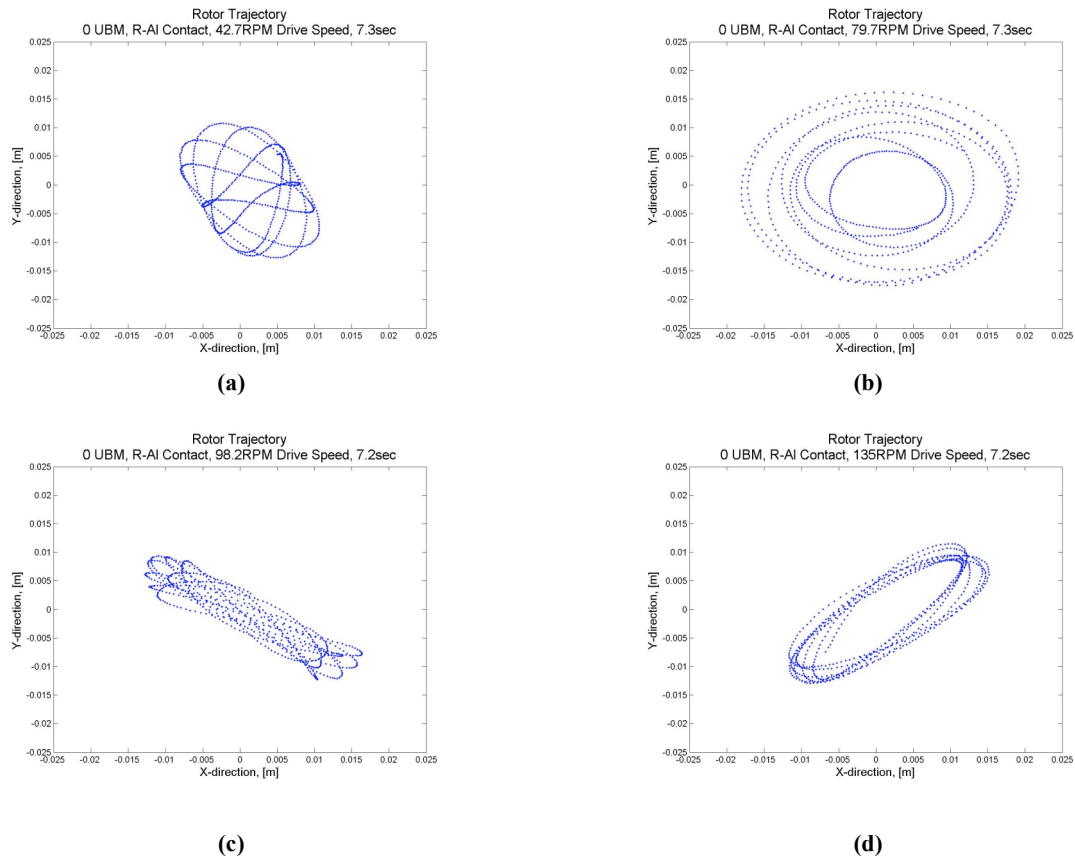


Figure 4. Rotor trajectories of rubber-covered rotor with aluminum shell: (a) rotation speed of 42.7 rpm, (b) rotating speed of 79.7 rpm, (c) rotation speed of 98.2 rpm, and (d) rotation speed of 135.0 rpm.

The results obtained for the case with highest friction coefficient, where the rubber-covered rotor can make contact with the rubber-covered shell surface are shown in Figure 5. It is no surprise that the rotor stays in the center for the low-speed case shown in Figure 5 (a), as seen previously in companion experiments. In Figure 5 (b) corresponding to the 79.7 rpm case, the rotor is seen to travel around the inner edge of the shell with some bumping. When the rotation speed is increased to 98.2 rpm, as seen in Figure 5 (c), the rotor stays within the center again.

By comparing the results for the cases with different RPM values and friction values, a few conclusions can be drawn. The rotor stays in the center of the borehole for low driving speeds, and has a high likelihood of moving towards the outer shell with increase in rotation speed. For high levels of friction, once the rotor makes contact with the shell, it is more likely to stick to the shell. This type of contact is undesirable as it can cause damage to the drill string as well as to the borehole wall. Therefore, one suggestion is to operate the drill string at a low rotation speed in high-friction environments.

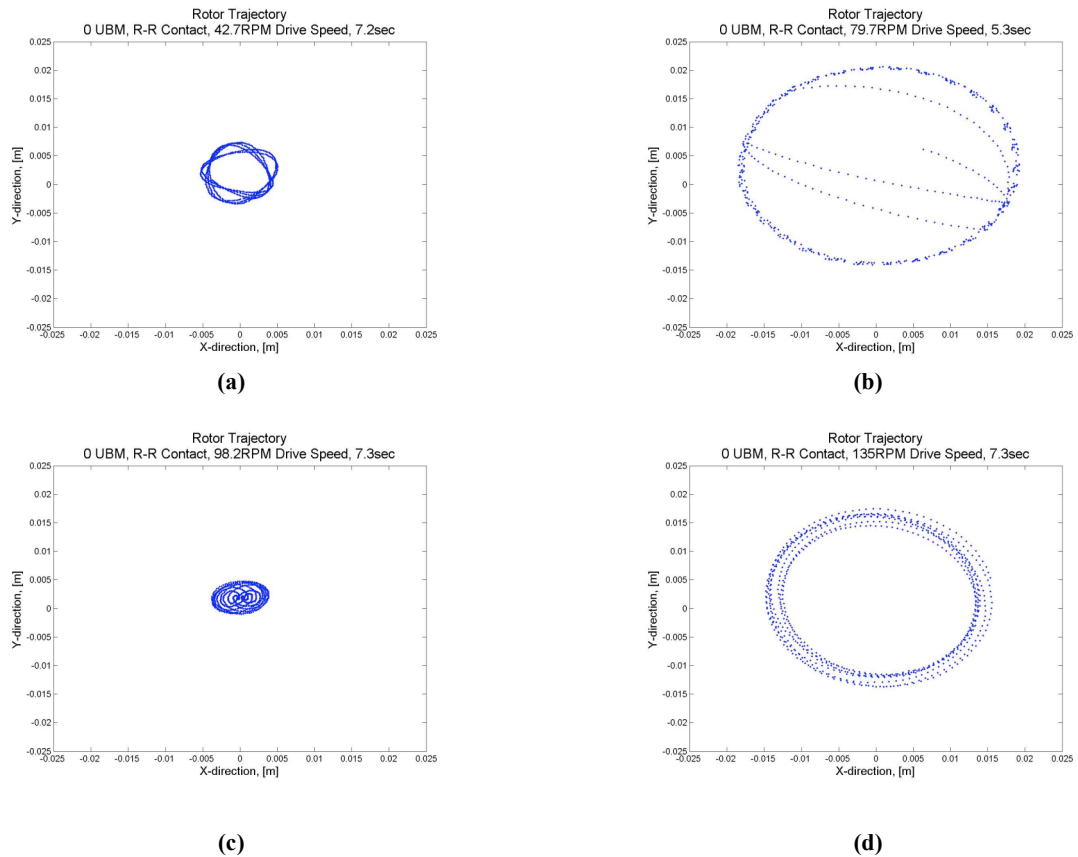


Figure 5. Rotor trajectories of rubber-covered rotor with rubber-covered shell surface: (a) rotation speed of 42.7 rpm, (b) rotation speed of 79.7 rpm, (c) rotation speed of 98.2 rpm, and (d) rotation speed of 135.0 rpm.

2.2 Numerical Investigations

In this section, the results obtained through numerical investigations are discussed and compared with experimental results. In addition, in Section 2.2.2, simulations conducted to understand the influence of the unbalanced mass are presented.

2.2.1 Numerical Results and Comparisons with Experimental Data

The numerical results were generated for the considered experimental system, and the results have been presented to understand the qualitative changes experienced by the system as a control parameter such as the rotation speed is quasi-statically varied. The radial displacement response, which is a measure of how far the drill string is from the center of the borehole, is sampled at a frequency corresponding to the drive speed, and the discrete samplings are displayed versus the rotation speed in Figure 6. If the motion is periodic at the driving frequency, a finite number of discrete points can be expected, and for aperiodic motions, an infinite number of such points are expected. Diagrams such as Figure 6 are also commonly referred to as bifurcation diagrams on a Poincaré section. In Figure 6, for a certain rotation frequency, contact occurs when the radial displacement reaches the value of 0.0195 meters.

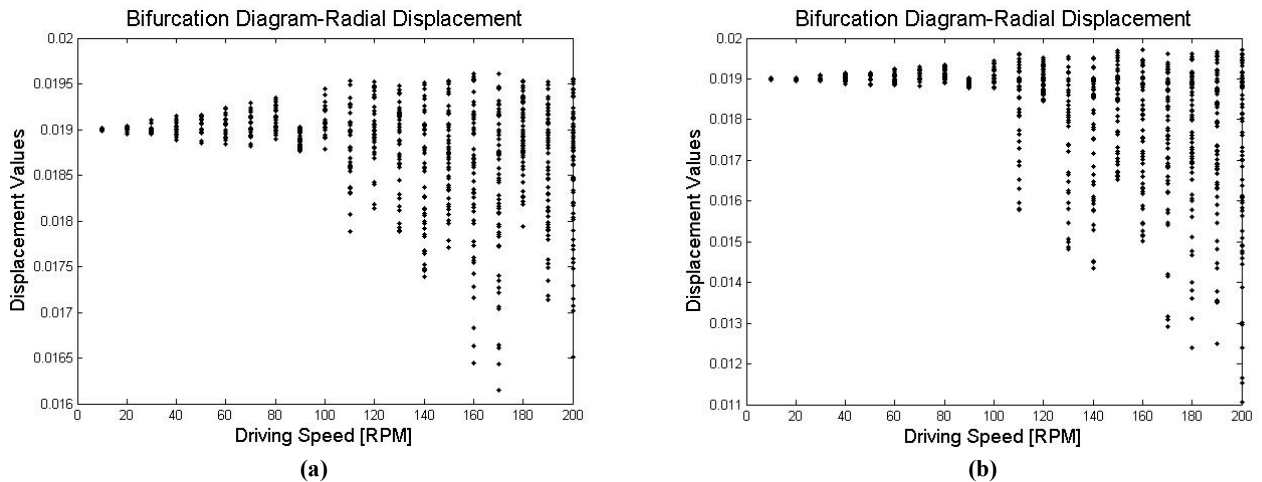


Figure 6. Bifurcation diagram of rotor radial response: (a) low level of friction and (b) moderate level of friction.

In Figure 6 (a), the qualitative changes are shown for an unbalanced mass of 10 grams and friction coefficient of 0.1. The rotor exhibits periodic motions at the low speed of 10 rpm. With increase of rotation speed to 80 rpm, there is an aperiodic motion which can be attributed to light bumping between the rotor and the shell; this bumping motion is reflected by the range of the dotted line on the y axis of the diagram. In Figure 6 (b), the results are presented for the same level of unbalanced mass as before, but for the increased friction value of 0.3. When the results are compared, it is seen that aperiodic motions occur over a broader span of rotation speeds with increase in friction.

2.2.2 Numerical Studies for Different Unbalanced Mass

In this section, results of numerical studies conducted to examine the influence of unbalanced mass are shown. In Figure 7 (a), the results are shown for a case with low friction and a moderate level of unbalanced mass (30 grams). Compared to the results shown for the 10 gram unbalanced mass case in Figure 6 (a), the rotor exhibits large movements. For the low friction coefficient case, the rotor starts to travel across the shell region at 100 rpm. By contrast, with the increase of the unbalance mass, the rotor stays close to the shell for a large range of rotation speeds. Results obtained for different friction values are shown in Figure 7.

These results help us understand the transition from periodic motions to aperiodic motions with respect to different levels of unbalanced mass, rotation speeds, and friction levels.

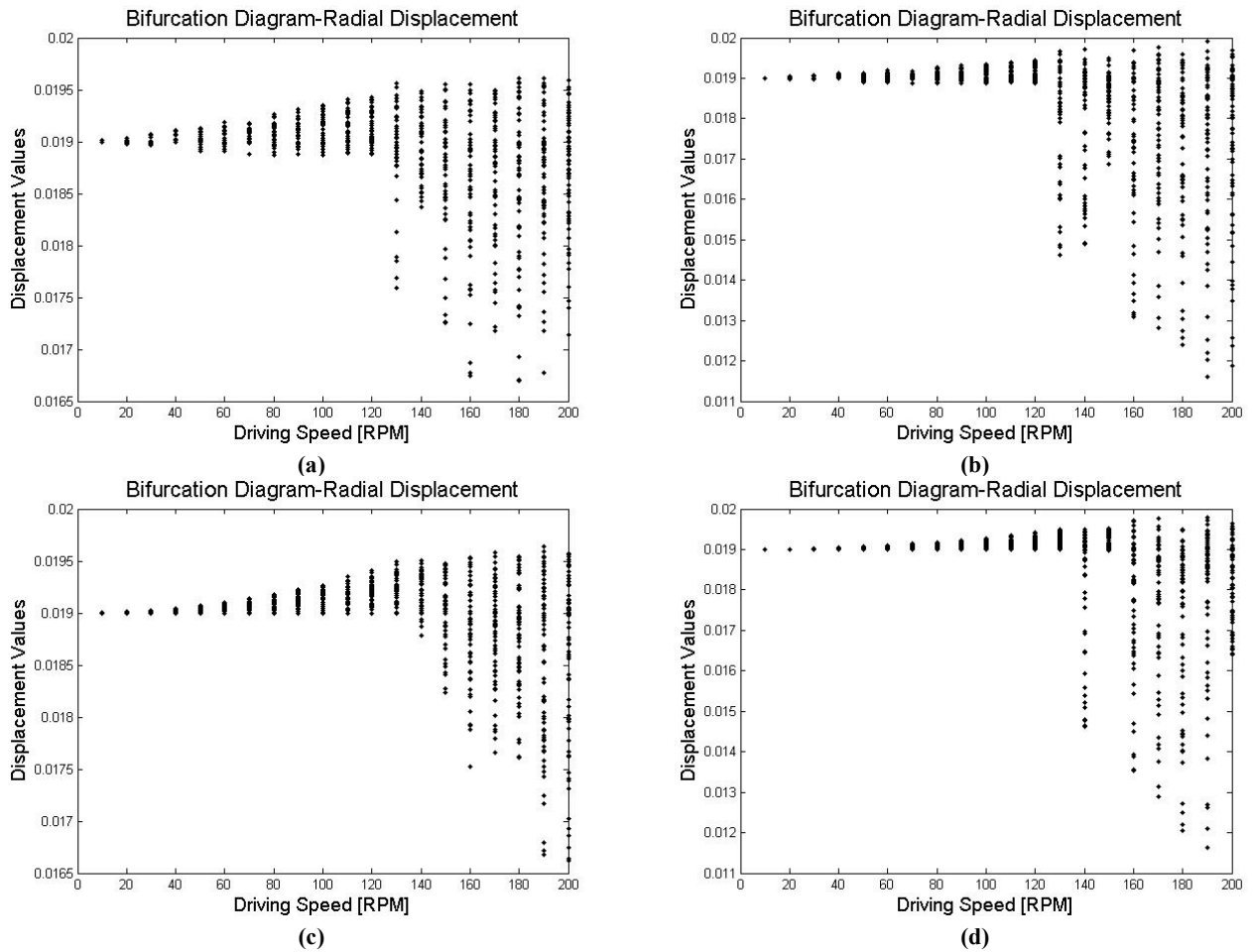


Figure 7. Bifurcation diagram of rotor for different levels of unbalanced mass and different levels of friction: (a) moderate level of unbalanced mass and low friction, (b) moderate level of unbalanced mass and moderate friction, (c) high level of unbalanced mass and low friction, and (d) high level of unbalanced mass and moderate friction.

2.3 Discussion and Future Work

Parametric studies of drill-string dynamics were conducted using experimental and numerical means, and the influence of different parameters such as the unbalanced mass, friction coefficient, and rotation speed on the system dynamics has been illustrated. The numerical results and experimental results show agreement, and one inference that can be drawn is the following. In high friction environments, it may be preferable to operate the system at low rotation speeds to avoid contact with the borehole and consequent undesirable dynamics.

The parametric studies are to be completed this fall, and the results are to be included in a journal manuscript. Further modeling and numerical studies will be pursued along with experiments.

3. Collaborations and Interactions

This summer, two PI junior students (Mr. Ghadayer Ali Al-Kaabi and Mr. Omar Abdulla Al-Suwaidi) visited the UMD to pursue summer internships from July 3 to August 15. They have

worked on the drill-string experiments, conducted data analyses, and helped with the construction of the horizontal drill-string arrangement.

Discussions also took place between Professor Balachandran and Mr. Walt Aldred of Schlumberger, UK in July 2010 in an IUTAM meeting in Aberdeen, Scotland to compare drill-string experimental data collected from field experiments with the data collected at UMD. The comparisons show that the laboratory experiments capture similar bumping, rolling, and sliding motions as seen in the field, and these comparisons strongly support the line of work being pursued by UMD and PI.

Appendix

Approach

A combined analytical, numerical, and experimental approach is being pursued at the University of Maryland and the Petroleum Institute. Specifically, the drill string is being modeled as a reduced-order nonlinear dynamical system. Appropriate attention is also to be paid to the interactions with the environment. The experiments at UMD and PI are tailored to address specific aspects of the drill-string dynamics as well as complement each other. Actuator and sensor choices are also to be explored to determine how best to control the system dynamics, in particular, through the control rpm. The studies will be initiated with drill strings located on fixed platforms, and later extended to systems located on floating platforms.

Three-Year Schedule

Phase II:

January 1, 2009 to December 31, 2009: Carry out quantitative comparisons between experimental results and predictions of reduced-order models for open-loop studies; understand stick-slip interactions and explore continuum mechanics based drill-string models for fixed platform environments; examine different configurations including horizontal drilling

January 1, 2010 to December 31, 2010: Construct control schemes; carry out experimental, analytical, and numerical studies; and identify appropriate schemes; study horizontal drilling configurations through experiments and analysis

January 1, 2011 to December 31, 2011: Continue horizontal drilling studies; carry out experiments, analysis, and numerical efforts and also examine drill-string operations in off-shore environments

January 1, 2012 to May 1, 2012: Compile results obtained for drill-string operations in vertical and horizontal configurations and provide guidelines for enhancing operations.

Key References

- [1] Akgun, F. 2004, "A Finite Element Model for Analyzing Horizontal Well BHA Behavior," *J. of Petrol. Sci & Eng.*, Vol. 42, pp. 121-132.
- [2] Bednarz, S., 2004, "Design and Exploitation Problems of Drill Strings in Directional Drilling," *Acta Montanistica Slovaca*, Vol. 9, pp. 152-155.
- [3] Downtown, G., 2009, "New Directions in Rotary Steerable Drilling", *Oilfield Review*, pp. 18-29.
- [4] Leine, R. I., van Campen, D. H., and Keultjes, W. J. G. (2002). "Stick-Slip Whirl Interaction in Drill String Dynamics," *ASME Journal of Vibration and Acoustics*, Vol. 124 (2), pp. 209-220.
- [5] Liao, C.-M., Balachandran, B., and Karkoub, M., (2009). "Drill-String Dynamics: Reduced Order Models," To appear in *Proceedings of ASME IMECE 2009*, Nov. 13-19 Lake Buena Vista, FL, USA, 2009; Paper No. IMECE2009-10339.
- [6] Melakhessou, H., Berlioz, A., and Ferraris, G. (2003). "A Nonlinear Well-Drillstring Interaction Model," *ASME Journal of Vibration and Acoustics*, Vol. 125, pp. 46-52.

- [7] Mihajlović, N., van Veggel, A. A., van de Wouw, N., and Nijmeijer, H. (2004) "Analysis of Friction-Induced Limit Cycling in an Experimental Drill-String System," *ASME Journal of Dynamic Systems, Measurement, and Control*, Vol. 126(4), pp. 709-720.
- [8] Mihajlović, N., van de Wouw, N., Rosielle, P.C.J.N., and Nijmeijer, H. (2007) "Interaction between torsional and lateral vibrations in flexible rotor systems with discontinuous friction," *Nonlinear Dynamics*, Vol. 50, pp. 679-699.
- [9] Nayfeh, A. H. and Balachandran, B. (1995). *Applied Nonlinear Dynamics: Analytical, Computational, and Experimental Methods*, Wiley, New York.
- [10] Spanos, P. D., Chevallier, A. M., Politis, N. P., and Payne, M. L. (2003). "Oil and Gas Well Drilling: A Vibrations Perspective," *Shock and Vibration Digest* Vol. 35(2), pp. 85-103.
- [11] Short, J. A. "Introduction to Directional and Horizontal Drilling " Pennwell Pub, 1993.
- [12] Singh, S.P. and Balachandran B. (2009). "Rolling Rub Translations of a Flexibility Connected Disk," pre-print.

Studies on Mobile Sensor Platforms

UMD Investigators: Balakumar Balachandran, Nikil Chopra

GRAs: Rubyca Jaai

PI Investigator: Hamad Karki, Sai Cheong Fok

GRAs: Hesham Ishmail (ADNOC Fellow)

Start Date: April 2009

1. Objective/Abstract

Mobile sensor platforms can be employed in a variety of operations including environmental and structural health monitoring operations in harsh and remote environments. In the proposed work, cooperating sensor platforms are to be studied for potential use in oil storage tanks, which are periodically tested for corrosion, cracks, and leaks. These platforms are envisioned for estimating geometrical profile parameters, such as, the tank bottom thickness. To this end, simultaneous localization and mapping (SLAM) algorithms (also known in the literature as concurrent mapping and localization [CML] algorithms) for cooperating sensor platforms operating in harsh environments are being investigated. While many solutions have been suggested for the single-agent SLAM problem, multiple-agent SLAM is still a difficult problem from an analytical and practical perspective. The use of multiple agents allows for greater and faster coverage in the exploration and searching tasks and provides a certain degree of redundancy in the completion of tasks. Additionally, map merging using overlapping information from different agents can possibly compensate for sensor uncertainty (Dudek *et al.*, 1996).

The overall objective of this project will be to carry out a combined analytical, numerical, and experimental effort to develop mobile sensor platforms and appropriate simultaneous localization and mapping (SLAM) algorithms for cooperative sensor platforms to operate in a harsh environment. Research objectives are the following: i) develop SLAM algorithms based platforms taking into account system constraints such as constrained communication, the type of sensors considered, allowable dynamics, and factors such as sensor failures and reliability of the considered sensors and ii) carry out experimental and supporting simulation studies by using mobile platform test platforms at the University of Maryland and the Petroleum Institute.

In this report, the problem of multi-agent SLAM in a dynamic network is addressed by using a decentralized algorithm that enables localization and map merging by exploiting the earlier work of Leung *et al.* (2009) and Zhou and Roumeliotis (2006). Leung *et al.* (2009) developed a generalized algorithm for localization of multiple agents in a dynamic network, whereas Zhou and Roumeliotis (2006) suggested techniques for map merging without knowledge of the relative initial positions of the agents. In Section 2, the basic issues in the SLAM problem are discussed, The main results are presented in Section 3, and an outline of the future work is provided in Section 4.

2. Approach

The basic aim of the SLAM algorithm is to make a mobile platform autonomous by providing the capability to navigate through an unknown environment from an initially unknown location. This is achieved by iteratively building a consistent map and simultaneously determining its location within the map (Durrant-Whyte and Bailey, 2006). In the SLAM problem, an agent or a mobile sensor platform uses relative sensing information between the agent and the surrounding environment in order to determine a map that constitutes the locations of landmarks or features in the surrounding environment as well as its own position within the map. The problem of single-agent SLAM has been addressed by several researchers using a variety of techniques such as the extended Kalman filter, unscented Kalman filter, particle filters, and grid-based occupancy maps. An efficient solution to the SLAM problem is important for the following reasons:

Uncertainty or sensor noise: Problems due to uncertainties in sensor measurements, leading to errors in determining landmark locations on the map or in determining the location of the mobile agent within the map. In particular, errors in the vehicle state can lead to convergence problems with the algorithm.

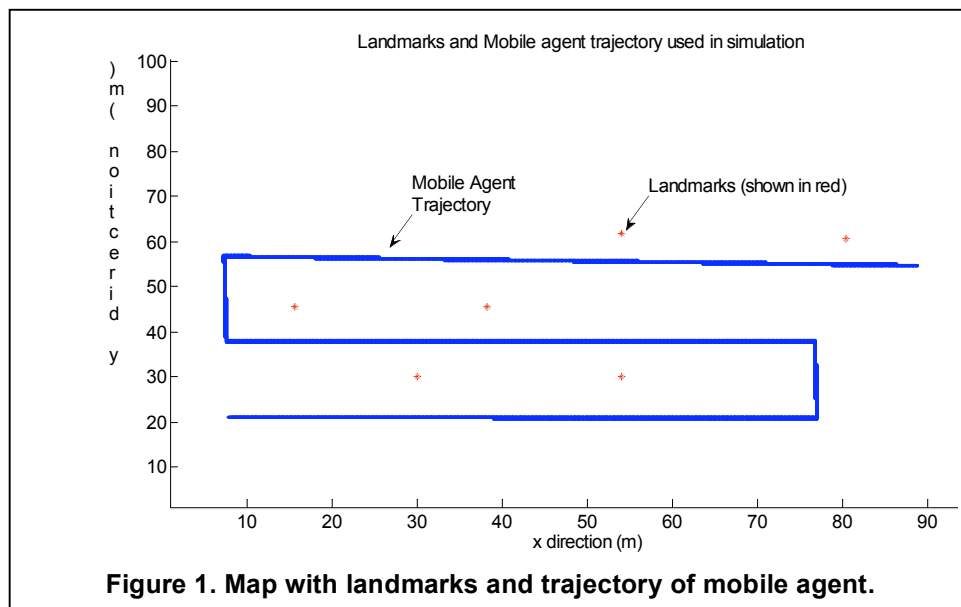
Data association or correspondence problem: This problem arises due to uncertainty in uniquely identifying landmarks. This can lead to errors not only in the locations of the landmarks but also in the locations of the mobile agent as well as the sensor readings of range and bearings of the landmarks used to determine the position of the mobile agent in the map.

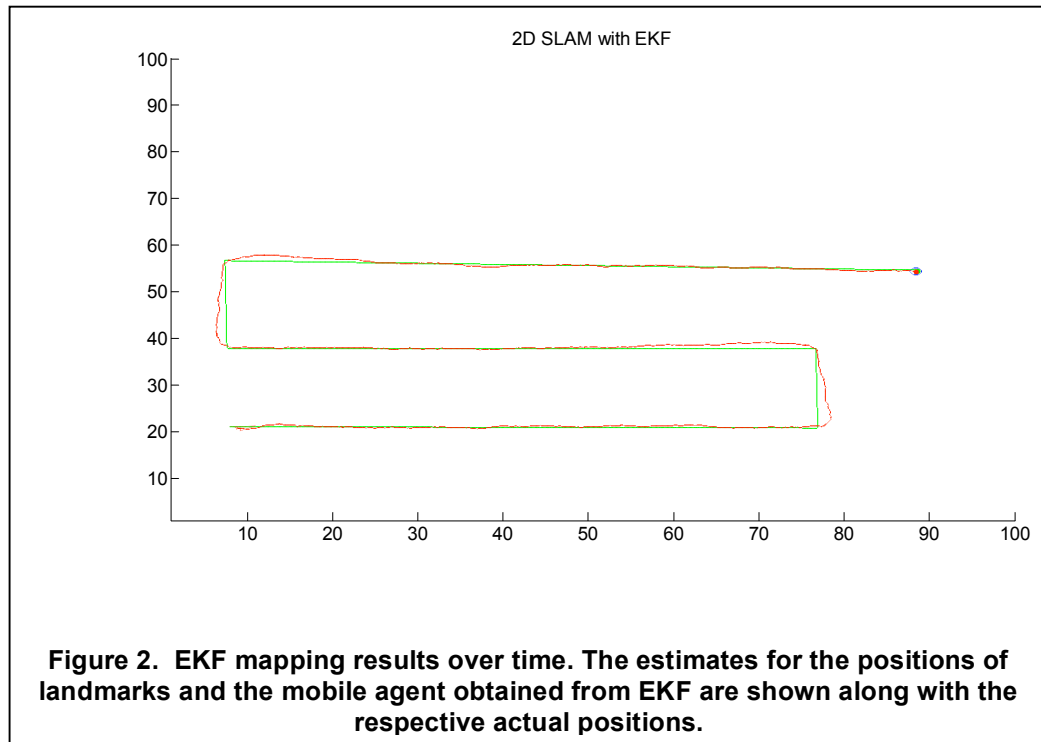
4. Summary of Results

The results presented in this report complement the source localization work reported in the previous report. In this section, results obtained through numerical simulations to gain fundamental insights are presented along with experimental work and details of interactions.

4.1 Numerical Studies

The extended Kalman filter algorithm used for this numerical study was adapted from (Thrun, *et al.*, 2006) and the results obtained for location estimation are shown in Figures 1 and 2.





4.2 Decentralized Simultaneous Localization and Mapping for Multi-agent Networks

Often studies in the area of multi-agent SLAM make certain simplifying assumptions regarding the communication network of the agents and the information that each agent possesses. Some examples of such assumptions are the following: i) every agent knows the initial positions of all the agents in the network, ii) each agent can communicate with all other agents, thereby broadcasting information to all of them at the same time, and iii) the network configuration of the agents remains static throughout. The assumption that all agents know their initial positions allows for the single-agent SLAM techniques to be extended to the multi-agent case with an increase in the dimensionality of the state estimations. Some complications in the multi-agent SLAM problem include building maps when the relative initial positions of the agents are unknown, map merging when the overlaps of the maps are unknown, complex correspondence problems related to the identification of individual agents, and dealing with out of sequence information that is communicated to a agent in a dynamic network.

Studies have been conducted to enable map merging from multiple agents when the relative initial positions of the agents are unknown by calculating transformation matrices for the conversion from one agent's reference frame to another based on relative observations between the two agents. The details are discussed in (Howard, 2006), and (Zhou and Roumeliotis, 2005).

The proposed multi-agent SLAM problem is formulated based on the work in (Leung *et al.*, 2010) and (Zhou and Roumeliotis, 2006). The various definitions can be found in (Leung *et al.*, 2010) and repeated below for completeness.

Assumptions and problem setup

Let $|N|$ represent the total number of agents being used in the mapping task. The set N is assumed to contain unique identifiers for each agent (indices ranging from 1 to $|N|$). $N_{i,k}$ is the set of agents known to agent i at a specific time step k .

A general discrete dynamic model for the agents is assumed as

$$x_{i,k} = g(x_{i,k-1}, u_{i,k}, \varepsilon_k)$$

$$y_{i,k}^{j,i} = h(x_{i,k}, x_{j,k}, \delta_k) (\square j) (d_{i,k}^{j,i} \leq r_{obs})$$

where for the time step k , $x_{i,k}$ is the pose of agent i , $u_{i,k}$ represents the odometry information of agent i , $g(\cdot)$ is the state transition function (with process noise ε_k), $y_{i,k}^{j,i}$ represents the range, bearing of agent j with respect to agent i , $h(\cdot)$ is the measurement function (with measurement noise, δ_k), and $d_{i,k}^{j,i}$ is the distance between agent i and j , and r_{obs} is the measurement range limit.

Agents within the communication range r_{comm} of each other are able to exchange and relay information. The information broadcast between agents at every communication stage includes all the knowledge the agent possesses such as its own state estimates, state estimates of the agents neighbors, odometry, and measurement data. In this report, the communication range and the observation range (i.e, the measurement range limit) are assumed to be equal ($r_{comm} = r_{obs}$); that is,

$X_k = \{x_{i,k}, L_{i,k}\} (\square i \square N)$ represents the set of all agent states and the landmark locations at time step k ,

$X_{Q,k} = \{x_{i,k}, L_{i,k}\} (\square i \square Q) (Q \square N)$ represents the set of states at time step k for the agents and landmarks in some subset Q of N .

Similarly, odometry data is represented by sets U_k and $U_{Q,k}$, which are represented as

$$U_k = \{u_{i,k}\} (\square i \square N) \text{ and}$$

$$U_{Q,k} = \{u_{i,k}\} (\square i \square Q) (Q \square N)$$

The measurement data are represented as

$Y_k = \{y_{i,k}^{j,i}\} (\square i, j) (d_{i,k}^{j,i} \leq r_{obs})$ represents the set of all measurements between agents made at time step k ,

$Y_{i,k} = \{y_{i,k}^{j,i}\} (\square j) (d_{i,k}^{j,i} \leq r_{obs})$ is the set of all measurements of agents j made by agent i at time step k ,

$Y_{Q,k} = \{y_{i,k}^{j,i}\} (\square i, j \square Q) (d_{i,k}^{j,i} \leq r_{obs})$ is the set of measurements made between agents in set Q .

Each $y_{i,k}^{j,i}$ is the measurement of the relative position of agent j with respect to agent i given by

$$y_{i,k}^{j,i} = \{\rho, \theta_j^i, \theta_i^j\}^T$$

where ρ is the relative distance between the agents i and j , and θ_j^i is the bearing of agent i towards agent j , and θ_i^j is the bearing of agent j towards agent i . These measurements are characterized by white zero mean Gaussian noise processes with variances $\sigma(\rho)^2$, $\sigma(\theta_j^i)^2$, and $\sigma(\theta_i^j)^2$ respectively.

The landmarks (map features) are assumed to be stationary, and the measurements of these landmarks by the agents are represented by the set L_k (within the set X_k , as this is needed for the estimation of the landmark positions in SLAM). The set L_k contains all the measurements made by the agents with respect to the landmarks, and $L_{i,k}$ is the set of all landmark measurements made by agent i .

Transformations between agent frames

This section provides the required transformation matrices that are used to express all the data transferred from the agent j to the agent i (such as measurements of agents and landmarks) in the initial global frame of the agent i . Each agent carries out explorations and measurements with respect to its initial global frame, $\{G_j\}$. The origins of these initial global frames are assumed to be at the initial pose of the agents. Therefore, all measurements made with respect the agents' initial global frame will be transformed based on the relative range and bearing measurements that are carried out with every communication. Based on the relative measurements between the agents, with every communication, each agent first calculates the transformation matrix between the global coordinate frames. The data sets of relative measurements are used to make this calculation, and the sets of landmark and agent measurements are first transformed into the agent's initial global frame and are subsequently stored. All further calculations are based on the agents' initial global frame of reference. The transformation matrix has the following components: the translation parameters and the rotation parameter, which is the rotation angle to calculate the cosine and sine terms in the rotation matrix. For two interacting agents as shown in Figure 3, in order to transform the landmarks from agent R_2 in its initial frame G_2 (G_2 not shown in figure), to the initial global frame G_1 of agent R_1 , the following transformation is required:

$$\rho^{G_1}_{Li} = \rho^{G_2}_{G_2} + T_{rot}(\varphi) \rho^{G_2}_{Li}$$

where the angle, $\varphi = \varphi_1 + \theta - \varphi_2$ is the angle between the frames G_2 and G_1 . This represents the sequence of rotations from G_2 to frame G_1 , (i.e., rotation of G_2 to R_2 (φ_2), R_2 to R_1 (θ) and finally R_1 to G_1 (φ_1)). φ_1 and φ_2 respectively represent the bearing of agents R_1 and R_2 , which can be obtained from the odometry data.

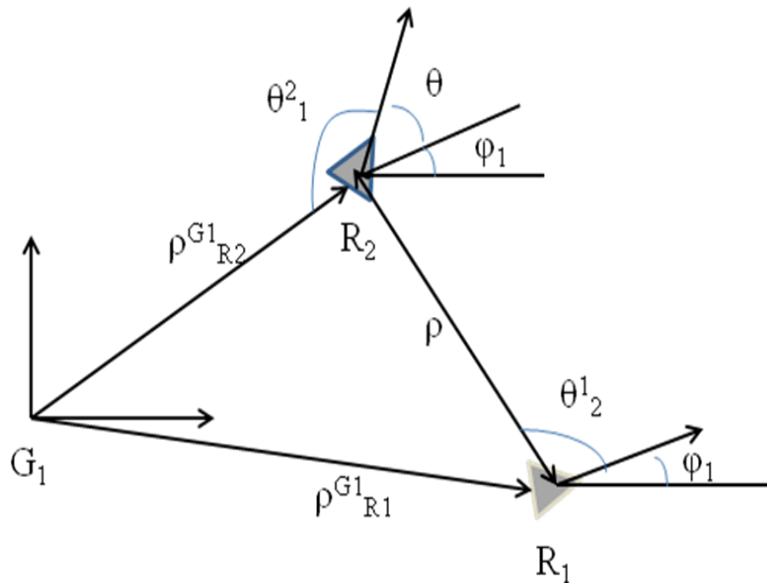


Figure 3. Example for calculation of transformation matrix.

The calculation of the transformation matrix for the two agents R_2 to R_1 (θ) in Figure 3 is given by $\theta = \pi + \theta^1_2 - \theta^2_1$.

where θ^1_2 (θ^2_1) is the bearing measurement of $R_2(R_1)$ with respect to $R_1(R_2)$. The translation from frame G_2 to G_1 can be obtained using

$$\rho^{G_1}_{G_2} = \rho^{G_1}_{R_1} + T_{\text{rot}}(\varphi_1) \rho^{R_1}_{R_2} - T_{\text{rot}}(\varphi) \rho^{G_2}_{R_2}$$

The translation matrix for R_2 to R_1 is given by

$$\rho^{R_1}_{R_2} = \rho [\cos \theta^2_1 \sin \theta^1_2]^T$$

where ρ is the measurement of the range (distance between the agents R_1 and R_2). These are the components needed to transform landmarks from the agent R_2 to R_1 . The transformation to express agent R_2 in the frame G_1 can be obtained using

$$\rho^{G_1}_{R_2} = \rho^{G_1}_{R_1} + T_{\text{rot}}(\varphi_1) \rho^{R_1}_{R_2}$$

Hence, by using the above transformations, all the communicated data is converted to the i^{th} agent's global frame and all further calculations are based on the converted data. In order to calculate the errors in the above transformations, it is required to linearize the equations at the estimated quantities which are in the state vector that includes the pose of both R_1 and R_2 and the landmarks detected by both agents. The Jacobians of the quantities $\rho^{G_1}_{R_2}$, $\rho^{R_1}_{R_2}$ and $\rho^{G_1}_{L_i}$ are calculated with respect to the state vector that includes both R_1 and R_2 . The calculation of the Jacobians can be found in Zhou and Roumeliotis (2005, 2006). The extended Kalman filter can be applied at every estimation step in the algorithm in order to calculate the state estimates.

Use of the Markov property

As in the case of the single agent SLAM problems, the true state of the system in the presence of noise is represented by a probability density function (pdf). In this case the pdf represents estimates for all agent states (beliefs) and it is calculated using the Markov property from odometry and measurement data.

$$\text{bel}(X_k) := p(X_k | \text{bel}(X_0), U_{1:k}, Y_{1:k}, L_{1:k}) = p(X_k | \text{bel}(X_{k-1}), U_k, Y_k, L_k)$$

Let the knowledge set $S_{i,k}$ consist of all odometry and measurement data, as well as the previous state estimates known to agent i at time k . At the initial time (for $k=0$), it is assumed that $S_{i,0} = \{\text{bel}(x_{i,0})\}$ which is the belief of the agents' own pose at the initial time. Before communicating with any agent, $S^-_{i,k}$ is the knowledge set after state transition and observations.

$$S^-_{i,k} = S_{i,k-1} \square \{u_{i,k}, Y_{i,k}, L_{i,k}\}$$

As mentioned earlier, the agents broadcast the information that they individually possess, making their knowledge sets the same at the time of communication. Therefore,

$$S_{i,k} = S_{j,k} = S^-_{i,k} \square S^-_{j,k}$$

The application of the Markov property makes the belief over the current state of a system independent of all its past states, and by eliminating the requirement for previous odometry and measurement data, reduces the memory requirements, as is the case with single agent SLAM problems. The complication in the multi-agent setting in dynamic networks arises because communications between agents can occur at different times, leading to out-of-sequence measurements. Application of the Markov property without considering the out-of-sequence measurements may lead to sub-optimal state estimates as compared to centralized estimators. Furthermore, the odometry and measurement data that may be needed by other agents for state estimation will be discarded once the Markov property is applied on that particular agent. Another complication that should be avoided is the reuse of data after state estimations have been updated, as this can lead to over-confident state estimates. The algorithm presented by Leung *et al.* (2010) provides a solution that overcomes these problems while providing state estimates that

are equivalent to centralized estimators whenever possible. This is accomplished by monitoring the information flow in the network and determining the right time at which to apply the Markov property for each agent. The concept of checkpoints and partial checkpoints for the multi-agent system provide the necessary framework for solving the aforementioned problem.

Definition 1: A checkpoint $C(k_c, k_e)$ is an event that occurs at the checkpoint time k_c that first comes into existence at k_e , ($k_c < k_e$) in which the set of knowledge for each agent i contains for all j : i) The previous state estimate of agent j at some time step $k_{s,j} \leq k_c$ and ii) All the odometry and measurement data of agent j from time step $k_{s,j}$ to k_c .

Therefore, a checkpoint occurs at time step k_c when $S_{i,k_e} \supseteq S_{j,k_c} (\forall i, j)$.

Using Figure 4 as an example, with $S_{i,0} = \{bel(x_{i,0})\}$, the checkpoint found in this figure is $C(1, 3)$. This means that at $k = 3$, each agent has the previous state estimate of all agents (in this case at $k = 0$). Also, each agent has the odometry and measurement data of all agents up to $k = 1$. Therefore, in this case $k_c = 1$ and $k_e = 3$. The existence of a checkpoint is used as a time at which to apply the Markov property, thereby replacing an old state estimate, odometry, and measurement data up to k_c , with a new state estimate so that all of agents have the information about every other agent in order to get the best possible state estimate at time k_c , which will be equal to that of a centralized estimate at k_c .

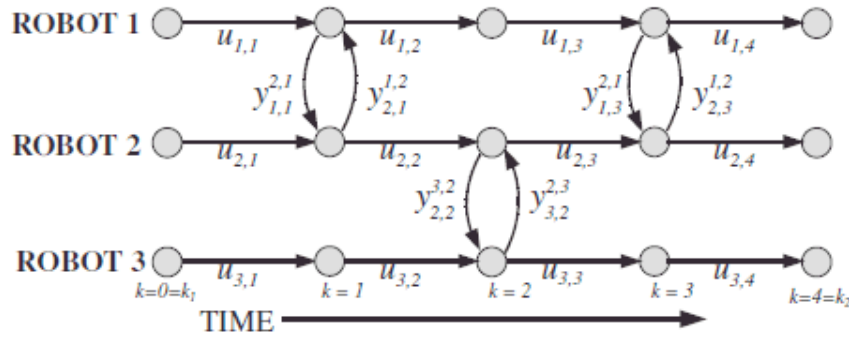


Figure 4. Example to show the existence of a checkpoint.

Definition 2: A partial checkpoint $C_p(k_{c,i}, k_{e,i})$ is an event that occurs for agent i at time $k_{c,i}$ that first comes into existence at $k_{e,i}$, in which the set of knowledge for agent i contains for all j : i) the previous state estimate of agent j at some time step $k_{s,j} \leq k_{c,i}$ and ii) all the odometry and measurement data of agent j from time step $k_{s,j}$ to $k_{c,i}$.

A partial checkpoint therefore occurs for agent i at time step $k_{c,i}$ when $S_{i,k_e} \supseteq S_{j,k_c} (\forall j)$. This means that when a partial checkpoint exists for every agent at a given time step k_c , then a checkpoint exists for the system. Partial checkpoints for each agent can occur at different times. The authors (Leung *et al.*, 2010) follow up these definitions with theorems to prove the existence of checkpoints and the existence of partial checkpoints. Another result of importance is the existence of a checkpoint when every agent has a partial checkpoint. This means that when an agent applies the Markov property at a partial checkpoint, the other agents do not lose information and it is still possible to calculate the centralized estimate at the time of the system checkpoint.

The assumptions made in using this work include the following:

Communication between the agents is bidirectional and the communication range limit is

greater than or equal to the measurement range limit. This ensures that the algorithm works without the need to know the total number of agents that are involved making the algorithm scalable to any N .

The only initial conditions known to each agent are estimates of its own pose ($S_{i,0} = \{bel(x_{i,0})\}$). This ensures that the algorithm can work when the relative initial positions are unknown.

The algorithm assumes that the network is dynamic (connectivity with every agent throughout is not required), but that once a set of agents communicate, they do not leave the network permanently. Violating this assumption can lead to an unbounded increase in the information in the knowledge set.

A unique identifier is assumed to exist for every agent (set N).

Map merging will be carried out under the assumption that all landmarks are stationary; that is, the environment is not dynamic.

The transformation matrices are calculated based on the relative measurements between the agents. Therefore, this requires that the agents observe each other at least once for map merging to take place.

Algorithm

The decentralized localization algorithm with additions for SLAM is presented below along with a step-by-step explanation of the algorithm in this section of the report. The framework, which is that used in (Leung *et al.*, 2010), is extended for achieving the desired results. The communicated data is transformed by using the transformations discussed earlier, and this is stored in the knowledge set. The same algorithm is implemented on every agent and iterates every time step. The required inputs are the current time step k , odometry data $u_{i,k}$, measurements $Y_{i,k}$ and $L_{i,k}$, the latest knowledge set $S_{i,k-1}$, and the knowledge sets of all agents (to which information exchange is possible at the current time step), $S_{j,k}$ ($\forall j \in R_{i,k}$). The initial condition for the agents at the first iteration is assumed to be the pose estimate of the individual agent.

Algorithm 1: Decentralized($k, u_{i,k}, Y_{i,k}, L_{i,k}, S_{i,k-1}, S_{j,k}$ ($\forall j \in R_{i,k}$))

```

1  $S_{i,k} \leftarrow S_{i,k-1} \cup \{u_{i,k}\} \cup \{Y_{i,k}\} \cup L_{i,k} \cup \{S_{j,k}\} (\forall j \in R_{i,k})$ 
2  $N_{i,k} \leftarrow \{Q \cup \{bel(X_{Q,k_s}) \cup S_{i,k}\}, (k_s \leq k)\}$ 
3 repeat
4     flagrepeat = false
5      $\{k_{s1}, Q_1\} \leftarrow$  find smallest  $k_{s1}$  such that  $bel(X_{Q1}, k_{s1}) \in S_{i,k}$ 
6      $k_{s2} \leftarrow k$ 
7     if  $Q_1 \neq N_{i,k}$  then
8      $\{k_{s2}, Q_2\} \leftarrow$  find smallest  $k_{s2}$  such that  $bel(X_{Q2}, k_{s2}) \in S_{i,k}$  ( $Q_1 \neq Q_2$ )
9     end
10    for  $k_c \leftarrow k_{s2} : k_{s1}$  do
11        if  $U_{Q1,k_c} \in S_{i,k}$  or  $k_c = k_{s1}$  then
12             $\hat{S}_{i,k_c} \leftarrow S_{i,k} - \{U_{Q1,k_r}, Y_{Q1,k_r}, L_{Q1,k_r}\} (\forall k_r > k_c)$ 
13             $bel(X_{Q1,k_c}) \leftarrow p(X_{Q1,k_c} | \hat{S}_{i,k_c})$ 
14             $S_{i,k} \leftarrow S_{i,k} \cup bel(X_{Q1,k_c})$ 
15             $S_{i,k} \leftarrow S_{i,k} - \{U_{Q1,k_r}, Y_{Q1,k_r}, L_{Q1,k_r}, bel(X_{Q1,k_r})\} (\forall k_r \leq k_c)$ 
16            break
17        end
18    end
19    if  $\{bel(X_{Q1,k_c}), bel(X_{Q2,k_c})\} \in S_{i,k}$  then
20         $bel(X_{Q3,k_c}) \leftarrow bel(X_{Q1,k_c}) bel(X_{Q2,k_c})$ 
21         $S_{i,k} \leftarrow S_{i,k} \cup bel(X_{Q3,k_c}) - \{bel(X_{Q1,k_c}), bel(X_{Q2,k_c})\}$ 

```

```

22         flagrepeat = true

23     end

24 until flagrepeat = false
25 { $k_{s1}, Q_1$ } ← find smallest  $k_{s1}$  such that  $bel \square (X_{Q_1, k_{s1}}) \square S_{i,k}$ 
26 while  $Q_1 \neq N_{i,k}$  do
27     { $k_{s2}, Q_2$ } ← find smallest  $k_{s2}$  such that
28      $bel (X_{Q_2, k_{s2}}) \square S_{i,k} (Q_1 \neq Q_2) (k_{s1} \leq k_{s2})$ 
29      $\hat{S}_{i, k_{s2}} \leftarrow S_{i,k} - \{U_{Q_1, k_u}, Y_{Q_1, k_r}, L_{Q_1, k_r}\} (\square k_u > k_{s2})$ 
30      $bel (X_{Q_1, k_{s2}}) \leftarrow p (X_{Q_1, k_{s2}} | \hat{S}_{i, k_{s2}})$ 

31      $bel (X_{Q_1, k_{s2}}, X_{Q_2, k_{s2}}) \leftarrow bel (X_{Q_1, k_{s2}}) bel (X_{Q_2, k_{s2}})$ 
32      $Q_1 \leftarrow Q_1 \square Q_2$ 
33      $k_{s1} \leftarrow k_{s2}$ 

34 end

35  $bel (X_{N_{i,k}}) \leftarrow p (X_{N_{i,k}} | S_{i,k})$ 

36 return { $bel (X_{N_{i,k}}), S_{i,k}, N_{i,k}$ }

```

From time step $k-1$ to k , the knowledge set of agent i is updated by appending to the knowledge set the odometry and measurement information as in line 1. In line 2, one determines the set of all agents known to i by looking for part beliefs $bel \square (X_{Q, k_s})$ in the knowledge set $S_{i,k}$, where Q represents a set of agents where $bel \square$ indicates a belief that is equivalent to the state estimate obtainable using a centralized state estimator. The loop beginning on line 3 repeats according to the flag variable set on line 4 until all independent subgroups of agents are found in the data. Independent subgroups are those groups of agents that have not communicated to each other until time k . The beliefs of these independent groups can be combined using the statistical independence property by simple multiplication of the beliefs as follows:

$$bel(X_{Q_1, k}, X_{Q_2, k}) = bel(X_{Q_1, k}) bel(X_{Q_2, k}).$$

This is done so as to combine multiple beliefs of these independent subgroups in $S_{i,k}$. Before this can be accomplished, the beliefs of the independent subgroups should all be calculated for the same time step. This is done using the Markov property at the partial checkpoints for each subgroup until their beliefs are calculated until the same time. In line 5, one determines the earliest state estimate $bel \square (X_{Q_1, k_{s1}})$ in the knowledge set. If $Q_1 = N$, then the belief over all known agents is already known. Otherwise, the next earliest estimate $bel \square (X_{Q_2, k_{s2}})$ is found on line 8. Next, the search for a partial checkpoint for the subgroup Q_1 begins on line 10. If $Q_1 = N$, the partial checkpoint that is closest to the current time step is found (this is why k_{s2} is initially set equal to k on line 6). Otherwise, an attempt to find the partial checkpoint at k_{s2} is made. If k_{s1} and k_{s2} are the same, the partial checkpoint search is skipped and the estimates on lines 5 and 8 are directly combined. In line 11, one uses Theorem 2.2 (from Leung *et al.*, 2010) to detect the existence of a partial checkpoint by searching for odometry data until the time k_c . If one is found, the knowledge up to the partial checkpoint time (line 12) is used to obtain the state estimate on line 13. The new estimate is entered into the knowledge set on line 14, and the Markov property is exploited to discard information replaceable by $bel \square$ on line 15.

In line 19, one checks if there are two estimates for the same time step in the knowledge set. If a pair is found, the beliefs are combined by simply multiplying the individual beliefs on line 20. Again the knowledge set is updated on line 21. This part of the algorithm is iterated until the beliefs for all the subgroups of agents in the knowledge set that can be combined are found (i.e., until $Q_1 = N$). In the next iteration of the line 3–24 loop, the newly combined belief on line 20 becomes the belief on line 5 (i.e., Q_1 becomes equal to $Q_1 + Q_2$). As mentioned previously, this

process repeats in the loop between lines 26 and 33 until we have a single state estimate over the states of all known agents.

Finally, the current state estimate is determined on line 35, based on the estimate at the last partial checkpoint and any information since then to the current time. This step makes use of all the available information and is the best estimate that can be produced at the current time. It is to be noted that the current estimate will not be equivalent to the centralized state estimator unless a partial checkpoint exists at the current step. In this situation, the last known velocity for the agents from which odometry data are not available are assumed to be the current velocity. The state estimate X_k contains both the localized positions of all the agents as well as the positions of all the landmarks that were observed.

4.3 Experimental Work

To test the decentralized multi-agent SLAM algorithm, it is necessary to set up mobile platforms that will contain the various sensors required for the localization and mapping as well as a feature-based environment.

Suitable ground-based mobile agents, necessary to carry out the experimental measurements necessary for simultaneous localization and mapping, have been acquired at UMD (see Figure 5). The ground-based agent houses a microcontroller, two encoders to provide information regarding the location of the mobile agent, infrared sensors for obstacle avoidance and a laser sensor for range and bearing measurement of landmarks. This agent is a wheeled platform that is actuated by using stepper motors.



Figure 5. Mobile agent Garcia to be used in SLAM experiments.

The microcontroller and the motors are battery powered. The agents also have in-built wireless networking that enables the exchange of information between the host computer and the agents as well as between the agents themselves. Infra-red sensors are placed on the front, the two sides and at the back of the agent in order to provide scans from multiple directions at the same time. The sensors have been set up for obstacle avoidance in order to allow the mobile agent to navigate without collisions. Furthermore, the laser sensor is to be used for measurements to carry out localization using range finder scans. Encoders are provided on the platform for use in experiments on SLAM in order to model the agent's movements in time. The agents are controlled by using C++ software from a host computer through a wireless network established in the laboratory. Currently, all necessary work has been carried out to configure the mobile agents to enable the host computer to control the robot in order to implement obstacle avoidance as well

as to collect the encoder, laser and infrared sensors data while the agent is in motion through the wireless network.

4.4 Interactions

Undergraduate students (Mr. Osama Al Ameri, an electrical engineering student, and Mr. Ahmed El Ali) from the Petroleum Institute interned at the University of Maryland from July 30 – August 15, 2010. The interns worked on a mobile sensor agent in order to implement obstacle avoidance by using ultra-sonic sensors on the agent. The mobile agent was controlled using a host computer and a C++ code. The students demonstrated the use of ultrasonic sensors for obstacle avoidance and further worked on adding redundancy to the program in case of sensor failure.

Planned Project Activities for the Next Quarter

The submission of paper abstract titled “Decentralized Simultaneous Localization and Mapping for Robotic Networks” to SPIE Smart Structures/NDE 2011 is planned. Details on subsequent activities such as the experimental setup are provided in following sections.

Construction of experimental setup

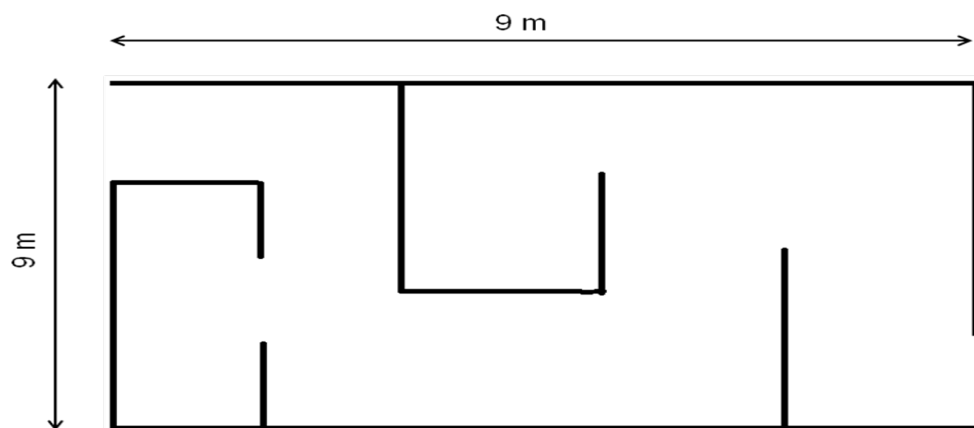


Figure 6. Set-up for SLAM experiments with ground based mobile agents.

A feature-based environment set-up will be built for the ground-based mobile agents so that the SLAM experiments can be carried out in a realistic setting. A top-view visualization of such an environment is shown in Figure 5.1. The setup will be created such that the internal features of the environment can be changed according to the sensor capabilities and the required dimensions required to enable multi-agent SLAM. As a first step, the extended Kalman filter (EKF) algorithm used in the numerical study will be implemented with experimental data from the Garcia platforms to implement SLAM.

Numerical and experimental analysis

The decentralized multi-agent SLAM algorithm presented previously in Section 4.2 will be analyzed and enhanced through numerical verifications. The idea behind this approach is to identify the strength and weakness of the various algorithms and to analyze their suitability for use in fluid environments. The fluid environment constrains the motion of the sensor platform, while preventing use of common localization devices such as the global positioning system. The acoustic medium constrains the inter-sensor platform communication and complicates the information fusion process. In addition, while most studies for SLAM have focused on single

platforms, numerical verification will give useful insights into their extension for cooperating sensor platforms.

Appendix

Approach

The basic aim of the SLAM algorithm is to make a mobile platform autonomous by providing the capability to navigate through an unknown environment from an initially unknown location. This is achieved by iteratively building a consistent map and by simultaneously determining its location within the map (Durrant-Whyte and Bailey, 2006). In the SLAM problem, an agent or a mobile sensor platform uses relative sensing information between the agent and the surrounding environment in order to determine a map that constitutes the locations of landmarks or features in the surrounding environment as well as its own position within the map. The problem of single agent SLAM has been addressed by several researchers by using a variety of techniques such as the extended Kalman filter, unscented Kalman filter, particle filters, and grid-based occupancy maps. An efficient solution to the SLAM problem is important due to the following reasons:

Uncertainty or sensor noise: Problems due to uncertainties in sensor measurements, leading to errors in determining landmark locations on the map or in determining the location of the mobile agent within the map. In particular, errors in the vehicle state can lead to convergence problems with the algorithm.

Data association or correspondence problem: This problem arises due to uncertainty in uniquely identifying landmarks. This can lead to errors not only in the locations of the landmarks but also in the locations of the mobile agent as well as the sensor readings of range and bearings of the landmarks used to determine the position of the mobile agent in the map.

Three-year schedule

Phase II:

April 1, 2009 to December 31, 2009: Carry out analytical and numerical investigations into SLAM algorithm based mobile platforms for representative geometrical profile measurements, construction of experimental test platforms, and preliminary experimental findings

January 1, 2010 to December 31, 2010: Continuation of analytical, experimental, and numerical efforts, with one of the focus areas to be development of appropriate communication and motion planning protocols for operations in harsh environments

January 1, 2011 to December 31, 2011: Continuation of experimental and numerical studies and formulation of recommendations for appropriate sensor and mobile platform configurations for use in oil tanks.

References

- [1] Durrant-Whyte, H. and Bailey, T., 2006, "Simultaneous localization and mapping: part I," IEEE Robotics & Automation Magazine, Vol.13, no.2, pp. 99-110, June.
- [2] Dudek, G., Jenkin, M., Milius, E. and Wilkes, D., "A Taxonomy for Multi-agent Robotics," Autonomous Robots, 3(4), 1996.
- [3] Howard, A., "Multi-robot simultaneous localization and mapping using particle filters," International Journal of Robotics Research, 25(12), 1243–1256, 2006.

- [4] Leung, K.Y.K, Barfoot, T.D., and Liu, H., “Decentralized Localization of Sparsely-Communicating Robot Networks: A Centralized-Equivalent Approach,” *Robotics, IEEE Transactions on*, 26(1), pp.62-77, 2010.
- [5] Thrun, S., Burgard, W., and Fox, D., 2006, “Probabilistic Robotics,” MIT Press.
- [6] Zhou, X.S. and Roumeliotis, S.I., “Multi-robot slam with unknown initial correspondence: The robot rendezvous case,” In: 2006 IEEE/RSJ International Conference on Intelligent Robots and Systems, October 2006, pp. 1785–1792, 2006.
- [7] Zhou X.S. and Roumeliotis, S. I., “Multi robot SLAM map alignment with rendezvous,” Department of Computer Science and Engineering, University of Minnesota, Tech. Rep., 2005. [Online]. Available: www.cs.umn.edu/~zhou/paper/rendTechRep.pdf

Development of a Probabilistic Model for Degradation Effects of Corrosion-Fatigue Cracking in Oil and Gas Pipelines

UMD Investigator: Mohammad Modarres
PI Investigators: Abdennour Seibi
GRA: Mohammad Nuhi
Start Date: Oct 2006

1. Objectives/Abstract

This research continues Phase-I mechanistic modeling of the *corrosion-fatigue* phenomenon for applications to pipeline health, risk and reliability management. The objective of this study is to perform additional mechanistic-based probabilistic models derived from physics of failure studies and validate them using the state-of-the-art experimental laboratory being developed at the PI as part of the Phase I of this study. Where possible, observed field data from ADNOC operating facilities will be used to supplement observations from the laboratory experiments based on the well-established Bayesian approach to mechanistic model updating and validation developed in Phase I. Uncertainties about the structure of the mechanistic models as well as their parameters will also be characterized and accounted for when such models are applied. The proposed models will allow the end users (e.g., maintenance analysts and Inspection crew) to integrate observed performance data from a wide range of pipelines and selected refinery equipment, such as pumps, compressors and motor-operated valves. Admitting the fact that modeling all degradation mechanisms would be a challenging undertaking, the proposed research will additionally address the following degradation phenomena related to the petroleum industry: creep, pitting corrosion, and stress cracking corrosion (SCC).

Deliverables for the Completed Quarter

The following tasks have been completed in the last three months and are discussed in detail in Section 3:

- 3.1 Theoretical effort in support of model development
 - 3.1.1. Literature review on specifying the stress dependencies of creep curve parameters (the literature review on specifying the temperature dependencies of creep curve parameters will be discussed in the next report).
 - 3.1.1.1. Results and discussion
 - 3.1.2. Review of mathematical and statistical methods for creep data evaluation
 - 3.1.3. Application of mathematical methods to pitting corrosion data (obtained from Summer 2010 intern program)
 - 3.1.4. Separation of corrosion fatigue WinBugs model program [1]
 - 3.1.5. Creep model categorization
- 3.2 Experimental effort in support of model development
 - 3.2.1. Pitting corrosion experiments

3. Summary of Results

3.1. Theoretical Effort in Support of Model Development

3.1.1. Literature Review on Specifying Stress Dependencies of Creep Curve Parameters

According to the American Standard for Testing Materials (ASTM), creep deformation is defined as any strain that occurs when a material is subjected to a sustained stress [2, 3]. During creep, a tensile specimen under a constant load will continually deform with time. This deformation depends on three major parameters: stress, time and temperature. Therefore, the most general form of creep equation is:

$$\varepsilon_c = f(\sigma, t, T)$$

Although different forms of stress dependencies have been reported for the creep strains [2-6], there are two forms that are widely used [4]:

Power law, given by Norton, Norton and Bailey (1929) [5] and Johnson et al. (1963) [6]:

$$\varepsilon_c = A \cdot \sigma^n \cdot t^m$$

where σ , is the applied stress, and σ_0 is the initial stress, (i.e. a material constant like the yield strength, σ_y).

To study the stress dependencies of creep parameters, we suggested the following empirical model (the details of which were described in the Fourth Quarterly report):

$$\varepsilon_c = A \cdot t^n + B \cdot t^m \cdot \exp(p \cdot t)$$

where ε_c is the creep strain, t is the time and A , n , B , m , and p are stress-dependent material parameters (they are dependent on temperature, but this will be addressed in our future expansions of the model).

Figure 1 shows Levi de Oliveira Bueno's experimental data versus the theta projection model [13]. We extended Levi de Oliveira Buneo's data used for 2-1/4Cr-1Mo high temperature pipeline steel (given for just one temperature and one stress) to different stress conditions.

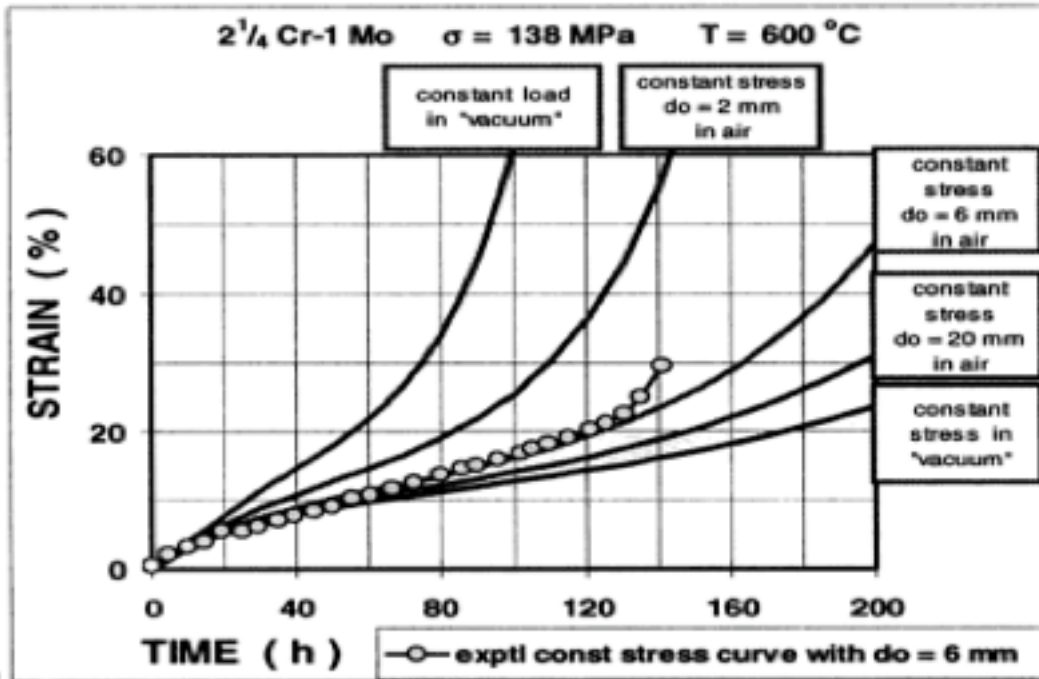


Figure 1. Strain versus time relation for 2-1/4Cr-1Mo pipeline alloy under applied stresses of $\sigma=138$ Mpa, and $T=600$ °C in vacuum and air [13].

3.1.1.1 Results and Discussion

Table 1 (a and b) show the extended-data for 2-1/4Cr-1Mo high temperature pipeline steel used for pressure vessels in power plants and oil refineries. The strain values versus time are calculated for different applied stress at 600°C.

Table 1. Data calculated used to develop our model at $T=600$ °C, evaluated under 15 different stress conditions for 2-1/4Cr-1Mo pipeline steel [13]

(a)

σ [MPa] →	34.5	51.75	69.000	86.25	94.875	103.50	107.80	112.125
time[h] ↓	ϵ [%]							
0	0	0	0	0	0	0	0	0
20	0.011296	0.033113	0.096411	0.277569	0.468226	0.786023	1.016286	1.311923
40	0.022164	0.064229	0.183663	0.514423	0.852094	1.400149	1.789092	2.281159
60	0.032624	0.093489	0.262793	0.717862	1.170583	1.890793	2.395104	3.028426
80	0.042694	0.121024	0.334718	0.893912	1.438558	2.293431	2.888361	3.63519
100	0.052389	0.146956	0.400255	1.047545	1.667658	2.634092	3.307038	4.15669
120	0.061728	0.171398	0.460131	1.182868	1.867006	2.931909	3.678203	4.63065
140	0.070725	0.194455	0.514991	1.303268	2.043758	3.200988	4.021151	5.083129
160	0.079396	0.216226	0.565408	1.411547	2.203532	3.451766	4.349752	5.53244
180	0.087754	0.236801	0.611891	1.510015	2.35074	3.692007	4.674089	5.991778
200	0.095813	0.256266	0.654893	1.600585	2.48886	3.927531	5.001617	6.470988

(b)

σ [MPa] →	120.75	125.00	129.375	133.60	138.000	142.00	146.625
time[h] ↓	ϵ [%]						
0	0	0	0	0	0	0	0
20	2.175632	2.794789	3.584536	4.591013	5.874266	7.513633	9.617751
40	3.688053	4.680661	5.939781	7.547645	9.626148	12.36587	16.08776
60	4.830696	6.110716	7.761583	9.934981	12.8877	17.08189	23.41829
80	5.783131	7.348191	9.434871	12.32079	16.52223	23.0668	34.1905
100	6.657173	8.551387	11.18779	15.05148	21.11479	31.48639	51.2334
120	7.524579	9.821562	13.17295	18.38857	27.20507	43.7026	78.65723
140	8.433734	11.2301	15.51099	22.57961	35.4156	61.57839	122.9471
160	9.419721	12.8341	18.31487	27.89953	46.54416	87.79529	194.5319
180	10.51047	14.68552	21.70439	34.67982	61.65392	126.2686	310.2524
200	11.73052	16.83686	25.81608	43.33454	82.1805	182.7374	497.3271

The stress dependencies of each parameter (A, n, B, m, and p) of our empirical model are given as follows:

$$A = \alpha_A \cdot \exp(\beta_A \cdot \sigma)$$

$$n = \alpha_n \cdot \sigma + \beta_n$$

$$B = \alpha_B \cdot \exp(\beta_B \cdot \sigma)$$

$$m = \alpha_m \cdot \sigma + \beta_m$$

$$p = \alpha_p \cdot \exp(\beta_p \cdot \sigma)$$

where parameters α_i , and β_i with (i=A, n, B, m, and p) are material constants.

The use of exponential stress dependencies for empirical parameters is justified by several investigations [11, 12, 14-16]. Figure 2 shows the creep curves estimated from the data given in Table 1.

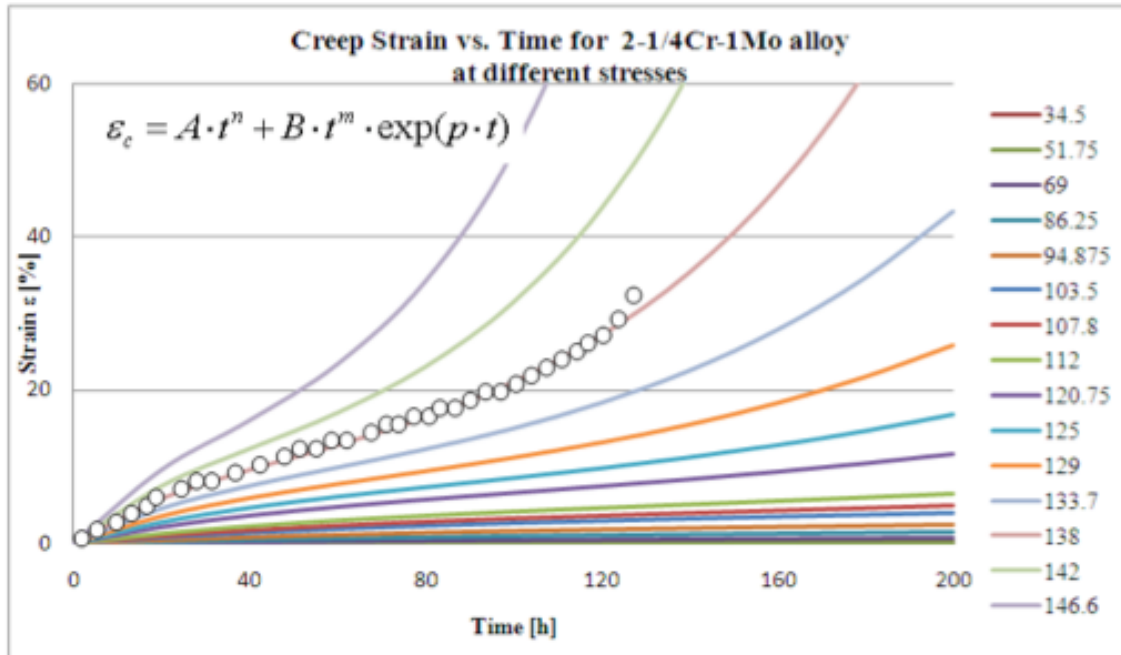


Figure 2. Creep curve chosen from literature to estimate temperature dependency of the empirical model; series 1 to 15 correspond to 15 different stress conditions.

Regarding the temperature dependencies of creep parameters, it should be mentioned that the change of temperature affects the creep strain. More specifically, the material parameters are altered in different temperatures. There are different mechanisms governing the creep curves (slip or diffusion processes) at low and high temperatures; besides, the activation energies for the primary and tertiary parts are not the same.

Since there are many factors and mechanisms involving in the temperature dependency of creep parameters, further investigation is needed to obtain the results; therefore, the details will be given in the next quarterly report.

3.1.2 Review of Mathematical and Statistical Methods for Creep Data Evaluation

Creep test results (even under the same conditions) contain a range of uncertainties. To consider (and therefore control) the presence of uncertainty in measurement (which affects the analyses), one should study the regression analyses and the parameter dependencies (autocorrelation).

Mathematical and statistical methods in reliability analysis can handle the uncertainties in data analysis [17, 18]. Therefore, the following methods were investigated and applied to pitting corrosion data (gathered in the Summer 2010 intern program).

Regression analyses: traditional method, maximum likelihood and matrix evaluation (details in Summer 2010 intern's report);

Autocorrelation analyses based on pit-depth data (taken from X70 carbon steel at different temperatures and stresses); the creep autocorrelation is under investigation;

Bayesian analyses with WinBugs' program [1] to compare the experimental data with the data estimated from the extended corrosion model;

Regression analyses with Excel (details in Summer 2010 intern's report);

Autocorrelation analysis.

3.1.3. Applying Mathematical Methods to Pitting Corrosion Data

The Summer 2010 intern program was held at UMD with the help of PI student Taher Abu Seer. The aim of this intern program was to measure the pit depths in corrosive environment at different times and temperatures.

In order to measure the pit depths, we did the experiments on both unstressed and stressed samples (X70 carbon steel). The samples were immersed in H₂S liquid environment for 5, 10 and 30 hours.

The pit depths of unstressed samples were measured at four different temperatures, 35 °C, 45 °C, 75 °C and 90 °C, while those of stressed ones were measured at 45 °C, and 60 °C (further experiments on stressed samples will be done in PI laboratories).

The results of our experiments are compared with those from Hoeppe and Kondo's model [19, 20].

Hoeppe and Kondo's model provides the relation between pit depth and time as follows [19, 20]:

$$a = C \cdot t^n; \quad n = 1/3$$

where a is pit depth, C is the material constant and t is the time.

The exponent of time in Hoeppe and Kondo model is $n = 1/3$, which was derived from the hemispherical shape assumption of the pit depth, and the linearity of pit growth in time.

The results are classified as:

Temperature dependency of pit depths:

The parameters of Hoeppe and Kondo's model [19, 20] have been expanded with temperature dependencies as follows:

$$(a = C \cdot t^n; \quad n = 1/3) \rightarrow a = D \cdot \exp(-Q/R \cdot T) \cdot t^{(mT+n)}$$

The first equation on the left is the Hoeppe and Kondo model [19, 20] and the one on the right is our extended equation, based on our experimental data; where a is the pit depth, t is time, Q is the activation energy of the pitting corrosion, and C , D , m and n are material parameters, R is the gas constant, and T is the absolute temperature in degree Kelvin.

It should be noted that the samples used for this part were unstressed ones at four different temperatures of 35 °C, 45 °C, 75 °C and 90 °C.

Stress dependency of pit depths:

The parameters of the Hoeppe-Kondo model have been expanded to include stress. The resultant model is:

$$(a = C \cdot t^n; n = 1/3) \rightarrow a = E \cdot \sigma^p \cdot t^n, \text{ with, } 1/4 \leq n \leq 1/3$$

where σ is the applied stress in, and C, E and p are material parameters. The left-hand side equation is Hoepfner-Kondo and the right hand side is the extended model. The experiments of this part were made on stressed samples at 45 °C, and 60 °C.

As can be seen, we have a range of different values for the time exponent $n(1/4 \leq n \leq 1/3)$, instead of $n = 1/3$ in the Hoepfner-Kondo model. This shows that our pit depths are not all hemispherical (which was supposed by Hoepfner-Kondo) [33].

In order to compare the pit depths observed at different temperatures, we made an autocorrelation plot. An autocorrelation plot is a tool to check the randomness in a data set. This randomness is checked by computing autocorrelations for data values at different lags (intervals). If random, the autocorrelation should be zero; if non-random, then one or more of the autocorrelations is significantly non-zero [34].

Figure 3 shows the estimated correlation among the data points (pit depths measured at different temperatures, 35 °C, 45 °C, 75 °C, and 90 °C for unstressed X70 carbon steel samples immersed for 5 hours in H₂S liquid environment). Each set of observations (pit depths at one specific temperature) is shown by four adjacent points in Figure 3; therefore, the first four points on the left side related to the pit depths at 35 °C, the next four points related to those of 45 °C, and so forth. As can be seen, the pit depths at 35 °C have the strongest autocorrelation (least randomness) while the ones at 90 °C have the weakest autocorrelation (most randomness); the values at 45 °C, 75 °C have the second and third ranks. Therefore, the pits generated at 35 °C have almost the same depths, while those produced at 90 °C have more depth variations.

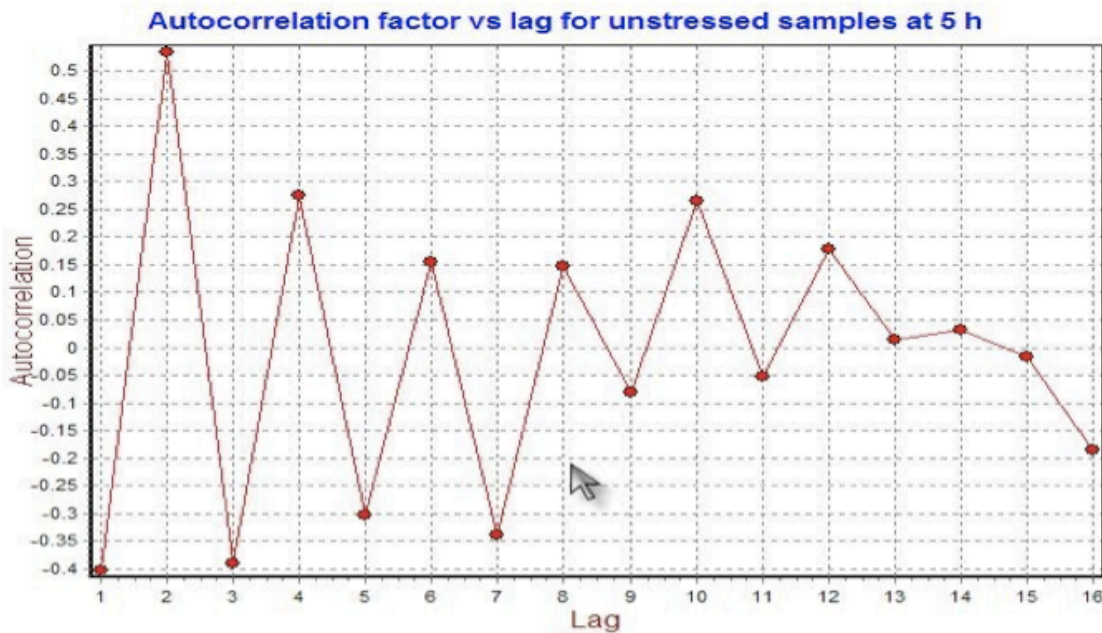


Figure 3. Autocorrelation factor versus lag for unstressed X70 carbon steel samples for 5 h in H₂S liquid environment at different temperatures.

3.1.4. Separation of Corrosion-Fatigue Winbugs' Model Program

To update Dr. Chookah's WinBugs- corrosion-fatigue model [35] in a reasonable way, we separated it to corrosion and fatigue terms; then we used the pitting corrosion data (from the intern program) to verify the corrosion model. In doing so, we had to modify some of the WinBugs' model parameters. The model is ready for further data updating.

3.1.5. Creep Model Categorization

Review of creep literature [21-32] shows that there are number of models suggested for creep curve. Some of them are the mere curve fitting, and some provide physical explanation for parts of the creep curve (primary, secondary, and tertiary regions). Among them, only a few models capture the whole creep curve (with or without physical explanation).

According to Dr. Seibi's suggestions (during his visits from our physical laboratory at UMD in July 2010), we are going to write a review article on creep model categorization according to:

- different parts of the creep curve (primary, secondary, and tertiary regions)
- their physical basis, and
- their empirical character.

The classification of the creep models should help to refine our proposed empirical model.

3.2. Experimental Effort in Support of Model Development.

3.2.1. Pitting Corrosion Experiments

We designed and made two three-point grips from steel material for applying definite stress on the samples. The three-point grips with their design schema and the setup for applying different definite stresses on the samples are shown in Figure 4.

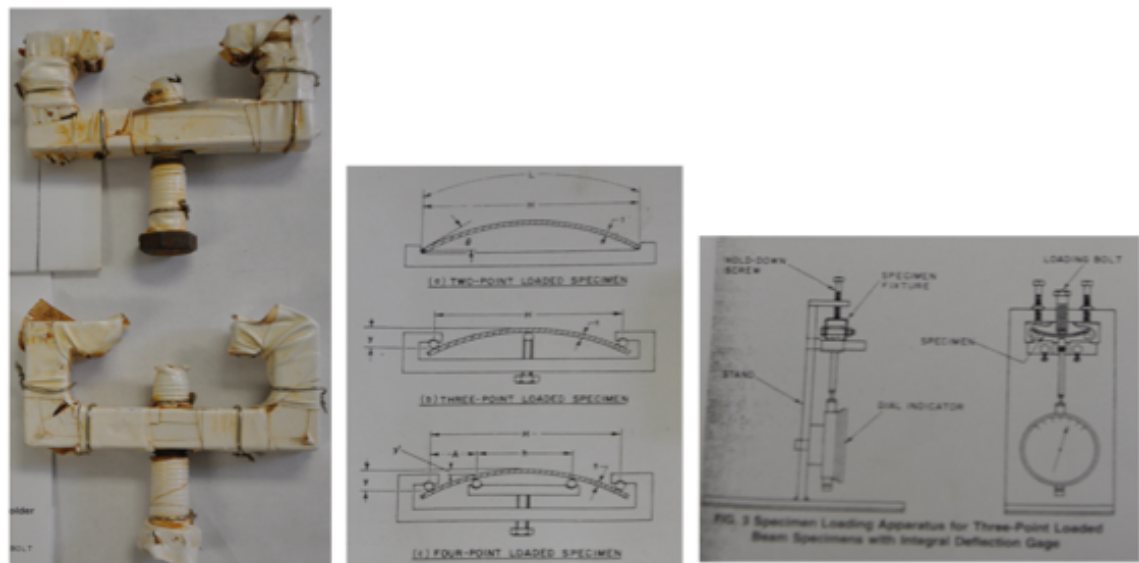


Figure 4. Three-point grips (A), specimens fixed in 3 and 4 point grips (B), and specimen fixed in three-point grip on a stand with dial gauge (C)

The holders are covered with tapes to prevent the reaction between the grips and the stressed sample in the corrosive media.

Since we borrowed our reading dial gauge and the related stand from the UMD physics workshop (and we had to return them every time), we are going to design and make an appropriate stand and buy a dial gauge for our further experiments. Dr. Seibi also suggested that we extend the creep experiment on steel tubes under different purged gases, corrosive environments, and multi-axial stress conditions (for high temperature alloys like 600- and 690 nickel-based stainless steels).

We are planning to realize this suggestion and design the related grips and extensometers. Meanwhile, the UMD PoF-based laboratory has been equipped with strain gauge from National Instrument Corporation (for strain rate estimation).

A long Plexiglas chamber designed (outside of this project) by Mr. Nuhi and Dr. Modarres can now be installed on the MTS machines of the PoF-laboratory and its workability tested for fatigue experiments for reinforced polymer materials.

4. Future Work

Future work will consist of continued model development including model verification and simplification by performing creep experiments of Al 7075 dog-bone shaped specimens and X-70 carbon steel CT specimens.

Near-Future Plans:

Simulation and refinement of the stress and temperature dependency of creep parameters of mechanistic models (PoF models) for creep will be performed. The related report will be submitted.

The corresponding simulation and statistical tool to help both model development and field applications will be done.

A stainless steel chamber is now planned to extend the measurements capabilities of the laboratory for measuring different samples under different gas atmospheres. The creep experiments should be performed according to an acceptable time schedule. These experiments would test the validity of stress and temperature dependencies of our creep model.

We are going to design the related grips and extensometers for a multiaxial creep experiments.

We will design and make the stand for three-point grips and buy a dial gauge for measuring the stress applied on the specimens. A dial gauge measures the amount of deflection (or bending) of the samples, which are under stressed in the grips.

Appendix

Background

A number of deterministic models have been proposed to assess reliability and life-remaining assessment of pipelines. Among these models is the ASME B31G code, which is most widely used for the assessment of corroded pipelines. However, these models are highly conservative and lack the ability to estimate the true life of the pipelines and other equipment used in the oil industry. To address this shortcoming one needs to develop a best-estimate assessment of the life (to assess reliability and risk imposed) by these structures and equipment and assess the uncertainties surrounding such estimates. The proposed probabilistic mechanistic models, when fully developed, would integrate the physics of failure of the leading failure degradation phenomena in the oil industry into the formal risk and reliability assessments. Such physical models will be validated using a state of the art reliability assessment laboratory (being developed at PI). Uncertainties about the model structures and parameters will also be quantified. Such models will incorporate inspection data (characterizing limited and uncertain evidences). The rate of degradation is influenced by many factors such as pipeline materials, process conditions, geometry and location. Based on these factors, a best estimate of the structure (pipeline) or equipment (primarily valves, pumps and compressors) service life (reliability and remaining life) is to be calculated and uncertainties associated with the service life quantified. This estimate would serve as a basis that guides decisions regarding maintenance and replacement practices.

Phase I of this research focused on developing a corrosion-fatigue model. It successfully proposed such a model and developed an advanced laboratory for testing this phenomenon at PI. The current research continues in the same line of research by investigating and developing additional degradation phenomena (SCC, pitting corrosion, and creep-fatigue) and integrates these phenomena with reliability and risk assessment through four different tasks. The long-term objective of this research is to develop a comprehensive library of probabilistic mechanistic models for all degradation phenomena pertinent to structures (piping, and pressure vessels) used in the oil industry.

Approach

The test rig, which is currently installed at UMD and is expected to be installed at PI later, will be used by the GRA, Mr. Mohammad Nuhi, to conduct an experimental study reflecting field conditions for model validation developed in EERC phase I & II. The equipment needed would include corrosion test cells, autoclaves, multiphase flow loops, and testing machines for slow strain rate and crack growth testing. This activity also requires a complete line of monitoring equipment for evaluation of corrosion, scaling, and chemical treatment for field and laboratory. This test rig will be a useful tool for teaching, research, and possibly training field engineers from operating companies.

Two-Year Schedule

This project involves three distinct tasks. The first task is the development of the mechanistic models, development of a corresponding simulation tool to help both model development and field applications. The second task focuses on experimental activities to generate relevant data to validate the proposed models of Task 1. Finally, the third task involves the actual validation of the models proposed in Task 1 with the experimental results obtained in Task 2, including Bayesian estimation of the model parameters.

Task 1: Develop the best estimate mechanistic (physics of failure) empirical models for creep, pitting corrosion, SCC. The model development involves the following activities.

Task1.1: Gather, review and select most promising physics of failure based methods and algorithms proposed in the literature.

Literature surveys for creep and stress corrosion cracking (SCC) degradation mechanisms are almost completed and will be classified for finding the relevant models (100% done).

Task1.2: Select, develop or adopt a detailed mechanistic model (one deterministic model for each phenomenon) that properly describes the degradation process.

Development of the mechanistic models and of a corresponding simulation tool to help both model development and field applications after classifying the models and choosing the appropriate one should be done in the next future (70% complete).

Task 1.3: Develop a Monte-Carlo based mathematical simulation routine on Matlab depicting the detailed mechanistic model of each degradation phenomenon (far faster than real-time).

This part was completed for the empirical model developed based on the works of the PI interns for pitting corrosion. After proposing the similar models for SCC and creep, it will be repeated (60% completed).

Task 1.4: Based on the results of the simulation a simplified empirical model that best describes the results of simulation will be proposed. Such a model relates the degradation (e.g., depth of the pit or the crack growth rate) to applied loads such as pipeline internal pressure and chemical composition of the product inside the pipeline, as a function of time or cycle of load application.

This part is completed for the pitting corrosion and corrosion-fatigue, but further work will be done for the other failure mechanisms (65% complete).

Task 2: A PoF reliability analysis laboratory has been designed and being developed at PI. Currently, the advanced corrosion-fatigue purchased by the PI was installed at the University of Maryland (the Cortest Rig) has already been sent to Cortest to ship to PI. The equipment is already in PI.

Task 2.1: Completing the remaining corrosion-fatigue tests being conducted by Mr. Nuhi and Chookah. (100% Completed)

Task 2.2: Pitting Corrosion Experiments (develop test plan, prepare samples and the facility, perform the test, and evaluate the test results) (100% Completed).

Task 2.3 SCC Experiments (develop test plan, prepare samples and the facility, perform the test, and evaluate the test results). (Not started yet)

This task will be done in the next future but SCC specimen holders have already designed and made according to the recent patents and ASTM-Standard.

Task 2.4 Creep Experiments: The equipments and samples are completely ready (100% completed); the tests will be performed in future and the results will be evaluated.

A small-scaled corrosion-fatigue (or creep) chamber has been designed (not as part of this project), made and tested for dog-bone specimens and checked its workability on the UMD MTS machines using an Aluminum alloy sample. Another more sophisticated one has been already designed and tested for CT-specimens and is tested. Moreover, another chamber has been made for long specimens.

A heating chamber has been designed and tested for creep experiments.

Task 3: This task involves modification, advancement and use of the WinBugs' Bayesian formalism for model validation using experimental data and integration of the field data and information including sensor-based data (acoustics and/or optical) to update the empirical models and estimate the remaining life of oil pipelines and structures. (60% Complete)

The WinBugs' Bayesian formalism for model estimation and validation was developed as part of Dr. Chookah's work. This formalism is being updated and new applications of the formalism have been performed using past experimental data and new data of corrosion and fatigue obtained since departure of Dr. Chookah. Further work with this software for integration the experimental data has already be done.

Schedule/Milestones/Deliverables

Tasks 1.1-1.3 (5/1/09-12/15/09); Task 1.4 (12/15/09-3/1/10); Task 2.1 (completed 7/1/09); Task 2.2 (7/1/09-12/15/09); Task 2.3 (12/15/09 – 6/1/10); Task 2.4 (6/1/10-2/1/11); Task 3 (12/15/09-3/15/11).

The Cortest rig was boxed and shipped to the Cortest Corporation to test and send to PI; Cortest equipment is already in PI.

The project is on schedules and there is no issue or delay at this point.

Dr. Seibi was appointed as a Co-Advisor of Mr. Nuhi.

Visits

Dr. A.Seibi visited UMD in July 2009

Dr. A.Seibi visited UMD in July 2010

Two PI students Abdullah Al Tamimi, and Mohammad Abu Daghah took parts at summer internship (2009).

PI student, Taher Abu Seer took parts at summer internship (2010).

Prof. Modarres attended the 1st Annual PI Partner Schools Research Workshop. The Petroleum Institute, Abu Dhabi, U.A.E. January 6-7, 2010.

Papers published and prepared for publishing by the team

M. Chookah, M. Nuhi, and M. Modarres, "Assessment of Integrity of Oil Pipelines Subject to Corrosion-Fatigue and Pitting Corrosion", presented by Prof. Modarres at the International Conference of Integrity- Reliability-Failure (IRF) in Porto, Portugal, July 20-24 2009. (The cost of the conference and associated travels was not covered by EERC)

M. Chookah, M. Nuhi, and M. Modarres, A. Seibi "A Probabilistic Physics of Failure Model for Prognostic Health Monitoring of Piping Subject to Pitting and Corrosion –Fatigue" is sent for publication to the "Journal of Reliability Engineering and System Safety".

A paper on "Development of a Database of Mechanistic Models of Failure for Application to Pipeline and Equipment Risk, Reliability and Health Management (Pitting Corrosion- Pit Depth and Density), prepared for publication at a conference. We are studying the possibility that the PI interns present the paper.

References on creep for evaluation of a new empirical model:

- [1] Spiegelhalter, D., Thomas, A., Best, N., and Lunn, D. (2003). WinBUGS 1.4 Manual
- [2] Metal Handbook,(ASTM), Jeffery C. Gibeling “Creep deformation of Metals, polymers, ceramics, and composites”.vol.8, Metal testing and evaluation p363-382, 2000
- [3] Metal Handbook,(ASTM), Howard R. Voorhees, “Assessment and use of Creep-Rupture properties”, vol. 8, Metal testing and evaluation p383-397, 2000
- [4] R.-K. Penny and D.L. Marriott, Design for Creep, Chapman & Hall, London. 1971
- [5] Norton, F.H., “The Creep of Steel at High Temperatures”, McGraw-Hill, London, 1929
- [6] Johnson, A.E. et. Al. Multi-axial creep strain/complex stress/time relations for metallic alloys with some applications to structures, in ASME/ASTM/I Mech. E, Proceedings Conference on creep, Inst. Mech. E., New York/London
- [7] Dorn, J.E. “Some fundamental experiments on high temperature creep, J.Mech.Phys.Solids,3,(1955)
- [8] Soderberg, C.R. The interpretation of creep tests for machine design Trans. ASME,58 (1936)
- [9] McVetty, P.G. Working stresses for high temperature service, Mech. Eng.,56,(1934);
- [10] Garofalo, F. “Fundamentals of creep and creep rupture in metals”, Mac Millan, New York.
- [11] R.W. Evans and B. Wilshire,” Introduction to creep”, The institute of materials,1993,
- [12] R.W. Evans and B. Wilshire, *Creep of Metals and Alloys* (London: The Institute of Metals, 1985), pp. 203–243.
- [13] Levi de Oliveira Bueno, “ Effect of oxidation on creep Data: Part 2- A procedure for Assessing the effect of oxidation on Constant Stress or Constant load Creep curves using the Theta-Projection Concept”, ECCC Creep Conference, 12-14 September 2005,London.p890-899.,
- [14] A.Klenk, et.al., “Experimental and Numerical Investigations on Creep Damage Evolution”, Key Eng. Mats., Vols. 171-174 (2000) pp.25-34, Trans. Tech. Publications, Switzerland
- [15] M.S.ABU-Haiba, et.al., “ Creep deformation and monotonic stress-strain behavior of Haynes Alloy 556 at elevated temperature”, Journal of material science 37 (2002) 2899-2907
- [16] T.H. Hyde, “Creep of materials and structures, Mechanical Engineering Publications,
- [17] London, 1994
- [18] Mohammad Modarres, et.al. “Reliability Engineering and Risk Analysis, a practical guide, CRC Press, Taylor and Francis Group, 2010
- [19] Andrew Gelman et.al. “ Bayesian Data Analysis”, Chapman and Hall, London, 1995
- [20] [Pitting corrosion fatigue model](#) : Hoepfner (1971), and Kondo (1989) -model, corrosion-doctors.org/Journal-2000/No3/No3-table-2.htm
- [21] Kondo, Y. (1989). “Prediction of Fatigue Crack Initiation Life Based on Pit Growth,
- [22] Corrosion, 45, 7-11.
- [23] B.F. Dyson ISI J International, Vol. 30 (1990), No, 10, pp. 802-81
www.ami.ac.uk/courses/topics/0124_seom/index.html
- [24] S.R. Holdsworth, et al.” Factors influencing creep model equation selection, International Journal of pressure vessels and piping 85 (2008) 80-88
- [25] K. Sawadw, et.al.” Analysis of long-term creep curves by constitutive equations”. Material
- [26] Science and engineering A 510-511(2009), 190-194
- [27] V. Srivastava, et al. “Low stress creep behavior of 7075 high strength aluminum alloy.
- [28] Material science and engineering A 382 (2004), 50-56
- [29] B. Wilshire and H. Burt, “A unified theoretical and practical approach to creep and creep fracture”, Materials science and engineering. 3-12.2005
- [30] S. Chaudhuri and R.N. Ghosh, “Creep behavior of 2.2Cr1Mo steel-Effects of thermal ageing and pre-strain, Material science and engineering A 510-511 (2009),136-141
- [31] M. Law et al. International journal of pressure vessels and piping 75 (1998) 437-442
- [32] SR. Holdsworth, “Developments in the assessment of creep strain and ductility data”. Material High Temperature 2004;21(1):125-132

- [33] R.W. Swindeman, M.J. Swindeman, "A comparison of creep models for nickel based alloys for advanced energy systems", *International journal of pressure vessels and piping* 85 (2008) 72-79
 A. Feher et al., in *FVW/FVHT*, Stahl-Zentrum Duesseldorf, Germany 28.Nov.2008
- [34] K. Maruyama and H. Oikawa, *Trans. ASME, J. Press. Vessel. Technol.* 109, 142 (1990)
- [35] K. Maruyama and H. Oikawa, *J. Jpn. Inst. Met.* 55, 189 (1991)
- [36] "Corrosion Pitting Shapes", [online], available at: <http://corrosion-doctors.org/Forms/pitting/shapes.htm>
- [37] Engineering Statistics Handbook; online; available at: http://www.itl.nist.gov/div898/handbook/eda/section3/autocopl.htmqualityamerica.com/knowledgecenter/knowctrInterpreting_an_Autocorrelation.htm
- [38] Mohamed Chookah, "Structuring a Probabilistic Model for Reliability Evaluation of Piping Subject to Corrosion-Fatigue Degradation", Doctor of Philosophy, University of Maryland;
- [40] 2009

References on creep for evaluation of a new empirical model

- [1] Metal Handbook,(ASTM), Jeffery C. Gibeling "Creep deformation of Metals, polymers, ceramics, and composites".vol.8, Metal testing and evaluation p363-382, 2000
- [2] Metal Handbook,(ASTM),Howard R. Voohees, "Assessment and use of Creep-Rupture properties", vol. 8, Metal testing and evaluation p383-397, 2000
- [3] R.-K.Penny and D.L.Marriott, *Design for Creep*, Chapman & Hall,London. 1971
- [4] T.H.Hyde, "Creep of materials and structures,Mechanical Engineering Publications, London,1994
- [5] R.W.Evans and B. Wilshire," Introduction to creep", The institute of materials,1993
- [6] S.R.Holdsworth ,et al." Factors influencing creep model equation selection, *International journal of pressure vessels and piping* 85 (2008) 80-88
- [7] K. Sawadw,et al.; "Analysis of long-term creep curves by constitutive equations"; *Material science and engineering A* 510-511(2009),190-194
- [8] V. Srivastava,et al. "Low stress creep behavior of 7075 high strength aluminium alloy. *Material science and engineering A* 382 (2004),50-56
- [9] B. Wilshire and H.Burt, "A unified theoretical and practical approach to creep and creep fracture", *Materials science and engineering*,p. 3-12.2005
- [10] S.Chaudhuri and R.N.Ghosh, "Creep behavior of 2.2Cr1Mo steel-Effects of thermal ageing and pre-strain, *Material science and engineering A* 510-511 (2009),136-141
- [11] B.F.Dyson *ISI J International*, Vol. 30 (1990), No. 10, pp. 802-81
- [12] www.ami.ac.uk/courses/topics/0124_seom/index.html
- [13] M. Law et al. *International journal of pressure vessels and piping* 75 (1998) 437-442
- [14] Woo-Gon et al.; "Creep Characterization of a Ni-Based Hastelloy-X Alloy by Using Theta Projection Method"; *Engineering Fracture Mechanics* 75 (2008) 4985-4995.
- [15] SR. Holdsworth, "Developments in the assessment of creep strain and ductility data". *Material High Temperature* 2004;21(1):125-132
- [16] R. W. Swindeman, M. J. Swindeman, "A comparison of creep models for nickel based alloys for advanced energy systems", *International journal of pressure vessels and piping* 85 (2008) 72-79
 A. Feher et al.; "An Interactive Application for Assessment of Creep Equations"; *FVW/FVHT*; 31. Vortragsveranstaltung am 28, November 2008.
- [17] R.W. Evans and B. Wilshire, *Creep of Metals and Alloys* (London: The Institute of Metals, 1985), pp. 203–243.
- [18] K. Maruyama and H. Oikawa, *Trans. ASME, J. Press. Vess. Technol.* 109, 142 (1990)
- [19] K. Maruyama and H. Oikawa, *J. Jpn. Inst. Met.* 55, 189 (1991).
- [20] "Creep and stress rupture" www.materialsengineer.com/CA-Creep-Stress-Rupture.htm
- [21] Xiao-Chi Nin et al." Creep damage prediction of the steam pipelines with high temperature and high pressure. *International Journal of Pressure Vessels and Piping* 86 (2009) 593–598ure".

- [22] T.H. Hyde, A. Yaghi and M. Proctor, Use of the reference stress method in estimating the life of pipe bends under creep conditions, *Int J Press Vessels and Piping* **75** (2) (1998), pp. 161-169.
- [23] W. Sun, T.H. Hyde, A.A. Becker and J.A. Williams, Comparison of the creep and damage failure prediction of the new, service-aged and repaired thick-walled circumferential CrMoV pipe welds using material properties at 640 °C, *Int J Press Vessels and Piping* **77** (7) (2000), pp. 389–398.
- [24] W. Sun, T.H. Hyde, A.A. Becker and J.A. Williams, Steady-state creep reference rupture stresses for internally pressurised pipes for use in life prediction, *Int J Press Vessels and Piping* **79** (2) (2002), pp. 135–143.
- [25] S.-T. Tu, R. Wu and R. Sandstrom, Design against creep failure for weldments in 0.5 Cr 0 Mo 0.25 V pipe, *Int J Press Vessels and Piping* **58** (3) (1994), pp. 345 – 354.
- [26] J.M. Gong, S.T. Tu and X. Ling, Research of welding effect on creep damage of high temperature furnace tubes, *Key Eng Mat* **171–174** (2000), pp. 189–196.
- [27] Chen JJ. Investigation of design criterion and welding repair principle of high temperature components using continuum damage mechanics based finite element method. Ms. D thesis. Nanjing University of Technology: Nanjing; 2002 [in Chinese].
- [28] T.H. Hyde, W. Sun and J.A. Williams, Prediction of creep failure life of internally pressurized thick walled CrMoV pipes, *Int J Press Vessels and Piping* **76** (14–15) (1999), pp. 925–933.
- [29] S.T. Tu, P. Segle and J.M. Gong, Creep damage and fracture of weldments at high temperature, *Int J Press Vessels and Piping* **81** (2) (2004), pp. 199–209.
- [30] S.T. Tu, P. Segle and J.M. Gong, Strength design and life assessment of welded structures subjected to high temperature creep, *Int J Press Vessels and Piping* **66** (1–3) (1996), pp. 171–186.
- [31] D.R. Hayhurst, P.R. Dimmer and C.J. Morrison, Development of continuum damage in the creep rupture of notched bars [J], *Philos Trans R Soc Lond* **A311** (1984), pp. 103–129.
- [32] W. Blume, P. Eisenlohr, “Understanding Creep—a Review”, *Metallurgical and Materials Transactions A* Vol. 33A, 2002—291.
- [33] Yongsun Yi et al.; “Stress and Temperature Dependence of Creep in Alloy 600 in Primary Water”, *Metallurgical and Materials Transactions A* Vol. 32A, OCTOBER 2001—2553.
- [34] J M Brear, C J Middleton, “ The applicability of weld failure prediction maps to new and service-exposed repair welds”, in www.seseurope.com
- [35] M. Aghaie-Khafri1 , S. Farahany, “ Creep Degradation of Thermally Exposed IN738C Superalloy”, *Journal of Engineering for Gas Turbines and Power*, MAY 2009, Vol. 131 / 034501-1
- [36] R. F. Miller R. L. Sindelar. “Analysis for Materials Test Reactor (MTR Fuel Assemblies in Dry Storage)”, WSRC-TR-95-OI 21
- [37] Yoshiharu Kariya et al.; “The Constitutive Creep Equation for a Eutectic Sn-Ag Alloy Using the Modified Theta Projection Concept”; *Journal of Electronic Materials*; Vol. 32, No. 12; 2003
- [38] Stefan Holmstroem, “Engineering Tools for Robust Creep Modeling”, VIT Publications 728.
- [39] T. Hullstein et al., “Fracture Mechanics characterization of crack growth under creep conditions.” *The Journal of Strain Analysis for Engineering Design*, Vol. 23, No 2. 1988
- [40] S.H Ryu et al. “Quasi steady state creep crack growth in a 3.5 NiCrMoV Steel.” *Metallurgical & Material Transactions A*. Vol. 28. No 3 1997.
- A. Conte. “Experimental and numerical investigations on the creep crack growth in IM 718.”
www.icf11.com/proceeding/Extended/5428.pdf